Relativistic dynamics in black hole systems and implications for observations

A thesis

submitted for the degree of

Doctor of Philosophy

in

The Department of Physics,
Pondicherry University,
Puducherry - 605 014, India

by

Prerna Rana
Indian Institute of Astrophysics,
Bangalore - 560 034, India

August 2020

Relativistic dynamics in black hole systems and implications for observations

Prerna Rana

Indian Institute of Astrophysics

Indian Institute of Astrophysics

Bangalore - 560 034, India

Title of the thesis	:	**Relativistic dynamics in black hole systems and implications for observations**
Name of the author	:	**Prerna Rana**
Address	:	Indian Institute of Astrophysics 2nd Block, Koramangala Bangalore - 560 034, India
Email	:	prernarana@iiap.res.in
Name of the supervisor	:	**Prof. Arun Mangalam**
Address	:	Indian Institute of Astrophysics 2nd Block, Koramangala Bangalore - 560 034, India
Email	:	mangalam@iiap.res.in

Declaration of Authorship

I hereby declare that the matter contained in this thesis is the result of the investigations carried out by me at the Indian Institute of Astrophysics, Bangalore, under the supervision of Prof. Arun Mangalam. This work has not been submitted for the award of any other degree, diploma, associateship, fellowship, etc. of any other university or institute.

Signed:  (Prerna Rana, SRF-IIA)

Date: 14/12/2020

Certificate

This is to certify that the thesis entitled **'Relativistic dynamics in black hole systems and implications for observations'** submitted to the Pondicherry University by Ms. Prerna Rana for the award of the degree of Doctor of Philosophy, is based on the results of the investigations carried out by her under my supervision and guidance, at the Indian Institute of Astrophysics. This thesis has not been submitted for the award of any other degree, diploma, associateship, fellowship, etc. of any other university or institute.

Signed: Anna Mangalam (Prof. A. Mangalam)

Date: 14/12/2020

List of Publications

Refereed Publications

1. *Astrophysically relevant bound trajectories around a Kerr black hole,*

   Prerna Rana & Mangalam, A. 2019, Class. Quant. Grav. 36, 045009 (pp28), doi: 10.1088/1361-6382/ab004c; arXiv:1901.02730 (pp49).

   Chapter 3 and 4

2. *A Geometric Origin for Quasi-periodic Oscillations in Black Hole X-Ray Binaries,*

   Prerna Rana & A. Mangalam, 2020, ApJ, 903 (2), 121 (pp41), doi: 10.3847/1538-4357/abb707; arXiv:2009.01832 (pp60).

   Chapter 5

3. *A Relativistic Orbit Model for Temporal Properties of AGN,*

   Prerna Rana & A. Mangalam, 2020, Galaxies, 8 (3), 67 (pp28), doi: 10.3390/galaxies8030067; arXiv:2009.03061 (pp28).

   Chapter 6

4. *Bound orbit domains in the phase space of the Kerr geometry,*

   Prerna Rana & Mangalam, A. 2020, submitted to the proceedings of The Fifteenth Marcel Grossmann Meeting. (under review)

   Chapters 3

5. *Eccentric equatorial trajectories around a Kerr black hole as a QPO model for M82X-1,*

   Prerna Rana & Mangalam, A. 2020, submitted to the proceedings of The Fifteenth Marcel Grossmann Meeting. (under review)

   Chapter 3 and 5

Under Preparation

6. *Separatrices in Kerr spacetime and energy level diagrams,*

   Prerna Rana & A. Mangalam, 2020, in preparation.

   Chapter 7

7. *Light echoes in Kerr spacetime,*

   Prerna Rana & A. Mangalam, 2020, in preparation.

   Chapter 7

Presentations

1. Oral presentation titled "A dynamical model for QPO frequencies in BHXRB" in REcent Trends in the study of Compact Objects - IV, April 17-20, 2019, IUCAA, Pune, India.

2. Oral presentation titled "Commensurability of QPO Frequencies in BHXRB" in The 15th Marcel Grossmann meeting, Rome, Italy, July 1-7, 2018, Italy.

3. Poster presentation titled "Alternate Forms for Trajectories of Bound Orbits in Kerr Geometry" in The 15th Marcel Grossmann meeting, Rome, Italy, July 1-7, 2018, Italy.

4. Oral presentation titled "Dynamics of bound orbits in Kerr geometry and QPO frequency ratios" in Astronomical Society of India meeting, March 6-10 , 2017, Jaipur, MP Birla Auditorium, India.

5. Oral presentation titled "Kinematic models for QPOs in BHXRBs" in Wide Band Spectral and Timing Studies of Cosmic X-ray Sources, January 10-13, 2017, TIFR, Mumbai, India.

6. Oral presentation titled "Parameter study of QPO models" in Jet Triggering Mechanisms in Black Hole Sources, January 20-23, 2016, TIFR, Mumbai, India.

Acknowledgements

First, I would like to express my immense gratitude and sincere regards to my supervisor Prof. Arun Mangalam for his invaluable guidance, encouragement, accessibility, and being constantly involved throughout my work. He has always helped me with the smallest of my doubts in physics. His perspectives, expertise in the subject, and immense knowledge were extremely useful for my Ph.D. work. It is a pleasure working with him.

My sincere thanks to my doctoral committee members Prof. G. Ramesh Babu and Prof. C. S. Stalin and the staff at the Pondicherry University for their timely help and relevant suggestions.

I would thank all the staff members of the Vainu Bappu Observatory, Kavalur (Indian Institute of Astrophysics), for the hospitality provided during my visits.

I am thankful to IIA for providing an excellent academic environment and the necessary facilities including the HPC for my research work during my tenure. I thank Mr. Saikat Das for help with a few schematic figures.

I acknowledge, with utmost regards and gratitude, the unconditional support, blessings, and love of my parents. I am lucky to have received huge emotional support. I would also like to thank my sister Urvashi and my brother-in-law Nitin for their love and always being there for me. Last, but not least, I would like to thank my niece Nishka for being a constant source of happiness for me. My words are never enough to thank them.

I also thank all my friends and fellow students at the IIA for their constant support and encouragement. I also thank my teachers for always supporting and encouraging me.

Dedicated to

my

loving parents

Abstract

The study of bound particle trajectories around a rotating black hole is crucial to the understanding of many astrophysical processes like accretion on to a black hole, relativistic precession, and Gravitational waves from extreme-mass ratio inspirals. We study various bound trajectories in the Kerr spacetime. We have derived new closed-form analytic solutions for the non-equatorial eccentric bound particle trajectories, $\{\phi\left(r,\theta\right),\ \ t\left(r,\theta\right),\ r\left(\theta\right)\}$, around a spinning black hole by using the transformation $1/r=\mu\left(1+e\cos\chi\right)$. The trajectories are completely expressed in the (e, μ, a, Q) parameter space by implementing the translation relations between energy and angular momentum of the particle, (E, L), and eccentricity and inverse-latus rectum, (e, μ), for a given spin, a, and Carter's constant, Q. We derive the necessary bound orbit conditions to select the allowed combinations of (e, μ, a, Q), and specialized formulae for equatorial, spherical and separatrix orbits. We study non-equatorial separatrix trajectories, where a homoclinic orbit asymptotes to an energetically bound spherical orbit of radius r_s, and derived exact expressions for e and μ as functions of $\{r_s,\ a,\ Q\}$, and their trajectories for ($Q\neq0$) separatrix orbits; they are also shown to reduce to the equatorial case. We also obtain closed-form expressions of the fundamental frequencies of non-equatorial eccentric trajectories. The application of these solutions is straightforward and numerically fast.

We apply these results to extend the relativistic precession model (RPM) for Quasi-periodic oscillations (QPOs) in black hole X-ray binaries (BHXRB) to associate the fundamental frequencies of the general eccentric trajectories with the QPO frequencies. We call this a generalized relativistic precession model (GRPM). For this study, we take up the cases of BHXRB GRO J1655-40, M82 X-1, XTE J1550-564, 4U 1630-47, and GRS 1915+105. For BHXRB M82 X-1 and GRO J1655-40, we find trajectory solutions at $\{e=0.230^{+0.067}_{-0.049},\ r_p=4.834^{+0.181}_{-0.268},\ a=0.299,\ Q=2.362^{+1.519}_{-1.439}\}$ for M82

X-1, and at $\{e = 0.071^{+0.031}_{-0.035},\ r_p = 5.25^{+0.171}_{-0.142},\ a = 0.283,\ Q = 0^{+0.623}\}$ for GRO J1655-40. We see that the trajectories within the range of parameter errors, giving frequencies in the range of width of the QPO, when taken together, span a torus region and should together give rise to a strong QPO signal in the power spectrum. We also suggest that the inner edge radius of the circular accretion disk, r_{in}, should be near this torus region. For BHXRB 4U 1630-47, and GRS 1915+105, we find highly eccentric and equatorial orbit solutions, where better estimates of spins are required to make a reasonable prediction for the orbital parameters. We also find spherical orbit solutions in the cases of BHXRB M82 X-1 and XTE J1550-564 with $\{r_s = 6.044^{+0.071}_{-0.072},\ a = 0.321 \pm 0.013,\ Q = 6.113^{+2.124}_{-1.645}\}$ and $\{r_s = 5.538 \pm 0.054,\ Q = 2.697^{+1.738}_{-1.627}\}$ respectively. We also find an equatorial eccentric solution for BHXRB XTE J1550-564 at $\{e = 0.262^{+0.090}_{-0.062},\ r_p = 4.365^{+0.169}_{-0.279}\}$. We also show that the eccentric orbit solution fits the PBK correlation observed in BHXRB GRO J1655-40. Our analysis of the fluid flow in the relativistic disk edge suggests that instabilities cause QPOs to originate in this region which, then, follows geodesic in the torus region.

We also discuss QPOs in the X-rays seen in Seyferts, γ-ray and optical band QPOs that are seen in Blazars which are attributed to plasma motion in the corona or jets of these AGN. We apply the GRPM and deduce orbital parameters like the radius of the emission region, and spin parameter a for a circular orbit, while we obtain Carter's constant Q, a, and the radius in the case of a spherical orbit solution for the two simultaneous QPOs seen in NLSy1 1H 0707-945. In other cases where only one QPO is seen we localize the orbital parameters for REJ 1034+396, 2XMM J123103.2+110648, MS 2254.9-3712, Mrk 766, and MCG-06-30-15. By applying the lighthouse model, we find that a kinematic origin of the jet QPOs in a relativistic MHD is plausible. Based on the inbuilt Hamiltonian formulation with a power-law distribution in the energy of the plasma consisting of only circular or spherical trajectories, we show that the resulting PSD has a break corresponding to the energy at ISCO. Further, we derive connection formulae between the slopes in the PSD and that of the energy distribution. Overall, given the preliminary but promising results of these relativistic orbit models,

to match the QPO frequencies and PSD at diverse scales in the inner corona and the jet, it motivates us to build detailed models for the energy spectrum in the corona and relativistic MHD jet models of plasma flow and polarization properties.

We are currently working on the study of the distribution of energy levels of closed and periodic non-equatorial orbits and deriving the simplest form of the separatrix surface in (e, Q, μ, a) space. We also discuss future work stemming from the ideas in this Thesis.

Contents

Abstract **i**

List of Figures **ix**

List of Tables **xix**

1 Overview **1**
1.1 Introduction 1
1.2 The Kerr black holes 3
1.2.1 Important properties of the Kerr geometry 4
1.2.2 Radial milestones in the Kerr geometry 5
1.3 Observations of black holes 12
1.3.1 Black hole X-ray binaries (BHXRB) 13
1.3.2 Intermediate mass black holes (IMBH) 18
1.3.3 Active galatic nuclei (AGN) 19
1.3.4 The spin and mass measurement of black holes 22
1.3.5 Importance of integrals of motion (IOM) in black hole dynamics 26
1.4 Goals of the Thesis 27
1.5 Plan of the Thesis 28
1.6 Resource summary 30

2 Hamilton-Jacobi dynamics in Kerr geometry **32**
2.1 Introduction 32
2.2 Equations of geodesic motion in the Kerr geometry 33
2.2.1 Hamilton-Jacobi equation 35
2.2.2 The radial effective potential 38
2.2.3 Positivity of $R(r)$ and $\Theta(\theta)$ 39
2.3 History of the solution to Hamilton-Jacobi equation in Kerr geometry 40
2.4 Resource summary 42

3 Bound orbit conditions for time-like trajectories in Kerr spacetime **44**
3.1 Introduction 44

3.2 Translation relations between (E, L) and (e, μ) 47
3.3 Conditions for bound trajectories around Kerr black hole 51
3.3.1 Dynamical parameter space (E, L, a, Q) 51
3.3.2 Conic parameter space (e, μ, a, Q) 61
3.4 Equatorial eccentric bound orbits ($Q = 0$) 70
3.4.1 Bound orbit conditions in the dynamical parameter space, $\{E, L, a\}$ 70
3.4.2 Bound orbit conditions in the conic parameter space $\{e, \mu, a\}$ 78
3.5 The prescription for selecting bound orbits 83
3.6 Summary 87

4 Astrophysically relevant bound trajectories around a Kerr black hole 90
4.1 Introduction 90
4.2 Integrals of motion and bound orbits around Kerr black hole 95
4.2.1 Analytic solutions of integrals of motion 95
4.2.2 Bound orbit conditions in conic parameter space 99
4.3 Fundamental oscillation frequencies 101
4.4 Equatorial and eccentric bound orbits ($e \neq 0$, $Q = 0$) 104
4.5 Spherical orbits ($e = 0$, $Q \neq 0$) 108
4.5.1 Energy and angular momentum of spherical orbits 108
4.5.2 Trajectory solution for spherical orbits 109
4.5.3 Fundamental frequencies of spherical trajectories 110
4.6 Non-equatorial separatrix trajectories 112
4.6.1 Exact expressions of conic variables for non-equatorial separatrix orbits 114
4.6.2 Exact forms for the non-equatorial separatrix trajectories . . 118
4.7 Consistency check with previous results 120
4.8 Trajectories 122
4.9 Applications 130
4.10 Summary 135
4.11 Discussion and Conclusions 138

5 A geometric origin for QPO frequencies in BHXRB 140
5.1 Introduction 140
5.2 Generalized Relativistic Precession model (GRPM) 145
5.2.1 Non-equatorial and equatorial eccentric orbits: eQ and $e0$. 152
5.2.2 Spherical orbits: $Q0$ 158
5.3 Parameter estimation of orbits in black hole systems with observed QPOs 160
5.3.1 Source selection 163
5.3.2 Method used and results 165
5.4 The PBK correlation 189

5.5 Gas flow near ISSO (ISCO) . . . 193
5.6 Discussion, caveats, and conclusions . . . 196

6 A relativistic orbit model for QPOs in AGN 206
6.1 Introduction . . . 206
6.2 Relativistic circular and spherical orbits as solutions to X-ray QPOs 209
6.2.1 Circular orbits . . . 211
6.2.2 Spherical orbits . . . 215
6.3 Relativistic jet model for the optical and γ ray QPOs . . . 219
6.4 Relativistic orbit model (ROM) and PSD shape . . . 221
6.4.1 The ROM . . . 223
6.5 Summary . . . 231
6.6 Discussion, caveats, and conclusions . . . 233

7 Summary, caveats, and conclusions 236
7.1 Highlights . . . 237
7.2 Novel aspects and their impact . . . 242
7.3 Caveats . . . 246
7.4 Future directions . . . 247

A 252
A.1 Solution of integrals I_1-I_8 . . . 252
A.2 Reduction to the equatorial plane ($Q = 0$) . . . 257
A.3 Innermost stable and marginally bound spherical radii . . . 261
A.4 Solution of (e_s, μ_s) in the equatorial separatrix case . . . 264
A.5 Reducing the radial integrals for the case of non-equatorial separatrix trajectories . . . 265
A.6 Derivations for the consistency check with the previous results . . . 267

B 274
B.1 Source history . . . 274

Bibliography 277

List of Figures

1.1 An artistic image of Cygnus X-1. Courtesy: NASA/CXC/M.Weiss. 2
1.2 The horizon of a rotating black hole with $a = 0.86$. Lines of constant ϕ and constant θ are shown on the surface. Courtesy: Hartle (2003). 5
1.3 The horizon and light radii are shown in the equatorial plane of a Kerr black hole with a =0.5, where the point at the center represents the real singularity at $r = 0$. 6
1.4 The Ergosphere along with the horizon radius is shown (a) on a flat plane for $a = 0.95$, Courtesy: Hartle (2003); (b) in the (r, a) plane for $\theta = \pi/2$. The region between r_+ and r_e is the Ergoregion. 7
1.5 The contours of various radii are shown in the (r, a) plane for $Q = 4$, which divide it into various regions, depicted as 1, 2, 3, 4, and 5, which are associated with different types of trajectories around a Kerr black hole (which we discuss in chapter 3 and 4). 10
1.6 The horizon radius (r_+, red), light radius [Eq. (1.9), green ring], MBSO (blue), and ISSO (black) (embedded in flat space), (a) side view, (b) top view, are shown together as the important radial milestones around a Kerr black hole, where $\{a = 0.5, Q = 4\}$. 11
1.7 The figure shows binding energy per unit rest mass $[1 - E(a)]$ of ISCO radius for a Kerr black hole as a function of a, where $a > 0$ is the prograde and $a < 0$ is the retrograde case. 13
1.8 A sketch of 16 BHXRB in the Milky Way is shown. A comparison of the distance is shown with respect to the Sun-Mercury distance at the top. The color of the companion star roughly represents their surface temperature. Courtesy: Remillard *et al.* (2006). 14
1.9 The detection of simultaneous HFQPOs is shown in the PSD of BHXRB GROJ1655-40. Courtesy: Strohmayer (2001a). 16
1.10 The X-ray hardness versus luminosity diagram showing the evolution track of the outburst in BHXRB. Courtesy: Fender and Belloni (2012). 17
1.11 The unification model for AGN showing the main features: accretion disk, BLR, NLR, and the torus region. Courtesy: Urry and Padovani (1995). 20
1.12 The PSD of a narrow-line Seyfert 1 galaxy PKS 0558-504 following the bending power-law, Eq. (1.19). Courtesy: Papadakis *et al.* (2010). 21

1.13 An illustration of (a) periastron, and (b) nodal precession of the relativistic orbits near the equatorial plane of a Kerr black hole. Courtesy: Belloni and Stella (2014). 26
1.14 The plan of the thesis is shown. 31

3.1 The figure shows different bound orbit regions in the (E, L) plane: (a) and (c) represent the prograde cases with $a = 0.5$ and $a = 0.9$ respectively; (b) and (d) show the retrograde cases with $a = -0.5$ and $a = -0.9$ respectively, where we have fixed $Q = 5$. The regions ς and Λ span from $E = 0$ to 1 and $E = 1$ to ∞ respectively, but a limited range of E is shown for convenience. The Δ region is bounded by the curves representing stable, unstable spherical orbits, and $E = 1$. The Λ region is bounded by the inner unstable spherical orbits (IUSO). The points A and B depict the innermost stable spherical orbit (ISSO) and marginally bound spherical orbit (MBSO) respectively. 57
3.2 The figure shows the radial effective potential [Eq. (3.3b)] for different regions of bound orbits, where the horizontal black curve and vertical dashed red curve correspond to $(E^2 - 1)/2$ and the horizon radius respectively, and the arrows depict the bounding region of the orbit. While (a) represents an orbit in region Δ with parameter values $\{E = 0.958818,\ L = 2.65917\}$, (b) represents an orbit in region ς with $\{E = 0.9,\ L = 5\}$, and (c) represents an orbit in the Λ region with $\{E = 2,\ L = 10\}$, where we have fixed $\{a = 0.5,\ Q = 5\}$. Each orbit corresponds to a single point in the Δ, ς, and Λ regions of Fig. 3.1(a). 58
3.3 The figure shows the radial effective potential [Eq. (3.3b)] for various types of spherical orbits, where the horizontal black curve corresponds to $(E^2 - 1)/2$ and the vertical dashed red curve corresponds to the horizon radius: (a) represents a stable spherical orbit with parameter values $\{E = 0.954215,\ L = 2.85451\}$, (b) represents an ISSO with $\{E = 0.926965,\ L = 2.12011\}$ (point A of Fig. 3.1(a)), (c) represents an unstable spherical orbit with $\{E = 0.952441,\ L = 2.38042\}$, (d) represents a MBSO with $\{E = 1,\ L = 2.74974\}$ (B of Fig. 3.1(a)), and (e) represents an IUSO with $\{E = 2.77331,\ L = 10.9958\}$, where we have fixed $\{a = 0.5,\ Q = 5\}$. The turning point $r_1 = \infty$ for both MBSO and IUSO. 59
3.4 The figure shows the bounding curves of the region Δ and Λ in (e, μ) plane each for (a) $a = 0.2$, (b) $a = -0.2$, (c) $a = 0.5$, and (d) $a = -0.5$ with $Q = 5$. The red, blue, and orange curves represent the stable spherical, $E = 1$, and the unstable spherical or separatrix orbits respectively. The points A and B depict ISSO and MBSO respectively. The regions Δ_1 and Δ_2 are replicas of region Δ, when (e_{13}, μ_{13}) and (e_{23}, μ_{23}) are calculated respectively [from Eq. (3.1)] using the real roots of the Δ region. 64

3.5 The upper boundaries of the Δ region are shown in the (e, μ) plane for different (labeled) values of a (a) for prograde, (b) for retrograde orbits with $Q = 5$, and for different values of Q (c) for prograde $a = 0.5$, and (d) retrograde $a = -0.5$ orbits. 67

3.6 The region ς in the (e, μ) plane is shown for (a) ($a = 0.2$, $Q = 2$), and (b) ($a = -0.2$, $Q = 2$). This region is bounded by curves of stable, unstable spherical orbits and the boundary where x gets complex. 69

3.7 The Δ region is shown for comparison in the (a) (E, L) and (b) (e, μ) plane for ($a = 0.5$, $Q = 5$), where points A and B represent ISSO and MBSO respectively. 70

3.8 The figure shows the Δ region for the equatorial eccentric orbits in the (E, L) plane for (a) $a = 0.5$ and (b) $a = -0.5$. The Δ region is bounded by the curves representing stable, unstable circular/separatrix orbits, and $E = 1$. The points A and B depict the innermost stable circular orbit (ISCO) and marginally bound circular orbit (MBCO) respectively. 75

3.9 The figure shows the radial effective potential [Eq. (3.35)] with $\{a = 0.5,\ Q = 0\}$ for (a) an eccentric orbit $\{E = 0.958328,\ L = 3.41768\}$, (b) stable circular orbit $\{E = 0.953775,\ L = 3.58939\}$, (c) unstable circular/separatrix orbit $\{E = 0.928746,\ L = 2.9858\}$, (d) inner unstable circular orbit $\{E = 1.41842,\ L = 5.40617\}$, and (e) innermost stable circular orbit (ISCO) $\{E = 0.917882,\ L = 2.90287\}$, where the horizontal black curve and vertical dashed red curve correspond to $(E^2 - 1)/2$ and the horizon radius respectively. 76

3.10 The (E, L) plane is shown for $a = 0.5$ in (a) and $a = -0.5$ in (b) where the condition for three distinct roots, $\Delta < 0$, is valid in the shaded region; moreover, the two inner roots, r_2 and r_3, are inside the horizon, while r_1 is outside. The radial effective potential [Eq. (3.35)] diagrams are shown in (c) and (d) for (E, L) chosen on the $\Delta = 0$ boundary of the shaded region; these cases have two inner equal roots, $r_2 = r_3$. The cases of three distinct roots are shown in diagrams (e) and (f) where the (E, L) points are chosen inside the shaded region ($\Delta < 0$). The parameter set $\{\Delta = 0, \cos\varphi = +1, E = 0.97, L = 0.57, a = 0.5\}$ is used for (c), $\{\Delta = 0, \cos\varphi = +1, E = 0.05, L = 0.0387, a = -0.5\}$ for (d), $\{\Delta < 0, \cos\varphi = 0.9995, E = 0.7, L = 0.3, a = 0.5\}$ for (e), and $\{\Delta < 0, \cos\varphi = 0.9931, E = 0.06, L = 0.02, a = -0.5\}$ for (f). 79

3.11 $L = aE$ curve for $a = 0.5$ is shown in (a) which lies in the shaded region of Fig. 3.10(a), while (b) shows the effective potential [Eq. (3.51)] diagram for one such orbit with $E = 0.2$ that has one turning point inside the horizon and another outside the horizon. 80

3.12 (a) The Δ region, defined by Eq. (3.56), is shown for the equatorial orbits in the (e, μ) plane, where points A and B depict the ISCO and MBCO respectively, and (b) the contours of $\cos\varphi$ are shown inside the Δ region, where $a = 0.5$. 82

4.1 (a) The shaded region depicts bound orbit region in the (e, μ) plane determined by Eqs. (4.8) for $a = 0.5$ and $Q = 5$. The red boundary of the region represents non-equatorial separatrix orbits with eccentricity of the orbit varying along the curve. The black dot represented by S corresponds to the ISSO with ($e = 0$, $\mu = 1/r_s$), whereas M represents the MBSO with ($e = 1$, $\mu = 1/2r_s$); (b) The effective potential, Eq. (3.3b), is shown for a non-equatorial separatrix orbit with $E = 0.92959309$, $L = 2.15349738$, $a = 0.5$, and $Q = 5$, where the horizontal line represents the total energy given by $(E^2 - 1)/2$. 115

4.2 The contours of different important radii around the Kerr black hole in the (r_s, a) plane for (a) $Q = 0$, (b) $Q = 5$, (c) $Q = 10$, and (d) $Q = 12$. 116

4.3 The shaded region depicts the bound orbit region defined by Eq. (4.7c) in the (e, μ) plane for $a = 0.5$ and $Q = 5$. The black curve represents the homoclinic orbits where the endpoints depict $e = 0$ and $e = 1$ homoclinic orbits corresponding to the ISSO and MBSO respectively. The red curve represents $e = 0.5$ and we study orbits with different μ values as depicted by the dots on this curve. . . . 126

4.4 The figure shows prograde eccentric bound orbits (a) E1, (b) E2, (c) E3, and (d) E4 in the Table 4.6, for various combinations of (e, μ, a, Q) satisfying Eq. (4.7c) and also presents the evolution of corresponding θ, ϕ and r with coordinate time, t. 127

4.5 The figure shows retrograde eccentric bound orbits (a) E5, (b) E6, (c) E7, and (d) E8 in the Table 4.6, for various combinations of (e, μ, a, Q) satisfying Eq. (4.7c) and also presents the evolution of corresponding θ, ϕ and r with coordinate time, t. 128

4.6 The figure shows the prograde homoclinic orbits (a) H1, (b) H2, (c) H3, and (d) H4 in the Table 4.6, for various combinations of (e, μ, a, Q) and also presents the evolution of corresponding θ, ϕ and r with coordinate time, t. 129

4.7 The figure shows the retrograde homoclinic orbits (a) H5, (b) H6, (c) H7, and (d) H8 in the Table 4.6, for various combinations of (e, μ, a, Q) and also presents the evolution of corresponding θ, ϕ and r with coordinate time, t. 130

4.8 The figure shows the spherical orbits for (a) prograde, S1, (b) retrograde, S2, in the Table 4.6 along with the corresponding evolution of θ, ϕ and r with coordinate time, t. 131

4.9 The figure shows zoom whirl orbits (a) Z1, (b) Z2, (c) Z3, (d) Z4, (e) Z5, and (f) Z6 in the Table 4.6, for various combinations of (e, μ, a, Q) satisfying Eq. (4.7c) and also presents the evolution of corresponding θ, ϕ and r with coordinate time, t. 132
4.10 The figure shows the eccentric trajectories on the red curve of Fig. 4.3 ($e = 0.5$, $a = 0.5$, $Q = 5$) for (a) $\mu = 0.05$, and (b) $\mu = 0.1$. . . . 133
4.11 The figure shows the eccentric trajectories on the red curve of Fig. 4.3 ($e = 0.5$, $a = 0.5$, $Q = 5$) for (a) $\mu = 0.15$, and (b) $\mu = 0.18$. We see that the trajectory shown in (b) represent a zoom-whirl orbit. 133

5.1 Flowchart of various Kerr orbits (with the nomenclature used here of nonequatorial eccentric (eQ), spherical ($Q0$), eccentric equatorial ($e0$), and circular (00) orbits) studied to explore QPO frequencies using the GRPM in various sections of this paper, where the most specialized case of circular orbits was previously studied (Motta *et al.* 2014a,b). Clearly, the GRPM is valid strictly only when $e \neq 0$. 144
5.2 Generalized relativistic precession phenomenon for $Q \neq 0$, near a black hole (BH) at the center, rotating anticlockwise, where $\Omega_{\rm pp}$ represents the periastron precession and $\Omega_{\rm np}$ represents the nodal precession frequency. The initial point of the trajectory is indicated by point A, from where the particle follows an eccentric trajectory before completing one (a) radial or (b) vertical oscillation to reach point B. The particle sweeps an extra $\Delta\phi$ azimuthal angle during one (a) radial or (b) vertical oscillation because the azimuthal motion is faster than the radial or vertical motion causing the periastron or nodal precession. 146
5.3 Example of eQ trajectory with parameters $\{e = 0.3,\ r_p = 5.917,\ a = 0.5,\ Q = 5\}$ around a Kerr black hole at the origin, with its spin pointing in the positive z-direction: (a) shows the side view of the orbit representing the nodal precession phenomenon of the orbital plane about the spin axis of the black hole; (b) top view of the orbit showing the periastron precession phenomenon. 147
5.4 Important radii: the ISCO (ISSO), MBCO (MBSO), light radius, and the horizon. These radii separate various kinds of orbits outside a Kerr black hole in the (r, a) plane, indicated by different regions that are depicted by numbers, for (a) the equatorial orbits with $Q = 0$, and (b) nonequatorial orbits with $Q = 4$. 148

5.5 (a) The shaded region represents all possible bound orbits in the (e, μ) plane for $\{a = 0.5, Q = 5\}$, where S depicts the ISSO and M depicts the MBSO radius, and the red curve represents separatrix orbits [see Fig. 4.1]; the corresponding effective potential diagrams are shown as a function of r for (b) ISSO and (c) MBSO, where the horizontal black curve represents $(E^2 - 1)/2$ and the vertical red curve represents the horizon radius, and $\{r_1, r_2, r_3, r_4\}$ are four roots of the effective potential, which are also the turning points of a trajectory, and where $r_1 = \infty$ for MBSO. 149

5.6 Dimensionless frequency contours are shown for circular and equatorial trajectories (00), using Equations (5.1a−5.1c), in the (r, a) plane outside the ISCO radius, which is indicated by a thick black contour as also depicted in Figure 5.4, for HFQPOs (a) $\bar{\nu}_\phi$, (b) $\bar{\nu}_{\rm pp}$, and type C LFQPO (c) $\bar{\nu}_{\rm np}$ assuming the RPM. 151

5.7 The contours of $\delta_\phi\,(e, r_p, a, Q)$ are shown in the (r_p, a) plane for eccentric orbits around a Kerr black hole, where the parameter combinations are (a) $\{e = 0.25, Q = 0\}$, (b) $\{e = 0.25, Q = 2\}$, (c) $\{e = 0.25, Q = 4\}$, (d) $\{e = 0.5, Q = 0\}$, (e) $\{e = 0.5, Q = 2\}$, and (f) $\{e = 0.5, Q = 4\}$. 153

5.8 The contours of $\delta_{\rm pp}\,(e, r_p, a, Q)$ are shown in the (r_p, a) plane for eccentric orbits around a Kerr black hole, where the parameter combinations are (a) $\{e = 0.25, Q = 0\}$, (b) $\{e = 0.25, Q = 2\}$, (c) $\{e = 0.25, Q = 4\}$, (d) $\{e = 0.5, Q = 0\}$, (e) $\{e = 0.5, Q = 2\}$, and (f) $\{e = 0.5, Q = 4\}$. 154

5.9 The contours of $\delta_{\rm np}\,(e, r_p, a, Q)$ are shown in the (r_p, a) plane for eccentric orbits around a Kerr black hole, where the parameter combinations are (a) $\{e = 0.25, Q = 0\}$, (b) $\{e = 0.25, Q = 2\}$, (c) $\{e = 0.25, Q = 4\}$, (d) $\{e = 0.5, Q = 0\}$, (e) $\{e = 0.5, Q = 2\}$, and (f) $\{e = 0.5, Q = 4\}$. 155

5.10 The HFQPO frequency ratio, $\bar{\nu}_\phi/\bar{\nu}_{\rm pp}$, contours are shown for eccentric orbits around a Kerr black hole in the (r_p, a) plane, assuming the GRPM, where the parameter combinations are (a) $\{e = 0.25, Q = 0\}$, (b) $\{e = 0.25, Q = 2\}$, (c) $\{e = 0.25, Q = 4\}$, (d) $\{e = 0.5, Q = 0\}$, (e) $\{e = 0.5, Q = 2\}$, and (f) $\{e = 0.5, Q = 4\}$. 156

5.11 The contours of $\delta_\phi\,(r_s, a, Q)$ are shown for (a) Q=2, (b) Q=4; $\delta_{\rm pp}\,(r_s, a, Q)$ for (c) Q=2, (d) Q=4; and $\delta_{\rm np}\,(r_s, a, Q)$ for (e) Q=2, (f) Q=4 in the (r_s, a) plane for the spherical orbits around a Kerr black hole. . 159

5.12 The HFQPO frequency ratio, $\bar{\nu}_\phi/\bar{\nu}_{\rm pp}$, contours are shown for the spherical orbits around a Kerr black hole in the (r_s, a) plane, assuming the GRPM for (a) $Q = 2$ and (b) $Q = 4$. 160

5.13 Flowchart of the method used to estimate the orbital solutions for QPOs and corresponding errors. 166

5.14 Figure showing s_3^2 and s_2^2 as a function of probability p given by Equations (5.9d) and (5.10d). 171

5.15 The figures show 1σ errors in the spin parameters for various Q values for exact solutions of (a) M82 X-1, and corresponding to the peak of the probability distributions for (b) GRO J1655-40, as given in the Table 5.4. The upper and lower dashed curves correspond to the limits of the calculated errors. Although each Q value corresponds to a different spin of the black hole, the calculated values, and corresponding errors are within a narrow band which puts a sharp and reasonable constraint on the spin of the black hole. 173

5.16 The probability contours in the parameter planes are shown in (a) $\{e,\, Q\}$, (b) $\{r_p,\, e\}$, and (c) $\{Q,\, r_p\}$, where the + sign marks the exact solution for the parameters for QPOs in M82 X-1 with $a = 0.2994$. The probability density profiles are shown in (d) $\mathcal{P}_1\,(e)$, (e) $\mathcal{P}_1\,(r_p)$, and (f) $\mathcal{P}_1\,(Q)$, where the black points represent integrated probability densities and the blue curves are their model fit. The dashed vertical lines enclose a region with 68.2% probability, and the solid vertical line marks the peak of the profiles. 175

5.17 The probability contours in the parameter planes are shown in (a) $\{e,\, Q\}$, (b) $\{r_p,\, e\}$, and (c) $\{Q,\, r_p\}$, where the + sign marks the peak of the probability density for GRO J1655-40 with $a = 0.283$. The probability density profiles are shown in (d) $\mathcal{P}_1\,(e)$, (e) $\mathcal{P}_1\,(r_p)$, and (f) $\mathcal{P}_1\,(Q)$, where the dashed vertical lines enclose a region with 68.2% probability and the solid vertical line marks the peak of the profiles. 176

5.18 The figures show various trajectories together having parameter combinations $\{e,\, r_p,\, Q\}$ within the estimated range of 1σ errors, as tabulated in the Table 5.5, for (a) M82 X-1 and (b) GRO J1655-40. The spin of the black hole is fixed to the most probable estimates, which are $a = 0.2994$ for M82 X-1 and $a = 0.283$ for GRO J1655-40. Each color corresponds to a different parameter combination, where $\{e = 0.18 - 0.29;\, r_p = 4.7 - 5;\, Q = 1 - 4\}$ for M82 X-1 and $\{e = 0.035 - 0.103;\, r_p = 5.11 - 5.42;\, Q = 0 - 0.6234\}$ for GRO J1655-40. 178

5.19 The integrated density profiles of BHXRB XTE J1550-564 are shown in (a) $\mathcal{P}_1\,(e)$ and (d) $\mathcal{P}_1\,(r_p)$, where the dashed vertical lines enclose a region with 68.2% probability, and the solid vertical line corresponds to the peak of the profiles. The probability contours of the parameter solution are shown in the (b) $(r_p,\, e)$ and (c) $(e,\, r_p)$ planes, where the + sign marks the exact solution. 182

5.20 The integrated density profiles are shown in (a) $\mathcal{P}_1\,(e)$ and (d) $\mathcal{P}_1\,(r_p)$ for BHXRB 4U 1630-47, where the dashed vertical lines enclose a region with 68.2% probability, and the solid vertical line corresponds to the peak of the profiles. The probability contours of the parameter solution are shown in the (b) $(r_p,\, e)$ and (c) $(e,\, r_p)$ planes, where the + sign marks the exact solution. 183

5.21 The integrated density profiles are shown in (a) $\mathcal{P}_1(e)$ and (d) $\mathcal{P}_1(r_p)$ for BHXRB GRS 1915+105, where the dashed vertical lines enclose a region with 68.2% probability, and the solid vertical line corresponds to the peak of the profiles. The probability contours of the parameter solution are shown in the (b) (r_p, e) and (c) (e, r_p) planes, where the + sign marks the exact solution. 184
5.22 Equatorial eccentric orbit solutions for QPOs observed in BHXRBs GRO J1655-40 (purple), XTE J1550-564 (cyan), 4U 1630-47 (brown), and GRS 1915+105 (orange) for (a) $Q = 0$; and (b) the nonequatorial eccentric orbit solution for BHXRB M82 X-1 (magenta) for $Q = 2.362$. 184
5.23 Spherical trajectories corresponding to the exact solutions calculated for (a) M82 X-1 at $\{r_s = 6.044,\ a = 0.321,\ Q = 6.113\}$ and for (b) XTE J1550-564 at $\{r_s = 5.538,\ a = 0.34,\ Q = 2.697\}$, as also provided in Table 5.7. 186
5.24 Probability density profiles in $\{r_s,\ a,\ Q\}$ dimensions for M82 X-1: (a) $\mathcal{P}_1(r_s)$, (b) $\mathcal{P}_1(a)$, and (c) $\mathcal{P}_1(Q)$. The black points represent normalized probability density profiles generated using the method described in §5.3.2, and the blue curves are the model fit, and the results are summarized in Table 5.7. The errors for the $\mathcal{P}_1(r_s)$ and $\mathcal{P}_1(Q)$ profiles are obtained such that the integrated probability between the vertical dashed curves is 68.2%, whereas the vertical thick curves correspond to the peak value of the reduced probability density distributions. 186
5.25 The integrated density profiles are shown in (a) $\mathcal{P}_1(r_s)$ and (d) $\mathcal{P}_1(Q)$ for the spherical orbit solution of BHXRB XTE J1550-564, where the dashed vertical lines enclose a region with 68.2% probability, and the solid vertical line corresponds to the peak of the profiles. The probability contours of the parameter solution are shown in the (b) (Q, r_s) and (c) (r_s, Q) planes, where the + sign marks the exact solution. 187
5.26 The PBK correlation is shown for BHXRB GRO J1655-40 as previously observed [data points are from Motta *et al.* (2014a)]. The observed correlation is in good agreement with the frequencies of the $e0$ solution estimated, where $\{e = 0.071,\ a = 0.283,\ Q = 0,\ \mathcal{M} = 5.4\}$, for GRO J1655-40 in §5.3.2.1, where (a) ν_ϕ, (b) $\nu_{\rm pp}$ in the high-frequency range, (c) $\nu_{\rm pp}$ in the low-frequency range, and (d) $\nu_{\rm np}$ are shown. The blue, black, and red data points represent the L_u, L_l, and $L_{\rm LF}$ components of the PDS, respectively. The magenta curves show the theoretical values of frequencies. 191
5.27 The frequencies (a) ν_ϕ and $\nu_{\rm pp}$, (b) $\nu_{\rm np}$ are shown as function of r_p, for the $e0$ solution vector $\{e = 0.071,\ a = 0.283,\ Q = 0,\ \mathcal{M} = 5.4\}$. . 191

5.28 Contours of (a) β_r and (b) Q_ϕ in the (r, a) plane in the edge region of the general-relativistic thin disk, and (c) $p^{\rm gas}/p^{\rm rad}$ as a function of r with $a = 0.5$ (where the dotted vertical curve corresponds to ISCO and the solid vertical curve corresponds to r when $p^{\rm gas}/p^{\rm rad} = 1$). We have fixed $\{\alpha = 0.1,\, m_1 = 1,\, \dot{m} = 0.1\}$. 195

5.29 The cartoon shows a geometric model explaining the region of origin of QPOs assuming the more general nonequatorial eccentric trajectories in the GRPM, where the torus extent is $R_{0-\Delta_2}^{+\Delta_1}$ (and torus width $\Delta r = \Delta_1 + \Delta_2$). 197

6.1 The figure shows a unified picture of the models for X-ray, optical, and γ ray QPOs and the origin of X-ray power spectral density (PSD) shape in AGN. The X-ray QPOs observed in NLSy1 galaxies are associated with the fundamental frequencies of the equatorial orbits in the accretion disk sandwiched by a corona region, which we call the outer corona (OC) region, $r_I < r < r_X$; the inner corona (IC) region, $r_M < r < r_I$, is associated with the fundamental frequencies of the spherical orbits around a Kerr black hole. The optical and γ ray QPOs in Blazars are shown as the harmonics of the timescale of a blob of matter moving along the jet. The shape of the PSD is studied using the fundamental frequency of matter which is governed by the radial effective potential, $V_{eff}(E, L, a, Q)$, providing the gravitational background responsible for the geodesic motion, in IC and OC regions to derive the energy distribution of the orbiting matter, $N(E)$, which is directly related to the observed intensity, $I(\nu)$, where ν is the temporal frequency. 210

6.2 The figure shows the circular orbit frequency contours of (a) ν_ϕ, Eq. (5.1a), for the QPO frequencies of RE J1034+396, MS 2254.9-3712, Mrk 766, and MCG-06-30-15, given in Table 6.1; (b) ν_ϕ and ν_{pp} contours, Eq. (5.1b), for two QPO frequencies of Mrk 766; and (c) ν_{np} contour, Eq. (5.1c), for the QPO frequency of 2XMM J123103.2+110648. 213

6.3 The integrated probability density profiles for 1H 0707-495 are shown in (a) $\mathcal{P}_1(r)$ and (d) $\mathcal{P}_1(a)$, where the dashed vertical lines enclose a region with 68.2% probability, and the solid vertical line corresponds to the peak of the profiles. The inner probability contours of the parameter solution are shown: (b) in the (a, r) plane, and (c) the outer contours in the (r, a) plane, where the + sign marks the exact solution. 216

6.4 The figure shows the solutions of spherical orbit parameters $\{r_{s0}$, a_0, $Q_0\}$ for QPO frequencies of 1H 0707-495 in (a) (Q, a), and in (b) (Q, r_s) plane. 217

6.5 The figure shows (a) χ^2_a/χ^2_p function for a, where the vertical solid black curve depicts a_p and the vertical dashed black curve encloses the 95% probability region, (b) the range of Q and (c) r_s corresponding to the 2σ region of a, where the vertical dashed black curves mark $\{a_p\ , r_{sp},\ Q_p\}$. 218
6.6 The figure shows $E\,(r)$ as a function of r for (a) the equatorial circular orbits ($Q = 0$) and for (b) the spherical orbits with $Q = 8$, where $a = 0.5$. The vertical black curves correspond to the innermost stable circular orbit (ISCO) and to the innermost stable spherical orbit (ISSO) for $Q = 8$. 223
6.7 The figure shows a comparison of the ISCO and ISSO radii in the $(r,\ a)$ plane. The ISSO radius moves outwards as Q increases. . . . 223
6.8 The figure shows E as a function of ν_ϕ for the circular orbits (a) outside r_I, and (b) inside r_I for $a = 0.25$ and $M_\bullet = 10^7 M_\odot$. The minima of E is at r_I in both diagrams. 226
6.9 The figure shows contours of (a) α_1, and (b) α_2 in the $(Q,\ a)$ plane. 230
6.10 The figure shows examples of PSD, $P(\bar{\nu}) \propto F(\bar{\nu})^2$, profile obtained using the ROM for the parameter combinations (a) #1, and (b) #2 given in Table 6.5. The red curve shows the bending power-law model fit, given by Eq. (6.4), where the fitting parameters are shown in Table 6.5. The vertical black dashed curve corresponds to the ISCO (break) frequency. 231

7.1 A flowchart of the theoretical development of work, the impact, and its future directions. 248

List of Tables

3.1 This table presents a formulary for different types of orbits in the non-equatorial and equatorial plane for both dynamical and conic parameter spaces. 84

4.1 This table summarizes all the integrals solved in §4.2.1 to calculate the integrals of motion in the Kerr geometry, where the constants are given by Eqs. (4.4a-4.4l). 102

4.2 This table summarizes the fundamental frequency formulae (with dimensions) derived using the long time average method in the Kerr geometry. The explicit expressions for integrals I_1, I_2, and I_8 are summarized in Table 4.1. 105

4.3 This table summarizes the trajectory formulae and fundamental frequency formulae for the equatorial and eccentric bound orbits in the Kerr geometry. 107

4.4 This table summarizes (E, L) formulae, the trajectory formulae, and the fundamental frequency formulae for the spherical orbits in the Kerr geometry. 113

4.5 This table summarizes the analytic form for the expressions of (e_s, μ_s) and the trajectory solution for the non-equatorial separatrix orbits. 121

4.6 The following table summarizes the values of conic parameters (e, μ) chosen in the listed orbit simulations to study eccentric, homoclinic and spherical orbits for different (a, Q) combinations for both prograde and retrograde cases constructed using Eqs. (4.6). 124

5.1 Summary of the Observed QPO Frequency Range in BHXRBs and Their Corresponding Dimensionless Values Derived from Data Given in Table 5.3. 151

5.2 Various GRPMs, Their Corresponding Unknown Parameters, and Underlying Assumptions for BHXRBs with Three and Two Simultaneous QPOs. *need to supply a from the best fit of χ^2; †a is fixed from the available data (see Table 5.3). 161

5.3 Summary of existing BHXRBs that exhibit either three or two simultaneous QPOs. The first two rows represent the cases having twin HFQPOs with simultaneous type-C QPO. The remaining rows show the cases of BHXRB having only twin HFQPOs. The columns show the source name, QPO frequencies, and previously measured mass through optical, infra-red or X-ray observations, previously known spin of the black hole measured by fit to the Fe Kα line or to the continuum spectrum (for 1 and 2 we calculate the parameter a from our method), and the class of GRPM applied to estimate the parameters. The references are indicated by lower case letters (a-m). **References**: (a) Pasham *et al.* (2014), (b) Pasham and Strohmayer (2013b), (c) Motta *et al.* (2014a), (d) Beer and Podsiadlowski (2002), (e) Miller *et al.* (2001), (f) Orosz *et al.* (2011), (g) Miller and Miller (2015), (h) Klein-Wolt *et al.* (2004), (i) Seifina *et al.* (2014), (j) King *et al.* (2014), (k) Strohmayer (2001b), (l) Steeghs *et al.* (2013), (m) Miller *et al.* (2013). 164

5.4 Summary of results corresponding to (Non)equatorial eccentric solutions (eQ and $e0$) for BHXRBs M82 X-1 and GRO J1655-40. The columns describe the range of parameter volume considered for $\{e,\, r_p,\, a\}$ with a chosen resolution to calculate the normalized probability density at each point inside the parameter volume using Equation (5.8b), the exact solutions for $\{e,\, r_p,\, a\}$ calculated using Eqs. (4.11), and the results of the model fit to $\mathcal{P}_1\,(e)$, $\mathcal{P}_1\,(r_p)$, and $\mathcal{P}_1\,(a)$, for each value of Q between 0 and 4. 180

5.5 Summary of results for $\{e,\, r_p,\, Q\}$ parameter solutions and corresponding errors for QPOs in BHXRBs M82 X-1 and GRO J1655-40. The columns describe the range of parameter volume taken for $\{e,\, r_p,\, Q\}$, and the chosen resolution to calculate the normalized probability density at each point inside the parameter volume, the exact solutions, and the results of the model fit to the integrated profiles. The spin of the black hole is fixed to the most probable estimates, which are $a = 0.2994$ for M82 X-1 and $a = 0.283$ for GRO J1655-40. 181

5.6 Summary of results corresponding to the equatorial eccentric orbit solutions for BHXRBs XTE J1550-564, 4U 1630-47, and GRS 1915+105. The columns describe the parameter range considered for $\{e,\, r_p\}$, its resolution, the exact solutions for $\{e,\, r_p\}$ calculated using $\{\nu_\phi,\, \nu_{\rm pp}\}$ for XTE J1550-564 and GRS 1915+105, and using $\{\nu_\phi,\, \nu_{\rm np}\}$ for 4U 1630-47 using Eqs. (4.14), and results of the model fit to $\mathcal{P}_1\,(e)$ and $\mathcal{P}_1\,(r_p)$. 182

5.7 Summary of results corresponding to the spherical orbit solutions for BHXRBs M82 X-1 and XTE J1550-564. The columns describe the range of parameter volume considered for $\{r_s, a, Q\}$ and its resolution to calculate the normalized probability density using Equation (5.8b), the exact solutions for $\{r_s, a, Q\}$ calculated using Equations (4.23-4.25c), the value of parameters corresponding to the peak of the integrated profiles in $\{r_s, a, Q\}$, and results of the model fit to $\mathcal{P}_1(r_s)$, $\mathcal{P}_1(Q)$, and $\mathcal{P}_1(a)$. 188

5.8 Nonequatorial eccentric Orbit (eQ) solutions for L_l and $L_{\rm LF}$ components detected in RXTE observations of GRO J1655-40 (Motta *et al.* 2014a), where the first row corresponds to the observation ID with three simultaneous QPOs. The mass of the black hole was fixed to $\mathcal{M} = 5.4$ and spin was fixed to $a = 0.283$. 192

5.9 Ranges of r, pressure ratio, $p^{\rm gas}/p^{\rm rad}$, quality factor, Q_ϕ, and radial velocity, β_r, in the edge and inner regions of fluid flow in the relativistic thin accretion disk around a Kerr black hole (Penna *et al.* 2012; Mohan and Mangalam 2014), where we have fixed $\{m_1 = 1, \alpha = 0.1\}$ for BHXRBs. 196

5.10 Summary of orbital solutions found for QPOs observed in five BHXRBs using the GRPM in this article, and the corresponding region of the (r_p, a) plane where QPOs originate. 198

6.1 A list of statistically significant QPOs detected in the X-ray band (0.3-10KeV) by the XMM-Newton in AGN along with their black hole masses. **References**: [1]Zhou *et al.* (2010); [2]Gierliński *et al.* (2008); [3]Ho *et al.* (2012); [4]Lin *et al.* (2013); [5]Grupe *et al.* (2004); [6]Alston *et al.* (2015); [7]Pan *et al.* (2016); [8]Zhang *et al.* (2018); [9]Wang and Lu (2001); [10]Zhang *et al.* (2017); [11]Boller *et al.* (2001); [12]Hu *et al.* (2016); [13]Gupta *et al.* (2018). 212

6.2 The table summarizes results of $\{r, a\}$ parameter solution, and corresponding errors for X-ray QPOs in NLSy1 1H 0707-495. The columns provide the range of parameter volume taken for $\{r, a\}$, the chosen resolution to calculate the normalized probability density at each point inside the parameter volume, the exact solutions, and the results of the model fit to the integrated profiles. The mass of the black hole is fixed to $M_\bullet = 5.2 \times 10^6 M_\odot$ (Pan *et al.* 2016). . . . 215

6.3 The table summarizes results of spherical orbit parameter solution, $\{r_s, a\}$, and corresponding errors for X-ray QPOs in NLSy1 1H 0707-495. The columns provide the range of parameter volume taken for $\{r_s, a\}$ by fixing $\{Q = 1, 4, 8, 12\}$, the chosen resolution to calculate the normalized probability density at each point inside the parameter volume, the exact solutions, the results of the model fit to the integrated profiles, and variance σ_a. The mass of the black hole is fixed to $M_\bullet = 5.2 \times 10^6 M_\odot$ (Pan *et al.* 2016). 219

6.4 A list of statistically significant QPOs detected in the γ ray and optical energy bands in BL Lacertae type of AGN, along with their redshifts and black hole masses. The theoretical timescales are calculated, using Eq. (6.3), such that the lower and upper limit correspond to $r_F = 30$ and $r_F = 80$ respectively. **References**: [1]Ackermann *et al.* (2015b); [2]Chen (2018); [3]Sandrinelli *et al.* (2014); [4]Sandrinelli *et al.* (2016a); [5]Sandrinelli *et al.* (2018); [5]Tavani *et al.* (2018); [6]Ackermann *et al.* (2015a); [7]Sandrinelli *et al.* (2016b); [8](Sandrinelli *et al.* 2017) 220

6.5 The table summarizes the computed values of (α_1, α_2) and the parameter fits to the bending power-law, Eq. (6.4), for various combinations of (a, Q), where we fixed $r_X = 10$ and $\{\beta_1 = -2, \beta_2 = -1\}$, and the frequencies were scaled by ($c^3/GM_\bullet$). 231

7.1 A list of novel formulae and advancement in the theoretical results made in this Thesis. 240

7.2 A summary of the results, tables, and figures related to the GRPM parameter extraction for BHXRB and AGN, GR gas-flow model, PBK analysis, ROM model for PSD, and MHD jet model. 243

7.3 A list of various types of trajectories around a Kerr black hole with their description, and the region in the (r, a) plane where they are found, as shown in Fig. 5.4. [a]The regions for $e0$ and 00 orbits are shown in Fig. 5.4(a), whereas eQ or $Q0$ orbits are shown in Fig. 5.4(b). [†](Rana and Mangalam 2019a,b); [‡](Levin and Perez-Giz 2009; Perez-Giz and Levin 2009); [^](Glampedakis and Kennefick 2002). 244

Glossary of symbols

t	Time coordinate
r	Radial distance from the black hole
θ	Polar angle
ϕ	Azimuthal angle
τ	Proper time
c	Speed of light
G	Gravitational constant
$M_\bullet$	Mass of the black hole
$\mathcal{M}$	$M_\bullet/M_\odot$
J	Angular momentum of the black hole
a	Spin of the black hole, $a = Jc/\left(GM_\bullet{}^2\right)$
R_g	$GM_\bullet/c^2$
u	$1/r$
r_+	Horizon radius
Q	Carter's constant
E	Energy per unit rest mass
L	z-component of angular momentum per unit rest mass
L_T	Total angular momentum per unit rest mass
p_t	Generalized momentum for t coordinate
p_ϕ	Generalized momentum for ϕ coordinate
p_r	Generalized momentum for r coordinate
δ_1	$=0$ for photon orbits and $= 1$ for particle orbits
V_{eff}	Radial effective potential
$\mathcal{L}$	Relativistic Lagrangian for the geodesic motion
$\mathcal{H}$	Relativistic Lagrangian for the geodesic motion
$\mathcal{S}$	Principal function of the Hamilton Jacobi equation
r_1	apastron distance $(= r_a)$
r_2	periastron distance $(= r_p)$
r_3	Third turning point of the test particle

r_4	Innermost turning point of the test particle
e	eccentricity parameter
μ	inverse latus-rectum parameter
χ	defined by $u = \mu\,(1 + e\cos\chi)$
ψ	$\dfrac{\chi}{2} - \dfrac{\pi}{2}$
y	$(1 + e\cos\chi)$
I	Terminology used for the radial integrals
H	Terminology used for the θ integrals
r_s	radius of the spherical orbit
r_c	radius of the circular orbit
e_s	eccentricity of the separatrix orbits
μ_s	inverse latus-rectum of the separatrix orbits
Z	ISSO (ISCO) radius
Y	MBSO (MBCO) radius
X	Light radius
ν_ϕ	Azimuthal frequency
ν_r	Radial frequency
ν_θ	Vertical oscillation frequency
ν_{np}	Nodal precession frequency, $(\nu_\phi - \nu_\theta)$
ν_{pp}	Periastron precession frequency, $(\nu_\phi - \nu_r)$
ν_0	Centroid frequency of the QPO
$\bar{\nu}$	Frequency scaled by the factor $\left(c^3/GM_\bullet\right)$
P	Probability density
$\mathcal{P}$	Normalized probability density
$\mathcal{N}$	Normalization factor
$\mathcal{J}$	Jacobian of transformation from frequency to parameter space
$N\,(E)$	Energy distribution of particles
F_1, F_2	Temporal frequency distribution inside and outside ISCO
α_1, α_2	Slopes of the energy distribution inside and outside ISCO
β_1, β_2	Slopes of the observed PSD before and after break frequency

ॐ असतो मा सद्गमय ।
तमसो मा ज्योतिर्गमय ।
मृत्योर्मा अमृतं गमय ।
ॐ शान्तिः शान्तिः शान्तिः ॥

Om Asato Maa Sad-Gamaya |
Tamaso Maa Jyotir-Gamaya |
Mrtyor-Maa Amrtam Gamaya |
Om Shaantih Shaantih Shaantih ||

Meaning:
Lead us from the unreal to the real
Lead us from darkness to light
Lead us from death to immortality
Aum peace, peace, peace!

- Brihadaranyaka Upanishad 1.3.28

Chapter 1

The first image of a black hole (M87). Courtesy: jpl.nasa.gov

Overview

1.1 Introduction

The modern study of black holes is rooted in the theory of general relativity developed by Albert Einstein in 1915. The theoretical ideas became the central focus in the field of general relativity when Karl Schwarzschild derived the solution of Einstein's vacuum field equations for a spherical non-rotating body of mass $M_\bullet$ (Schwarzschild 1916), which led to the Schwarzschild radius, $R_s = 2GM/c^2 = 2.95\,(M_\bullet/M_\odot)$km, defined as the horizon radius of a non-rotating black hole. Initially, the existence of black holes was considered only virtual, as mathematical ideas, and their real existence was questioned by Albert Einstein himself. The late twentieth century (1960s) changed this situation when a revolution started in the field of observations of black holes with the discovery of quasars and other active galactic nuclei (AGN) in distant galaxies ($M_\bullet \geq 10^6 M_\odot$) because the most

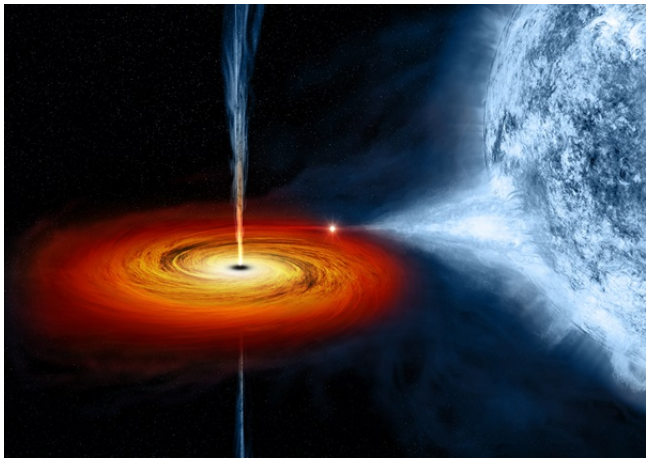

FIGURE 1.1: An artistic image of Cygnus X-1. Courtesy: NASA/CXC/M.Weiss.

natural explanation for their extraordinary luminosity can only be the release of gravitational potential energy due to accretion of matter onto the supermassive black holes (Rees 1984). This was an indirect detection of the astrophysical black holes. The further boost in black hole astrophysics started in the 1970s when an X-ray binary, Cygnus X-1 (Fig. 1.1), was discovered (Bolton 1972). The compact object in this binary was found to have it's mass greater than the maximum mass limit of a neutron star, $M \lesssim 2.17 M_{\odot}$ (Margalit and Metzger 2017; Oppenheimer and Volkoff 1939), hence it was inferred to be a black hole. The formation process of black holes, with such high masses, is believed to be due to its self-gravity leading to the gravitational collapse of high mass objects. From a simple Newtonian treatment, it is seen that the escape velocity of a very dense object having a radius R_s is

$$v_{esc} = \left(\frac{2GM}{R_s}\right)^{1/2} = c. \tag{1.1}$$

This implies that light cannot escape from a region where $R < R_s$, and a general relativistic treatment is required to study the objects with $v_{esc} \sim c$. Here, we discuss the dynamics of the more general case of rotating black holes in the general relativistic regime.

1.2 The Kerr black holes

The solution to Einstein's vacuum field equations for a rotating object with mass M and angular momentum J was derived by Roy Kerr, where the line element is called the Kerr geometry (Kerr 1963), is given by ($c = G = 1$ units)

$$\mathrm{d}s^2 = g_{\mu\nu}\mathrm{d}x^\mu \mathrm{d}x^\nu, \tag{1.2a}$$

where $\{x^1, x^2, x^3, x^4\} \equiv \{t, r, \theta, \phi\}$, and

$$g_{tt} = -\left(1 - \frac{2r}{\rho^2}\right), \qquad g^{tt} = -\frac{\left(r^2 + a^2\right)^2 - a^2\Delta\sin^2\theta}{\rho^2\Delta}, \tag{1.2b}$$

$$g_{\phi\phi} = \left(r^2 + a^2 + \frac{2ra^2\sin^2\theta}{\rho^2}\right)\sin^2\theta, \qquad g^{\phi\phi} = \frac{\Delta - a^2\sin^2\theta}{\Delta\rho^2\sin^2\theta}, \tag{1.2c}$$

$$g_{t\phi} = -\frac{2ar\sin^2\theta}{\rho^2}, \qquad g^{t\phi} = -\frac{2ar}{\rho^2\Delta}, \tag{1.2d}$$

$$g_{rr} = \frac{\rho^2}{\Delta},\ g_{\theta\theta} = \rho^2, \qquad g^{rr} = \frac{\Delta}{\rho^2},\ g^{\theta\theta} = \frac{1}{\rho^2}, \tag{1.2e}$$

where $a \equiv J/M^2$ is the Kerr parameter, $\rho^2 \equiv r^2 + a^2\cos^2\theta$, and $\Delta \equiv r^2 - 2r + a^2$. We have scaled r and a by M to make them dimensionless. The coordinates (t, r, θ, ϕ) are called the Boyer-Lindquist coordinates, which are related to the Cartesian coordinates as

$$x' = \sqrt{r^2 + a^2}\sin\theta\cos\phi, \tag{1.3a}$$

$$y' = \sqrt{r^2 + a^2}\sin\theta\sin\phi, \tag{1.3b}$$

$$z' = r\cos\theta, \tag{1.3c}$$

which differs from the spherical coordinate system, and where the radial equivalent is given by $\sqrt{r^2 + a^2}$ in x' and y' equations [Eqs. (1.3a, 1.3b)].

1.2.1 Important properties of the Kerr geometry

The important properties of the Kerr geometry, that the metric [Eq. (1.2a)] obeys, are:

- *Asymptotically Flat*: The line element approaches the geometry of flat spacetime for $r >> 1$ and $r >> a$, given by

$$\mathrm{d}s^2 = r^2 \left(\mathrm{d}\theta^2 + \sin^2\theta \ \mathrm{d}\phi^2\right). \tag{1.4}$$

- *Schwarzschild when $a = 0$*: The Schwarzschild metric is a special case of the Kerr family, which is obtained when $a = 0$ and given by

$$\mathrm{d}s^2 = \ -\left(1 - \frac{2}{r}\right)\mathrm{d}t^2 \ + \ \left(1 - \frac{2}{r}\right)^{-1}\mathrm{d}r^2 \ + \ r^2\mathrm{d}\theta^2 + r^2\sin^2\theta \ \mathrm{d}\phi^2. \tag{1.5}$$

- *Stationarity, Axisymmetric*: The metric is independent of t and ϕ, making it stationary and axisymmetric. In addition, the Kerr metric has a reflection symmetry with respect to the equatorial plane, which means that the metric remains unchanged when $\theta \to (\pi - \theta)$.

- *Singularities and Horizon*: The metric has singularities at $\rho = 0$ and $\Delta = 0$; where $\rho = 0$ is the real singularity (when $r = 0$ and $\theta = \pi/2$), and $\Delta = 0$ is the coordinate singularity which has solutions at

$$r_\pm = 1 \pm \sqrt{1 - a^2}. \tag{1.6}$$

  This defines the outer and inner horizon radii for a Kerr black hole, $r_\pm$, where only r_+ is physically relevant. It can be seen from the expression of r_+, Eq. (1.6), that the horizon radius is real only when $-1 \leq a \leq 1$, hence constraining the value of spin for a Kerr black hole.

1.2.2 Radial milestones in the Kerr geometry

There are important radii around a Kerr black hole, which have physical significance in the study of the motion of matter near a rotating black hole, and hence set important radial milestones. We discuss their details and significance below:

- *Horizon surface*: The horizon surface is a null three-surface, generated by light rays that neither fall into the black hole nor escape to infinity. A null three-surface is defined as the one where at each point there is one tangent direction, l, that points along a light ray,

$$g_{\mu\nu} l^\mu l^\nu = 0, \tag{1.7}$$

which is also orthogonal to two independent spacelike directions (Hartle 2003). This implies that l is a null vector that is normal to the null surface and also lies in it. It can be shown that the surface $r = r_+$ is a null three-surface in the Kerr spacetime. Although, the horizon in the Kerr geometry has a constant Boyer-Lindquist coordinate, $r = r_+$, the geometry of the horizon surface is not spherically symmetric. The substitution of $r = r_+$ and t =constant (constant time slice) in Eq. (1.2a) gives the line element of

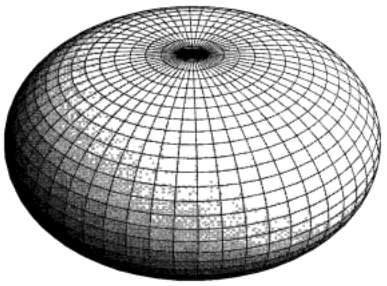

FIGURE 1.2: The horizon of a rotating black hole with $a = 0.86$. Lines of constant ϕ and constant θ are shown on the surface. Courtesy: Hartle (2003).

a two-dimensional surface

$$\mathrm{d}s^2 = \rho_+^2 \mathrm{d}\theta^2 + \left(\frac{2r_+}{\rho_+}\right)^2 \sin^2\theta \, \mathrm{d}\phi^2, \tag{1.8}$$

where $\rho_+ \equiv \rho\,(r_+, \theta)$. This line element does not have geometry of a sphere. A two-surface with geometry given by Eq. (1.8) is shown in flat space in Fig. 1.2.

- *Light radius*: A light radius defines the innermost limit for the spherical (circular) orbits of particles around a black hole. The radius of a photon orbit in the equatorial plane of the Kerr geometry is given by

$$r = X = 2\{1 + \cos\left[2\arccos\left(-a\right)/3\right]\}, \tag{1.9}$$

which was derived by Bardeen *et al.* (1972), by setting the energy per unit rest mass of the particles to infinity, $E = \infty$ (also see §4.6.1). An example of a light radius in the equatorial plane of the Kerr black hole is shown in Fig. 1.3.

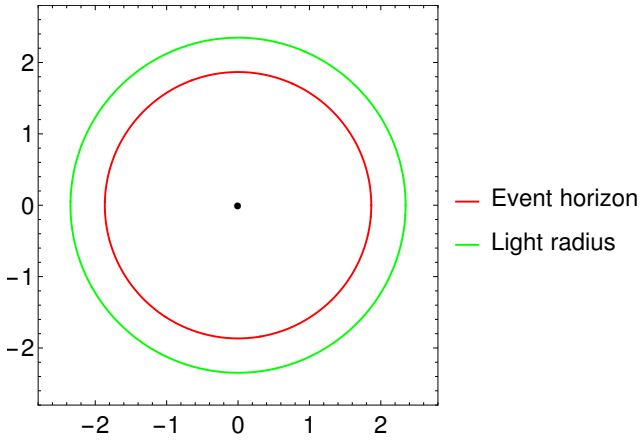

FIGURE 1.3: The horizon and light radii are shown in the equatorial plane of a Kerr black hole with a =0.5, where the point at the center represents the real singularity at $r = 0$.

- *Ergosphere and frame-dragging*: The concept of relativistic frame-dragging is a natural consequence of spinning black holes. Let us consider the frame

of a zero angular momentum observer (ZAMO), $L = u_\phi = 0$, near a Kerr black hole. The contravariant four-velocity for ZAMO is given by $u^\mu = \dfrac{\mathrm{d}x^\mu}{\mathrm{d}\tau}$, where τ is the proper time and $u^\phi = g^{\phi t}u_t \neq 0$. The angular velocity of the frame of ZAMO will be

$$\Omega = \frac{\mathrm{d}\phi}{\mathrm{d}t} = \frac{u^\phi}{u^t}, \tag{1.10a}$$

and $u_\phi = 0 = g_{\phi\phi}u^\phi + g_{\phi t}u^t$, which gives

$$\Omega = -\frac{g_{\phi t}}{g_{\phi\phi}} \neq 0, \tag{1.10b}$$

where the substitution of Eqs. (1.2c) and (1.2d) yields

$$\Omega = \frac{2ar}{\left(r^2 + a^2\right)^2 - a^2\Delta\sin^2\theta}. \tag{1.10c}$$

It is easy to see that the denominator in the above equation is always positive, implying that $(\Omega/a) > 0$, which means that the ZAMO is forced to rotate or frame-dragged along the direction of the spin of the black hole.

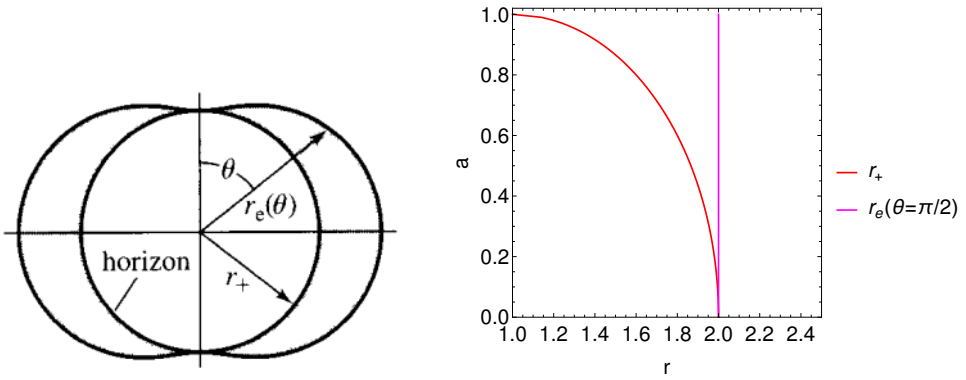

(a) (b)

FIGURE 1.4: The Ergosphere along with the horizon radius is shown (a) on a flat plane for $a = 0.95$, Courtesy: Hartle (2003); (b) in the $(r,\ a)$ plane for $\theta = \pi/2$. The region between r_+ and r_e is the Ergoregion.

Now, the four-velocity for a stationary observer is given by

$$u^{\mu} = (u^{t}, 0, 0, 0), \tag{1.11}$$

which is a unit timelike vector

$$g_{\mu\nu} u^{\mu} u^{\nu} = g_{tt} \left(u^{t}\right)^{2} = -\left(1 - \frac{2r}{\rho^{2}}\right) \left(u^{t}\right)^{2} = -1; \tag{1.12}$$

where this condition is solved to obtain u^{t}. However, it can not be satisfied when $g_{tt} = 0$ which gives a solution for the stationary surface as

$$r = r_{e}\left(\theta\right) = 1 + \sqrt{1 - a^{2}\cos^{2}\theta}, \tag{1.13}$$

that defines the radius of the Ergosphere. There are no possible stationary observers, seen from infinity, which follow Eq. (1.12) inside this surface, $r < r_{e}\left(\theta\right)$, because g_{tt} changes its sign at $r_{e}\left(\theta\right)$ and is positive inside it. The region defined by $r_{+} < r < r_{e}\left(\theta\right)$ is called the Ergoregion. The radius of the Ergosphere and the Ergoregion are shown in Fig. 1.4.

As we see that $r_{+} > r_{e}\left(\theta\right)$ (except for $\theta = 0$ and $\theta = \pi$, when $r_{+} = r_{e}$), which means that an observer in the Ergoregion can be in causal contact with the outside Universe. If an orbiting body fragments into two parts within the Ergoregion, it is possible to arrange the decay so that the escaping particle carries more energy than the one which falls into the black hole, having effectively extracted the rotational energy (angular momentum) of the black hole. This phenomenon is called the Penrose process (Penrose 1969).

- *Marginally bound spherical (circular) orbit (MBSO/MBCO)*: The Kerr geometry is not spherically symmetric but axisymmetric, which allows the motion of matter in a non-equatorial manner around the black hole. The marginally bound spherical (circular) orbits are the ones having $E = 1$, and they are unstable orbits. They are spherical (circular) in geometry but parabolic in their energetics (Bardeen *et al.* 1972). Hence, the unstable

spherical (circular) orbits exist only locally at MBSO (MBCO), and any infinitesimal outward perturbation to a particle in such orbit will escape it to infinity in a parabolic trajectory. The expression for MBCO was derived by Bardeen *et al.* (1972), which is given by

$$r = Y = 2 - a + 2\sqrt{1-a}, \tag{1.14}$$

whereas the expression for $MBSO$ is much more complicated (which we derive in chapter 4). An example of MBSO radius (blue) with Carter's constant, $Q = 4$ (Carter 1968), is shown in Fig. 1.5. A diagram of MBSO is shown in Fig. 1.6 (blue), representing a local unstable spherical orbit with $E = 1$.

- *Innermost stable spherical (circular) orbit (ISSO/ISCO)*: The ISSO (ISCO) defines the innermost radial limit for the stable spherical (circular) bound orbits. The conditions for a ISSO (ISCO) radius are (derived in §4.6.1)

$$V_{eff}(r) = \frac{E^2-1}{2}, \quad \frac{\mathrm{d}V_{eff}(r)}{\mathrm{d}r} = 0, \quad \frac{\mathrm{d}^2 V_{eff}(r)}{\mathrm{d}r^2} = 0, \tag{1.15a}$$

where $V_{eff}(r)$ is the radial effective potential given by

$$V_{eff}(r) = -\frac{1}{r} + \frac{L^2 - a^2(E^2-1)}{2r^2} - \frac{(L-aE)^2}{r^3}, \tag{1.15b}$$

for the equatorial orbits, where E and L are the energy and z-component of the angular momentum per unit rest mass of the orbiting particle. Any radial perturbation at ISSO (ISCO) makes the particle to fall in the unstable orbit region (region 2 and 3 in Fig. 1.5). The solution of Eq. (1.15) gives $r(a)$, $E(a)$, and $L(a)$. Hence, the radius for ISCO, $r = Z$, is given by

(Bardeen *et al.* (1972), also derived in Appendix A.3)

$$r = Z = \left\{3 + Z_2 \mp \left[(3 - Z_1)(3 + Z_1 + 2Z_2)\right]^{1/2}\right\}, \tag{1.16a}$$

$$Z_1 = 1 + \left(1 - a^2\right)^{1/3}\left[(1 + a)^{1/3} + (1 - a)^{1/3}\right], \tag{1.16b}$$

$$Z_2 = \left(3a^2 + Z_1^2\right)^{1/2}, \tag{1.16c}$$

where the upper sign represents the prograde and the lower sign represents the retrograde case. And the expressions of $E(a)$ and $L(a)$ for ISCO are given by (also derived in §4.5.1)

$$E(a) = \frac{\left[Z(a)^2 - 2Z(a) + a\sqrt{Z(a)}\right]}{Z(a)\left[Z(a)^2 - 3Z(a) + 2a\sqrt{Z(a)}\right]^{1/2}}, \tag{1.17a}$$

$$L(a) = \frac{\left[Z(a)^2 + a^2 - 2a\sqrt{Z(a)}\right]}{\sqrt{Z(a)}\left[Z(a)^2 - 3Z(a) + 2a\sqrt{Z(a)}\right]^{1/2}}. \tag{1.17b}$$

An example of the ISSO radius (black) is shown in Fig. 1.5. A diagram of ISSO is shown in Fig. 1.6 (black), representing a spherical radial limit for the stable bound orbits.

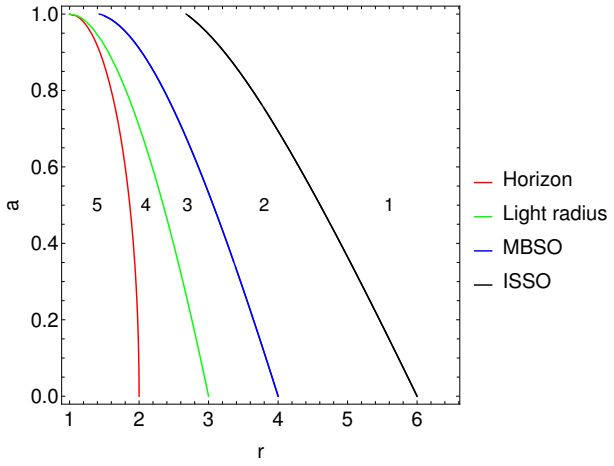

FIGURE 1.5: The contours of various radii are shown in the $(r,\ a)$ plane for $Q = 4$, which divide it into various regions, depicted as 1, 2, 3, 4, and 5, which are associated with different types of trajectories around a Kerr black hole (which we discuss in chapter 3 and 4).

The regions depicted in Fig. 1.5 correspond to different types of bound particle orbits around a Kerr black hole, as described below (for an analysis see §4.6.1 and 5.2):

1. Region 1 contains the stable spherical (circular) and the eccentric orbits.
2. Region 2 corresponds to the unstable spherical (circular) and the separatrix (Levin and Perez-Giz 2009) types of orbits.
3. Region 3 contains unstable spherical (circular) orbits with $E > 1$.
4. There are no bound (stable or unstable) orbits found in region 4, and region 5 is inside the horizon.
5. The Ergoregion overlaps with region 4 (for small a) and with region 3 (for large a).

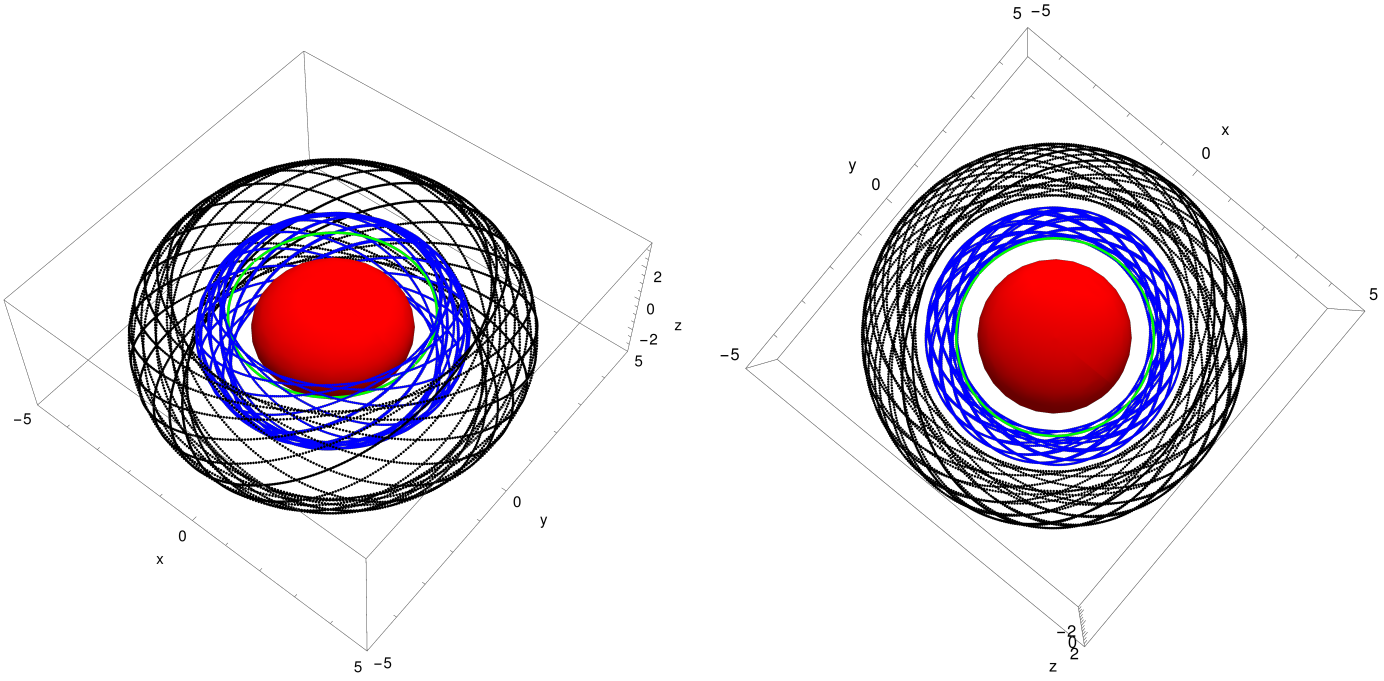

(a) (b)

FIGURE 1.6: The horizon radius (r_+, red), light radius [Eq. (1.9), green ring], MBSO (blue), and ISSO (black) (embedded in flat space), (a) side view, (b) top view, are shown together as the important radial milestones around a Kerr black hole, where $\{a = 0.5, Q = 4\}$.

1.3 Observations of black holes

It has now been established with observational evidence that black holes with masses ranging from 4-20$M_\odot$ in black hole X-ray binaries (BHXRB), to 10^6-$10^9 M_\odot$ in galactic nuclei, are ubiquitous. One among such important evidences is the recent detection of gravitational waves from the black hole binary merger (Abbott et al. 2016) and more such events are being detected, and are awaited by future missions like Laser Interferometer Space Antenna (LISA) (Glampedakis 2005). Another remarkable milestone in the field of black hole astrophysics was set by the Event Horizon Telescope (EHT) Collaboration, which recently reported the observations of the galactic nucleus of M87 from 1.3 mm Very Long Baseline Interferometry (VLBI). It achieved a very high angular resolution by observing an annular region with typical radius of $\theta_{obs} \sim 21\mu as$, which is comparable to the size of the galactic nuclei (Event Horizon Telescope Collaboration *et al.* 2019a,b,c,d,e,f).

The release of gravitational potential energy due to the process of accretion onto black holes is a powerful and efficient mechanism for producing high-energy radiation. To provide a simple order-of-magnitude estimate, we consider a body of mass M and radius R. The gravitational potential energy released by the accretion of a mass m on to its surface is

$$\Delta E_{acc} = \frac{GMm}{R}, \tag{1.18a}$$

when this is compared with the energy released per unit rest mass, we obtain the fraction of the gravitational potential energy released

$$\varepsilon = \frac{\Delta E_{acc}}{mc^2} = \frac{GM}{Rc^2}. \tag{1.18b}$$

Hence, the fraction of the energy released due to the accretion mechanism is strongly dependent on the compactness ratio of the central object, M/R, which

is very high for black holes. A precise estimate of the efficiency of energy release due to accretion is obtained from the binding energy per unit rest mass $[1-E(a)]$ at the ISCO, where $E(a)$ is given by Eq. (1.17a), in the equatorial plane of a rotating black hole. This is shown in Fig. 1.7, where we see that for a Kerr black hole with extreme spin, $a = 1$, the maximum fractional binding energy is $\eta = 1 - E(1) = \left(1 - \frac{1}{\sqrt{3}}\right) \simeq 0.42$, which is lower for the retrograde case as the ISCO radius is higher, and it is $\eta = 1 - E(0) = \left(1 - \frac{2\sqrt{2}}{3}\right) \simeq 0.057$ for $a = 0$; this has implications for the evolution of the black hole (Bhattacharyya and Mangalam 2020). Hence, accretion of matter on to a black hole is a very efficient mechanism for the release of energy in keV to MeV range (X-rays) (Novikov and Thorne 1973; Shakura and Sunyaev 1973).

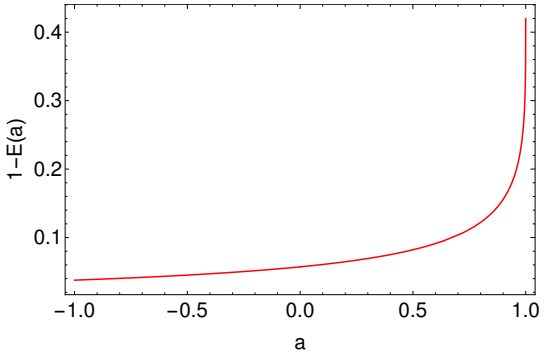

FIGURE 1.7: The figure shows binding energy per unit rest mass $[1-E(a)]$ of ISCO radius for a Kerr black hole as a function of a, where $a > 0$ is the prograde and $a < 0$ is the retrograde case.

1.3.1 Black hole X-ray binaries (BHXRB)

Black hole X-ray binaries (BHXRB) are systems with a primary black hole gravitationally bound to a non-degenerate companion star. These systems display transient behavior exhibiting high X-ray luminosities ($L_X \sim 10^{38}$ erg s^{-1}) during the outburst state, lasting from a few days to many months, followed by a long quiescent state ($L_X \sim 10^{30}$ erg s^{-1}) (Remillard *et al.* 2006). During the outburst

phase, the X-ray intensity shows rapid variations with time-scale ranging from milliseconds to a few seconds, which is most likely to arise in proximity to the black hole ($r \sim r_{ISSO}$, where ISSO stands for the innermost stable spherical orbit). The triggering of these X-ray outbursts has been modeled as an instability arising in the accretion disk when the accretion rate is not adequate for the continuous matter flow to the black hole, and when a critical surface density is reached (Dubus *et al.* 2001). However, the disk instability model has not been able to explain the outbursts of much shorter or longer time-scales; for example, BHXRB GRS 1915+105 has shown high X-ray luminosity state for nearly 20 years (Fender and Belloni 2004). An artistic sketch of 16 BHXRB in the Milky Way is shown in Fig. 1.8.

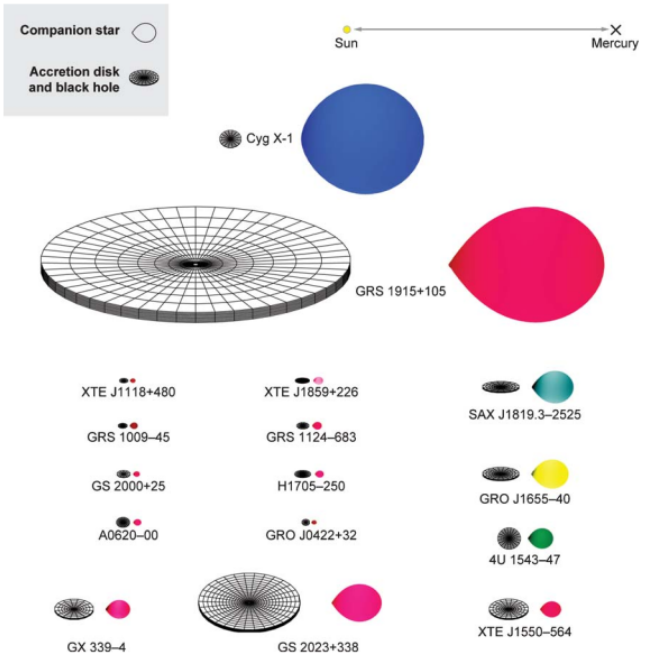

FIGURE 1.8: A sketch of 16 BHXRB in the Milky Way is shown. A comparison of the distance is shown with respect to the Sun-Mercury distance at the top. The color of the companion star roughly represents their surface temperature. Courtesy: Remillard *et al.* (2006).

1.3.1.1 Quasi-periodic oscillations (QPOs) in BHXRB

The power spectral density (PSD) of the X-ray intensity, which is commonly used to probe this fast variability, exhibit distinct features called quasi-periodic oscillations (QPOs) during the outburst period with their peak frequency, ν_0, ranging from 0.01 Hz to 450 Hz (Remillard *et al.* 2006; Belloni and Stella 2014). QPOs can be distinguished from other broad features of the PDS by their high-quality factor $\nu_0/FWHM \gtrsim 2$, where $FWHM$ is full width half maximum. Hence, the study of properties and origin of QPOs in BHXRB is crucial to understanding the properties of inner accretion flow close to the black hole where general relativistic effects are ascendant. QPOs in BHXRB are categorized as (Remillard *et al.* 2006):

1. *Low-frequency QPOs (LFQPOs)*: $\nu_0 < 30$Hz, which are again classified as type-A, B, and C based on their various properties. The type-A QPOs are usually weak and broad with $(\nu_0/FWHM) \leq 3$, seen in the range 6-8 Hz. The type-B QPOs are observed to be relatively strong and narrow around 1-3 Hz or 6 Hz with $(\nu_0/FWHM) \geq 6$. Type-C is the most frequent QPO with very strong and narrow peak, $(\nu_0/FWHM) \geq 10$, and having a wide frequency range from mHz to 30 Hz (Motta 2016).

2. *High-frequency QPOs (HFQPOs)*: $\nu_0 > 30$Hz with $10 \leq (\nu_0/FWHM) \leq 40$. The launch of the Rossi X-ray Timing Explorer (RXTE) in 1995 with its high sensitivity significantly increased the detection of BHXRB, and made it possible to detect HFQPOs in their PSD in the late 1990s (Belloni and Stella 2014); for example, the detection of 300 Hz and 450 Hz QPOs in GROJ1655-40 (Remillard *et al.* 1999a; Strohmayer 2001a) (Fig. 1.9) and many more.

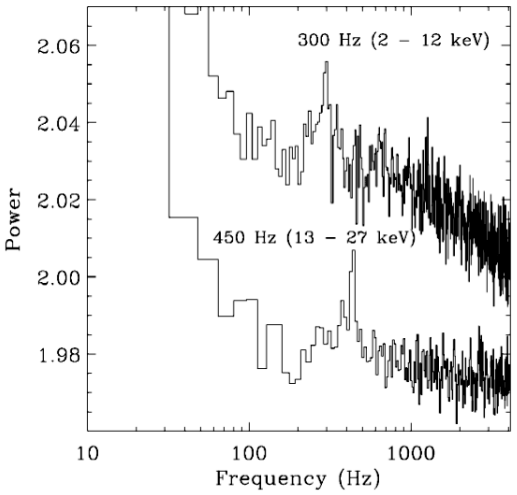

FIGURE 1.9: The detection of simultaneous HFQPOs is shown in the PSD of BHXRB GROJ1655-40. Courtesy: Strohmayer (2001a).

1.3.1.2 Spectral states in BHXRB

The energy spectrum of BHXRB shows a superposition of different components arising from different regions of the accretion flow, and it is also time-dependent. These systems transit through various spectral states during their outburst period and show a hysteresis behavior seen as a Q-shaped loop in the hardness-intensity diagram (HID) (Fig. 1.10) (Fender *et al.* 2004; Fender and Belloni 2012; Remillard *et al.* 2006). Initially, the spectral states were categorized as thermal (high/soft state, HSS), hard (low/hard state, LHS), and steep power-law (very high or ultra-luminous state, SPL) states (Remillard *et al.* 2006) based on whether the thermal component (multi-temperature blackbody spectra arising from a thin accretion disk) or the power-law component (most probably arising from a coronal region) is dominant in the X-ray spectrum. Later, the states between low/hard and high/soft in the HID was further classified as Hard Intermediate State (HIMS) and Soft Intermediate State (SIMS) according to the photon index value of the power-law component, Γ, and the association of these states with the type-A, B, C, and HFQPOs (Motta 2016). An X-ray outburst starts with the LHS (A$\rightarrow$B in Fig.

1.10), and moves towards the HIMS (B→C in Fig. 1.10) and then SIMS (C→D in Fig. 1.10), where it reaches the SPL state (D→E in Fig. 1.10). Finally, the outburst comes back to LHS through E→F→A (Fig. 1.10). The timescale of this Q-track in the hardness-intensity diagram varies from a few months to years in BHXRB.

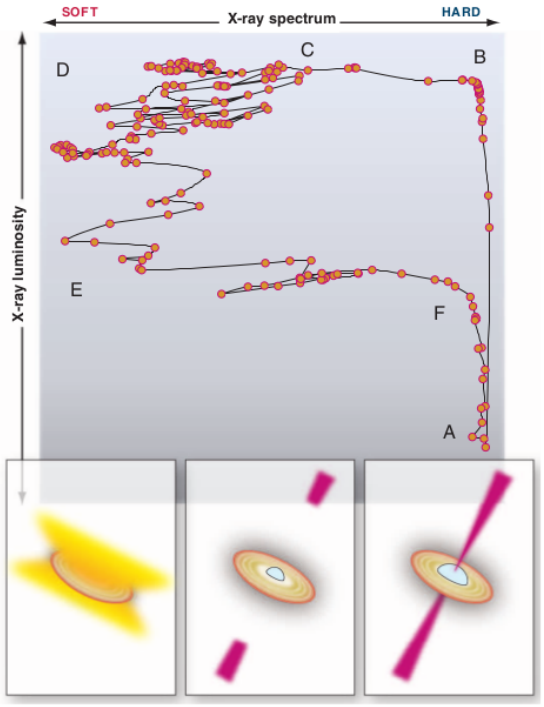

FIGURE 1.10: The X-ray hardness versus luminosity diagram showing the evolution track of the outburst in BHXRB. Courtesy: Fender and Belloni (2012).

The type-A LFQPOs (6-8 Hz) are usually observed during the HSS, whereas type-B LFQPOs (1-3 Hz or 6 Hz) are associated with the SIMS. The centroid frequency of the type-C LFQPOs transits from mHz during the LHS to a few Hz during the HIMS, and finally attains the maximum value around $\sim 10-30$ Hz when the spectral state reaches the HSS. On the other hand, the HFQPOs have been observed to have a high-quality factor, 5 to 20, and they are always detected during the anomalous or SPL state when the X-ray flux is very high (Remillard *et al.* 2006; Belloni and Stella 2014; Motta 2016). Also, the HFQPOs are found to

be stable in their frequency values even when the luminosity of BHXRB changes by a factor of $2-3$, for example, 67 Hz QPO of GRS 1915+105 (Strohmayer 2001b); this is a characteristic of the system, a *voice print* that might only depend on the spin and mass of the black hole.

1.3.1.3 PBK correlation

There is an interesting and positive correlation that was found between the frequencies of HFQPOs and LFQPOs in different BHXRB, called the Psaltis-Belloni-van der Klis (PBK) (Psaltis *et al.* 1999) correlation. In the cases of BHXRB where HFQPOs are not detected, the same correlation was followed by the characteristic frequency of a broad feature (not a QPO) in the PSD with the LFQPOs, during the low/hard state. Such a strong correlation suggests a single phenomenon responsible for the origin of these QPOs in various BHXRB.

1.3.2 Intermediate mass black holes (IMBH)

The black holes with mass range $M_\bullet = 10^2 - 10^5 M_\odot$ provide the evidence for IMBH (Miller and Colbert 2004). The existence of these black holes is still considered to be controversial, however, there are a few candidates that show strong evidence of IMBH. For example, the ultra-luminous X-ray sources (ULX), like M82 X-1, with $L_X > 10^{40}$erg/s are considered to be the IMBH candidates (Pasham *et al.* 2014; Bambi 2019). However, only a dynamical measurement of the mass of the compact object in the ULX can unveil the presence of an IMBH. Another example of an IMBH is HLX-1 in the spiral galaxy ESO 243-49 with a black hole mass of over $500 M_\odot$ (Farrell *et al.* 2009, 2012). Other evidence of IMBH comes from the gravitational wave observations, for example, the formation of $142 M_\odot$ from

the merger of $85M_{\odot}$ and $66M_{\odot}$ black holes was reported (Abbott and Abbott 2020b,a).

1.3.3 Active galatic nuclei (AGN)

Most of the galaxies in the Universe are thought to possess a supermassive black hole at their centers. Active galactic nuclei (AGN) are the compact regions at the center of certain galaxies having very high luminosities $10^{42} - 10^{48}$erg/s. The emission from these central engines is observed in a wide range of wavelengths, like radio, infra-red, ultra-violet, X-rays, and γ-rays. The standard unification model for an AGN explains the origin of the wide range of wavelengths originating from different regions around a black hole (Rees 1984; Blandford and Rees 1992; Antonucci 1993; Urry and Padovani 1995), which are:

1. An accretion disk around the central supermassive black hole with mass range $M_{\bullet} = 10^6 M_{\odot}$ (Seyfert galaxies) to $10^9 M_{\odot}$ (Blazars), which is the source of UV, optical, and soft X-rays emission.

2. A torus-shaped region of gas and dust of size > 0.1 pc, which is found to be cooler than the accretion disk because it exists further away from the central black hole.

3. The broad line region (BLR) of gas clouds with a typical size of ~ 10 light days, and gravitationally bound to the central black hole.

4. The narrow line region (NLR) of gas clouds at a distance of 1 to 1000 pc from the central region.

Along with these components of the standard model, the radio loud AGN with powerful jets are modeled as jets consisting of accelerated particles aligned with the

rotation axis of the black hole. The observational properties of different types of AGN are believed to be associated with the observer's line of sight passing through various components mentioned above. A cartoon diagram of this unification model is shown in Fig. 1.11.

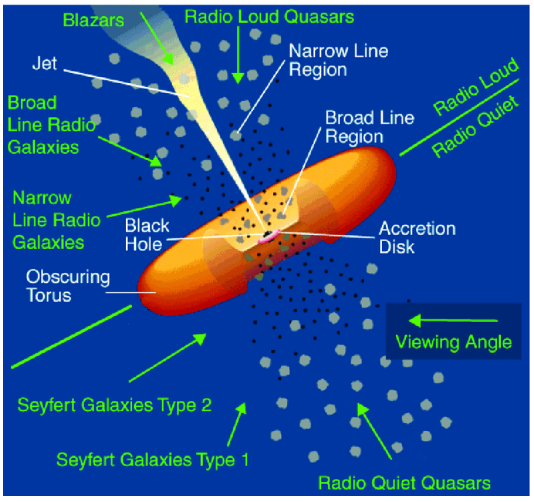

FIGURE 1.11: The unification model for AGN showing the main features: accretion disk, BLR, NLR, and the torus region. Courtesy: Urry and Padovani (1995).

1.3.3.1 Power spectral density (PSD) and QPOs in AGN

The X-ray variability is a key diagnostic for understanding the physical processes in the innermost regions of the accretion flow. The similarity in the behavior of X-ray variability in AGN and BHXRB is an important aspect of the AGN-BHXRB connection (McHardy *et al.* 2006; McHardy 2010). The AGN are known to have a characteristic shape mathematically described by a bending power-law model (McHardy *et al.* 2004; Papadakis *et al.* 2010) given by

$$P(\nu) = P_0 \left(\frac{\nu}{\nu_b}\right)^{-\alpha_l} \left[1 + \left(\frac{\nu}{\nu_b}\right)^{(\alpha_h - \alpha_l)}\right]^{-1}, \tag{1.19}$$

where P_0 is the normalization constant, and α_l, α_h are the PSD slopes below and above the break frequency, ν_b. Typically, it is observed that $\alpha_h \sim 2$ and $\alpha_l \sim 1$ for higher and lower frequencies respectively in various types of AGN with ν_b ranging from $\sim 10^{-6} - 10^{-4}$ (Papadakis *et al.* 2010; González-Martín and Vaughan 2012). An explanation for this PSD slopes was first proposed by Mangalam and Wiita (1993) as a Fourier sum of contributions from time signals induced at different annuli of the accretion disk. An example of a typical PSD shape is shown in Fig. 1.12.

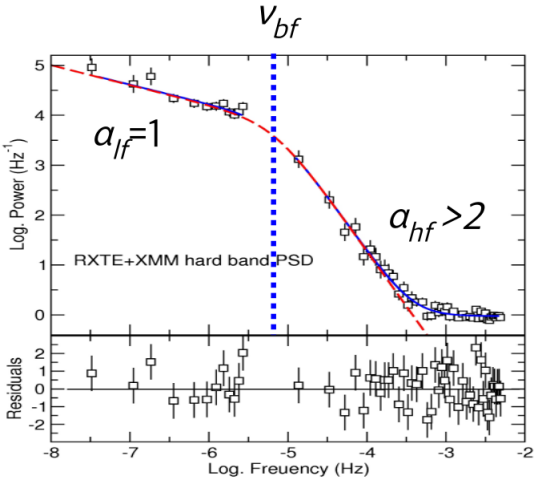

FIGURE 1.12: The PSD of a narrow-line Seyfert 1 galaxy PKS 0558-504 following the bending power-law, Eq. (1.19). Courtesy: Papadakis *et al.* (2010).

Over the last decade, there are also various claims of the detection of QPOs in different classes of AGN with timescales ranging from a few tens of minutes to hours in X-rays, days and also years in optical and γ ray light curves (Gierliński *et al.* 2008; Lin *et al.* 2013; Alston *et al.* 2015; Ackermann *et al.* 2015a; Sandrinelli *et al.* 2014, 2016a,b, 2017, 2018; Gupta *et al.* 2009; Graham *et al.* 2015; King *et al.* 2013; Fan *et al.* 2014). A X-ray QPO with $\sim$ 2 hour timescale was detected in MS 2254.9-3712 (Alston *et al.* 2015). Later, 1H 0707-495 also showed the detection of a significant QPO at $\sim$ 3800s and another at timescale $\sim$ 8265s with relatively low significance in the X-ray light curve (Pan *et al.* 2016; Zhang *et al.* 2018). A highly significant X-ray QPO of timescale $\sim$ 6450s was reported in NLSy1 Mrk

766 (Zhang *et al.* 2017), while another QPO (but not simultaneous) with a period of $\sim$ 4200s was also reported (Boller *et al.* 2001), making these two signals in $\sim 3:2$. Another significant X-ray QPO was reported in NLSy1 MCG-06-30-15 of timescale $\sim$ 3600s (Gupta *et al.* 2018). Very recently, the detection of two QPOs was reported at timescales $\sim$ 8064.5s and $\sim$ 14706s in ESO 113-G010 (Peng *et al.* 2020).

QPOs are also observed in the γ ray and optical light curves in various Blazars, for example, a QPO of timescale 2.18 ± 0.08 year was discovered in γ ray light curve of PG 1553+113 (Ackermann *et al.* 2015a), where correlated oscillations were found in the radio and optical light curves. Later, an optical QPO of similar timescale, $\sim$ 810 days, was confirmed in PG 1553+113 (Sandrinelli *et al.* 2018). Another γ ray QPO with a timescale of a few months, $T \sim 280$ days, was reported in PKS 0537-441, where an optical QPO of timescale $\sim T/2$ was also discovered (Sandrinelli *et al.* 2016b). A pair of optical and γ ray QPO was also reported in BL Lac, having similar timescales of $\sim$ 680 days (Sandrinelli *et al.* 2017, 2018).

The understanding of the PSD shape and QPO frequencies are fundamental for probing the inner region close to the black hole, that is taken up in chapter 6.

1.3.4 The spin and mass measurement of black holes

There are various techniques that have been developed to measure spin and mass of the black hole in BHXRB and AGN. We discuss some of these methods below:

1.3.4.1 Mass measurement techniques

The most accurate mass measurement technique in black hole astrophysics is through dynamical methods. For a test particle orbiting in Keplerian orbits around a black hole of mass $M_\bullet$ (Narayan 2005), we have

$$M_\bullet = \frac{4\pi^2 r^3}{G T_{orb}^2} = \frac{v^3 T_{orb}}{2\pi G}, \tag{1.20}$$

where v is the velocity of the orbiting particle, T_{orb} is the period of the orbit, and r is radius if it is a circular orbit and the semi-major axis if it is an elliptical orbit.

- *Mass function*: In the case of BHXRB, one measures the mass function given by

$$f(M_\bullet) = \frac{K^3 T_{orb}}{2\pi G} = \frac{M_\bullet \sin^3 i}{(1 + M_c/M_\bullet)^2}, \tag{1.21}$$

  where M_c is mass of the companion star and K is the maximum line-of-sight Doppler velocity, $K = v \sin i$, of the companion star and i is the inclination angle of the binary orbit. The values for T_{orb} and K are obtained from the optical or infra-red observations of the companion star. One requires an independent measurement of i and M_c, which combines with those of T_{orb} and K to estimate $M_\bullet$. The masses of many compact objects in the binary systems have been measured through this method.

- *Stellar dynamics*: Using the accurate measurement and modeling of the elliptical orbits of stars near a supermassive black hole, and by using Eq. (1.20) is another method for estimating the mass of the black hole. For example, the mass of the black hole at the center of the Milky Way galaxy estimated through this method is measured to be $(3.7 \pm 1.5) \times 10^6 M_\odot$ (Schödel *et al.* 2002), and a more recent estimation is $(4.5 \pm 0.4) \times 10^6 M_\odot$ (Ghez *et al.* 1997, 2000, 2008). For a review of this method, see Kormendy and Ho (2013).

- *Water maser emission*: The observation of H2O maser emission at ~ 22 GHz is also used to trace gas clouds orbiting the massive black holes in galactic nuclei. Radio interferometry measurements, such as the VLBA, have shown that the gas clouds in the extended disk follow Keplerian orbits and hence follow

$$v = \left(\frac{GM_\bullet}{r}\right)^{1/2} \sin i, \tag{1.22}$$

  where i is the disk inclination with respect to the line of sight and r is the radial distance from the center of the galaxy. The observation of such velocity profile gives a direct measurement of the mass of the supermassive black hole, for example in the case of galaxy NGC 4258, a mass of $3.6\times10^7 M_\odot$ was inferred for the central black hole (Miyoshi *et al.* 1995).

- *Reverberation mapping*: The reverberation mapping of the BLR clouds (Peterson 1993) is also a much-favored technique. For a virialized gas cloud,

$$M_\bullet = \frac{frv^2}{G}, \tag{1.23}$$

  where f is a covering fraction that accounts for the shape of the BLR clouds, r is distance to the BLR region, and v is the average velocity of the gas. The continuum emission from the accretion disk shows fluctuations due to the perturbations in the flow. These fluctuations are imprinted on the outgoing radiation. The BLR clouds close to the inner region will re-process this incoming radiation before it reaches the observer. The time delay between the continuum and line variations, $\Delta\tau$, then gives an upper limit on $r = c\Delta\tau$.

1.3.4.2 Spin measurement techniques

There are various techniques for spin measurements of black holes, which are discussed below:

- *Continuum spectral fitting*: In the high-soft spectral state of BHXRB, when the accretion rate and hence the luminosity, L_{acc}, is very high, the accreting gas is optically thick and radiates approximately as a blackbody. Using the flux of radiation, $F(r)$, emitted by the accretion disk, and one can theoretically estimate the effective temperature profile $T_{eff}(r) = [F(r)/\sigma]^{1/4}$, where σ is the Stefan-Boltzmann constant. The comparison of this quantity with the observed spectral flux, $F_\nu \Delta\nu$, one obtains an estimate of $r_{in}^2 \cos i/D^2$ (the projected solid angle of the disk), where D is the distance to the source and i is the inclination angle. The dependence of r_{in} on the spin of the black hole then provides an estimate of spin (Zhang *et al.* 1997; Mudambi *et al.* 2020; Zhao and Dong 2020).

- *Iron line emission*: The observation of the relativistic Kα fluorescent emission line from gas in the accretion disk also provides an estimate of the spin of the black hole (Fabian *et al.* 1995, 1989). The observed line ranges from about 4-7 keV, whereas the rest energy of this emission line is 6.4−6.9 keV, this is a result of broadening due to the Doppler shifts. The shape of the observed emission line depends on: (i) the range of radius over which the emission occurs, where the black hole spin has a significant effect, (ii) the line emissivity as a function of r, (iii) the disk inclination, i, because the Doppler effects are much less for a face-on disk than an edge-on disk. For an observed broad iron line, and assuming that the radiating gas is orbiting in a Keplerian orbit with radii $r \geq Z$, one can fit the shape of the line profile to estimate a, i, and the emissivity function (Brenneman *et al.* 2011; Walton *et al.* 2012).

- *QPOs*: The frequencies of QPOs have an imprint of relativistic motion of gas close to the black hole. Using the relativistic precession model (Stella and Vietri 1999; Stella *et al.* 1999), one associates the fundamental frequencies of the relativistic bound orbits, $\{\nu_\phi, (\nu_\phi - \nu_r), (\nu_\phi - \nu_\theta)\}$, in the Kerr spacetime, with the QPO frequencies to infer the spin of the black hole (see Fig.

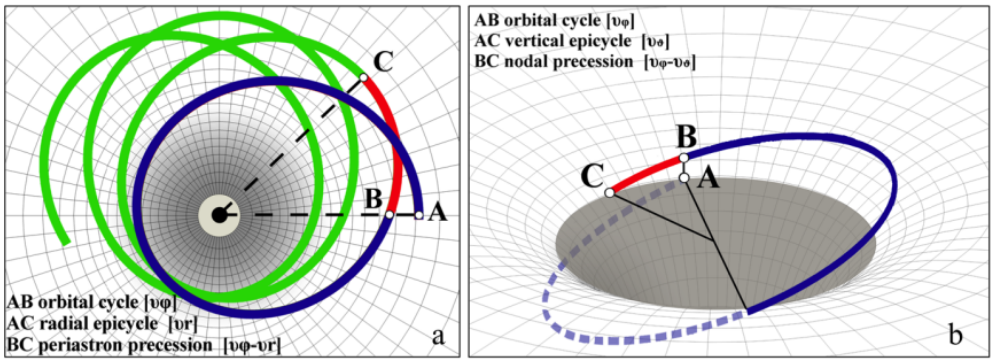

FIGURE 1.13: An illustration of (a) periastron, and (b) nodal precession of the relativistic orbits near the equatorial plane of a Kerr black hole. Courtesy: Belloni and Stella (2014).

1.13). This technique was applied to BHXRB GRO J1655-40 for estimating mass and spin of the black hole (Strohmayer 2001a; Motta *et al.* 2014a).

1.3.5 Importance of integrals of motion (IOM) in black hole dynamics

The study of trajectories and accretion of matter around the black holes is a critical input to our understanding of the physical processes and their observational consequences like PSD, relativistic precession, QPOs, and gravitational waves from extreme-mass ratio inspirals, etc (Narayan 2005; Bambi 2019; Remillard *et al.* 2006; Glampedakis 2005). The study involves the dynamics of test particle motion in a most general and non-equatorial scenario, and finding solutions to the integrals of motion around a Kerr black hole. *Any progress made in the analytic solutions will advance the current understanding of the observations of black holes.*

1.4 Goals of the Thesis

1. To identify and classify of various types of general bound timelike trajectories, for example, non-equatorial eccentric, spherical orbits, etc, and special radii in the $\{r, a\}$ plane of the Kerr spacetime.

2. The identification of the general bound trajectories as regions and curves in the energy and angular momentum space $\{E, L, a, Q\}$, and the eccentricity and inverse-latus rectum space $\{e, \mu, a, Q\}$, and the mathematical forms of the conditions for these bound orbits.

3. The comparison of $\{E, L, a, Q\}$ and $\{e, \mu, a, Q\}$ parameter space and translation relations between them.

4. Building the compact analytic forms for the integrals of motion of the most general bound timelike trajectories in the Kerr spacetime using $\{e, \mu, a, Q\}$ parameter space, which removes the singularity at the turning points of the orbit.

5. Reduction of the general trajectory solution to the special cases of equatorial eccentric and spherical orbits to obtain simpler forms.

6. To study the special kind of trajectories, called the non-equatorial separatrix orbits, and obtaining their trajectory solution while finding the locus of these trajectories in the $\{e, \mu\}$ space.

7. To develop a simpler method to derive the analytic forms of the fundamental frequencies $\{\nu_\phi, \nu_r, \nu_\theta\}$ for general bound timelike trajectories.

8. To sketch and visualize these orbits using the analytic forms of the trajectory solutions.

9. To apply the analytic forms of the integrals of motion and the fundamental frequencies to develop a general relativistic precession model (GRPM)

to comprehend the origin of QPO frequencies in BHXRB and AGN, and estimation of the orbital parameters and the spin of the black hole.

10. To develop a general relativistic orbit model, based on distribution functions of integrals of motion, for the observed PSD in AGN, and to motivate a relativistic MHD jet model for the γ ray QPOs observed in Blazars from the fundamental timescale of the orbits around a Kerr black hole.

11. To provide a context for future work.

1.5 Plan of the Thesis

The chapter-wise plan of the thesis is given below and the concept flow chart is shown in Fig. 1.14.

- In chapter 2, we derive the fundamental equations for the integrals of motion defining the solution for timelike trajectories using the Hamiltonian dynamics, and obtain the conserved quantities, E and L, associated with the symmetries in the Kerr geometry, and also derive the Carter's constant, Q, from the separability of the Hamilton-Jacobi equation. We discuss the Hamilton-Jacobi theory and the history of its application to dynamics of Kerr black holes.

- In chapter 3, we derive the translation relations between $\{E,\, L,\, a,\, Q\}$ and $\{e,\, \mu,\, a,\, Q\}$ parameter space. We classify various types of timelike bound trajectories as regions and curves in the $(E,\, L)$ and $(e,\, \mu)$ planes, and also derive corresponding mathematical conditions for these orbits. We also provide a mathematical prescription to obtain bound trajectories in the $(E,\, L)$ and $(e,\, \mu)$ space.

- In chapter 4, we present a compact and analytic form for the integrals of motion of the bound timelike trajectories, using (e, μ, a, Q) parameter space, in terms of the standard Elliptic integrals. These expressions increase the computation efficiency for obtaining trajectory solutions. We also derive the analytic forms of the fundamental frequencies using an asymptotic average method. We reduce our trajectory solutions to the special formulae for the equatorial eccentric and spherical orbits. We write the general expressions for important radii like ISSO, MBSO, and the light radius. We also derive the analytic form for (e, μ) for the non-equatorial separatrix trajectories, and also obtain their trajectory solutions. We finally sketch different non-equatorial trajectories using our analytic solutions.

- In chapter 5, we develop a general relativistic precession model (GRPM) for QPOs observed in BHXRB. We apply our analytic expressions for the fundamental frequencies of general non-equatorial and eccentric trajectories to understand the origin of QPO frequencies and deduce the physical parameters of the orbits. We also study the PBK correlation, seen in BHXRB, using our model. We finally connect our results with a GR fluid model and determine the region around a Kerr black hole which is associated with the genesis of QPOs.

- In chapter 6, we apply the GRPM to study the origin of X-ray QPOs observed in AGN. We motivate a jet model to explain the γ ray QPOs observed in Blazars. We also present a relativistic orbit model to obtain the PSD shape observed in AGN.

- In chapter 7, we summarize our work, discuss the novel aspects, and the implications for future work. We also present caveats and future theoretical approaches.

1.6 Resource summary

In this chapter, we presented a basic introduction to the theory of Kerr black holes, and an overview of the observations of various kinds of astrophysical black holes, their literature survey along with the motivation and plan of the Thesis. We also present a schematic of the Thesis and its goals in Fig. 1.14. The main resources we used for discussion are - Hartle (2003), Middleton (2016), Remillard *et al.* (2006), Belloni and Stella (2014), Fender and Belloni (2012), Rees (1984), Narayan (2005), and references within.

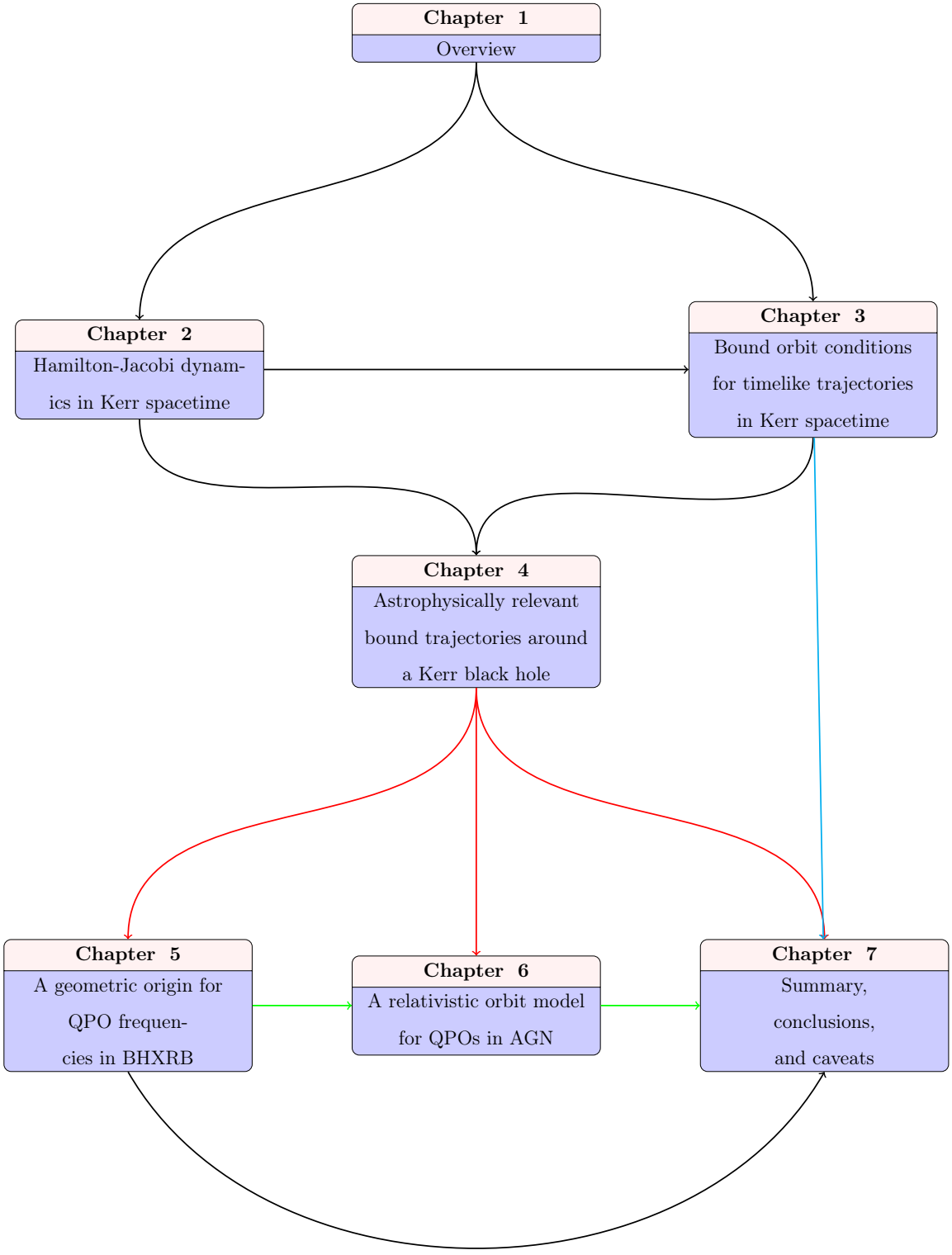

FIGURE 1.14: The plan of the thesis is shown.

Chapter 2

An artistic image of a black hole with edge-on accretion disk. Courtesy: Wikipedia

Hamilton-Jacobi dynamics in Kerr geometry

2.1 Introduction

The trajectories in the Kerr (Kerr 1963) and Schwarzschild (Schwarzschild 1916) geometries have been studied extensively. The formulation of the Hamilton-Jacobi equation was first used by Carter (1968) for the axisymmetric background, where it was shown that the general trajectory solution can be expressed in terms of quadratures. Consequently, another conserved quantity, called Carter's constant, was deduced using a simplistic idea of separability of the Hamilton-Jacobi equation into r and θ parts. Hence, the addition of a constant of motion in the Kerr orbital dynamics, then, revolutionized the understanding of trajectories around a rotating black hole.

In this chapter, we derive the basic equations of motion and associated integrals in quadrature form using the Hamilton-Jacobi equation. The formulation of these equations is more straightforward than solving the Euler-Lagrange equation. In §2.2, we first write the Lagrangian to obtain conserved quantities E and L, and corresponding equations of motion for $\dot{t}$ and $\dot{\phi}$. We then move to Hamilton-Jacobi formulation in §2.2.1, where we derive the quadrature forms for $\{t,\, r,\, \theta,\, \phi\}$ and also equations of motion $\{\dot{t},\, \dot{r},\, \dot{\theta},\, \dot{\phi}\}$. In §2.2.2, we obtain the radial effective potential for the most general and non-equatorial trajectory around a Kerr black hole. In §2.2.3, we discuss the domains in the (r-θ) plane where equations of motion have real solutions. We discuss the history of the solution to the Hamilton-Jacobi equation in the Kerr geometry. We provide a resource summary in §2.4.

2.2 Equations of geodesic motion in the Kerr geometry

Here, we start with the basic Lagrangian formulation and then motivate the Hamilton-Jacobi method. The simplest and generalized form of the Lagrangian can be written as

$$\mathcal{L} = \frac{1}{2} g_{\mu\nu} \frac{\mathrm{d}x^{\mu}}{\mathrm{d}\lambda} \frac{\mathrm{d}x^{\nu}}{\mathrm{d}\lambda} = \frac{1}{2} u_{\mu} u^{\mu} = -\frac{1}{2} \delta_1, \tag{2.1}$$

where λ is an affine parameter, which turns out to be the proper time for the time-like geodesics [see Misner *et al.* (1973)] and $u_{\mu}u^{\mu} = -\delta_1$ is the normalization condition of the four-velocity where

$$\delta_1 = \begin{cases} +1 & \text{for time-like geodesics,} \\ 0 & \text{for null geodesics,} \end{cases}$$

is a constant of motion. Now, using $g_{\mu\nu}$ defined for the Kerr geometry, Eq. (1.2), $\mathcal{L}$ gets the form

$$2\mathcal{L} = -\left(1 - \frac{2r}{\rho^2}\right)\dot{t}^2 + \left(r^2 + a^2 + \frac{2ra^2\sin^2\theta}{\rho^2}\right)\sin^2\theta\,\dot{\phi}^2 - \frac{4ar\sin^2\theta}{\rho^2}\,\dot{t}\,\dot{\phi} + \frac{\rho^2\dot{r}^2}{\Delta} + \rho^2\dot{\theta}^2. \tag{2.2}$$

The symmetries of the metric lead to the constants of motion through $\mathcal{L}$. In the case of Kerr geometry, the metric elements are independent of t and ϕ. Thus, the conserved quantities are given by the corresponding conjugate momenta:

$$p_\mu = \frac{\partial\mathcal{L}}{\partial\dot{x}^\mu} = g_{\mu\nu}\dot{x}^\nu, \tag{2.3a}$$

which are

$$p_t = g_{tt}\dot{t} + g_{t\phi}\dot{\phi} = -E = -\left(1 - \frac{2r}{\rho^2}\right)\dot{t} - \frac{2ar\sin^2\theta}{\rho^2}\dot{\phi}, \tag{2.3b}$$

$$p_\phi = g_{\phi\phi}\dot{\phi} + g_{\phi t}\dot{t} = L = -\frac{2ar\sin^2\theta}{\rho^2}\dot{t} + \left(r^2 + a^2 + \frac{2ra^2\sin^2\theta}{\rho^2}\right)\sin^2\theta\,\dot{\phi}. \tag{2.3c}$$

Hence, the equations for $\dot{t}$ and $\dot{\phi}$ are deduced by solving above equations, (2.3b, 2.3c), which yields

$$\dot{t} = \frac{(\Sigma^2 E - 2arL)}{\Delta\rho^2}, \tag{2.4a}$$

$$\dot{\phi} = \frac{1}{\Delta\rho^2}\left(2raE + \frac{\rho^2 - 2r}{\sin^2\theta}L\right), \tag{2.4b}$$

where

$$\Sigma^2 = \left(r^2 + a^2\right)^2 - a^2\Delta\sin^2\theta. \tag{2.4c}$$

The equations governing the evolution of t and ϕ coordinates are easily obtained using the Lagrangian method. However, the derivation of $\dot{r}$ and $\dot{\theta}$ involves the analysis of basis null vectors in the integrals of geodesic motion (Chandrasekhar 1983). Next, we now discuss the elegant derivation using the Hamilton-Jacobi formulation to derive the equations of motion leading to the quadrature forms.

2.2.1 Hamilton-Jacobi equation

We know by definition that the Hamiltonian for Kerr geometry follows from the Lagrangian, Eq. (2.1), as

$$\mathcal{H} = p_\mu \dot{x}^\nu - \mathcal{L} = -\frac{1}{2}\delta_1 \equiv \frac{\partial S}{\partial \lambda}, \tag{2.5}$$

where the equivalance is the action principle acting on the characteristic function S. Therefore the Hamilton-Jacobi equation defining the geodesic motion in a given metric is (Misner *et al.* 1973)

$$-2\frac{\partial S}{\partial \lambda} = g^{\mu\nu}\frac{\partial S}{\partial x^\mu}\frac{\partial S}{\partial x^\nu}, \tag{2.6}$$

and the generalized momentum is given by

$$p_\mu = g_{\mu\nu}\dot{x}^\nu = \frac{\partial S}{\partial x^\mu}. \tag{2.7}$$

The equation (2.6) expands for the Kerr metric to

$$-2\frac{\partial S}{\partial \lambda} = g^{tt}\left(\frac{\partial S}{\partial t}\right)^2 + g^{\phi\phi}\left(\frac{\partial S}{\partial \phi}\right)^2 + 2g^{t\phi}\left(\frac{\partial S}{\partial t}\right)\left(\frac{\partial S}{\partial \phi}\right) + g^{rr}\left(\frac{\partial S}{\partial r}\right)^2 + g^{\theta\theta}\left(\frac{\partial S}{\partial \theta}\right)^2, \tag{2.8a}$$

where the substitution of metric tensor elements, $g^{\mu\nu}$, using Eq. (1.2) gives

$$-2\frac{\partial S}{\partial \lambda} = -\frac{1}{\rho^2\Delta}\left[(r^2+a^2)\left(\frac{\partial S}{\partial t}\right) + a\left(\frac{\partial S}{\partial \phi}\right)\right]^2 + \frac{1}{\rho^2 \sin^2\theta}\left[a\sin^2\theta\left(\frac{\partial S}{\partial t}\right) + \left(\frac{\partial S}{\partial \phi}\right)\right]^2 + \frac{\Delta}{\rho^2}\left(\frac{\partial S}{\partial r}\right)^2 + \frac{1}{\rho^2}\left(\frac{\partial S}{\partial \theta}\right)^2. \tag{2.8b}$$

Since, the above equation has no explicit dependence on t, ϕ, and λ, the solution for S must take the form

$$S = \frac{1}{2}\delta_1\lambda - Et + L\phi + S^{r,\theta}(r,\theta). \tag{2.9a}$$

Assuming that r and θ variables are separable, a solution of the following form is sought:

$$S = \frac{1}{2}\delta_1 \lambda - Et + L\phi + S^r(r) + S^\theta(\theta), \tag{2.9b}$$

where the integration constants follow from Eq. (2.7)

$$\frac{\partial S}{\partial t} = p_t = -E, \quad \frac{\partial S}{\partial \phi} = p_\phi = L, \tag{2.9c}$$

and

$$\frac{\partial S}{\partial \lambda} = \frac{1}{2}\delta_1. \tag{2.9d}$$

Hence, by substituting Eq. (2.9b) in Eq. (2.8b), we obtain

$$\rho^2 \delta_1 = \frac{\left[(r^2+a^2)E - aL\right]^2}{\Delta} - \frac{\left(aE\sin^2\theta - L\right)^2}{\sin^2\theta} - \Delta\left(\frac{\mathrm{d}S^r}{\mathrm{d}r}\right)^2 - \left(\frac{\mathrm{d}S^\theta}{\mathrm{d}\theta}\right)^2. \tag{2.10}$$

With the aim of separating r and θ parts in the above equation, we use the following trigonometric identity:

$$\left(aE\sin^2\theta - L\right)^2 \csc^2\theta = \left(L^2\csc^2\theta - a^2E^2\right)\cos^2\theta + (L - aE)^2, \tag{2.11}$$

which yields

$$-\left[\left(\frac{\mathrm{d}S^r}{\mathrm{d}r}\right)^2\Delta - \frac{\left[(r^2+a^2)E - aL\right]^2}{\Delta} + (L-aE)^2 + \delta_1 r^2\right] = \left[\left(\frac{\mathrm{d}S^\theta}{\mathrm{d}\theta}\right)^2 + \delta_1 a^2\cos^2\theta + \left(L^2\csc^2\theta - a^2E^2\right)\cos^2\theta\right]. \tag{2.12}$$

We see that r and θ parts are separable in the above equation. Hence, both should equate to a constant which is called Carter's constant, Q. We finally obtain the separated equations

$$-\left[\left(\frac{\mathrm{d}S^r}{\mathrm{d}r}\right)^2\Delta - \frac{\left[(r^2+a^2)E - aL\right]^2}{\Delta} + (L-aE)^2 + \delta_1 r^2\right] = Q, \tag{2.13a}$$

and

$$\left[\left(\frac{\mathrm{d}S^{\theta}}{\mathrm{d}\theta}\right)^{2}+\delta_{1}a^{2}\cos^{2}\theta+\left(L^{2}\csc^{2}\theta-a^{2}E^{2}\right)\cos^{2}\theta\right]=Q, \tag{2.13b}$$

which yields

$$\left(\frac{\mathrm{d}S^{r}}{\mathrm{d}r}\right)^{2}=\frac{R\left(r\right)}{\Delta^{2}} \quad \Rightarrow \quad S^{r}\left(r\right)=\int\frac{\sqrt{R\left(r\right)}}{\Delta}\mathrm{d}r, \tag{2.14a}$$

$$\left(\frac{\mathrm{d}S^{\theta}}{\mathrm{d}\theta}\right)^{2}=\Theta\left(\theta\right) \quad \Rightarrow \quad S^{\theta}\left(\theta\right)=\int\sqrt{\Theta\left(\theta\right)}\mathrm{d}\theta, \tag{2.14b}$$

where

$$R\left(r\right)=\left[\left(r^{2}+a^{2}\right)E-aL\right]^{2}-\Delta\left[\left(L-aE\right)^{2}+Q+\delta_{1}r^{2}\right], \tag{2.14c}$$

$$\Theta\left(\theta\right)=Q-\cos^{2}\theta\left[a^{2}\delta_{1}+L^{2}\csc^{2}\theta-a^{2}E^{2}\right]. \tag{2.14d}$$

Hence, by substituting $S^{r}\left(r\right)$ and $S^{\theta}\left(\theta\right)$ using Eqs. (2.14a, 2.14b), S [Eq. (2.9b)] takes the final form

$$S=\frac{1}{2}\delta_{1}\lambda-Et+L\phi+\int\frac{\sqrt{R\left(r\right)}}{\Delta}\mathrm{d}r+\int\sqrt{\Theta\left(\theta\right)}\mathrm{d}\theta. \tag{2.15}$$

The basic equations defining the geodesic motion can now be deduced using the standard procedure of setting the partial derivatives of S with respect to the constants of motion to zero, that is (Carter 1968; Schmidt 2002)

$$\frac{\partial S}{\partial Q}=0\Rightarrow \quad \int\frac{\mathrm{d}r}{\sqrt{R\left(r\right)}}=\int\frac{\mathrm{d}\theta}{\sqrt{\Theta\left(\theta\right)}}, \tag{2.16a}$$

$$\frac{\partial S}{\partial L}=0\Rightarrow \quad \phi=-\frac{1}{2}\left[\int\frac{1}{\Delta\sqrt{R\left(r\right)}}\frac{\partial R\left(r\right)}{\partial L}\mathrm{d}r+\int\frac{1}{\sqrt{\Theta\left(\theta\right)}}\frac{\partial\Theta\left(\theta\right)}{\partial L}\mathrm{d}\theta\right], \tag{2.16b}$$

$$\frac{\partial S}{\partial E}=0\Rightarrow \quad t=\frac{1}{2}\left[\int\frac{1}{\Delta\sqrt{R\left(r\right)}}\frac{\partial R\left(r\right)}{\partial E}\mathrm{d}r+\int\frac{1}{\sqrt{\Theta\left(\theta\right)}}\frac{\partial\Theta\left(\theta\right)}{\partial E}\mathrm{d}\theta\right], \tag{2.16c}$$

$$\frac{\partial S}{\partial\delta_{1}}=0\Rightarrow \quad \lambda=\int\frac{r^{2}}{\sqrt{R\left(r\right)}}\mathrm{d}r+a^{2}\int\frac{\cos^{2}\theta}{\sqrt{\Theta\left(\theta\right)}}\mathrm{d}\theta, \tag{2.16d}$$

where $\lambda = \tau$ for the time-like trajectories. We see that the radial and polar motion are coupled, Eq. (2.16a).

To obtain the equations for momenta or $\{\dot{t},\, \dot{r},\, \dot{\theta},\, \dot{\phi}\}$, we use Eq. (2.7) which gives

$$\frac{\partial S}{\partial r} = g_{r\nu}\dot{x}^{\nu} \Rightarrow \qquad \rho^2 \dot{r} = \sqrt{R\left(r\right)}, \tag{2.17a}$$

$$\frac{\partial S}{\partial \theta} = g_{\theta\nu}\dot{x}^{\nu} \Rightarrow \qquad \rho^2 \dot{\theta} = \sqrt{\Theta\left(\theta\right)}, \tag{2.17b}$$

and $\dfrac{\partial S}{\partial t} = g_{t\nu}\dot{x}^{\nu}$ and $\dfrac{\partial S}{\partial \phi} = g_{\phi\nu}\dot{x}^{\nu}$ combine together to yield

$$\Delta\rho^2 \dot{t} = \left(\Sigma^2 E - 2arL\right), \tag{2.17c}$$

$$\Delta\rho^2 \dot{\phi} = \left(2raE + \frac{\rho^2 - 2r}{\sin^2\theta} L\right). \tag{2.17d}$$

The equations of motion, Eq. (2.17a-2.17d), can also be obtained by differentiating and combining Eqs. (2.16a-2.16d).

It is evident from Eq. (2.14d) that $\Theta\left(\theta\right) = Q$ for the equatorial plane ($\theta = \pi/2$). This implies that at the turning points of the orbit, when $\dot{\theta} = 0$ [Eq. (2.17b)] in the equatorial plane, we get $\rho^2\dot{\theta} = \sqrt{Q} = 0$. Hence, $Q = 0$ is a solution for the equatorial trajectories, and $\dot{\theta}$ is always zero in the equatorial plane which implies that the equatorial trajectories always remain confined to the same plane.

2.2.2 The radial effective potential

The radial motion of a general trajectory in the Kerr spacetime is governed by Eq. (2.17a), which is expanded further to obtain

$$\frac{\left(E^2 - \delta_1\right)}{2} = \frac{\rho^4}{2r^4}\left(\frac{\mathrm{d}r}{\mathrm{d}\lambda}\right)^2 + V_{eff}\left(r, a, E, L, Q, \delta_1\right), \tag{2.18a}$$

where

$$V_{eff}\left(r,a,E,L,Q,\delta_1\right)=-\frac{\delta_1}{r}+\frac{L^2-a^2\left(E^2-\delta_1\right)+Q}{2r^2}-\frac{\left(L-aE\right)^2+Q}{r^3}+\frac{a^2Q}{2r^4}. \tag{2.18b}$$

For the equatorial plane ($Q=0$), the radial effective potential reduces to a simpler form:

$$V_{eff}\left(r,a,E,L,\delta_1\right)=-\frac{\delta_1}{r}+\frac{L^2-a^2\left(E^2-\delta_1\right)}{2r^2}-\frac{\left(L-aE\right)^2}{r^3}. \tag{2.19}$$

It is evident that the potential reduces to the classical Kepler potential for very large r and $\delta_1=1$:

$$V_{eff}\left(r\right)=-\frac{1}{r}. \tag{2.20}$$

2.2.3 Positivity of $R\left(r\right)$ and $\Theta\left(\theta\right)$

The equations (2.17a) and (2.17b) need to follow $R\left(r\right)\geq 0$ and $\Theta\left(\theta\right)\geq 0$ to obtain real values of $\dot{r}$ and $\dot{\theta}$. This gives a domain in the (r-θ) plane where the equations of motion are valid. For the radial motion, the trajectories are found in the region $R\left(r\right)>0$, and $R\left(r\right)=0$ gives the boundaries for the real domain of the radial equation of motion, also defining the turning points of the orbit. We solve for $R\left(r\right)=0$ to obtain the analytic form of the turning points of the time-like bound trajectories in chapter 3. For the polar motion, the conditions for $\Theta\left(\theta\right)\geq 0$ can be categorized as (Carter 1968)

- $Q>0$: There are always real solutions, where θ varies symmetrically below and above the equatorial plane, $\cos\theta=0$. This region extends to $\sin\theta=0$ plane (axis of symmetry) only when $L=0$ and $Q+a^2\left(E^2-\delta_1\right)\geq 0$.

- $Q < 0$: The real solutions exist only when $a^2\left(E^2-\delta_1\right) > L^2$ and $Q \geq -\{[a^2\left(E^2-\delta_1\right)]^{1/2} - |L|\}^2$. The variation of θ is in such a range that the orbit does not reach the equatorial plane.

2.3 History of the solution to Hamilton-Jacobi equation in Kerr geometry

The first results in the theory of orbital solutions go back to Bardeen *et al.* (1972) who derived analytic expressions of E and L for circular orbits [cf. Eqs. (2.12, 2.13)], which was calculated from the Lagrangian. Subsequently, the vast majority of the solutions cited in the literature involve expressing the solutions in terms of quadrature using the Hamilton-Jacobi theory as summarized in (Chandrasekhar 1983; Schmidt 2002). Schmidt (2002) introduced a clever way of deriving the fundamental frequencies in terms of quadratures, making use of a theorem in implicit functions (Hille 1979). The key idea is that the action-angle variables are expressed as $P_\beta = \{-E, J_k\} \equiv \mathcal{F}_\beta(\mathcal{I}_i)$, where J_k are the three actions, and $\mathcal{I}_i$ are four integrals of motion, for example, $\{-m^2/2, E, L, Q\}$. Given this relationship, where the actual form of the Hamiltonian, $\mathcal{H}(\mathcal{I}_i)$, is not known, one can apply the implicit function theorem which states that

$$\mathcal{J}P \cdot \mathcal{J}P^{-1} = \mathcal{J}P.(\mathcal{J}P)^{-1} = I, \tag{2.21}$$

provided that the Jacobian $\mathcal{J}P$ and P are non-zero. It turns out, fortunately, that this equation simplifies to a set of 8 linear equations relating the unknowns, $(\partial\mathcal{H}/\partial J_i)$, and fundamental frequencies, $\omega_i = (\partial\mathcal{H}/\partial J_i)$, and the known functions, $\partial P_i/\partial\mathcal{I}_j$, which is a sparse matrix as $P_0 = -E$ and $J_\phi = L$ are constants. This way, the three fundamental frequencies, $\{\omega_r, \omega_\theta, \omega_\phi\}$, are expressed in terms of quadratures given in (Eqs. 2.16a -2.16d). Independently, and in contrast, in

chapter 4 we have used the asymptotic ratios of these integrals to derive these frequencies which is easier than the method used by Schmidt (2002).

After Schmidt (2002), the task that remained to complete the solution, was to reduce the quadratures to algebraic relations by integrating them. One such attempt by Fujita and Hikida (2009) resulted in a complicated set of functions involving Mino time λ, as the choice of parameters were still restricted to $\mathcal{I}_i$. In contrast, we were able to choose the parameter space of eccentricity and inverse latus rectum, $\{e, \mu\}$ in addition to $\{a, Q\}$ to carry out the integrations in a far less cumbersome and cleaner way that opens the path to fast computations using these fully analytic but simple expressions involving Elliptic functions for the full three-dimensional trajectory. All trajectories are not useful but only a subset leading to bound trajectories is astrophysically meaningful. A study devoted to prescribing the bound orbits in both spaces $\{E, L, a, Q\}$ and $\{e, \mu, a, Q\}$ is carried out in chapter 3, that includes classifying orbits both in two and three dimensions, determining the condition for bound orbits and translating this to a prescription of input parameters in both spaces.

It is well known that the powerful structure of Hamiltonian dynamics is applicable when a separation of variables is accomplished, which critically depends on the proper choice of generalized coordinates and ingenuity is required to find separable coordinate that makes the analysis simpler. So the last word on Hamiton-Jacobi equations in Kerr geometry is yet to be written and further theory can be explored to make the solutions simpler.

2.4 Resource summary

In this chapter, we presented the basic derivation of obtaining constants of motion E and L, the equations of motion, and the separability of radial and polar motion in the Hamilton-Jacobi equation to obtain Carter's constant. We write the radial effective potential for the most general trajectory and discuss the domains of real solutions for the equations of motion in the (r-θ) plane. A discussion on the history of the solution to Hamilton-Jacobi equations in the Kerr geometry is also presented. The main resources we used for discussion are - Hartle (2003), Misner *et al.* (1973), Chandrasekhar (1983), Carter (1968), and Schmidt (2002).

Chapter 3

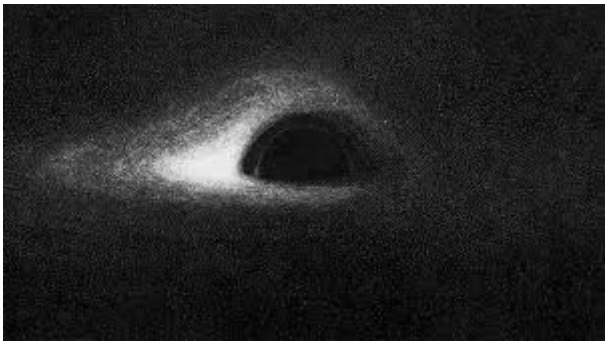

A simulated image of a black hole with thin accretion disk. Courtesy: Luminet (1979)

Bound orbit conditions for time-like trajectories in Kerr spacetime*

3.1 Introduction

The study of bound time-like trajectories in the Kerr spacetime has been a prime focus for many astrophysical applications, for example, the study of accretion of matter onto a black hole in the relativistic regime (Shakura and Sunyaev 1973; Novikov and Thorne 1973), and comprehending the gravitational wave signals from inspiral of a compact object onto a supermassive black hole (Glampedakis *et al.* 2002; Drasco *et al.* 2005). Some of the important results related to time-like trajectories in the Kerr and other geometries are presented in pioneering work (Chandrasekhar 1983).

*A part of the work in this chapter is published in a paper: Rana and Mangalam (2019a,b). The remaining work is submitted as proceedings: Rana and Mangalam (2020c,d)

In Bardeen *et al.* (1972), the energy, E, and angular momentum, L, of the circular orbits were expressed in terms of the circular orbit radius and the spin parameter a in the Kerr spacetime; the specific solution for the radius of the innermost stable circular orbit (ISCO) was also derived. The necessary conditions for bound geodesics for spherical orbits and the dragging of nodes along the direction of spin of a black hole was discussed (Wilkins 1972). The formulae have proved to be extremely useful in predicting observables in astrophysical applications like accretion around the black holes. For example, a general solution for a star in orbit around a rotating black hole was expressed in terms of quadratures (Vokrouhlicky and Karas 1993) using the formulation given by Carter (1968); the resulting integrals have been calculated numerically. The general expression in terms of quadratures for fundamental orbital frequencies ν_θ, ν_ϕ and ν_r, for a general eccentric orbit, were first derived by Schmidt (2002), where different cases for circular and equatorial orbits are also discussed but complete analytic trajectories were not calculated. An exact solution for non-spherical polar trajectories in Kerr geometry and an exact analytic expression for $t(r)$ for eccentric orbits in the equatorial plane were derived (Kraniotis 2007). These were used to obtain the expressions for the periapsis advance and Lense-Thirring frequencies. The time-like geodesics were expressed in terms of quadratures involving hyper-elliptic, elliptic and Abelian integrals for Kerr and Kerr-(anti) de Sitter spacetimes including cosmological constant (Kraniotis 2004) and applied in a semi-analytic treatment of Lense Thirring effect.

We discussed earlier (in Chapter 2) that the conserved quantities for time-like trajectories in the Kerr geometry are: energy per unit rest mass, E, z-component of angular momentum per unit rest mass, L, of the test particle and the Carter's constant, Q (Carter 1968). Hence, once E, L, Q, and spin of the black hole, a, are fixed, a time-like trajectory and its evolution can be completely described. We call the (E, L, a, Q) space as the dynamical parameter space. Another important parameter space can be defined using the eccentricity, e, and inverse-latus rectum,

μ, of the bound orbit, which are defined as

$$e = \frac{r_a - r_p}{r_a + r_p}, \qquad \mu = \frac{r_a + r_p}{2 r_a r_p}, \tag{3.1}$$

where r_a and r_p are the apastron and periastron of the bound trajectory respectively. A bound time-like trajectory can again be completely described in the (e, μ, a, Q) space, which we call as the conic parameter space. Such a parameter choice is possible because (E, L) parameters are easily translated to (e, μ) for bound orbits. It is also important to construct the essential conditions in both dynamical and conic parameter space which are necessary for bound trajectories.

In this chapter, we focus on the time-like trajectories. We first derive the translation relations between (E, L) and (e, μ) for fixed a and Q in §3.2. In §3.3, we then derive the essential bound orbit conditions in dynamical parameter space for the non-equatorial eccentric bound orbits and then derive the analog of these conditions in the conic parameter space. These conditions are applicable for $Q \geq 0$ orbits. The regions of different bound orbits were graphically separated in the (E, L) plane by Hackmann *et al.* (2010), according to the pair of roots of the effective potential spanning the radius of the bound orbit. The essential conditions, that we derive, thus give a complete mathematical construction of these regions, by specifying the loci of the bounding curves. In §3.4, we study the special case of equatorial eccentric orbits, $Q = 0$, where we again define different bound orbit regions and their bounding curves in the (E, L) and (e, μ) space, and also derive the corresponding bound orbit conditions. Finally, in §3.5, we provide a mathematical prescription to choose the parameters (E, L) and (e, μ) to obtain an astrophysically relevant bound time-like trajectory. We summarize the results presented in this chapter in §3.6.

3.2 Translation relations between $(E,\, L)$ and $(e,\, \mu)$

In this section, we derive the relation translating $(E,\, L)$ to $(e,\, \mu)$ parameter space for non-equatorial bound trajectories for fixed a and Q, i.e. $E\left(e, \mu, a, Q\right)$ and $L\left(e, \mu, a, Q\right)$. These relations make it possible to completely describe the bound orbit dynamics in the conic parameter space. We start with the equation governing the radial motion, Eq. (2.17a), given by

$$\rho^4 \dot{r}^2 = R\left(r\right), \tag{3.2a}$$

where

$$R\left(r\right) = \left(E^2 - \delta_1\right) r^4 + 2\delta_1 r^3 + \left(a^2 E^2 - Q - L^2 - a^2 \delta_1\right) r^2 + 2\left[Q + \left(L - aE\right)^2\right] r - a^2 Q. \tag{3.2b}$$

The radial equation, Eq. (2.18a), for time-like trajectories ($\delta_1 = 1$) is given by

$$\frac{\left(E^2 - 1\right)}{2} = \frac{\rho^4}{2r^4}\left(\frac{\mathrm{d}r}{\mathrm{d}\tau}\right)^2 + V_{eff}\left(r, a, E, L, Q\right), \tag{3.3a}$$

where

$$V_{eff}\left(r, a, E, L, Q\right) = -\frac{1}{r} + \frac{L^2 - a^2\left(E^2 - 1\right) + Q}{2r^2} - \frac{\left(L - aE\right)^2 + Q}{r^3} + \frac{a^2 Q}{2r^4}, \tag{3.3b}$$

which is the radial effective potential experienced by a test particle orbiting in a general non-equatorial eccentric trajectory near a rotating black hole. The expression of $R\left(r\right)$ determines the turning points of the bound trajectory which are the first two roots of $R\left(r\right)$, that is r_1 and r_2 where $r_1 > r_2 > r_3 > r_4$. We express $R\left(r\right)$ as function of $u = 1/r$ variable, which is easy to work with, and given by

$$R\left(u\right) \quad = -a^2 Q u^4 + 2\left(x^2 + Q\right) u^3 + \left(a^2 E^2 - Q - L^2 - a^2 \delta_1\right) u^2 + 2\delta_1 u + \left(E^2 - \delta_1\right), \tag{3.4a}$$

$$= -a^2 Q \left[u^4 + a^{'} u^3 + b^{'} u^2 + c^{'} u + d^{'} \right], \tag{3.4b}$$

where $x = (L - aE)$ and

$$a^{'} = -\frac{2\left(x^2 + Q\right)}{a^2 Q}, \quad b^{'} = \frac{\left(x^2 + 2aEx + a^2\delta_1 + Q\right)}{a^2 Q}, \quad c^{'} = -\frac{2\delta_1}{a^2 Q}, \quad d^{'} = \frac{\left(\delta_1 - E^2\right)}{a^2 Q}. \tag{3.4c}$$

Now, the quartic in Eq. (3.4b) can be further factorized into two quadratics given by

$$u^4 + a^{'} u^3 + b^{'} u^2 + c^{'} u + d^{'} = \left(u^2 + {a_1}^{'} u + {b_1}^{'}\right)\left(u^2 + {a_2}^{'} u + {b_2}^{'}\right), \tag{3.5}$$

and the comparison of coefficients on both sides yields the following relations

$${a_1}^{'} + {a_2}^{'} = a^{'}, \tag{3.6a}$$

$${a_1}^{'}{a_2}^{'} + {b_1}^{'} + {b_2}^{'} = b^{'}, \tag{3.6b}$$

$${b_1}^{'}{a_2}^{'} + {b_2}^{'}{a_1}^{'} = c^{'}, \tag{3.6c}$$

$${b_1}^{'}{b_2}^{'} = d^{'}. \tag{3.6d}$$

Assuming that the roots of first quadratic $\left(u^2 + {a_1}^{'} u + {b_1}^{'}\right)$ in Eq. (3.5) are the turning points of the orbit given by

$$u_1 = \frac{1}{r_a} = \mu\left(1 - e\right), \qquad u_2 = \frac{1}{r_p} = \mu\left(1 + e\right), \tag{3.7}$$

this would imply that

$${a_1}^{'} = -\left(u_1 + u_2\right) = -2\mu, \qquad {b_1}^{'} = u_1 u_2 = \mu^2\left(1 - e^2\right). \tag{3.8}$$

. Now, substituting the above equation in Eqs. (3.6a) and (3.6d) gives the expressions of ${a_2}^{'}$ and ${b_2}^{'}$ which are

$${a_2}^{'} = a^{'} + 2\mu, \qquad {b_2}^{'} = \frac{d^{'}}{\mu^2\left(1 - e^2\right)}. \tag{3.9}$$

Next, the substitution of $a_1{}'$, $b_1{}'$, $a_2{}'$, and $b_2{}'$ from Eqs. (3.8,3.9) into Eqs. (3.6b) and (3.6c) yields

$$-2\mu\left(a^{'}+2\mu\right)+\mu^2\left(1-e^2\right)+\frac{d^{'}}{\mu^2\left(1-e^2\right)}=b^{'}, \tag{3.10a}$$

$$\mu^2\left(1-e^2\right)\left(a^{'}+2\mu\right)-\frac{2d^{'}}{\mu\left(1-e^2\right)}=c^{'}, \tag{3.10b}$$

respectively. The substitution of $a^{'}$, $b^{'}$, $c^{'}$ and $d^{'}$ from Eq. (3.4c) into Eq. (3.10a) and (3.10b) gives

$$\frac{\left(\delta_1-E^2\right)}{\mu^2\left(1-e^2\right)} = Q=x^2+2aEx+a^2\delta_1-a^2Q\mu^2\left(1-e^2\right)+4\mu\left[\mu a^2Q-\left(x^2+Q\right)\right], \tag{3.11a}$$

$$E^2\left(e,\mu,a,Q,\delta_1\right) = \delta_1-\mu^3\left(1-e^2\right)^2\left(\mu a^2Q-Q-x^2\right)-\delta_1\mu\left(1-e^2\right), \tag{3.11b}$$

respectively. Finally, replacing E^2 in Eq. (3.11a) from Eq. (3.11b) yields

$$\begin{aligned} E &= \frac{1}{2ax}\left[-x^2-a^2\delta_1+a^2Q\mu^2\left(1-e^2\right)-Q+\frac{\delta_1}{\mu}-\left(3+e^2\right)\mu\left(\mu a^2Q-Q-x^2\right)\right], \\ &= C_1x+\frac{C_2}{x}, \end{aligned} \tag{3.12a}$$

where

$$C_1=\frac{1}{2a}\left[\left(3+e^2\right)\mu-1\right], \tag{3.12b}$$

$$C_2=\frac{1}{2a}\left[\frac{\delta_1}{\mu}-a^2\delta_1-Q+a^2Q\mu^2\left(1-e^2\right)-\mu\left(3+e^2\right)\left(\mu a^2Q-Q\right)\right]. \tag{3.12c}$$

Next, the substitution of Eq. (3.12a) in Eq. (3.11b) completely replaces E from the equation and gives

$$x^4\left[C_1^2-\mu^3\left(1-e^2\right)^2\right]+x^2\left[\mu\left(1-e^2\right)\delta_1+2C_1C_2+\mu^3\left(1-e^2\right)^2\left(\mu a^2Q-Q\right)-\delta_1\right]+C_2^2=0, \tag{3.13}$$

which is further solved for x^2 to obtain

$$x^2\left(e,\mu,a,Q,\delta_1\right)=\frac{-S-\sqrt{S^2-4PT}}{2P}, \tag{3.14a}$$

where

$$P\left(e,\mu,a,Q,\delta_1\right) = \quad \frac{1}{4a^2}\left[\left(3+e^2\right)\mu-1\right]^2-\mu^3\left(1-e^2\right)^2, \tag{3.14b}$$

$$S\left(e,\mu,a,Q,\delta_1\right) = \quad \mu\left(1-e^2\right)\delta_1+\mu^3\left(1-e^2\right)^2\left(\mu a^2Q-Q\right)-\delta_1+\frac{1}{2a^2}\left[\left(3+e^2\right)\mu-1\right]\times$$
$$\left[\frac{\delta_1}{\mu}-a^2\delta_1-Q+a^2Q\mu^2\left(1-e^2\right)-\mu\left(3+e^2\right)\left(\mu a^2Q-Q\right)\right], \tag{3.14c}$$

$$T\left(e,\mu,a,Q,\delta_1\right) = \quad \frac{1}{4a^2}\left[\frac{\delta_1}{\mu}-a^2\delta_1-Q+a^2Q\mu^2\left(1-e^2\right)-\mu\left(3+e^2\right)\left(\mu a^2Q-Q\right)\right]^2. \tag{3.14d}$$

Finally, the expression of L is given by

$$L\left(e,\mu,a,Q,\delta_1\right) = x\left(e,\mu,a,Q,\delta_1\right)+aE\left(e,\mu,a,Q,\delta_1\right). \tag{3.15}$$

Hence, the translation relations between (E, L) and (e, μ) parameter space can be summarized [from Eqs. (3.11b,3.14a,3.15)] as

$$E\left(e,\mu,a,Q,\delta_1\right) \quad = \left[\delta_1-\mu^3\left(1-e^2\right)^2\left(\mu a^2Q-Q-x^2\right)-\delta_1\mu\left(1-e^2\right)\right]^{1/2}, \tag{3.16a}$$

$$L\left(e,\mu,a,Q,\delta_1\right) \quad = x\left(e,\mu,a,Q\right)+aE\left(e,\mu,a,Q\right), \tag{3.16b}$$

$$x^2\left(e,\mu,a,Q,\delta_1\right) \quad = \frac{-S-\sqrt{S^2-4PT}}{2P}. \tag{3.16c}$$

These relations further reduce for bound time-like trajectories ($\delta_1 = 1$) to

$$E\left(e,\mu,a,Q\right) = \left[1-\mu^3\left(1-e^2\right)^2\left(\mu a^2Q-Q-x^2\right)-\mu\left(1-e^2\right)\right]^{1/2}, \tag{3.17a}$$

$$x^2\left(e,\mu,a,Q\right) = \frac{-S-\sqrt{S^2-4PT}}{2P}, \tag{3.17b}$$

where

$$P\left(e,\mu,a,Q\right) = \quad \frac{1}{4a^2}\left[\left(3+e^2\right)\mu-1\right]^2-\mu^3\left(1-e^2\right)^2, \tag{3.17c}$$

$$S(e,\mu,a,Q) = \mu\left(1-e^2\right)+\mu^3\left(1-e^2\right)^2\left(\mu a^2Q-Q\right)-1+\frac{1}{2a^2}\left[\left(3+e^2\right)\mu-1\right]\times \left[\frac{1}{\mu}-a^2-Q+a^2Q\mu^2\left(1-e^2\right)-\mu\left(3+e^2\right)\left(\mu a^2Q-Q\right)\right], \quad (3.17d)$$

$$T(e,\mu,a,Q) = \frac{1}{4a^2}\left[\frac{1}{\mu}-a^2-Q+a^2Q\mu^2\left(1-e^2\right)-\mu\left(3+e^2\right)\left(\mu a^2Q-Q\right)\right]^2, \quad (3.17e)$$

$$L(e,\mu,a,Q) = x(e,\mu,a,Q)+aE(e,\mu,a,Q), \quad (3.17f)$$

which reduce to the equatorial case, $Q=0$, derived by Bini *et al.* (2016a).

3.3 Conditions for bound trajectories around Kerr black hole

In this section, we derive the bound orbit conditions for general non-equatorial trajectories in both dynamical and conic parameter space, by obtaining the roots of the $R(r)=0$ for the turning points of the bound trajectory as functions of (E,L,a,Q). We then obtain the essential bound orbit conditions based on the conditions on these roots.

3.3.1 Dynamical parameter space (E,L,a,Q)

We see from Eq. (3.2a) that the turning points of a bound orbit are obtained when

$$R(r)=0, \quad (3.18a)$$

which can be written in the form

$$r^4 + \frac{2\delta_1}{(E^2-\delta_1)}r^3 + \frac{(a^2E^2 - L^2 - Q - a^2\delta_1)}{(E^2-\delta_1)}r^2 + \frac{2\,(x^2+Q)}{(E^2-\delta_1)}r - \frac{a^2Q}{(E^2-\delta_1)} = 0. \tag{3.18b}$$

We apply Ferrari's method to solve a quartic (Cardano 1968) to obtain the roots of above equation. We summarize Ferrari's method below:

- *Step 1*: For a general quartic equation given by

$$y^4 + \alpha y^3 + \beta y^2 + \gamma y + \delta = 0, \tag{3.19a}$$

a substitution given by $y = Y - \frac{\alpha}{4}$ reduces the quartic to the form

$$Y^4 + GY^2 + HY + M = 0, \tag{3.19b}$$

where

$$G = \frac{(8\beta - 3\alpha^2)}{8}, \quad H = \frac{(\alpha^3 + 8\gamma - 4\alpha\beta)}{8}, \quad M = \frac{(256\delta - 64\alpha\gamma + 16\beta\alpha^2 - 3\alpha^4)}{256}. \tag{3.19c}$$

- *Step 2*: Rewriting Eq. (3.19b) in the form

$$\left(Y^2 + \frac{G}{2} + z\right)^2 = 2zY^2 - HY + \frac{G^2}{4} + z^2 + zG - M, \tag{3.20a}$$

where z is an arbitrary real number chosen such that the R.H.S of above equation forms a perfect square which is given by

$$2zY^2 - HY + \frac{G^2}{4} + z^2 + zG - M = \left(\sqrt{2z}Y - \frac{H}{2\sqrt{2z}}\right)^2. \tag{3.20b}$$

This further reduces to a cubic equation of z given by

$$8z^3 + 8Gz^2\left(2G^2 - 8M\right)z - H^2 = 0. \tag{3.20c}$$

Hence, z is chosen to be the real root of the cubic equation, Eq. (3.20c), which is [from Cardano's method (Cardano 1968)]

$$z = U + V - \frac{G}{3}, \tag{3.20d}$$

where

$$U = \left(I + \sqrt{I^2 + J^3}\right)^{1/3}, \quad V = \left(I - \sqrt{I^2 + J^3}\right)^{1/3}, \tag{3.20e}$$

and

$$I = \frac{(2G^3 - 72MG + 27H^2)}{432}, \quad J = \frac{-(G^2 + 12M)}{36}. \tag{3.20f}$$

- *Step 3*: The perfect square form of Eq. (3.20a) is given by

$$\left(Y^2 + \frac{G}{2} + z\right)^2 = \left(\sqrt{2z}Y - \frac{H}{2\sqrt{2z}}\right)^2, \tag{3.21a}$$

which further reduces to

$$Y^2 + \frac{G}{2} + z = \pm\left(\sqrt{2z}Y - \frac{H}{2\sqrt{2z}}\right). \tag{3.21b}$$

The above equation, Eq. (3.21b), gives two quadratic equations of Y which are solved further to give four roots of the quartic equation, Eq. (3.19b). Hence making the back substitution $Y = y + \frac{\alpha}{4}$ yields four roots of the quartic equation, Eq. (4.31a), which are

$$y_1 = \quad -\frac{\alpha}{4} + \sqrt{\frac{z}{2}} + \frac{1}{2}\sqrt{-2z - 2G - \frac{\sqrt{2}H}{\sqrt{z}}}, \tag{3.22a}$$

$$y_2 = -\frac{\alpha}{4} + \sqrt{\frac{z}{2}} - \frac{1}{2}\sqrt{-2z - 2G - \frac{\sqrt{2}H}{\sqrt{z}}}, \tag{3.22b}$$

$$y_3 = -\frac{\alpha}{4} - \sqrt{\frac{z}{2}} + \frac{1}{2}\sqrt{-2z - 2G + \frac{\sqrt{2}H}{\sqrt{z}}}, \tag{3.22c}$$

$$y_4 = -\frac{\alpha}{4} - \sqrt{\frac{z}{2}} - \frac{1}{2}\sqrt{-2z - 2G + \frac{\sqrt{2}H}{\sqrt{z}}}. \tag{3.22d}$$

Hence, the four roots of the quartic equation defining the turning points of the radial motion in the Kerr spacetime, Eq. (3.18b), are

$$r_1 = \frac{1}{2}\left[\frac{\delta_1}{(\delta_1 - E^2)} + \sqrt{2z} + \sqrt{D_1}\right], \tag{3.23a}$$

$$r_2 = \frac{1}{2}\left[\frac{\delta_1}{(\delta_1 - E^2)} + \sqrt{2z} - \sqrt{D_1}\right], \tag{3.23b}$$

$$r_3 = \frac{1}{2}\left[\frac{\delta_1}{(\delta_1 - E^2)} - \sqrt{2z} + \sqrt{D_2}\right], \tag{3.23c}$$

$$r_4 = \frac{1}{2}\left[\frac{\delta_1}{(\delta_1 - E^2)} - \sqrt{2z} - \sqrt{D_2}\right], \tag{3.23d}$$

where $r_1 > r_2 > r_3 > r_4$ when all roots are real, and

$$D_1 = -2G - 2z - \frac{\sqrt{2}H}{\sqrt{z}}, \quad D_2 = -2G - 2z + \frac{\sqrt{2}H}{\sqrt{z}}, \tag{3.23e}$$

$$z = U + V - \frac{G}{3}, \quad U = \left(I + \sqrt{I^2 + J^3}\right)^{1/3}, \quad V = \left(I - \sqrt{I^2 + J^3}\right)^{1/3}, \tag{3.23f}$$

$$I = \frac{(2G^3 + 27H^2 - 72GM)}{432}, \quad J = -\frac{(G^2 + 12M)}{36}, \tag{3.23g}$$

$$G = \frac{[L^2 - a^2(E^2 - \delta_1) + Q]}{(\delta_1 - E^2)} - \frac{3{\delta_1}^2}{2(\delta_1 - E^2)^2}, \tag{3.23h}$$

$$H = \frac{\delta_1[L^2 - a^2(E^2 - \delta_1) + Q]}{(\delta_1 - E^2)^2} - \frac{2(x^2 + Q)}{(\delta_1 - E^2)} - \frac{{\delta_1}^3}{(\delta_1 - E^2)^3}, \tag{3.23i}$$

$$M = \frac{{\delta_1}^2[L^2 - a^2(E^2 - \delta_1) + Q]}{4(\delta_1 - E^2)^3} - \frac{3{\delta_1}^4}{16(\delta_1 - E^2)^4} - \frac{\delta_1(x^2 + Q)}{(\delta_1 - E^2)^2} + \frac{a^2 Q}{(\delta_1 - E^2)}. \tag{3.23j}$$

Now, for the time-like trajectories ($\delta_1 = 1$), the above equations reduce to

$$r_1 = \frac{1}{2}\left[\frac{1}{(1-E^2)} + \sqrt{2z} + \sqrt{D_1}\right], \tag{3.24a}$$

$$r_2 = \frac{1}{2}\left[\frac{1}{(1-E^2)} + \sqrt{2z} - \sqrt{D_1}\right], \tag{3.24b}$$

$$r_3 = \frac{1}{2}\left[\frac{1}{(1-E^2)} - \sqrt{2z} + \sqrt{D_2}\right], \tag{3.24c}$$

$$r_4 = \frac{1}{2}\left[\frac{1}{(1-E^2)} - \sqrt{2z} - \sqrt{D_2}\right], \tag{3.24d}$$

where $r_1 > r_2 > r_3 > r_4$ when all roots are real, and

$$G = \frac{[L^2 - a^2(E^2-1) + Q]}{(1-E^2)} - \frac{3}{2(1-E^2)^2}, \tag{3.24e}$$

$$H = \frac{[L^2 - a^2(E^2-1) + Q]}{(1-E^2)^2} - \frac{2(x^2+Q)}{(1-E^2)} - \frac{1}{(1-E^2)^3}, \tag{3.24f}$$

$$M = \frac{[L^2 - a^2(E^2-1) + Q]}{4(1-E^2)^3} - \frac{3}{16(1-E^2)^4} - \frac{(x^2+Q)}{(1-E^2)^2} + \frac{a^2 Q}{(1-E^2)}, \tag{3.24g}$$

where all the other constants D_1, D_2, z, U, V, I, and J have the same form as given in Eqs. (3.23e-3.23g).

Next, we derive the essential conditions on (E, L, a, Q) parameters to classify different types of bound orbits. These bound orbits were graphically separated as regions in the (E, L) plane by Hackmann *et al.* (2010), according to the pair of roots of the $R(r) = 0$ spanning the radius of the bound orbit. We algebraically classify these regions using the expressions of roots, Eqs. (3.24a-3.24d), in the (E, L, a, Q) parameter space as follows:

1. Region Δ: $D_1 > 0$, $D_2 > 0$, and $E < 1$: Bound orbit between r_1 and r_2 or r_3 and r_4.

2. Region Λ: $D_1 > 0$, $D_2 > 0$, and $E > 1$: Bound orbit between r_2 and r_3 with $r_4 < 0$ and $r_1 > r_2$.

3. Region ς: $(D_1 \cdot D_2) < 0$: Bound orbit between r_1 and r_2 if $D_1 < 0$ or r_3 and r_4 if $D_2 < 0$. This region exists for both $E < 1$ and $E > 1$.

Note that for D_1 and D_2 to have real values, z should be positive [see Eq. (3.23e)]. Hence z is always positive for regions Δ, ς, and Λ, which is followed from corresponding conditions of these regions. Hence, through D_1 and D_2, which are functions of (E, L, a, Q) [Eqs. (3.23e)-(3.23g), (3.24e)-(3.24g)], we have provided the mathematical conditions in the dynamical parameter space for various bound orbit regions. The Fig. 3.1 depicts all these three bound orbit regions in the (E, L) plane. We also show the radial effective potential [Eq. (3.3b)] diagrams corresponding to these region in Fig. 3.2.

Now, we discuss these regions and their boundaries in the (E, L) plane below:

1. Δ *region*: The Fig. 3.1 shows the Δ region for various (a, Q) combinations. All points inside the Δ region corresponds to the eccentric non-equatorial bound orbits existing between r_1 and r_2 or r_3 and r_4, where all roots are real ($r_1 > r_2 > r_3 > r_4$). Fig. 3.2(a) shows the radial effective potential [Eq. (3.3b)] for a typical point inside the Δ region. We see that the smallest root, r_4, is usually found inside the horizon radius; this implies that the bound orbit spanning its radius between r_1 and r_2 is an astrophysically relevant orbit. The boundaries of the Δ region correspond to $E = 1$ and the spherical orbits, where they can be again categorized into stable and unstable spherical orbits which we discuss below:

   (a) *Stable spherical orbits*: The red curves in Figs. 3.1(a)-3.1(d) show combinations of E and L corresponding to stable spherical orbits with

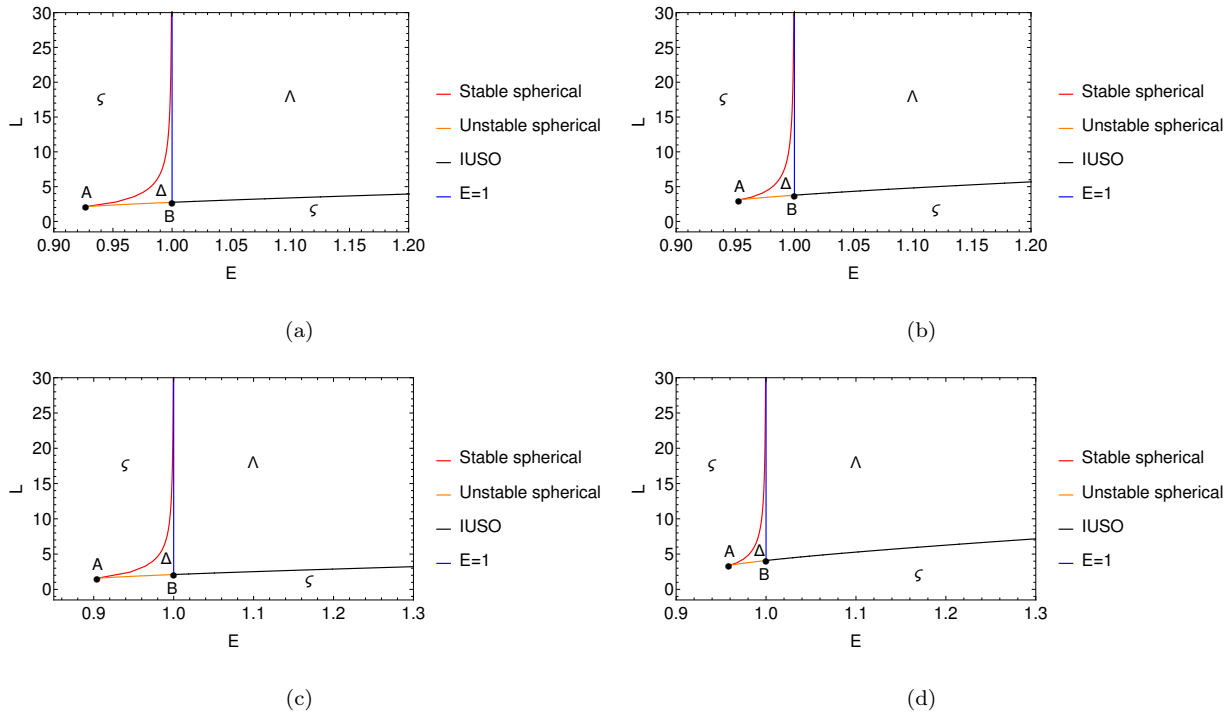

FIGURE 3.1: The figure shows different bound orbit regions in the (E, L) plane: (a) and (c) represent the prograde cases with $a = 0.5$ and $a = 0.9$ respectively; (b) and (d) show the retrograde cases with $a = -0.5$ and $a = -0.9$ respectively, where we have fixed $Q = 5$. The regions ς and Λ span from $E = 0$ to 1 and $E = 1$ to ∞ respectively, but a limited range of E is shown for convenience. The Δ region is bounded by the curves representing stable, unstable spherical orbits, and $E = 1$. The Λ region is bounded by the inner unstable spherical orbits (IUSO). The points A and B depict the innermost stable spherical orbit (ISSO) and marginally bound spherical orbit (MBSO) respectively.

$\{a = 0.5, a = 0.9\}$ for prograde and $\{a = -0.5, a = -0.9\}$ for retrograde, where $Q = 5$. The radius of the stable spherical orbits decreases as we move along these curves from a very large value (corresponding to very large L) to the radius corresponding to the innermost stable spherical orbit (ISSO), represented by point A in Fig. 3.1. We have shown the radial effective potential [Eq. (3.3b)] for a stable spherical orbit in Fig. 3.3(a).

(b) *Unstable spherical/separatrix orbits*: The orange curves in Figs. 3.1(a)-3.1(d) represent all the combinations of E and L for the unstable spherical orbits for $\{a = 0.5, 0.9, -0.5, -0.9\}$ with $Q = 5$. These orbits are

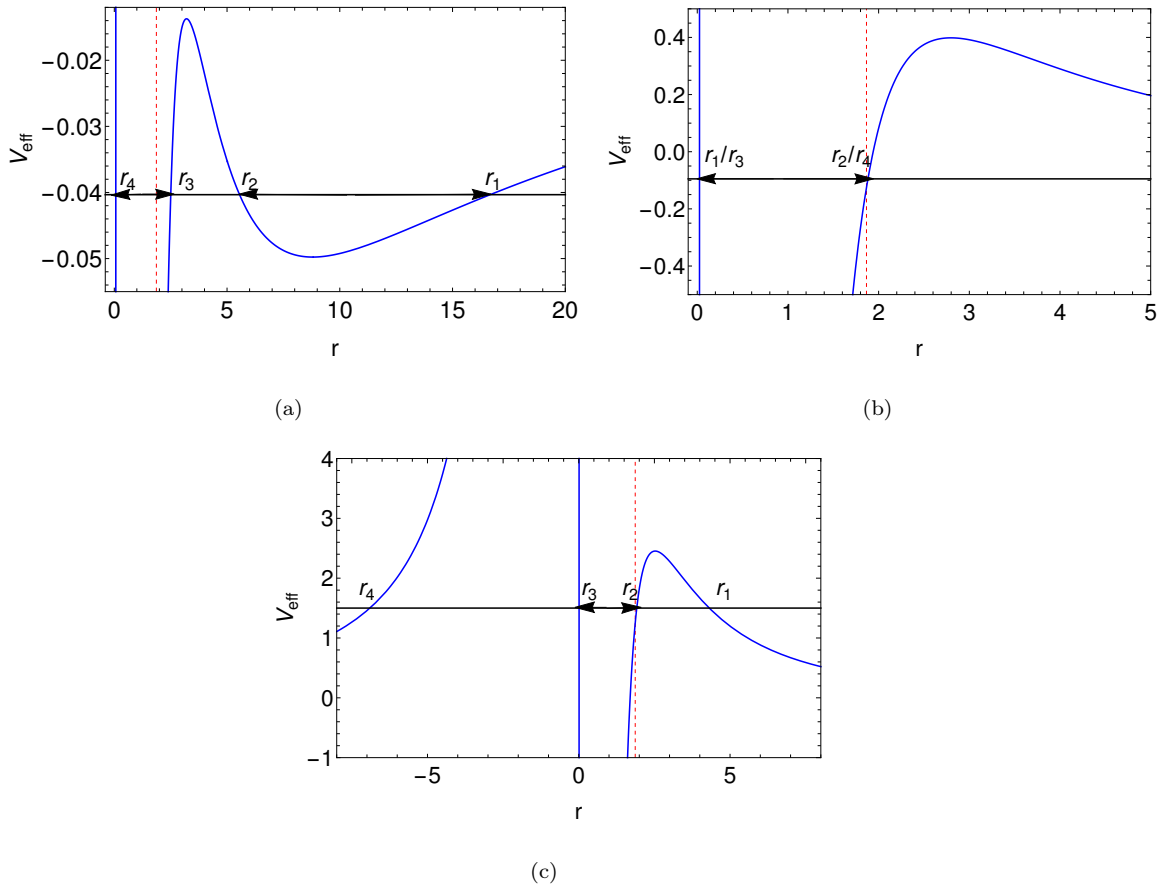

FIGURE 3.2: The figure shows the radial effective potential [Eq. (3.3b)] for different regions of bound orbits, where the horizontal black curve and vertical dashed red curve correspond to $\left(E^2-1\right)/2$ and the horizon radius respectively, and the arrows depict the bounding region of the orbit. While (a) represents an orbit in region Δ with parameter values $\{E = 0.958818,\ L = 2.65917\}$, (b) represents an orbit in region ς with $\{E = 0.9,\ L = 5\}$, and (c) represents an orbit in the Λ region with $\{E = 2,\ L = 10\}$, where we have fixed $\{a = 0.5,\ Q = 5\}$. Each orbit corresponds to a single point in the Δ, ς, and Λ regions of Fig. 3.1(a).

also called the non-equatorial separatrix orbits. The periastron point, r_p, of a separatrix orbit corresponds to an unstable spherical orbit with its apastron, r_a, at a finite radius. Fig. 3.3(c) shows an example of the radial effective potential [Eq. (3.3b)] of a separatrix orbit, where $r_p = r_2 = r_3$ and $r_a = r_1$. The end points of the separatrix (orange) curve correspond to the ISSO and marginally bound spherical orbit (MBSO), which means that r_p or the unstable spherical orbit radius for

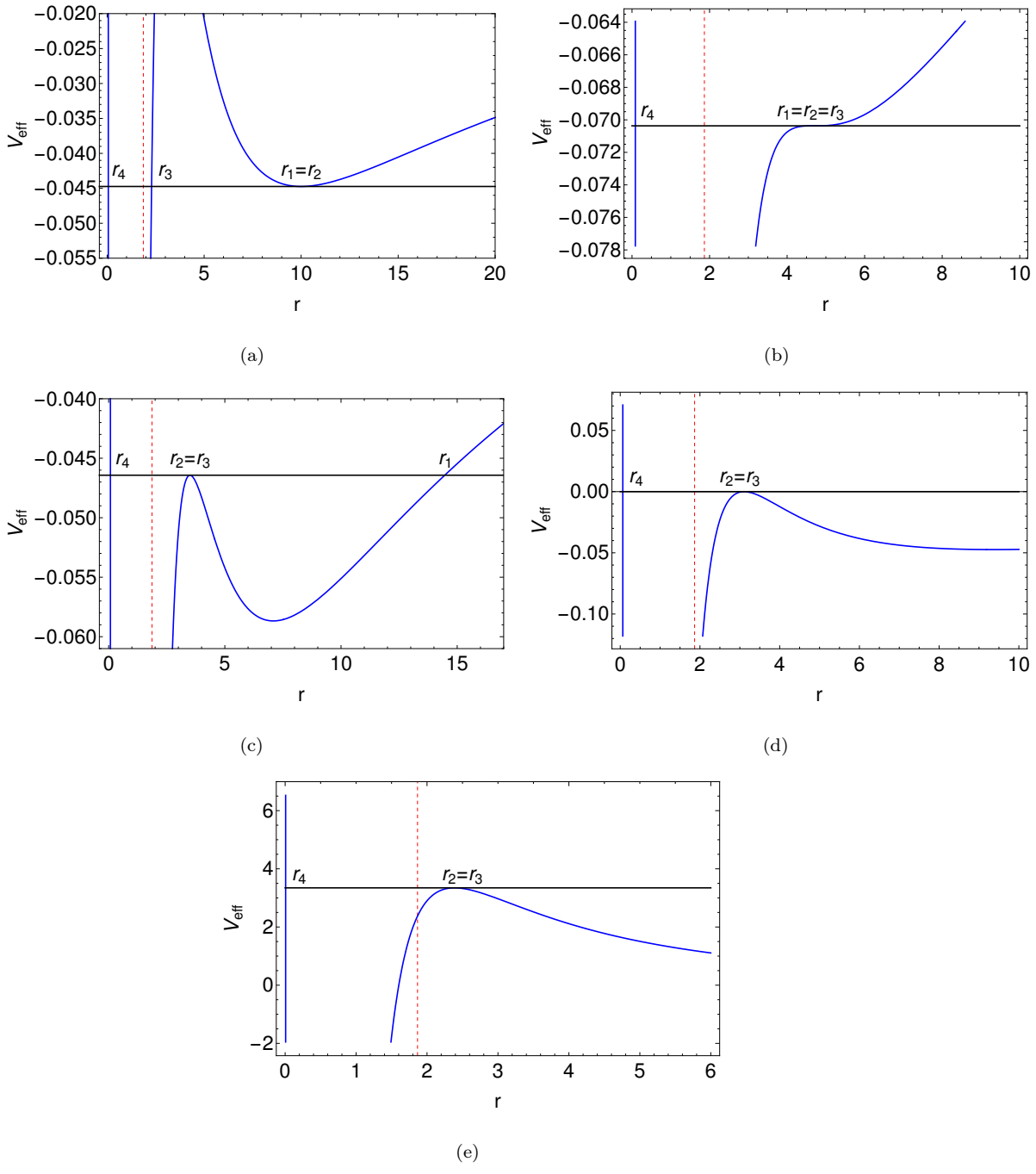

FIGURE 3.3: The figure shows the radial effective potential [Eq. (3.3b)] for various types of spherical orbits, where the horizontal black curve corresponds to $\left(E^2-1\right)/2$ and the vertical dashed red curve corresponds to the horizon radius: (a) represents a stable spherical orbit with parameter values $\{E = 0.954215,\ L = 2.85451\}$, (b) represents an ISSO with $\{E = 0.926965,\ L = 2.12011\}$ (point A of Fig. 3.1(a)), (c) represents an unstable spherical orbit with $\{E = 0.952441,\ L = 2.38042\}$, (d) represents a MBSO with $\{E = 1,\ L = 2.74974\}$ (B of Fig. 3.1(a)), and (e) represents an IUSO with $\{E = 2.77331,\ L = 10.9958\}$, where we have fixed $\{a = 0.5,\ Q = 5\}$. The turning point $r_1 = \infty$ for both MBSO and IUSO.

a separatrix orbit decreases from ISSO to MBSO while moving from point A to B, as shown in Fig. 3.1. Figs. 3.3(b) and 3.3(d) show examples of the radial effective potentials [Eq. (3.3b)] for ISSO and MBSO respectively.

(c) *Limiting bound orbit*: The blue curves in Fig. 3.1(a)-3.1(d) represent the $E = 1$ curve. These curves correspond to the orbits where a test particle starts from infinity at rest, $r_1 = \infty$.

(d) *Change of the shape of Δ region with a*: Fig. 3.1 shows the Δ region in (E, L) plane for $\{a = 0.5, -0.5, 0.9, -0.9\}$ for $Q = 5$. A comparison of these figures shows that the increase in a shifts the Δ region towards lower values of E for prograde orbits and higher values of E for retrograde orbits. This shows that the prograde bound orbits exist closer to the black hole for a high spin black hole than for a low spin black hole, and vice-versa for retrograde orbits.

2. *Λ region*: The region Λ is shown in the (E, L) plane for $\{a = 0.5, -0.5, 0.9, -0.9\}$ with $Q = 5$ in Fig. 3.1. This region corresponds to $E > 1$ where all the roots are real and $r_4 < 0$. The eccentric bound orbit exists between r_2 and r_3, where $r_1 > r_2$. Fig. 3.2(c) shows the radial effective potential [Eq. (3.3b)] for a typical point of the Λ region shown in Fig. 3.1(a). For this region also, it is seen that either one or both roots making the bound orbit (r_2 and r_3) are found inside the horizon radius, hence this region is also not astrophysically relevant. The Λ region is bounded by $E = 1$ (blue curves) and the inner unstable spherical orbits (IUSO) (black curves), as shown in Fig. 3.1. IUSO are the orbits where an unstable spherical orbit exists at $r_2 = r_3$, where $r_1 = \infty$ and $r_4 < 0$. An example of the radial effective potential of an IUSO is shown in Fig. 3.3(e). The IUSO exist inside the MBSO radius ($r < MBSO$), whereas the innermost limit for these orbits is given by the light radius, where $E = \infty$.

3. *ς region*: In Fig. 3.1, the ς region is shown in the (E, L) plane for $\{a = 0.5, -0.5, 0.9, -0.9\}$ with $Q = 5$. This region ranges from $E = 0$ to ∞, where an eccentric bound orbit exist either between r_1 and r_2 when $\{r_3, r_4\}$ forms a complex conjugate pair or between r_3 and r_4 when $\{r_1, r_2\}$ forms a complex conjugate pair. Fig. 3.2(b) shows the radial effective potential [Eq. (3.3b)] for a typical point of the ς region shown in Fig. 3.1(a). It is seen that either one or both roots of the real pair [(r_1, r_2) or (r_3, r_4)] are found inside the horizon radius for the ς region, hence this region is not astrophysically relevant.

Hence, we can conclude that the astrophysically relevant general eccentric bound orbits belong to the Δ region of the (E, L) plane, where the orbit exists between r_1 and r_2.

3.3.2 Conic parameter space (e, μ, a, Q)

In §3.3.1, we mathematically distributed bound orbit regions (Δ, ς, Λ) in the (E, L) plane, as previously defined by Hackmann *et al.* (2010). Here, we derive the mathematical conditions for these regions in the (e, μ, a, Q) space and also graphically analyze them in the (e, μ) plane. The translation relations between dynamical and conic parameter space, derived in §3.2, are the key to write the bound orbit conditions in the conic parameter space. It is due to these translation relations that the dynamics and evolution of the bound trajectories can be completely determined using the conic parameter space.

We discuss (Δ, ς, Λ) regions in the (e, μ) plane and derive corresponding conditions below:

1. *Δ region*: As we discussed earlier that for the Δ region the realistic bound orbit exists between r_1 and r_2 (see Fig. 3.2(a)), we write the eccentricity and inverse-latus rectum as $\{e_{12}, \mu_{12}\}$ by definition, Eq. (3.1). We start with the equation of radial motion for time-like trajectories ($\delta_1 = 1$), Eq. (3.4a-3.4c),

$$R(u) = 0, \tag{3.25a}$$

$$u^4 + a^{'}u^3 + b^{'}u^2 + c^{'}u + d^{'} = 0, \tag{3.25b}$$

where

$$a^{'} = -\frac{2(x^2+Q)}{a^2Q}, \quad b^{'} = \frac{(x^2+2aEx+a^2+Q)}{a^2Q}, \quad c^{'} = -\frac{2}{a^2Q}, \quad d^{'} = \frac{(1-E^2)}{a^2Q}. \tag{3.25c}$$

We factorize Eq. (3.25b), as also shown in Eq. (3.5), where the first quadratic contains the turning points of the orbit $u_1 = \mu_{12}(1-e_{12})$ and $u_2 = \mu_{12}(1+e_{12})$. Hence we get

$$u^4 + a^{'}u^3 + b^{'}u^2 + c^{'}u + d^{'} = (u-u_1)(u-u_2)\left(u^2 + {a_2}^{'}u + {b_2}^{'}\right), \tag{3.26a}$$

where from Eq. (3.9), we have

$${a_2}^{'} = -\frac{2(x^2+Q)}{a^2Q} + 2\mu_{12}, \qquad {b_2}^{'} = \frac{(1-E^2)}{a^2Q{\mu_{12}}^2(1-{e_{12}}^2)}. \tag{3.26b}$$

This implies that the factor $\left(u^2 + {a_2}^{'}u + {b_2}^{'}\right)$ contains roots u_3 and u_4, where

$$u_{4,3} = \frac{-{a_2}^{'} \pm \sqrt{{{a_2}^{'}}^2 - 4{b_2}^{'}}}{2}, \tag{3.27a}$$

and we require

$$u_1 < u_2 < u_3 < u_4. \tag{3.27b}$$

Here $u_1 < u_2$ and $u_3 < u_4$ are valid by definition, hence the necessary condition is given by

$$u_2 < u_3, \tag{3.28a}$$

$$\mu_{12}\left(1+e_{12}\right) < \frac{-{a_2}' - \sqrt{{a_2}'^2 - 4{b_2}'}}{2}, \tag{3.28b}$$

$${a_2}' + 2\mu_{12}\left(1+e_{12}\right) < -\sqrt{{a_2}'^2 - 4{b_2}'}, \tag{3.28c}$$

$$-\left[{a_2}' + 2\mu_{12}\left(1+e_{12}\right)\right] > \sqrt{{a_2}'^2 - 4{b_2}'}, \tag{3.28d}$$

$${a_2}'^2 + 4\mu_{12}^2\left(1+e_{12}\right)^2 + 4{a_2}'\mu_{12}\left(1+e_{12}\right) > {a_2}'^2 - 4{b_2}', \tag{3.28e}$$

$$\left[{b_2}' + \mu_{12}^2\left(1+e_{12}\right)^2 + {a_2}'\mu_{12}\left(1+e_{12}\right)\right] > 0. \tag{3.28f}$$

The substitution of ${a_2}'$ and ${b_2}'$ from Eq. (3.26b) into Eq. (3.28f) yields

$$\left\{\frac{\left(1-E^2\right)}{a^2 Q {\mu_{12}}^2\left(1-{e_{12}}^2\right)} + \mu_{12}^2\left(1+e_{12}\right)^2 + 2\left[\mu_{12} - \frac{\left(x^2+Q\right)}{a^2 Q}\right]\mu_{12}\left(1+e_{12}\right)\right\} > 0, \tag{3.29a}$$

and using the translation relation given by Eq. (3.17a) to replace $\left(1-E^2\right)$ in the above equation, we finally obtain

$$\left[{\mu_{12}}^3 a^2 Q\left(1+e_{12}\right)^2 + {\mu_{12}}^2\left(\mu_{12} a^2 Q - Q - x^2\right)\left(3-e_{12}\right)\left(1+e_{12}\right) + 1\right] > 0. \tag{3.29b}$$

Along with the above condition, $E < 1$ and $r_p > r_+$ are other necessary conditions for the Δ region, as also discussed in §3.3.1. Hence we can together write the conditions for the Δ region as

$$\left[{\mu_{12}}^3 a^2 Q\left(1+e_{12}\right)^2 + {\mu_{12}}^2\left(\mu_{12} a^2 Q - Q - x^2\right)\left(3-e_{12}\right)\left(1+e_{12}\right) + 1\right] > 0, \tag{3.30a}$$

$$E\left(e,\mu,a,Q\right) < 1, \tag{3.30b}$$

$$\mu_{12}\left(1+e_{12}\right)\left(1+\sqrt{1-a^2}\right) < 1. \tag{3.30c}$$

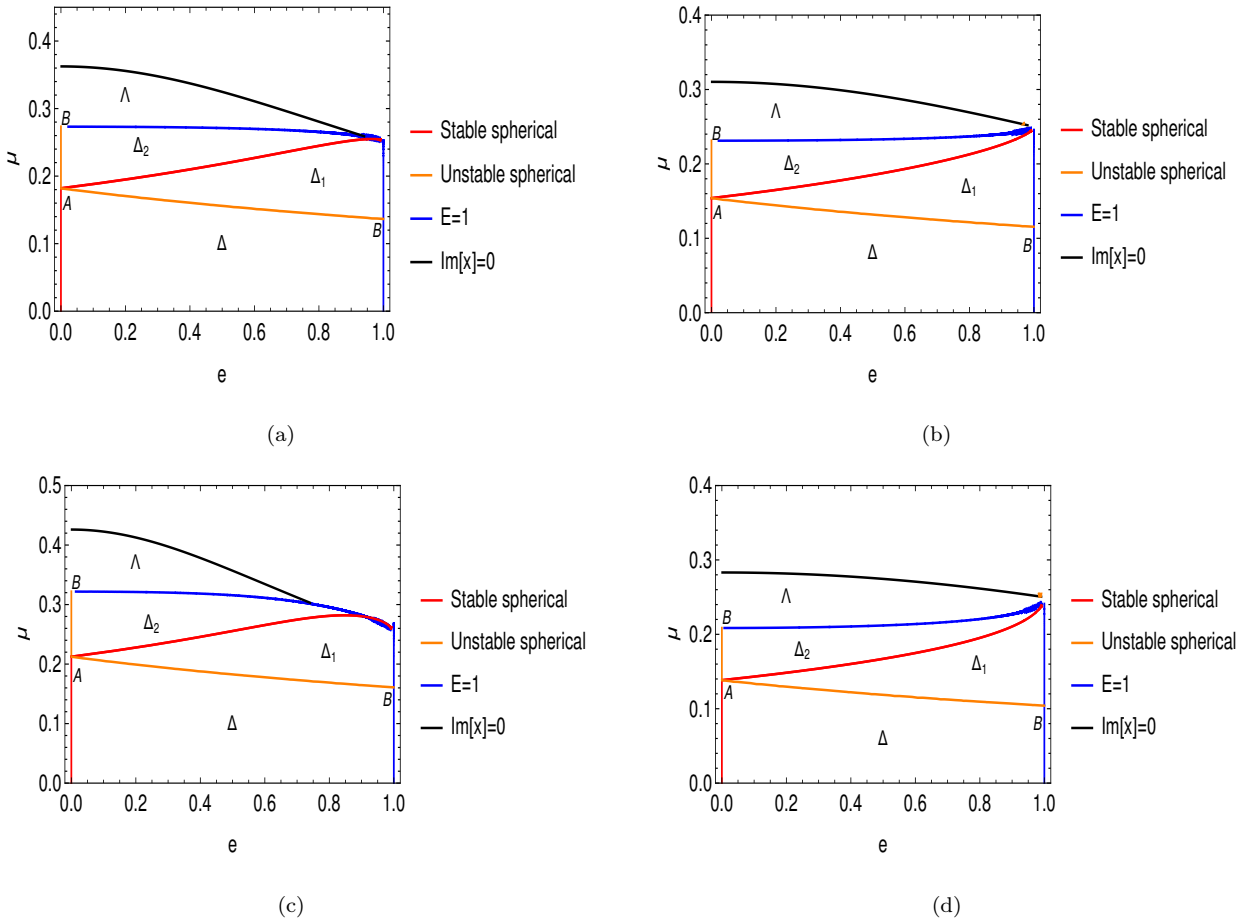

FIGURE 3.4: The figure shows the bounding curves of the region Δ and Λ in (e, μ) plane each for (a) $a = 0.2$, (b) $a = -0.2$, (c) $a = 0.5$, and (d) $a = -0.5$ with $Q = 5$. The red, blue, and orange curves represent the stable spherical, $E = 1$, and the unstable spherical or separatrix orbits respectively. The points A and B depict ISSO and MBSO respectively. The regions Δ_1 and Δ_2 are replicas of region Δ, when (e_{13}, μ_{13}) and (e_{23}, μ_{23}) are calculated respectively [from Eq. (3.1)] using the real roots of the Δ region.

We now discuss the Δ region, its boundaries, and the distribution of different kinds of bound orbits in the (e, μ) plane for different a and Q combinations below:

(a) Fig. 3.4 shows the boundaries of the Δ region in the (e, μ) plane for different a and Q combinations. All points within the Δ region follow the bound orbit condition, Eq. (3.30), (for the fixed a and Q values) and represent eccentric bound orbits between r_1 and r_2, and hence $\{e, \mu\}=\{e_{12}, \mu_{12}\}$. The Δ region is bounded by the stable spherical,

unstable spherical (or separatrix) orbits and $e = 1$ (or $E = 1$) curves, which we discuss below:

- *Bounding curves*: The $e_{12} = 0$ curves (red) in the Δ region in Fig. 3.4 represent the stable spherical orbits. The upper boundaries (orange) drawn in Fig. 3.4, correspond to the unstable spherical or separatrix orbits. The $e_{12} = 1$ curves (blue) in the Δ region in Fig. 3.4 represent the orbits where the particle is falling from infinity ($E = 1$).
- *ISSO*: This is labeled as A in Fig. 3.4 which is the intersection point of the stable spherical and separatrix curves.
- *MBSO*: This is labeled as B in Fig. 3.4 which is the intersection point of the separatrix and $e_{12} = 1$ curves.

(b) There is a one to one parametric correspondence between the points in the Δ region to regions outside it in the $(e,\ \mu)$ plane when the mathematical definition of (e, μ) is changed. The Fig. 3.4 shows the Δ region and its boundaries for different a with each point inside the region representing a unique eccentric orbit having a unique combination of (e_{12}, μ_{12}) and the corresponding unique set of (E, L) or x. The regions Δ_1 and Δ_2 in Fig. 3.4 are replicas of region Δ, where

- When (e, μ) are chosen to be (e_{13}, μ_{13}) using Eq. (3.1) to represent the corresponding set of roots, r_1 and r_3, that is physically allowed by the Δ region, with each point in it corresponding to a point in the Δ_1 region. The boundaries of the Δ region correspond to the boundaries of Δ_1 region and the one to one correspondence of the boundaries are indicated by the colors.
- Similarly, when (e, μ) are chosen to be (e_{23}, μ_{23}) using Eq. (3.1), then each point in the Δ region corresponds to a point in the Δ_2 region, where the one to one correspondence of the boundaries is indicated by the colors.

The regions Δ_1 and Δ_2 do not give any new information, but represent the degeneracy of the Δ region in the (e, μ) plane when their definitions are swicthed to (e_{13}, μ_{13}) and (e_{23}, μ_{23}).

(c) *Evolution of Δ region with a and Q*: From Fig. 3.5, we see that the boundary of Δ region evolves with different a and Q combinations. As Q increases, the Δ region move towards smaller μ and larger μ values for prograde and retrograde orbits respectively (see Figs. 3.5(c) and 3.5(d)), indicating that the orbits with higher Q values move outwards from the black hole and closer to the black hole for prograde and retrograde cases respectively. The Figs. 3.5(a) and 3.5(b) show the boundary of the Δ region for different values of a with $Q = 5$. It is seen that the Δ region moves towards the higher values of μ as a increases for the prograde orbits and vice-versa for the retrograde orbits. This indicates that the prograde bound orbits exist closer to the black hole for higher a than for a lower a and vice-versa for the retrograde bound orbits.

2. *Λ region*: The region Λ is defined by the condition that a bound orbit exists between r_2 and r_3 (or u_2 and u_3) with $r_1 > r_2$ (or $u_1 < u_2$) and $r_3 > r_4$ (or $u_3 < u_4$), where all roots are real and $E > 1$. We can express Eq. (3.26a) for this region as

$$u^4 + a^{'}u^3 + b^{'}u^2 + c^{'}u + d^{'} = [u - \mu_{23}(1 - e_{23})]\,[u - \mu_{23}(1 + e_{23})]\left(u^2 + {a_2}^{'}u + {b_2}^{'}\right), \tag{3.31a}$$

where $u_2 = \mu_{23}(1 - e_{23})$ and $u_3 = \mu_{23}(1 + e_{23})$. The remaining roots u_1 and u_4 can be derived from the factor $\left(u^2 + {a_2}^{'}u + {b_2}^{'}\right)$, which are given by

$$u_{4,1} = \frac{-{a_2}^{'} \pm \sqrt{{a_2}^{'2} - 4{b_2}^{'}}}{2}. \tag{3.31b}$$

The necessary condition for roots is $u_1 < u_2 < u_3 < u_4$. As $u_2 < u_3$ is valid by definition in the Λ region, the remaining conditions are $u_1 < u_2$ and

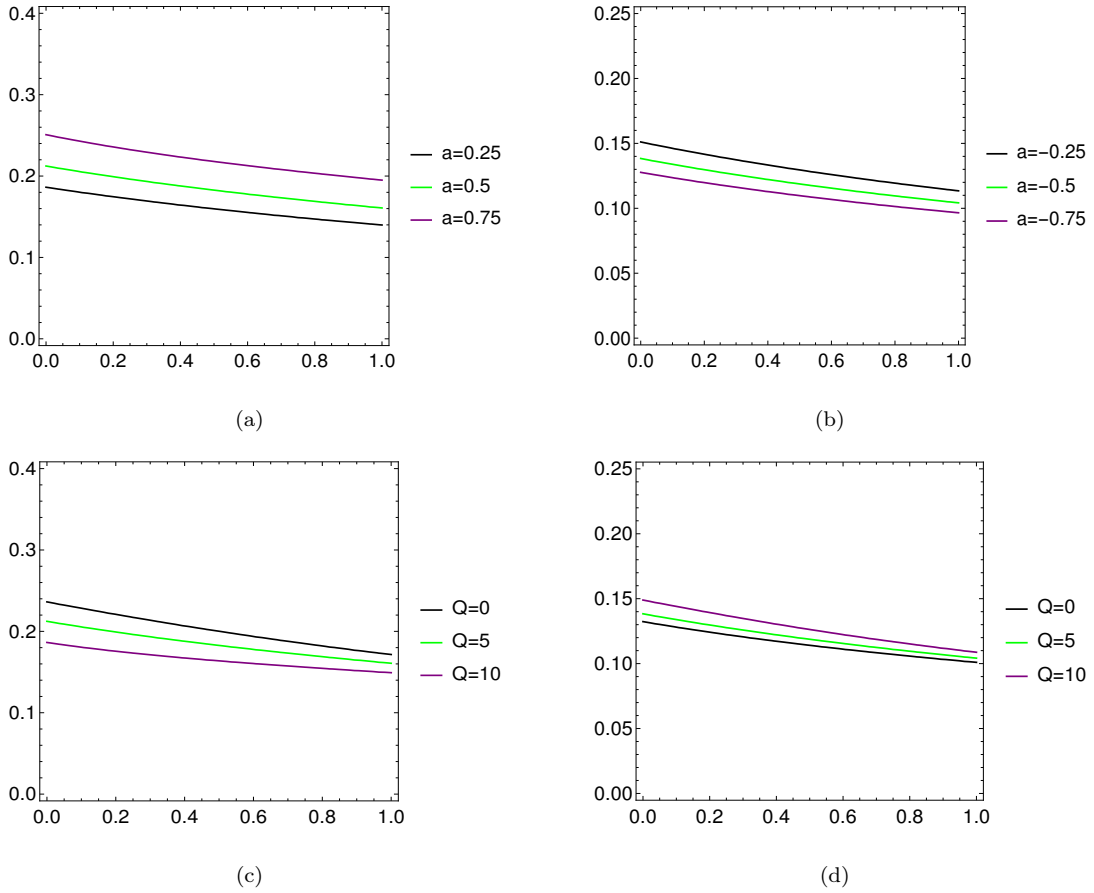

FIGURE 3.5: The upper boundaries of the Δ region are shown in the (e, μ) plane for different (labeled) values of a (a) for prograde, (b) for retrograde orbits with $Q = 5$, and for different values of Q (c) for prograde $a = 0.5$, and (d) retrograde $a = -0.5$ orbits.

$u_3 < u_4$. Now, $u_1 < u_2$ can be written as

$$\frac{-a_2{}' - \sqrt{a_2{}'^2 - 4b_2{}'}}{2} < \mu_{23}\left(1 - e_{23}\right), \tag{3.32a}$$

which further reduces to

$$\left[b_2{}' + \mu_{23}{}^2\left(1 - e_{23}\right)^2 + a_2{}'\mu_{23}\left(1 - e_{23}\right)\right] < 0, \tag{3.32b}$$

where further substitution of $a_2^{'}$ and $b_2^{'}$ from Eq. (3.26b), and E from Eq. (3.17a) finally yields

$$\left[\mu_{23}^3 a^2 Q\left(1-e_{23}\right)^2+\mu_{23}^2\left(\mu_{23} a^2 Q-x^2-Q\right)\left(3+e_{23}\right)\left(1-e_{23}\right)+1\right]<0. \tag{3.32c}$$

Similarly, the condition $u_3 < u_4$ gives

$$\left[\mu_{23}^3 a^2 Q\left(1+e_{23}\right)^2+\mu_{23}^2\left(\mu_{23} a^2 Q-x^2-Q\right)\left(3-e_{23}\right)\left(1+e_{23}\right)+1\right]<0. \tag{3.32d}$$

Next, as the region Λ corresponds to the orbits with $E > 1$; this implies [using Eq. (3.17a)]

$$\left[\mu_{23}^2\left(1-e_{23}^2\right)\left(\mu_{23} a^2 Q-Q-x^2\right)+1\right]<0. \tag{3.32e}$$

In effect, Eqs. (3.32c, 3.32d, 3.32e) together define Λ region the (e, μ) plane. The Fig. 3.4 shows region Λ for different (a, Q) combinations. The line $E = 1$ (blue curve) gets mapped to the region above the unstable spherical or separatrix curve when (e_{23}, μ_{23}) definition of (e, μ) is used, and this region above $E = 1$ is effectively representing the region Λ which is bounded by the curve where x becomes complex.

3. ς *region*: The region ς is defined by two complex roots of r or $u = 1/r$ with a bound orbit existing between the two remaining real roots, either between r_1 and r_2 or between r_3 and r_4, depending on which roots are making a complex conjugate pair. Hence in the (e, μ) space, we will either have $\{e_{12}, \mu_{12}\}$ or $\{e_{34}, \mu_{34}\}$ by definition, Eq. (3.1). We can rewrite Eq. (3.26a) for the region ς in the form

$$u^4+a^{'}u^3+b^{'}u^2+c^{'}u+d^{'}=\left[u-\mu\left(1-e\right)\right]\left[u-\mu\left(1+e\right)\right]\left(u^2+a_2^{'}u+b_2^{'}\right), \tag{3.33}$$

where the form of $a_2^{'}$ and $b_2^{'}$ is given by Eq. (3.26b). As the remaining two roots should be complex conjugates, which are the solutions of quadratic

$\left(u^2 + a_2{}'u + b_2{}'\right)$ in Eq. (3.33), the condition for the ς region is given by

$$\left(a_2{}'^2 - 4b_2{}'\right) < 0. \tag{3.34a}$$

Next, the substitution of $a_2{}'$ and $b_2{}'$ from Eq. (3.26b) gives

$$4\left\{\left[\mu - \frac{(x^2+Q)}{a^2Q}\right]^2 - \frac{(1-E^2)}{a^2Q\mu^2\,(1-e^2)}\right\} < 0, \tag{3.34b}$$

where replacing factor $(1-E^2)$ in the $(e,\,\mu,\,a,\,Q)$ form, using the translation relation given by Eq. (3.17a), finally yields

$$\left\{\left(Q+x^2\right)^2\mu + a^4e^2Q^2\mu^3 - a^2Q\left[1+\left(1+e^2\right)\left(Q+x^2\right)\mu^2\right]\right\} < 0, \tag{3.34c}$$

where $\{e,\,\mu\}$=$\{e_{12},\,\mu_{12}\}$ or $\{e_{34},\,\mu_{34}\}$. The ς region defined by the above equation, Eq. (3.34c), is shown in Fig. 3.6 for non-equatorial orbits with a prograde and retrograde case.

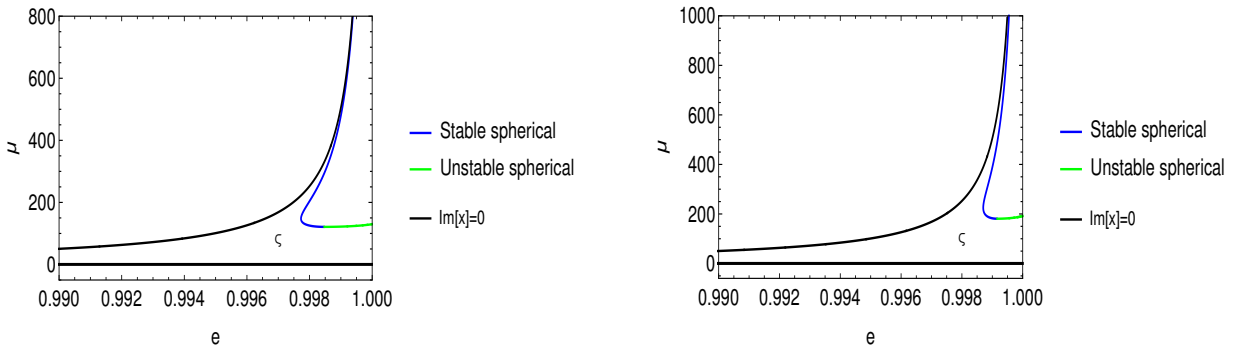

(a) (b)

FIGURE 3.6: The region ς in the $(e,\,\mu)$ plane is shown for (a) $(a = 0.2,\, Q = 2)$, and (b) $(a = -0.2,\, Q = 2)$. This region is bounded by curves of stable, unstable spherical orbits and the boundary where x gets complex.

Hence we conclude that only Δ region is relevant to the astrophysical scenarios. A comparison of the Δ region in the $(E,\,L)$ and $(e,\,\mu)$ plane is shown in Fig. 3.7. The results presented in this section are summarized in Table 3.1.

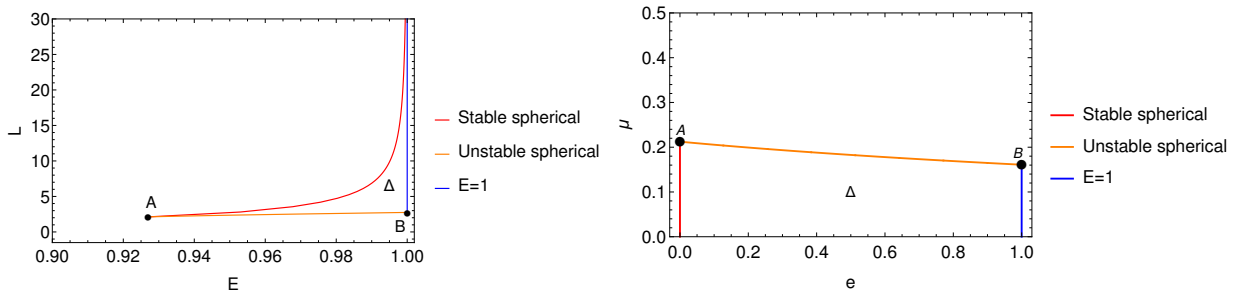

(a) (b)

FIGURE 3.7: The Δ region is shown for comparison in the (a) (E, L) and (b) (e, μ) plane for ($a = 0.5$, $Q = 5$), where points A and B represent ISSO and MBSO respectively.

3.4 Equatorial eccentric bound orbits ($Q = 0$)

In this section, we focus on the equatorial orbits and derive the bound orbit conditions in (E, L, a) and (e, μ, a) space.

3.4.1 Bound orbit conditions in the dynamical parameter space, $\{E, L, a\}$

Here, we derive the conditions in the dynamical parameter space for the equatorial eccentric bound orbits. The effective potential, Eq. (3.3b), for the equatorial orbits ($Q = 0$), reduces to a form given by

$$V_{eff}\left(r, a, E, L\right) = -\frac{1}{r} + \frac{L^2 - a^2\left(E^2 - 1\right)}{2r^2} - \frac{\left(L - aE\right)^2}{r^3}. \tag{3.35}$$

The radial equation for the turning points for a test particle motion in the equatorial plane, Eq. (3.18b) ($Q = 0$), reduces to

$$\left(1 - E^2\right) r^3 \; - \; 2r^2 \; + \; \left[L^2 - a^2\left(E^2 - 1\right)\right] \; r \; - \; 2(L - aE)^2 = 0. \tag{3.36}$$

We apply the Cardano's method (Cardano 1968) to obtain the roots of the cubic equation, Eq. (3.36), which we describe below:

- *Step 1*: For a general cubic equation given by

$$\alpha y^3 + \beta y^2 + \gamma y + \delta = 0, \tag{3.37}$$

we first make the substitution $y = Y - \frac{\beta}{3\alpha}$, which reduces it to a form

$$Y^3 + Yw + s = 0, \tag{3.38a}$$

where

$$w = \frac{-\beta^2}{3\alpha^2} + \frac{\gamma}{\alpha}, \tag{3.38b}$$

$$s = \frac{2\beta^3}{27\alpha^3} - \frac{\gamma\beta}{3\alpha^2} + \frac{\delta}{\alpha}. \tag{3.38c}$$

- *Step 2*: Next, we make another substitution $Y = \zeta + \eta$ and impose the constraints

$$\zeta^3\eta^3 = \frac{-w^3}{27}, \tag{3.39a}$$

$$\zeta^3 + \eta^3 = -s, \tag{3.39b}$$

this system gives sum and product of ζ^3 and η^3, which helps to determine a quadratic equation whose roots are ζ^3 and η^3 given by

$$t^2 + st - \frac{w^3}{27} = 0, \tag{3.40a}$$

whose solutions are

$$\zeta = \left[\frac{-s}{2} + \sqrt{\frac{s^2}{4} + \frac{w^3}{27}}\right]^{1/3}, \tag{3.40b}$$

$$\eta = \left[\frac{-s}{2} - \sqrt{\frac{s^2}{4} + \frac{w^3}{27}}\right]^{1/3}. \tag{3.40c}$$

- *Step 3*: We define

$$\Delta = \frac{s^2}{4} + \frac{w^3}{27}, \tag{3.41}$$

which gives three possibilities for ζ and η and hence for roots of Y or y, which are

1. $\Delta < 0$, three real and distinct roots.
2. $\Delta = 0$, two equal and one distinct real root.
3. $\Delta > 0$, two complex and one real root.

- *Step 4*: The case of $\Delta > 0$ gives scattering orbits and are non-circular and unbound by definition, so this is precluded from our study of bound orbits. Therefore, we focus on the cases of $\Delta \leq 0$ for which ζ and η are given by

$$\zeta = l^{1/3} e^{i\varphi/3}, \tag{3.42a}$$

$$\eta = l^{1/3} e^{-i\varphi/3}, \tag{3.42b}$$

where $l = \left(\frac{s^2}{4} - \Delta\right)^{1/2}$ and $\tan\varphi = \frac{-2\sqrt{-\Delta}}{s}$ and the corresponding distinct and real roots of the cubic equation, Eq. (3.37), are

$$y_1 = 2l^{1/3}\cos\left(\frac{\varphi}{3}\right) - \frac{\beta}{3\alpha}, \tag{3.43a}$$

$$y_2 = 2l^{1/3}\cos\left(\frac{\varphi - 2\pi}{3}\right) - \frac{\beta}{3\alpha}, \tag{3.43b}$$

$$y_3 = 2l^{1/3}\cos\left(\frac{\varphi + 2\pi}{3}\right) - \frac{\beta}{3\alpha}. \tag{3.43c}$$

From Eq. (3.41), we obtain the corresponding Δ (the discriminant of the cubic) for Eq. (3.36), which is given by

$$\begin{aligned}\Delta = \quad & 27\left(1-E^2\right)^2(L-aE)^4 - \left(L^2-a^2\left(E^2-1\right)\right)^2 + 16\,(L-aE)^2 \\ & -18\,(L-aE)^2\left(1-E^2\right)\left(L^2-a^2\left(E^2-1\right)\right) + \left(1-E^2\right)\left(L^2-a^2\left(E^2-1\right)\right)^3 .\end{aligned} \tag{3.44}$$

Hence the condition on $\{E, L, a\}$ to get three real and distinct roots of r, which is possible only when the orbit is an eccentric bound orbit, is given by

$$\Delta < 0 \qquad \text{and} \qquad 0 < E < 1. \tag{3.45}$$

The above condition, Eq. (3.45), spans a region in the (E, L) plane, which we call the Δ region as before, which represents all the equatorial eccentric bound orbits for a fixed spin, a. The Δ region is shown in Fig. 3.8 for $\{a = 0.5, -0.5; Q = 0\}$, bounded by the circular orbits and $E = 1$. The radial effective potential, Eq. (3.35), diagram for an equatorial eccentric orbit is shown in Fig. 3.9(a), which corresponds to a typical point inside the Δ region shown in Fig. 3.8(a) with $a = 0.5$.

We obtain the expressions for the three roots of the Eq. (3.36) using Eq. (3.43), which are

$$r_1 = \frac{2\left[1+\left[4-3\left(1-E^2\right)\left(L^2-a^2\left(E^2-1\right)\right)\right]^{1/2}\cos\frac{\varphi}{3}\right]}{3\left(1-E^2\right)}, \tag{3.46a}$$

$$r_2 = \frac{2\left[1+\left[4-3\left(1-E^2\right)\left(L^2-a^2\left(E^2-1\right)\right)\right]^{1/2}\cos\frac{\varphi-2\pi}{3}\right]}{3\left(1-E^2\right)}, \tag{3.46b}$$

$$r_3 = \frac{2\left[1+\left[4-3\left(1-E^2\right)\left(L^2-a^2\left(E^2-1\right)\right)\right]^{1/2}\cos\frac{\varphi+2\pi}{3}\right]}{3\left(1-E^2\right)}, \tag{3.46c}$$

where $r_1 > r_2 > r_3$, r_1 and r_2 are the apastron and periastron distances (turning points) respectively for the eccentric orbits, and where φ is given by

$$\cos\varphi = \frac{\left[8 - 9\left(1-E^2\right)\left(L^2 - a^2\left(E^2-1\right)\right) + 27\left(1-E^2\right)^2\left(L-aE\right)^2\right]}{\left[4 - 3\left(1-E^2\right)\left(L^2 - a^2\left(E^2-1\right)\right)\right]^{3/2}}; \quad (3.46d)$$

it follows that

$$-1 < \cos\varphi < +1 \quad \text{holds for eccentric orbits.} \quad (3.46e)$$

On the other hand, the case of two equal roots and one distinct real root is possible when

$$\Delta = 0, \quad (3.47)$$

which corresponds to the cases of the stable circular, the separatrix orbit or the inner unstable circular orbit, which are classified using $\cos\varphi$ as:

1. *Stable circular orbits*: The condition for these orbits is given by

$$\cos\varphi = -1 \;\Rightarrow\; r_1 = r_2 \;\text{ and }\; 0 < E < 1. \quad (3.48a)$$

   The red curves in Figs. 3.8(a) and 3.8(b) correspond to the contours of the stable circular orbits [cf. Eq. (3.48a)] for $a = 0.5$ and $a = -0.5$ respectively. These orbits exist outside the innermost stable circular orbit (ISCO) radius. The Fig. 3.9(b) shows the radial effective potential, Eq. (3.35), diagram for a typical point on the red curve of Fig. 3.8(a).

2. *Unstable circular/separatrix orbits*: The condition for such orbits is given by

$$\cos\varphi = +1 \;\Rightarrow\; r_2 = r_3 \;\text{ and }\; 0 < E < 1. \quad (3.48b)$$

   The orange curves in Figs. 3.8(a) and 3.8(b) represent the contours for the separatrix orbits [cf. Eq. (3.48b)] for $a = 0.5$ and $a = -0.5$ respectively.

These orbits exist between the marginally bound circular orbit (MBCO) and ISCO radius. The Fig. 3.9(c) shows the radial effective potential, Eq. (3.35), for a typical point on the orange curve of Fig. 3.8(a).

3. *Inner unstable circular orbits (IUCO)*: The condition for these orbits is

$$\cos\varphi = +1 \;\Rightarrow\; r_2 = r_3 \quad \text{and} \quad E > 1. \tag{3.48c}$$

The black curves in Figs. 3.8(a) and 3.8(b) represent the contours for IUCO [cf. Eq. (3.48c)] for $a = 0.5$ and $a = -0.5$ respectively. These orbits exist inside the MBCO radius, and the innermost limit for IUCO is given by the light radius. The Fig. 3.9(d) shows the radial effective potential, Eq. (3.35), for a typical point on the black curve of Fig. 3.8(a).

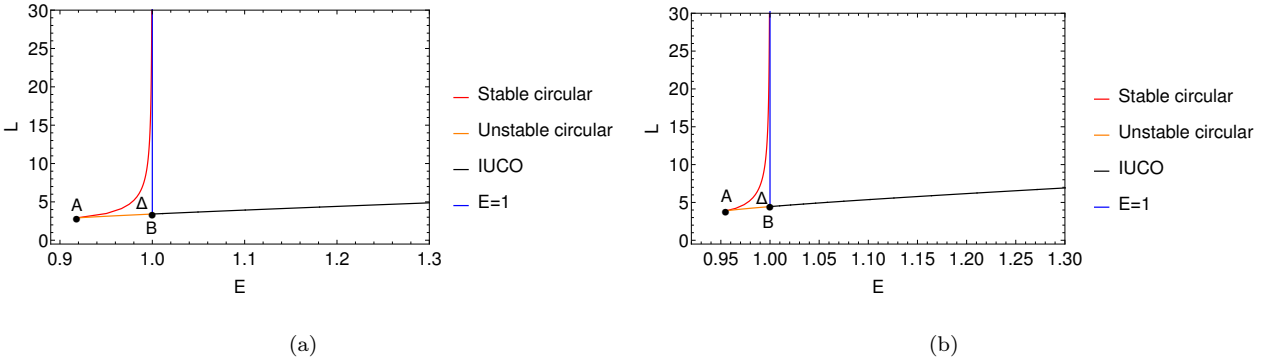

(a) (b)

FIGURE 3.8: The figure shows the Δ region for the equatorial eccentric orbits in the (E, L) plane for (a) $a = 0.5$ and (b) $a = -0.5$. The Δ region is bounded by the curves representing stable, unstable circular/separatrix orbits, and $E = 1$. The points A and B depict the innermost stable circular orbit (ISCO) and marginally bound circular orbit (MBCO) respectively.

The radius of ISCO is determined by the condition that the first and second derivative of radial effective potential vanish (i.e. $r_1 = r_2 = r_3$). This is possible only when the factor in front of the cosine term vanishes in Eqs. (3.46a - 3.46c) which leads to

$$\left[4 - 3\left(1 - E^2\right)\left(L^2 - a^2\left(E^2 - 1\right)\right)\right] = 0; \tag{3.49}$$

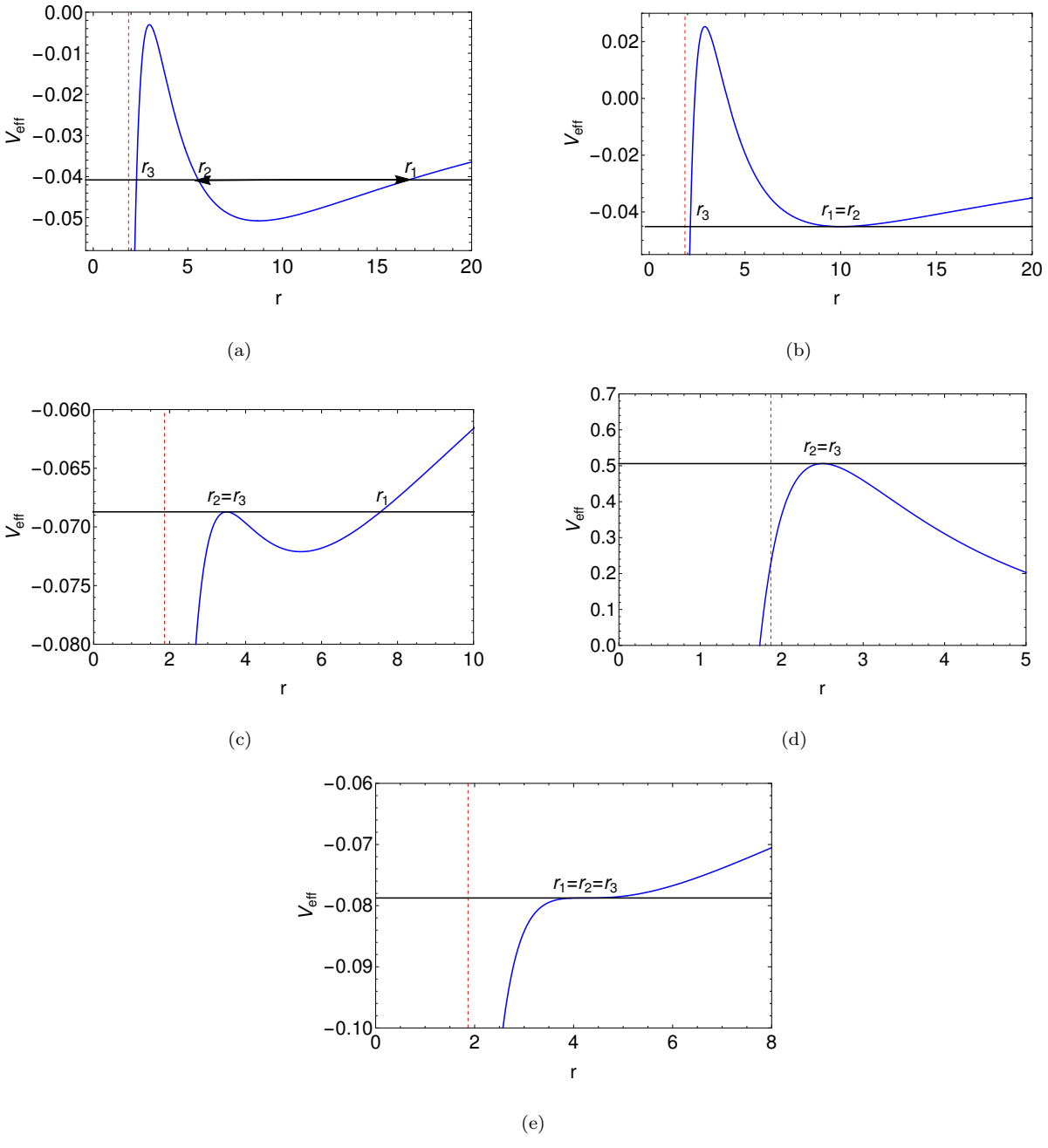

FIGURE 3.9: The figure shows the radial effective potential [Eq. (3.35)] with $\{a = 0.5,\ Q = 0\}$ for (a) an eccentric orbit $\{E = 0.958328,\ L = 3.41768\}$, (b) stable circular orbit $\{E = 0.953775,\ L = 3.58939\}$, (c) unstable circular/separatrix orbit $\{E = 0.928746,\ L = 2.9858\}$, (d) inner unstable circular orbit $\{E = 1.41842,\ L = 5.40617\}$, and (e) innermost stable circular orbit (ISCO) $\{E = 0.917882,\ L = 2.90287\}$, where the horizontal black curve and vertical dashed red curve correspond to $\left(E^2 - 1\right)/2$ and the horizon radius respectively.

this represents the condition for ISCO in terms of parameters E, L and a. The radial effective potential diagram, Eq. (3.35), of an ISCO is shown in Fig. 3.9(e).

The eccentricity and latus rectum parameters which are the mathematical counterparts of orbits in relativistic precession to the closed conic sections in Newtonian mechanics (and hence are referred to conic parameters) are defined using periastron and apastron distances as

$$e = \frac{r_1 - r_2}{r_1 + r_2} = \frac{\left(\cos\frac{\varphi}{3} - \cos\frac{\varphi - 2\pi}{3}\right)}{\left[2\left[4 - 3\left(1 - E^2\right)\left(L^2 - a^2\left(E^2 - 1\right)\right)\right]^{-1/2} + \left(\cos\frac{\varphi}{3} + \cos\frac{\varphi - 2\pi}{3}\right)\right]}, \tag{3.50a}$$

$$\begin{aligned} \ell = & \frac{2r_1 r_2}{r_1 + r_2} \\ = & \frac{4\left[1 + \left[4 - 3\left(1 - E^2\right)\left(L^2 - a^2\left(E^2 - 1\right)\right)\right]^{1/2}\cos\frac{\varphi}{3}\right] \cdot \left[1 + \left[4 - 3\left(1 - E^2\right)\left(L^2 - a^2\left(E^2 - 1\right)\right)\right]^{1/2}\cos\frac{\varphi - 2\pi}{3}\right]}{3\left(1 - E^2\right)\left[2 + \left[4 - 3\left(1 - E^2\right)\left(L^2 - a^2\left(E^2 - 1\right)\right)\right]^{1/2}\left(\cos\frac{\varphi}{3} + \cos\frac{\varphi - 2\pi}{3}\right)\right]}. \end{aligned} \tag{3.50b}$$

Now, we analyze the condition, $\Delta < 0$, for the orbits having one or both turning points inside the horizon radius and describe their distribution in the (E, L) plane for a fixed a:

- *Inside horizon*: The shaded region in the Figs. 3.10(a) and 3.10(b) represent orbits with two roots inside and one outside the horizon radius for $a = 0.5$ and $a = -0.5$ respectively; whereas the boundary of the shaded region represent unstable bound orbit with $r_2 = r_3$ inside the horizon, and r_1 outside the horizon. These are not visible to a distant observer. Figs. 3.10(c) - 3.10(f) show the radial effective potentials for such orbits. The case of

$L = aE$, previously discussed in (Chandrasekhar 1983), for equatorial orbits, lies inside this shaded region as shown in Fig. 3.11(a). The radial effective potential, given by Eq. (3.35) reduces to

$$V_{eff}\,(r, a) = -\frac{1}{r} + \frac{a^2}{2r^2}. \tag{3.51}$$

The Fig. 3.11(b) shows the effective potential of an orbit of this kind, where one of the turning points lies inside the horizon; hence, the particle plunges into the horizon. When the dynamics is formulated in a coordinate system that contains no coordinate singularity at the horizon, i.e., a generalization of Eddington-Finkelstein or Kruskal-Szekeres coordinates to Kerr background, it is observed that a particle crossing the horizon inevitably falls into the singularity at $r = 0$; furthermore, no light signals from inside the horizon are accessible to distant observers.

3.4.2 Bound orbit conditions in the conic parameter space $\{e, \mu, a\}$

Here, we discuss the bound orbit conditions in the conic parameter space which is useful in the study of orbit geometries.

The apastron, r_a, and the periastron distances, r_p, are defined in the terms of e and μ for an eccentric orbit, as

$$r_1 = r_a = \frac{1}{\mu\,(1-e)}, \qquad r_2 = r_p = \frac{1}{\mu\,(1+e)}. \tag{3.52}$$

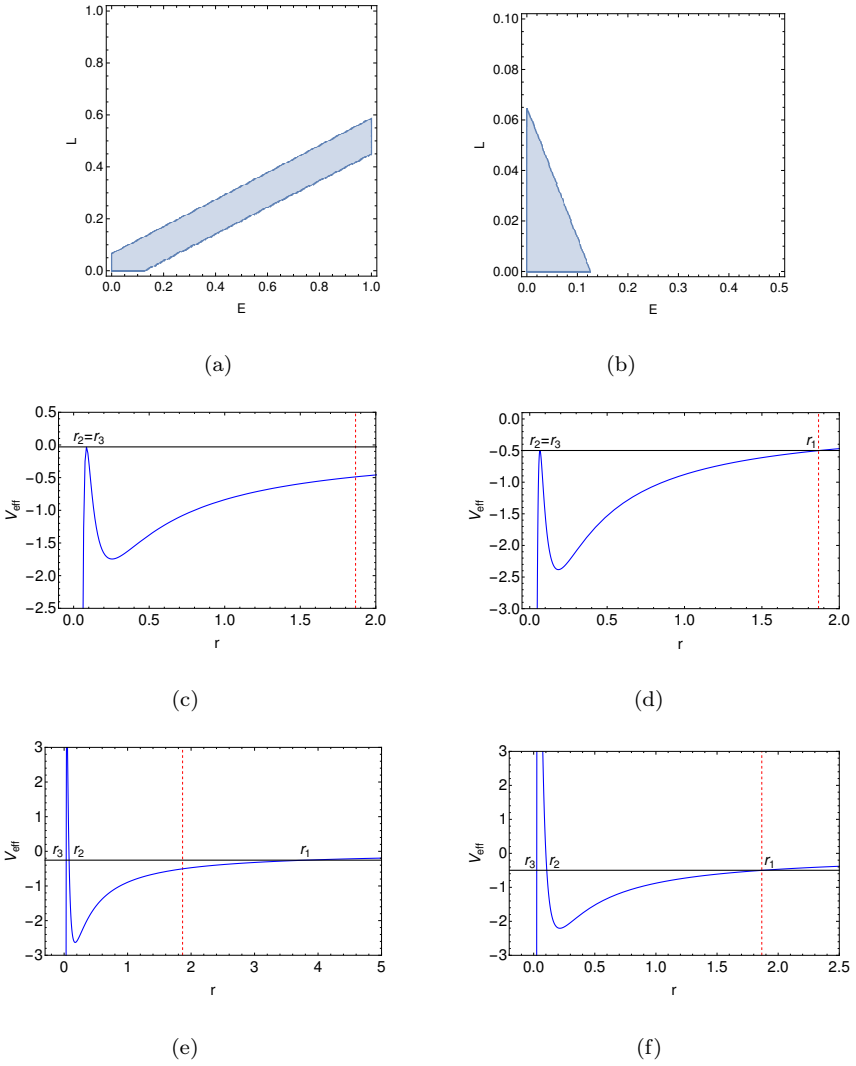

FIGURE 3.10: The $(E,\, L)$ plane is shown for $a = 0.5$ in (a) and $a = -0.5$ in (b) where the condition for three distinct roots, $\Delta < 0$, is valid in the shaded region; moreover, the two inner roots, r_2 and r_3, are inside the horizon, while r_1 is outside. The radial effective potential [Eq. (3.35)] diagrams are shown in (c) and (d) for $(E,\, L)$ chosen on the $\Delta = 0$ boundary of the shaded region; these cases have two inner equal roots, $r_2 = r_3$. The cases of three distinct roots are shown in diagrams (e) and (f) where the $(E,\, L)$ points are chosen inside the shaded region ($\Delta < 0$). The parameter set $\{\Delta = 0, \cos\varphi = +1, E = 0.97, L = 0.57, a = 0.5\}$ is used for (c), $\{\Delta = 0, \cos\varphi = +1, E = 0.05, L = 0.0387, a = -0.5\}$ for (d), $\{\Delta < 0, \cos\varphi = 0.9995, E = 0.7, L = 0.3, a = 0.5\}$ for (e), and $\{\Delta < 0, \cos\varphi = 0.9931, E = 0.06, L = 0.02, a = -0.5\}$ for (f).

Using the Eqs. (3.52, 3.36), the third root of the cubic equation is derived, which is given by (Bini *et al.* 2016a)

$$r_3 = \frac{2x^2\mu^2\,(1-e^2)}{(1-E^2)};\; x \equiv L - aE. \tag{3.53}$$

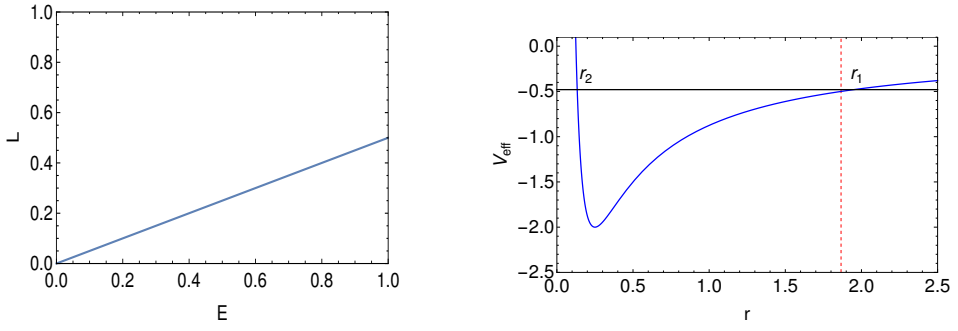

(a) (b)

FIGURE 3.11: $L = aE$ curve for $a = 0.5$ is shown in (a) which lies in the shaded region of Fig. 3.10(a), while (b) shows the effective potential [Eq. (3.51)] diagram for one such orbit with $E = 0.2$ that has one turning point inside the horizon and another outside the horizon.

Using the translation relations for $Q = 0$, Eqs. (3.17), the expression for Δ, which is given by Eq. (3.44), is written in terms of $(e,\, \mu,\, a)$ as

$$\begin{aligned}\Delta = & \quad \frac{-e^2}{\mu^2}\left[1 + 2\left(e^2 - 3\right)x^2\mu^2 + \left(9 - 10e^2 + e^4\right)x^4\mu^4\right]^2, \\ = & \quad \frac{-e^2}{\mu^2}\left[1 - x^2\mu^2\left(1 + e\right)\left(3 - e\right)\right]^2\left[1 - x^2\mu^2\left(1 - e\right)\left(3 + e\right)\right]^2, \\ = & \quad \frac{-e^2}{\mu^2}\Delta_1^2\Delta_2^2. \end{aligned} \tag{3.54}$$

It is seen that $\Delta \leq 0$ for all the real values of x and $\Delta = 0$ if any one of the following conditions is satisfied,

$$e = 0, \tag{3.55a}$$

$$\Delta_1 = 0 \Rightarrow \mu^2 x^2\left(3 - e\right)\left(1 + e\right) = 1, \tag{3.55b}$$

$$\Delta_2 = 0 \Rightarrow \mu^2 x^2\left(3 + e\right)\left(1 - e\right) = 1, \tag{3.55c}$$

where Eq. (3.55a) corresponds to the stable circular orbits, Eq. (3.55b) corresponds to the separatrix orbits and both lie on the boundary of the Δ region (a region specified by $\Delta \leq 0$) in the $(e,\, \mu)$ plane. The condition on $\{e, \mu, a\}$ for an eccentric bound orbit is given by $r_3 < r_p$, which is a necessary condition for a

particle to oscillate between $r_1 = r_a$ and $r_2 = r_p$. The Eqs. (3.52, 3.53, 3.17a) are solved to reduce this condition to

$$\mu_{12}^2 x^2 \left(3 - e_{12}\right)\left(1 + e_{12}\right) \leq 1, \tag{3.56}$$

which represents the ordering of roots, $r_1 > r_2 > r_3$, where the equality in Eq. (3.56) corresponds to the separatrix orbits. The above equation, Eq. (3.56), can also be obtained by substituting $Q = 0$ in Eq. (3.30a). The Fig. 3.12(a) shows the Δ region spanned by Eq. (3.56) in the (e, μ) plane. This region is bounded by the stable, unstable circular orbits, and $E = 1$.

The equality in Eq. (3.56) automatically follows from $\Delta = 0$ and it matches with Eq. (3.55b), which implies that $r_3 < r_2$ becomes the operative condition for eccentric bound orbits. The points satisfying Eq. (3.55c) lie outside the Δ region in (e, μ) plane, but represent the stable circular orbits when other combinations of roots are chosen to define e and μ instead of $\{e = e_{12}, \mu = \mu_{12}\}$; for example, $\{e_{13}, \mu_{13}\}$ or $\{e_{23}, \mu_{23}\}$. This would naturally occur outside the Δ region where the condition for ordering of roots is not obeyed.

<u>*Eccentric orbits*</u>: The distribution of eccentric orbits within the Δ region in the (e, μ) plane is studied through the variable $\cos\varphi$. The Fig. 3.12(b) shows the contours of $\cos\varphi$ in the Δ region for $a = 0.5$. Using Eqs. (3.17), the expression of $\cos\varphi$, Eq. (3.46d), in terms of $\{e_{12},\ \mu_{12},\ a\}$ is given by

$$\cos\varphi = \frac{\left[1 - 3x^2\mu_{12}^2\left(1 - e_{12}^2\right)\right]\left[-1 + 3e_{12} + 3x^2\mu_{12}^2\left(1 - e_{12} - e_{12}^2 + e_{12}^3\right)\right] \cdot \left[1 + 3e_{12} - 3x^2\mu_{12}^2\left(1 + e_{12} - e_{12}^2 - e_{12}^3\right)\right]}{\left[1 + 3e_{12}^2 + \left(e_{12}^2 - 1\right)\left[6x^2\mu_{12}^2\left(1 + e_{12}^2\right) + 3x^4\mu_{12}^4\left(e_{12}^2 - 1\right)\left(3 + e_{12}^2\right)\right]\right]^{3/2}}. \tag{3.57}$$

The value of $\cos\varphi$ varies from -1 to +1 from left to right in the Fig. 3.12(b), where $\cos\varphi = -1$ for stable circular orbit ($e_{12} = 0$), and $\cos\varphi = +1$ for the separatrix orbits and for $e_{12} = 1$; this is also seen from Eq. (3.57) as described below:

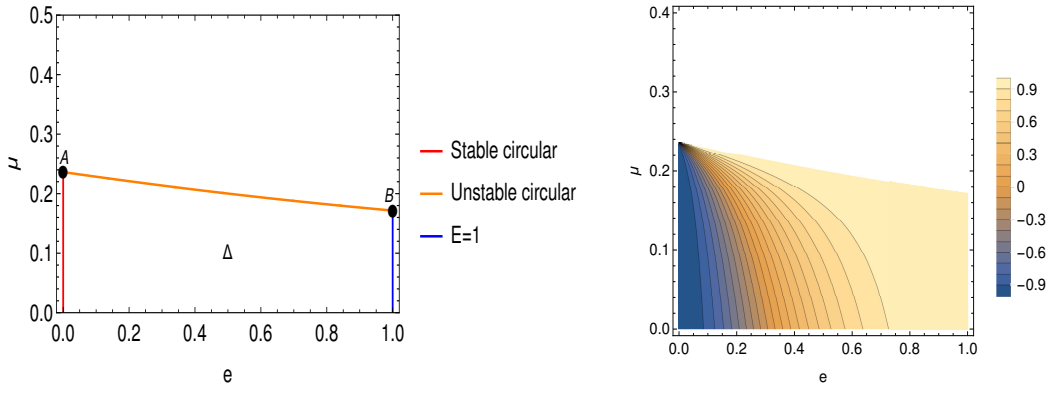

(a) (b)

FIGURE 3.12: (a) The Δ region, defined by Eq. (3.56), is shown for the equatorial orbits in the (e, μ) plane, where points A and B depict the ISCO and MBCO respectively, and (b) the contours of $\cos\varphi$ are shown inside the Δ region, where $a = 0.5$.

1. For the stable circular orbit case, $e_{12} = 0$, Eq. (3.57) reduces to

$$\begin{aligned} \cos\varphi = & \frac{[1-3x^2\mu_{12}^2]\,[-1+3x^2\mu_{12}^2]\,[1-3x^2\mu_{12}^2]}{[1-6x^2\mu_{12}^2+9x^4\mu_{12}^4]^{3/2}}, \\ = & -\frac{[1-3x^2\mu_{12}^2]^3}{[1-3x^2\mu_{12}^2]^3} = -1. \end{aligned} \tag{3.58a}$$

2. For the $e_{12} = 1$ case, Eq. (3.57) reduces to

$$\cos\varphi = \frac{8}{4^{3/2}} = +1, \tag{3.58b}$$

3. For the separatrix orbits, Eq. (3.56) gives

$$\mu_{12}^2 x^2 = \frac{1}{(3-e_{12})\,(1+e_{12})}, \tag{3.58c}$$

and the substitution of Eq. (3.58c) in (3.57) gives

$$\cos\varphi = \frac{\dfrac{2e_{12}}{(3-e_{12})}\cdot\dfrac{4e_{12}}{(3-e_{12})}\cdot\dfrac{8e_{12}}{(3-e_{12})}}{\left[\dfrac{(e_{12}-1)\left[6\left(1+e_{12}^2\right)(3-e_{12})+3\left(e_{12}-1\right)\left(3+e_{12}^2\right)\right]+\left(1+3e_{12}^2\right)(3-e_{12})^2}{(3-e_{12})^2}\right]^{3/2}}$$

$$= \frac{\dfrac{64e_{12}^3}{(3-e_{12})^3}}{\left[\dfrac{16e_{12}^2}{(3-e_{12})^2}\right]^{3/2}} = +1. \tag{3.58d}$$

The results presented in this section are summarized in Table 3.1.

3.5 The prescription for selecting bound orbits

In this section, we present the scaling formulae for the parameters (E, L) and (e, μ) in terms of the variables (x_1, y_1) and (x_2, y_2), where x_i, $y_i \in [0,1]$, $i = 1, 2$, to produce valid combinations of (E, L) and (e, μ) for bound orbits in the Δ region, which corresponds to the astrophysically relevant bound trajectories. These scaling formulae are derived using the expressions of (E, L) for spherical (circular) orbits and the expressions of (e, μ) for separatrix orbits, which we derive later in Chapter 4 and 5.

1. *Dynamical parameter space*: The scaling formulae for (E, L) to choose bound orbits in the Δ region depend upon the (E, L) formulae of the spherical (circular) orbits (which we derive in Chapter 4) because the Δ region is bounded by the spherical (circular) orbits. The range of E in the Δ region for a fixed (a, Q) combination is bounded between E at the ISSO (ISCO) radius and

TABLE 3.1: This table presents a formulary for different types of orbits in the non-equatorial and equatorial plane for both dynamical and conic parameter spaces.

Dynamical parameter space E, L, a, Q			Conic parameter space e, μ, a, Q		
Type of orbit	Region in the (E, L) plane	Conditions for the orbit	Type of orbit	Region in the (e, μ) plane	Conditions for the orbit
Bound orbit between r_1 and r_2 or r_3 and r_4	Δ Fig. 3.1	$D_1 > 0$, $D_2 > 0$, and $E < 1$; Bounded by stable, unstable spherical orbits, and $E = 1$.	Bound orbit with (e_{12}, μ_{12}) or (e_{34}, μ_{34})	Δ Fig. 3.4	$[{\mu_{12}}^2 (\mu_{12} a^2 Q - Q - x^2)(3 - e_{12})(1 + e_{12}) + {\mu_{12}}^3 a^2 Q (1 + e_{12})^2 + 1] > 0$, $\mu_{12}(1 + e_{12})\left(1 + \sqrt{1 - a^2}\right) < 1$, and $E(e, \mu, a, Q) < 1$; Eq. (3.30).
Bound orbit between r_2 and r_3	Λ Fig. 3.1	$D_1 > 0$, $D_2 > 0$, and $E > 1$; Bounded by IUSO.	Bound orbit with (e_{23}, μ_{23})	Λ Fig. 3.4	$[\mu_{23}^2 (1 - e_{23}^2)(\mu_{23} a^2 Q - Q - x^2) + 1] < 0$, $[\mu_{23}^2 (\mu_{23} a^2 Q - x^2 - Q)(3 + e_{23})(1 - e_{23}) + \mu_{23}^3 a^2 Q (1 - e_{23})^2 + 1] < 0$, $[\mu_{23}^2 (\mu_{23} a^2 Q - x^2 - Q)(3 - e_{23})(1 + e_{23}) \mu_{23}^3 a^2 Q (1 + e_{23})^2 + 1] < 0$; Eqs. (3.32c, 3.32d, 3.32e).
Bound orbit between r_1 and r_2 or r_3 and r_4	ς Fig. 3.1	$(D_1 \cdot D_2) < 0$ and $E < 1$; Bounded by stable and unstable spherical orbits.	Bound orbit with (e_{12}, μ_{12}) or (e_{34}, μ_{34})	ς Fig. 3.6	$\{a^4 e^2 Q^2 \mu^3 - a^2 Q [1 + (1 + e^2)(Q + x^2)\mu^2] + (Q + x^2)^2 \mu\} < 0$, Eq. (3.34c).
$Q = 0$, Bound orbit between r_1 and r_2	Δ Fig. 3.8	$\Delta < 0$, $0 < E < 1$, Eq. (3.45), $-1 < \cos\varphi < 1$, Eq. (3.46e), Bounded by stable [Eq. (3.48a)], unstable circular [Eq. (3.48b)] orbits, and $E = 1$.	$Q = 0$, Bound orbit with (e_{12}, μ_{12})	Δ Fig. 3.12(a)	$\mu_{12}^2 x^2 (3 - e_{12})(1 + e_{12}) \leq 1$, Eq. (3.56), $-1 < \cos\varphi < 1$, Eq. (3.57).
$Q = 0$, Inner unstable circular orbits (IUCOs)	Curve in region Λ Fig. 3.8	$\Delta = 0$, $E > 1$, Eq. (3.47), $\cos\varphi = +1$, Eq. (3.48c), r_c ranges from MBCO (Y) to light radius (X).	$Q = 0$, Inner unstable circular orbits (IUCOs)	$e_{23} = 0$ curve in region Λ	$e_{12} > 1$, $e_{23} = 0$, $\cos\varphi = +1$, Eq. (3.58b), μ_{23} from ranges $1/Y$ to $1/X$.
$Q = 0$, no bound orbit	ς		$Q = 0$, no bound orbit	ς	

$E = 1$ [at MBSO (MBCO) radius]. Hence, the formula for selecting E for bound orbits written in terms of the variable x_1, a, and Q is given by

$$E\left(x_1, a, Q\right) = E_Z\left(a, Q\right) + x_1\left[1 - E_Z\left(a, Q\right)\right], \tag{3.59a}$$

where $x_1 \in [0, 1]$ defines the range of the parameter E for bound orbits. The parameter $E_Z\left(a, Q\right)$ is the energy at the ISSO (ISCO) radius, given by

$$E_Z\left(a, Q\right) = \frac{\left\{\begin{array}{l}\left(Z-3\right)\left(Z-2\right)^2 Z^4 - a^2 Z\left[Z^2\left(3Z-5\right) + Q\left(Z\left(Z-4\right)+5\right)\right] \\ \quad + 2a^4 Q - 2a\left[Z\left(Z-2\right)+a^2\right]\sqrt{a^2Q^2 - Z^3 Q\left(Z-3\right) + Z^5}\end{array}\right\}^{1/2}}{Z^2\left[Z\left(Z-3\right)^2 - 4a^2\right]^{1/2}}, \tag{3.59b}$$

where $Z(a, Q)$ is the ISSO (ISCO) radius. We will derive the above expression, Eq. (3.59b), for a general spherical orbit and also the expression for $Z(a, Q)$ in Chapter 4.

For a fixed x_1, a, and Q, the range of L is bounded between L of a stable and an unstable spherical (circular) orbit. We attribute this range of L to the parameter $y_1 \in [0, 1]$ to define L for bound orbits in the Δ region. Hence, the formula for selecting L for the bound orbits written in terms of the variables $\{x_1, y_1\}$, a, and Q is given by

$$\frac{1}{L\left(x_1, y_1, a, Q\right)} = \frac{1}{L_-\left(x_1, a, Q\right)} - y_1\left[\frac{1}{L_-\left(x_1, a, Q\right)} - \frac{1}{L_+\left(x_1, a, Q\right)}\right], \tag{3.60a}$$

where $L_+\left(x_1, a, Q\right)$ and $L_-\left(x_1, a, Q\right)$ are given by

$$L_+\left(x_1, a, Q\right) = x(r_v\left(x_1, a, Q\right), a, Q) + a \cdot E(r_v\left(x_1, a, Q\right), a, Q), \tag{3.60b}$$

$$L_-\left(x_1, a, Q\right) = x(r_u\left(x_1, a, Q\right), a, Q) + a \cdot E(r_v\left(x_1, a, Q\right), a, Q), \tag{3.60c}$$

where $r_v\left(x_1,a,Q\right)$ and $r_u\left(x_1,a,Q\right)$ are the two roots of r_s in the equation

$$\frac{\left\{\begin{array}{c}\left(r_s-3\right)\left(r_s-2\right)^2r_s^4-a^2r_s\left[r_s^2\left(3r_s-5\right)+Q\left(r_s\left(r_s-4\right)+5\right)\right]\\ +2a^4Q-2a\left[r_s\left(r_s-2\right)+a^2\right]\sqrt{a^2Q^2-r_s^3Q\left(r_s-3\right)+r_s^5}\end{array}\right\}^{1/2}}{r_s^2\left[r_s\left(r_s-3\right)^2-4a^2\right]^{1/2}}$$
$$=E_Z\left(a,Q\right)+x_1\left[1-E_Z\left(a,Q\right)\right]. \tag{3.60d}$$

The radii $r_v\left(x_1,a,Q\right)$ and $r_u\left(x_1,a,Q\right)$ are chosen such that they are in the range given by $r_v\left(x_1,a,Q\right)>Z(a,Q)$ and $Y\left(a,Q\right)<r_u\left(x_1,a,Q\right)<Z\left(a,Q\right)$, where $Y\left(a,Q\right)$ is the MBSO (MBCO) radius (which we derive in Chapter 4). They give the upper, $L_+\left(x_1,a,Q\right)$, and lower, $L_-\left(x_1,a,Q\right)$, limits of L for a fixed x_1, a, and Q respectively.

2. *Conic parameter space*: The range of e in the Δ region is already between 0 to 1, and the range of μ is bounded between 0 and the value of μ of a separatrix orbit [or unstable spherical (circular) orbit] for a given e. Hence, in the (e,μ) space, the corresponding formulae are given by

$$e\left(x_2\right)= \quad x_2, \tag{3.61a}$$
$$\mu\left(y_2,r_x,a,Q\right)= \quad y_2\cdot\mu_s\left(r_x,a,Q\right), \tag{3.61b}$$

where x_2, $y_2\in[0,1]$ and hence the allowed range of μ is $0<\mu<\mu_s\left(r_x,a,Q\right)$ for a given x_2, and where $\mu_s\left(r_x,a,Q\right)$ corresponds to a separatrix orbit (which we derive in Chapter 5) given by

$$\mu_s\left(r_x,a,Q\right)=\frac{1}{4r_x}\left[-a'r_x-\sqrt{\left(r_xa'+2\right)^2-4d'r_x^4}\right]; \tag{3.62a}$$

and r_x is a root of r_s in the equation

$$x_2=\frac{4+a'r_s+\sqrt{\left(r_sa'+2\right)^2-4d'r_s^4}}{-a'r_s-\sqrt{\left(r_sa'+2\right)^2-4d'r_s^4}}, \tag{3.62b}$$

which lies between $Y(a,Q)$ and $Z(a,Q)$ for a given a and Q, and where $a^{'}$ and $d^{'}$ are given by

$$a^{'} = \frac{2\left\{\begin{array}{l} 2a^4Q - r_s^2(r_s-3)\left[r_s^2-(r_s-3)Q\right] - a^2r_s\left(r_s^3+r_s^2-2Qr_s+8Q\right) \\ \quad + 2a\left[r_s(r_s-2)+a^2\right]\sqrt{a^2Q^2 - r_s^3Q(r_s-3)+r_s^5} - Qr_s\left[r_s(r_s-3)^2-4a^2\right] \end{array}\right\}}{a^2Qr_s\left[r_s(r_s-3)^2-4a^2\right]}, \tag{3.62c}$$

$$d^{'} = \frac{\left\{\begin{array}{l} -2a^4Q - (r_s-3)(r_s-2)^2r_s^4 + a^2r_s\left[r_s^2(3r_s-5)+Q(r_s(r_s-4)+5)\right] \\ \quad + r_s^4\left[r_s(r_s-3)^2-4a^2\right] + 2a\left[r_s(r_s-2)+a^2\right]\sqrt{a^2Q^2 - r_s^3Q(r_s-3)+r_s^5} \end{array}\right\}}{a^2Qr_s^4\left[r_s(r_s-3)^2-4a^2\right]}. \tag{3.62d}$$

Hence, for a fixed a and Q, the range of $x_2, y_2 \in [0,1]$ defines the range of (e,μ).

3.6 Summary

1. We first translate the dynamical parameters (E, L, a, Q) to the conic parameters (e, μ, a, Q) by deriving the translation formulae, Eqs. (3.16), in terms of δ_1 (= 0 for null and = 1 for time-like trajectories). We then write these translation relations for the time-like trajectories, Eqs. (3.17). These formulae help to completely describe the bound orbit conditions in the conic parameter space.

2. We presented the algebraic conditions for the non-equatorial bound time-like trajectories in the (E, L, a, Q) and (e, μ, a, Q) spaces. We first solve the general radial equation of motion to find four roots of the effective potential as functions of (E, L, a, Q, δ_1) using the Ferrari's method, Eqs. (3.23). We then reduce them for the time-like trajectories ($\delta_1 = 1$), Eqs. (3.24). Using these formulae of roots, we derive the bound orbits conditions in the (E, L, a, Q) parameter space. We show how these conditions classify the bound orbits into various regions, Δ, ς, and Λ, in the (E, L) plane, which was previously

discussed graphically in Hackmann *et al.* (2010); see Fig. 3.1. Later, we write these bound orbit conditions for various regions in the (e, μ, a, Q) parameter space, Eqs. (3.30), (3.32c-3.32e), (3.34c), using the translation relations [Eqs. (3.17)]. The bound orbit regions in the (e, μ) plane, Figs. 3.4 and 3.6, are geometrically specified by their bound curves and vertices. For astrophysically relevant orbits, only the region Δ is applicable. These results are summarized in Table 3.1.

3. We discussed the bound orbit conditions for the eccentric equatorial orbits in the $\{E, L, a\}$, and $\{e, \mu, a\}$ spaces. We first derive the roots of the effective potential for the eccentric equatorial orbits, Eqs. (3.46a-3.46c), using the Cardano's method, and write the bound orbit condition in terms of $\{E, L, a\}$, Eq. (3.45). The bound orbit region is shown in the $\{E,\ L\}$ plane in Fig. 3.8. We then translate these conditions to $\{e, \mu, a\}$ space, Eq. (3.56), where the bound orbit region for the equatorial orbits is shown in the (e, μ) plane in Fig. 3.12. These results are summarized in Table 3.1.

4. We also provided a useful prescription to select the parameters (E, L) and (e, μ) in the Δ region, Eqs. (3.59a, 3.60a) and Eqs. (3.61a, 3.61b), which are canonical inputs to the trajectory solutions for studying their evolution in various applications like gravitational wave emission from extreme-mass ratio inspirals (Drasco *et al.* 2005; Drasco 2006; Drasco and Hughes 2006; Glampedakis and Kennefick 2002; Glampedakis *et al.* 2002), relativistic precession around black holes (Burgay *et al.* 2003; Lyne *et al.* 2004), and the study of gyroscope precession as a test of general relativity (Bini *et al.* 2016a).

Chapter 4

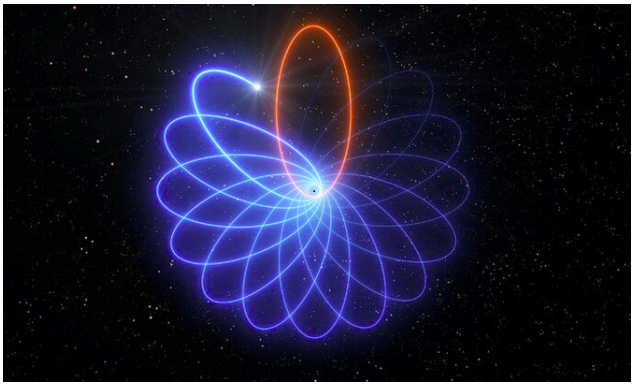

A sketch of the precessing orbit around a black hole. Courtesy: ESO/L. Calçada

Astrophysically relevant bound trajectories around a Kerr black hole*

4.1 Introduction

The exploration of analytic forms of various kinds of trajectories around Kerr and Schwarzschild black holes is one of the important problems in the field of general relativity. The study of some of these trajectories has been carried out before (Chandrasekhar 1983). There are several notable results in the vast literature discussing various aspects of dynamics in the Kerr geometry such as the

*The major part of the work in this chapter is published in a paper: Rana and Mangalam (2019a,b). The remaining work is published in a paper: Rana and Mangalam (2020b)

quadrature formulae for the trajectories (Chandrasekhar 1983; Carter 1968), circular orbit formulae (Bardeen *et al.* 1972), conditions for spherical orbits (Wilkins 1972), expressions in terms of quadratures for the oscillation frequencies (Schmidt 2002), formulae for trajectories in terms of quadratures for spherical polar motion (Kraniotis 2004), trajectories for non-spherical polar motion (Kraniotis 2007), and expressions for the trajectories and oscillation frequencies (Fujita and Hikida 2009) in terms of the Mino time (Mino 2003). Besides these key results, there are other useful expressions reported for example on separatrix orbits (Levin and Perez-Giz 2009), and on eccentric equatorial bound orbits (Chandrasekhar 1983; Bini *et al.* 2016a).

A time-like orbital parameter λ called Mino time (Mino 2003) was introduced to decouple the r and θ equations, which was then used to express a wider class of trajectory functions in terms of the orbital frequencies ν_θ, ν_ϕ and ν_r (Drasco and Hughes 2004). These methods are applied to calculate closed-form solutions of the trajectories and their orbital frequencies (Fujita and Hikida 2009), using the roots of the effective potential. However, the solutions are expressed in terms of Mino time. The commensurability of radial and longitudinal frequencies, their resonance conditions for orbits in Kerr geometry, and their location in terms of spin and orbital parameter values were studied using numerical implementations of Carlson's elliptic integrals (Brink *et al.* 2015). Considering the problem of the precession of a test gyroscope in the equatorial plane of Kerr geometry, the analytic expressions to transform energy, angular momentum of the orbiting test particle, and spin of the black hole (E, L, a) to eccentricity, inverse-latus rectum of the bound orbit (e, μ, a) parameters were obtained (Bini *et al.* 2016a). The expressions for radial and orbital frequencies are obtained to the order e^2 for bound orbits and analytically for the marginally bound homoclinic orbits (Bini *et al.* 2016b). The dynamical studies of an important family of Kerr orbits called separatrix or homoclinic orbits are important for computing the transition of spiralling to plunge in EMRIs emitting gravitational waves (Levin and Perez-Giz 2009; Glampedakis

and Kennefick 2002). The test particles (compact objects in this case) transit through an eccentric separatrix orbit in EMRIs, while progressing adiabatically, before they merge with the massive black hole.

In this chapter, we present the study of the generic bound trajectories, which are eccentric and inclined, around a Kerr black hole, and then we investigate the eccentric and equatorial orbits, the spherical orbits, and the non-equatorial separatrix orbits as special cases. We have solved the equations of motion and produce alternate and new closed-form solutions for the trajectories in terms of the elliptic integrals without using the Mino time, $\{\phi(r,\theta),\ t(r,\theta), r(\theta)\ \text{ or }\ \theta(r)\}$, which makes them numerically faster. We also implement the essential bound orbit conditions to choose the parameters (e, μ, a, Q) of an allowed bound orbit, derived from the essential conditions on the parameters for the elliptic integrals involved in the trajectory solutions. We find that the $e-\mu$ space is more convenient for integrating the equations of motion as the turning points of the integrands are naturally specified in terms of the bound orbit conditions. The exact solutions for the trajectories are found in terms of not overly long expressions involving elliptic integrals. We implement the translation formulae between (E, L) and (e, μ) parameters, Eq. (3.17), that help us to express the trajectory solutions completely in the (e, μ, a, Q) parameter space, which we call the conic parameter space. We then study the case of non-equatorial separatrix trajectories in the conic parameter space. First, we write the essential equations for the important radii like innermost stable spherical orbit ($ISSO$), marginally bound spherical orbit ($MBSO$), and spherical light radius. Similar to the equatorial separatrix orbits, the non-equatorial separatrix or homoclinic trajectories asymptote to an energetically bound unstable spherical orbit, where the spherical orbit radius can vary between $MBSO$ and $ISSO$. We show that the formulae for (e, μ) for the non-equatorial separatrix orbits can be expressed as functions of the radius of the corresponding spherical orbit, r_s, a, and Q, which also reduce to their equatorial counterpart (Levin and Perez-Giz 2009) by implementing the limit $Q \to 0$. These

formulae are obtained by using the expressions of E and L for the spherical orbits. Next, we derive the exact solutions for the non-equatorial separatrix trajectories by reducing our general eccentric trajectory solutions to this case. These solutions are important for investigating the behavior of gravitational waveforms emitted by inspiralling and inclined test objects near non-equatorial separatrix trajectories in the case of EMRIs. The ab-initio specification of the allowed geometry of bound orbits in the parameter space is crucial for the calculation of the orbital trajectories and its frequencies. These criteria are used in building, studying and sketching different types of trajectories around a Kerr black hole: for instance, spherical, non-equatorial eccentric, non-equatorial separatrix and zoom-whirl orbits, using our closed-form expressions for trajectories are constructed. We also derive closed-form analytic expressions for the fundamental frequencies of the general non-equatorial trajectories as functions of elliptic integrals around the Kerr black holes. We use a time-averaging method on the first-order equations of motion to derive these frequencies and show that our closed-form analytic expressions of frequencies match with the formulae given by Schmidt (2002) which were left in the quadrature forms. We also reduce the general trajectory forms and the frequency formulae to the equatorial eccentric and spherical orbit cases, which are also new forms that are easier to implement and faster, for example by a factor of ~ 20 for the equatorial eccentric orbits.

These novel results are useful for various applications and simulations related to astrophysical scenarios involving relativistic precession like QPOs and accretion disks. We also derive the locus of the $Q \neq 0$ separatrix curve in the $e - \mu$ plane besides providing the form of the trajectories. Using this, further studies can be carried for chaotic motion and study of gravitational waves from zoom-whirl orbits which can be set-up by locating them near the separatrix locus, in the same spirit, as was done for the equatorial case (Levin and Perez-Giz 2009; Glampedakis and Kennefick 2002). The analytic results have direct application to the study of non-equatorial separatrix orbits which has not been discussed before. They also help

in understanding the highly eccentric behavior of trajectories seen in numerical simulations (Glampedakis *et al.* 2002) just before plunging onto the massive black hole in the case of EMRIs which is possibly related to the eccentric and inclined homoclinic orbits, besides relativistic precession in other astrophysical systems like binary pulsars and black holes, spin precession of gyroscopes around rotating black holes for the test of general relativity, and the study of chaotic orbits in the phase space.

In §4.2.1, we derive the analytic form of the integrals of motion governing the time-like bound trajectories in the Kerr geometry ($e \neq 0$, $Q \neq 0$). We then write the necessary and sufficient conditions in (e, μ, a, Q) parameter space for the bound trajectories using these integrals in §4.2.2. We derive the analytic form of the fundamental frequencies in terms of the elliptic integrals for the general bound trajectories in §4.3. In §4.4, we reduce the trajectory solution and the fundamental frequencies to the case of equatorial and eccentric orbits ($e \neq 0$, $Q = 0$). In §4.5, we write the formulae for (E, L), trajectory solutions, and the fundamental frequencies for the spherical orbits ($e = 0$, $Q \neq 0$). We then derive the analytic expressions for the eccentricity and inverse latus rectum (e_s, μ_s) for the non-equatorial separatrix trajectories, and derive the reduced form of their trajectory solution in §4.6. In §4.7, we make the consistency check of our formulae by reducing them to the previously known results. We plot various types of trajectories using our analytic formulae in §4.8 and discuss various important astrophysical applications of our results in §4.9. Finally, we summarize all results in §4.10 and conclude in §4.11.

4.2 Integrals of motion and bound orbits around Kerr black hole

We derived the integrals of motion in the Kerr spacetime in Chapter 2, Eqs. (2.16d-2.16a), given by (Carter 1968; Schmidt 2002)

$$\tau - \tau_0 = \int_{r_0}^{r} \frac{r'^2 dr'}{\sqrt{R}} + \int_{\theta_0}^{\theta} \frac{a^2 \cos^2\theta' \mathrm{d}\theta'}{\sqrt{\Theta}}, \tag{4.1a}$$

$$\phi - \phi_0 = -\frac{1}{2}\int_{r_0}^{r} \frac{1}{\Delta\sqrt{R}}\frac{\partial R}{\partial L}\mathrm{d}r' - \frac{1}{2}\int_{\theta_0}^{\theta} \frac{1}{\sqrt{\Theta}}\frac{\partial \Theta}{\partial L}\mathrm{d}\theta' = -\frac{1}{2}I_1 - \frac{1}{2}H_1, \tag{4.1b}$$

$$t - t_0 = \frac{1}{2}\int_{r_0}^{r} \frac{1}{\Delta\sqrt{R}}\frac{\partial R}{\partial E}\mathrm{d}r' + \frac{1}{2}\int_{\theta_0}^{\theta} \frac{1}{\sqrt{\Theta}}\frac{\partial \Theta}{\partial E}\mathrm{d}\theta' = \frac{1}{2}I_2 + \frac{1}{2}H_2, \tag{4.1c}$$

$$\int_{r_0}^{r} \frac{\mathrm{d}r'}{\sqrt{R}} = \int_{\theta_0}^{\theta} \frac{\mathrm{d}\theta'}{\sqrt{\Theta}} \Rightarrow I_8 = H_3, \tag{4.1d}$$

where $\Delta = r'^2 - 2r' + a^2$ and

$$R = \left[\left(r^2 + a^2\right)E - aL\right]^2 - \left(r^2 + a^2 - 2r\right)\left[r^2 + (L - aE)^2 + Q\right], \tag{4.1e}$$

$$\Theta = Q - \left[\left(1 - E^2\right)a^2 + \frac{L^2}{\sin^2\theta}\right]\cos^2\theta, \tag{4.1f}$$

for the time-like trajectories.

4.2.1 Analytic solutions of integrals of motion

We solve for the integrals of motion, i.e. Eqs. (4.1b-4.1d) and reduce them to a simple form involving elliptic integrals. We first derive the expressions for the radial integrals I_1, I_2, and I_8. We assume the starting point of the radial motion to be apastron point of the bound orbit, $r_0 = r_a$. The steps taken to obtain the reduced form of the radial integrals are as follows:

1. We make the substitution $1/r^{'} = \mu\left(1 + e\cos\chi\right)$ and implement the method of partial fractions, where the variable χ varies from π (periastron) to 2π (apastron). The motivation to use this variable transformation is to remove the singularity in the integrands of the radial integrals (I_1, I_2, I_8) at the turning points, r_p and r_a.

2. Then make the substitutions, $\cos\chi = 2\cos^2\frac{\chi}{2} - 1$ and $\psi = \frac{\chi}{2} - \frac{\pi}{2}$.

3. Implement the variable transformation given by $\sin\alpha = \frac{\sqrt{1-m^2}\sin\psi}{\sqrt{1-m^2\sin^2\psi}}$, where m^2 is defined by Eq. (4.4i). Such variable transformation reduces the form of the radial integrals in terms of the standard elliptic integrals defned by (Gradshteyn and Ryzhik 2007)

$$F\left(\alpha, k^2\right) = \int_0^{\alpha} \frac{\mathrm{d}\alpha}{\sqrt{1 - k^2\sin^2\alpha}}, \tag{4.2a}$$

$$K\left(\alpha, k^2\right) = \int_0^{\alpha} \sqrt{1 - k^2\sin^2\alpha}\cdot\mathrm{d}\alpha, \tag{4.2b}$$

$$\Pi\left(s^2, \alpha, k^2\right) = \int_0^{\alpha} \frac{\mathrm{d}\alpha}{\left(1 - s^2\sin^2\alpha\right)\sqrt{1 - k^2\sin^2\alpha}}. \tag{4.2c}$$

As a result, the integrals of motion are expressed as functions of standard elliptic integrals, given by

$$I_1\left(\alpha, e, \mu, a, Q\right) = -\left[C_3 I_3\left(\alpha, e, \mu, a, Q\right) + C_4 I_4\left(\alpha, e, \mu, a, Q\right)\right], \tag{4.3a}$$

$$I_2\left(\alpha, e, \mu, a, Q\right) = \left[C_5 I_5\left(\alpha, e, \mu, a, Q\right) + C_6 I_6\left(\alpha, e, \mu, a, Q\right) + C_7 I_3\left(\alpha, e, \mu, a, Q\right) + C_8 I_4\left(\alpha, e, \mu, a, Q\right)\right], \tag{4.3b}$$

$$I_3\left(\alpha, e, \mu, a, Q\right) = \frac{1}{\sqrt{1-m^2}\left(m^2 + p_2^2\right)}\left[m^2 F\left(\alpha, k^2\right) + p_2^2\Pi\left(\frac{-\left(p_2^2 + m^2\right)}{1-m^2}, \alpha, k^2\right)\right], \tag{4.3c}$$

$$I_4\left(\alpha, e, \mu, a, Q\right) = \frac{1}{\sqrt{1-m^2}\left(m^2 + p_3^2\right)}\left[m^2 F\left(\alpha, k^2\right) + p_3^2\Pi\left(\frac{-\left(p_3^2 + m^2\right)}{1-m^2}, \alpha, k^2\right)\right], \tag{4.3d}$$

$$I_5\left(\alpha, e, \mu, a, Q\right) = \frac{1}{\sqrt{1-m^2}\left(m^2 + p_1^2\right)^2}\left[m^4 F\left(\alpha, k^2\right) + 2p_1^2 m^2\Pi\left(s^2, \alpha, k^2\right) + p_1^4 I_7\left(\alpha, e, \mu, a, Q\right)\right], \tag{4.3e}$$

$$I_6(\alpha,e,\mu,a,Q) = \frac{1}{\sqrt{1-m^2}\,(m^2+p_1^2)}\left[m^2F\left(\alpha,k^2\right)+p_1^2\Pi\left(s^2,\alpha,k^2\right)\right], \tag{4.3f}$$

$$I_7(\alpha,e,\mu,a,Q) = \frac{s^4\sin\alpha\cos\alpha\sqrt{1-k^2\sin^2\alpha}}{2\left(1-s^2\right)\left(k^2-s^2\right)\left(1-s^2\sin^2\alpha\right)} - \frac{s^2}{2\left(1-s^2\right)\left(k^2-s^2\right)}K\left(\alpha,k^2\right)$$
$$-\frac{1}{2\left(1-s^2\right)}F\left(\alpha,k^2\right)+\frac{\left[s^4-2s^2\left(1+k^2\right)+3k^2\right]}{2\left(1-s^2\right)\left(k^2-s^2\right)}\Pi\left(s^2,\alpha,k^2\right), \tag{4.3g}$$

$$I_8(\alpha,e,\mu,a,Q) = \frac{2\mu\left(1-e^2\right)}{\sqrt{C-A+\sqrt{B^2-4AC}}}F\left(\alpha,k^2\right), \tag{4.3h}$$

where

$$C_3 = \frac{2\left(1-e^2\right)\mu\left[La^2-2xr_+\right]}{\sqrt{(A-B+C)\left(1-a^2\right)}\left(a^2\mu-a^2\mu e-r_+\right)}, \tag{4.4a}$$

$$C_4 = \frac{2\left(1-e^2\right)\mu\left[-La^2+2xr_-\right]}{\sqrt{(A-B+C)\left(1-a^2\right)}\left(a^2\mu-a^2\mu e-r_-\right)}, \tag{4.4b}$$

$$C_5 = \frac{4E\left(1+e\right)}{\mu\sqrt{(A-B+C)\left(1-e\right)}}, \quad C_6 = \frac{8E\left(1+e\right)}{\sqrt{(A-B+C)}}, \tag{4.4c}$$

$$C_7 = \frac{4a^2\mu\left(1-e^2\right)\left(-La+2Er_-\right)}{r_-\sqrt{(A-B+C)\left(1-a^2\right)}\left(a^2\mu-a^2\mu e-r_+\right)}, \tag{4.4d}$$

$$C_8 = \frac{4a\mu\left(1-e^2\right)\left(-2Lr_-\sqrt{1-a^2}-2Ear_-+La^2\right)}{r_-\sqrt{(A-B+C)\left(1-a^2\right)}\left(a^2\mu-a^2\mu e-r_-\right)}, \tag{4.4e}$$

$$A = Qa^2e^2\mu^4\left(1-e^2\right)^2, \tag{4.4f}$$

$$B = 2e\mu^3\left(1-e^2\right)^2\left[2Qa^2\mu-x^2-Q\right], \tag{4.4g}$$

$$C = \mu^3\left(1-e^2\right)^2\left[3\mu Qa^2-2x^2-2Q\right]+\left(1-E^2\right)\left(1-e^2\right), \tag{4.4h}$$

$$n^2 = \frac{4A}{2A-B-\sqrt{B^2-4AC}}, \quad m^2 = \frac{4A}{2A-B+\sqrt{B^2-4AC}}, \tag{4.4i}$$

$$k^2 = \frac{n^2-m^2}{1-m^2}, \quad s^2 = \frac{-p_1^2-m^2}{1-m^2}, \tag{4.4j}$$

$$p_1^2 = \frac{2e}{1-e}, \quad p_2^2 = \frac{2ea^2\mu}{a^2\mu-a^2\mu e-r_+}, \quad p_3^2 = \frac{2ea^2\mu}{a^2\mu-a^2\mu e-r_-}, \tag{4.4k}$$

$$x_{1,2} = \frac{-B\pm\sqrt{B^2-4AC}}{2A}, \tag{4.4l}$$

and where the variables E, L and x can be written as functions of (e, μ, a, Q) using Eqs. (3.17), which makes all the integrals to be only functions of (e, μ, a, Q).

A complete derivation of these integrals is given in Appendix A.1. Next, to solve the integrals H_1, H_2, and H_3 of Eqs. (4.1b- 4.1d), we make the substitutions $z = \cos\theta^{'}$ and $z = z_{-}\sin\beta$ (Fujita and Hikida 2009) which reduces these integrals to

$$H_1\left(\theta,\theta_0,e,\mu,a,Q\right) = \frac{2L}{z_{+}a\sqrt{1-E^2}}\left\{F\left(\arcsin\left(\frac{\cos\theta_0}{z_{-}}\right),\frac{z_{-}^2}{z_{+}^2}\right) - F\left(\arcsin\left(\frac{\cos\theta}{z_{-}}\right),\frac{z_{-}^2}{z_{+}^2}\right) + \Pi\left(z_{-}^2,\arcsin\left(\frac{\cos\theta}{z_{-}}\right),\frac{z_{-}^2}{z_{+}^2}\right) - \Pi\left(z_{-}^2,\arcsin\left(\frac{\cos\theta_0}{z_{-}}\right),\frac{z_{-}^2}{z_{+}^2}\right)\right\}, \tag{4.5a}$$

$$H_2\left(\theta,\theta_0,e,\mu,a,Q\right) = \frac{2Eaz_{+}}{\sqrt{1-E^2}}\left\{K\left(\arcsin\left(\frac{\cos\theta}{z_{-}}\right),\frac{z_{-}^2}{z_{+}^2}\right) - F\left(\arcsin\left(\frac{\cos\theta}{z_{-}}\right),\frac{z_{-}^2}{z_{+}^2}\right) - K\left(\arcsin\left(\frac{\cos\theta_0}{z_{-}}\right),\frac{z_{-}^2}{z_{+}^2}\right) + F\left(\arcsin\left(\frac{\cos\theta_0}{z_{-}}\right),\frac{z_{-}^2}{z_{+}^2}\right)\right\}, \tag{4.5b}$$

$$H_3\left(\theta,\theta_0,e,\mu,a,Q\right) = \frac{1}{a\sqrt{1-E^2}z_{+}}\left\{F\left(\arcsin\left(\frac{\cos\theta_0}{z_{-}}\right),\frac{z_{-}^2}{z_{+}^2}\right) - F\left(\arcsin\left(\frac{\cos\theta}{z_{-}}\right),\frac{z_{-}^2}{z_{+}^2}\right)\right\}, \tag{4.5c}$$

where

$$z_{\pm}^2 = \frac{-P^{'}\pm\sqrt{P^{'2}-4Q^{'}}}{2},\quad P^{'} = \frac{-L^2-Q-a^2\left(1-E^2\right)}{a^2\left(1-E^2\right)},\quad Q^{'} = \frac{Q}{a^2\left(1-E^2\right)}. \tag{4.5d}$$

Hence, the equations of motion can now be written in short as

$$\phi-\phi_0 = \frac{1}{2}\left[C_3I_3\left(\alpha,e,\mu,a,Q\right) + C_4I_4\left(\alpha,e,\mu,a,Q\right) - H_1\left(\theta,\theta_0,e,\mu,a,Q\right)\right], \tag{4.6a}$$

$$t-t_0 = \frac{1}{2}\left[C_5I_5\left(\alpha,e,\mu,a,Q\right) + C_6I_6\left(\alpha,e,\mu,a,Q\right) + C_7I_3\left(\alpha,e,\mu,a,Q\right) + C_8I_4\left(\alpha,e,\mu,a,Q\right) + H_2\left(\theta,\theta_0,e,\mu,a,Q\right)\right], \tag{4.6b}$$

$$I_8\left(\alpha,e,\mu,a,Q\right) = H_3\left(\theta,\theta_0,e,\mu,a,Q\right), \tag{4.6c}$$

where I_3, I_4, I_5, I_6, I_8, H_1, H_2 and H_3 are given by Eqs. (4.3c-4.3h; 4.5) respectively, these integrals are also summarized in Table 4.1. Hence, all the integrals are written explicitly as functions of parameters (e, μ, a, Q) through variables

$\alpha\,(e, \mu, a, Q; \chi)$ and $\beta\,(e, \mu, a, Q; \theta)$ which are directly used to calculate (r, θ, t) through Eqs. (4.6a-4.6c). The radial motion, which varies with the α, is assumed to have the starting point at the apastron distance, r_a or $\alpha = 0$, of the orbit and the starting point of the polar motion, β_0 or θ_0, is an extra variable which can be chosen in the range $\{\theta_-, \pi - \theta_-\}$. This is tantamount to shifting the starting point of the motion in time or adjusting the initial value of the observed time, t_0.

Once the initial points are fixed ($\alpha = 0$, $\theta = \theta_0$), Eqs. (4.6a) and (4.6b) are used to calculate $\phi\,(r, \theta)$ and $t\,(r, \theta)$ respectively, whereas Eq. (4.6c) gives $r\,(\theta)$ or $\theta\,(r)$, which can be used to obtain $t\,(r)$ or $t\,(\theta)$ and $\phi\,(r)$ or $\phi\,(\theta)$.

The elegant alternate forms presented here help us to write useful and simpler expressions of (ϕ, t) for the equatorial eccentric trajectories, as shown later in §4.4. Also, these results can be used to reduce the radial integrals for non-equatorial separatrix trajectories in the form of logarithmic and trigonometric functions, presented in §4.6.2, which are useful in the study of gravitational waves from EMRIs.

4.2.2 Bound orbit conditions in conic parameter space

The bound orbit regions have been studied and divided in the (E, L) space according to the different types of possible r motion by Hackmann *et al.* (2010). The most relevant astrophysical bound orbit region corresponds to the case where $E < 1$ and there are four real roots of $R(r)$, $r_1 > r_2 > r_3 > r_4 > 0$, such that the bound orbit either exists between r_1 and r_2 or r_3 and r_4, this has been defined as region III in the (E, L) plane by Hackmann *et al.* (2010). Since r_1 and r_2 are the outer most turning points of the effective potential, the bound orbit should exist between these two in the astrophysical situations. We can implement this

constraint in the (e, μ, a, Q) space by imposing the condition $k^2 < 1$ on the parameter k used in the radial integrals in §4.2.1, where we have assumed that a bound orbit exists between r_1 and r_2, which requires $k^2 < 1$ as an essential condition for the elliptic integrals to have real values, Eqs. (4.2a-4.2c). This further implies

$$n^2 < 1; \tag{4.7a}$$

where the substitution of Eq. (4.4i) in the above expression yields

$$(A + B + C) > 0, \tag{4.7b}$$

and by using Eqs. (6.8c-4.4h) and (3.17) this implies

$$\left[\mu^3 a^2 Q\,(1+e)^2 + \mu^2\left(\mu a^2 Q - x^2 - Q\right)(3-e)\,(1+e) + 1\right] > 0. \tag{4.7c}$$

Another necessary condition is that the periastron of the orbit $r_2 = 1/\left[\mu\,(1+e)\right]$ is outside the horizon, which gives

$$\left[\mu\,(1+e)\left(1+\sqrt{1-a^2}\right)\right] < 1. \tag{4.7d}$$

Hence, the necessary and independent conditions for this region can be collectively given as

$$\mu^3 a^2 Q\,(1+e)^2 + \mu^2\left(\mu a^2 Q - x^2 - Q\right)(3-e)\,(1+e) + 1 > 0, \tag{4.8a}$$

$$\mu\,(1+e)\left(1+\sqrt{1-a^2}\right) < 1, \tag{4.8b}$$

$$E(e, \mu, a, Q) < 1. \tag{4.8c}$$

There exists unstable bound orbits for $E > 1$ specified as region IV in the (E, L) plane by Hackmann *et al.* (2010), where the bound orbit exists between r_2 and r_3. Such a situation is not important from the astrophysical point of view, because the particle will follow a bound trajectory between the outermost turning points, i.e. r_1 and r_2, and hence the above conditions, Eq. (4.8), together represent a

necessary and sufficient condition for the existence of bound orbits. These results, Eq. (4.8), were also derived in chapter 3, Eq. (3.30), using the roots of the effective potential.

4.3 Fundamental oscillation frequencies

In this section, we derive the expressions for fundamental frequencies (ν_ϕ, ν_r, ν_θ) in terms of the integrals derived analytically in §4.2.1. We take a long time average of Eq. (4.1d) on both the sides so that

$$\lim_{T\to\infty}\frac{1}{T}\int_{r_0}^{r}\frac{dr}{\sqrt{R}}=\lim_{T\to\infty}\frac{1}{T}\int_{\theta_0}^{\theta}\frac{d\theta}{\sqrt{\Theta}}. \tag{4.9a}$$

As $T\to\infty$, there exist large integer solutions, which can be found with arbitrary precision, so that $N_r t_r = N_\theta t_\theta = T$, where N_r and N_θ are the number of radial and vertical oscillations; hence Eq. (4.9a) reduces to

$$\lim_{N_r\to\infty}\frac{2N_r\int_{r_p}^{r_a}\frac{dr}{\sqrt{R}}}{N_r\cdot t_r}=\lim_{N_\theta\to\infty}\frac{2N_\theta\int_{\theta_-}^{\pi-\theta_-}\frac{d\theta}{\sqrt{\Theta}}}{N_\theta\cdot t_\theta}, \tag{4.9b}$$

where r_p and r_a are the periastron and apastron of the orbit and θ_- corresponds to the starting point of the vertical oscillation, and where $\theta_- = \arccos(z_-)$ and $\pi-\theta_- = -\arccos(z_-)$, which results in β varying from $-\pi/2$ to $\pi/2$. Hence, using Eqs. (4.3h, 4.5c) we find

$$\frac{\nu_\theta}{\nu_r}=\frac{\int_{r_p}^{r_a}\frac{dr}{\sqrt{R}}}{\int_{\theta_-}^{\pi-\theta_-}\frac{d\theta}{\sqrt{\Theta}}}=\frac{a\sqrt{1-E^2}z_+ I_8\left(\frac{\pi}{2},e,\mu,a,Q\right)}{2\cdot F\left(\frac{\pi}{2},\frac{z_-^2}{z_+^2}\right)},. \tag{4.9c}$$

TABLE 4.1: This table summarizes all the integrals solved in §4.2.1 to calculate the integrals of motion in the Kerr geometry, where the constants are given by Eqs. (4.4a-4.4l).

	Analytic solution of ϕ and t for $Q \neq 0$
	$\phi - \phi_0 = \frac{1}{2}\left(C_3 I_3 + C_4 I_4 - H_1\right);\ t - t_0 = \frac{1}{2}\left(C_5 I_5 + C_6 I_6 + C_7 I_3 + C_8 I_4 + H_2\right)$
I_1	$\int_{r_a}^{r} \frac{1}{\Delta\sqrt{R}} \frac{\partial R}{\partial L} \mathrm{d}r' = -\left[C_3 I_3 + C_4 I_4\right]$
I_2	$\int_{r_a}^{r} \frac{1}{\Delta\sqrt{R}} \frac{\partial R}{\partial E} \mathrm{d}r' = \left[C_5 I_5 + C_6 I_6 + C_7 I_3 + C_8 I_4\right]$
I_3	$\int_0^{\psi} \frac{\mathrm{d}\psi}{\left(1 + p_2^2 \sin^2\psi\right)\sqrt{1 - m^2\sin^2\psi}\sqrt{1 - n^2\sin^2\psi}} = \frac{1}{\sqrt{1-m^2}\left(m^2 + p_2^2\right)}\left[m^2 F\left(\alpha, k^2\right) + p_2^2 \Pi\left(\frac{-p_2^2 - m^2}{1-m^2}, \alpha, k^2\right)\right]$, where $\sin\alpha = \frac{\sqrt{1-m^2}\sin\psi}{\sqrt{1-m^2\sin^2\psi}}$, $\psi = \frac{\chi}{2} - \frac{\pi}{2}$ and $1/r = \mu\left(1 + e\cos\chi\right)$
I_4	$\int_0^{\psi} \frac{\mathrm{d}\psi}{\left(1 + p_3^2 \sin^2\psi\right)\sqrt{1 - m^2\sin^2\psi}\sqrt{1 - n^2\sin^2\psi}} = \frac{1}{\sqrt{1-m^2}\left(m^2 + p_3^2\right)}\left[m^2 F\left(\alpha, k^2\right) + p_3^2 \Pi\left(\frac{-p_3^2 - m^2}{1-m^2}, \alpha, k^2\right)\right]$
I_5	$\int_0^{\psi} \frac{\mathrm{d}\psi}{\left(1 + p_1^2 \sin^2\psi\right)^2\sqrt{1 - m^2\sin^2\psi}\sqrt{1 - n^2\sin^2\psi}} = \frac{1}{\sqrt{1-m^2}\left(m^2 + p_1^2\right)^2}\left[m^4 F\left(\alpha, k^2\right) + 2p_1^2 m^2 \Pi\left(s^2, \alpha, k^2\right) + p_1^4 I_7\left(\alpha, e, \mu, a, Q\right)\right]$
I_6	$\int_0^{\psi} \frac{\mathrm{d}\psi}{\left(1 + p_1^2 \sin^2\psi\right)\sqrt{1 - m^2\sin^2\psi}\sqrt{1 - n^2\sin^2\psi}} = \frac{1}{\sqrt{1-m^2}\left(m^2 + p_1^2\right)}\left[m^2 F\left(\alpha, k^2\right) + p_1^2 \Pi\left(s^2, \alpha, k^2\right)\right]$
I_7	$\int_0^{\psi} \frac{\mathrm{d}\psi}{\left(1 + s^2\sin^2\psi\right)^2\sqrt{1 - k^2\sin^2\psi}} = \frac{s^4 \sin\alpha\cos\alpha\sqrt{1 - k^2\sin^2\alpha}}{2\left(1-s^2\right)\left(k^2 - s^2\right)\left(1 - s^2\sin^2\alpha\right)} + \frac{\left[s^4 - 2s^2\left(1 + k^2\right) + 3k^2\right]}{2\left(1-s^2\right)\left(k^2 - s^2\right)}\Pi\left(s^2, \alpha, k^2\right) - \frac{1}{2\left(1-s^2\right)}F\left(\alpha, k^2\right) - \frac{s^2}{2\left(1-s^2\right)\left(k^2 - s^2\right)}K\left(\alpha, k^2\right)$
I_8	$\int_{r_a}^{r} \frac{\mathrm{d}r'}{\sqrt{R}} = \frac{2\mu\left(1-e^2\right)\cdot F\left(\alpha, k^2\right)}{\sqrt{C - A + \sqrt{B^2 - 4AC}}}$
H_1	$\int_{\theta_0}^{\theta} \frac{1}{\sqrt{\Theta}} \frac{\partial\Theta}{\partial L} \mathrm{d}\theta' = \frac{2L}{z_+ a\sqrt{1-E^2}}\left\{\Pi\left(z_-^2, \arcsin\left(\frac{\cos\theta}{z_-}\right), \frac{z_-^2}{z_+^2}\right) - \Pi\left(z_-^2, \arcsin\left(\frac{\cos\theta_0}{z_-}\right), \frac{z_-^2}{z_+^2}\right) - F\left(\arcsin\left(\frac{\cos\theta}{z_-}\right), \frac{z_-^2}{z_+^2}\right) + F\left(\arcsin\left(\frac{\cos\theta_0}{z_-}\right), \frac{z_-^2}{z_+^2}\right)\right\}$
H_2	$\int_{\theta_0}^{\theta} \frac{1}{\sqrt{\Theta}} \frac{\partial\Theta}{\partial E} \mathrm{d}\theta' = \frac{2Eaz_+}{\sqrt{1-E^2}}\left\{K\left(\arcsin\left(\frac{\cos\theta}{z_-}\right), \frac{z_-^2}{z_+^2}\right) - K\left(\arcsin\left(\frac{\cos\theta_0}{z_-}\right), \frac{z_-^2}{z_+^2}\right) - F\left(\arcsin\left(\frac{\cos\theta}{z_-}\right), \frac{z_-^2}{z_+^2}\right) + F\left(\arcsin\left(\frac{\cos\theta_0}{z_-}\right), \frac{z_-^2}{z_+^2}\right)\right\}$
H_3	$\int_{\theta_0}^{\theta} \frac{\mathrm{d}\theta'}{\sqrt{\Theta}} = \frac{1}{a\sqrt{1-E^2}z_+}\left\{F\left(\arcsin\left(\frac{\cos\theta_0}{z_-}\right), \frac{z_-^2}{z_+^2}\right) - F\left(\arcsin\left(\frac{\cos\theta}{z_-}\right), \frac{z_-^2}{z_+^2}\right)\right\}$

A similar expression can also be derived using formulae given in Fujita and Hikida (2009). Again, we take a long time average of Eq. (4.1c), so that

$$\lim_{T\to\infty}\frac{t-t_0}{T}=\lim_{T\to\infty}\frac{1}{T}\left[\frac{1}{2}\int_{r_0}^{r}\frac{1}{\Delta\sqrt{R}}\frac{\partial R}{\partial E}\mathrm{d}r'+\frac{1}{2}\int_{\theta_0}^{\theta}\frac{1}{\sqrt{\Theta}}\frac{\partial\Theta}{\partial E}\mathrm{d}\theta'\right], \tag{4.10a}$$

where using the same argument, again, of large possible integer solutions, so that $N_r t_r = N_\theta t_\theta = T$ to find

$$1 = \frac{2N_r\int_{r_p}^{r_a}\frac{1}{\Delta\sqrt{R}}\frac{\partial R}{\partial E}\mathrm{d}r'}{2N_r t_r}+\frac{2N_\theta\int_{\theta_-}^{\pi-\theta_-}\frac{1}{\sqrt{\Theta}}\frac{\partial\Theta}{\partial E}\mathrm{d}\theta'}{2N_\theta t_\theta}=\nu_r I_2+\nu_\theta H_2, \tag{4.10b}$$

which gives

$$\nu_r\left(e,\mu,a,Q\right) = \frac{1}{I_2\left(\frac{\pi}{2},e,\mu,a,Q\right)+\frac{\nu_\theta}{\nu_r}H_2\left(-\frac{\pi}{2},\frac{\pi}{2},e,\mu,a,Q\right)}, \tag{4.10c}$$

$$\nu_\theta\left(e,\mu,a,Q\right) = \frac{1}{\frac{\nu_r}{\nu_\theta}I_2\left(\frac{\pi}{2},e,\mu,a,Q\right)+H_2\left(-\frac{\pi}{2},\frac{\pi}{2},e,\mu,a,Q\right)}. \tag{4.10d}$$

The limits of integral I_2 are $\alpha=\{0,\pi/2\}$, and that of H_2 are $\beta_0=\{\pi/2,-\pi/2\}$. The substitution of $H_2\left(-\frac{\pi}{2},\frac{\pi}{2},e,\mu,a,Q\right)$ and $\frac{\nu_\theta}{\nu_r}$ from Eqs. (4.5b) and (4.9c) in the above equations give

$$\nu_r\left(e,\mu,a,Q\right)=\frac{F\left(\frac{\pi}{2},\frac{z_-^2}{z_+^2}\right)}{\left\{\begin{array}{r}\left[I_2\left(\frac{\pi}{2},e,\mu,a,Q\right)+2a^2z_+^2EI_8\left(\frac{\pi}{2},e,\mu,a,Q\right)\right]F\left(\frac{\pi}{2},\frac{z_-^2}{z_+^2}\right)\\ -2a^2z_+^2EI_8\left(\frac{\pi}{2},e,\mu,a,Q\right)K\left(\frac{\pi}{2},\frac{z_-^2}{z_+^2}\right)\end{array}\right\}}, \tag{4.11a}$$

$$\nu_\theta\left(e,\mu,a,Q\right)=\frac{a\sqrt{1-E^2}z_+I_8\left(\frac{\pi}{2},e,\mu,a,Q\right)}{2\left\{\begin{array}{r}\left[I_2\left(\frac{\pi}{2},e,\mu,a,Q\right)+2a^2z_+^2EI_8\left(\frac{\pi}{2},e,\mu,a,Q\right)\right]F\left(\frac{\pi}{2},\frac{z_-^2}{z_+^2}\right)\\ -2a^2z_+^2EI_8\left(\frac{\pi}{2},e,\mu,a,Q\right)K\left(\frac{\pi}{2},\frac{z_-^2}{z_+^2}\right)\end{array}\right\}}. \tag{4.11b}$$

Similarly, taking the long time average of Eq. (4.1b) and the substitution of H_1 and H_2 from Eqs. (4.5a) and (4.5b) yields

$$\nu_\phi\left(e,\mu,a,Q\right)=\frac{\left\{\begin{array}{r}\left[-I_1\left(\frac{\pi}{2},e,\mu,a,Q\right)-2LI_8\left(\frac{\pi}{2},e,\mu,a,Q\right)\right]F\left(\frac{\pi}{2},\frac{z_-^2}{z_+^2}\right)\\ +2LI_8\left(\frac{\pi}{2},e,\mu,a,Q\right)\Pi\left(z_-^2,\frac{\pi}{2},\frac{z_-^2}{z_+^2}\right)\end{array}\right\}}{2\pi\left\{\begin{array}{r}\left[I_2\left(\frac{\pi}{2},e,\mu,a,Q\right)+2a^2z_+^2EI_8\left(\frac{\pi}{2},e,\mu,a,Q\right)\right]F\left(\frac{\pi}{2},\frac{z_-^2}{z_+^2}\right)\\ -2a^2z_+^2EI_8\left(\frac{\pi}{2},e,\mu,a,Q\right)K\left(\frac{\pi}{2},\frac{z_-^2}{z_+^2}\right)\end{array}\right\}},\tag{4.11c}$$

where I_1, I_2, and I_8 are given by Eqs. (4.3a)-(4.3g) and (4.3h). Hence, the fundamental frequencies are explicit functions of input parameters (e, μ, a, Q), which can be chosen using the bound orbit conditions, Eq. (4.8), presented in §4.2.2. These dimensionless frequency formulae also match with the quadrature formulae derived in Schmidt (2002); but here we have explicitly solved the integrals I_1, I_2, and I_8 in §4.2.1. The frequency formulae with dimensions are summarized in Table 4.2.

4.4 Equatorial and eccentric bound orbits ($e \neq 0$, $Q = 0$)

In this section, we reduce the integrals of motion, Eqs. (4.6a, 4.6b), to the case of eccentric and equatorial trajectories, where $Q = 0$ ($\theta = \pi/2$). We show that the forms derived in §4.2.1 reduce to very compact expressions of (ϕ, t) involving trigonometric functions and elliptic integrals for the equatorial eccentric orbits. We implement the limit, $Q \to 0$ which leads to $A \to 0$, Eq. (6.8c), and reduces the factors $(1 + x_1)$, $A\,(1 + x_2)$, using Eq. (4.4l), to

$$(1+x_1)\to\left(1-\frac{C}{B}\right),\ \text{and}\ A\,(1+x_2)\to -B,\tag{4.12a}$$

TABLE 4.2: This table summarizes the fundamental frequency formulae (with dimensions) derived using the long time average method in the Kerr geometry. The explicit expressions for integrals I_1, I_2, and I_8 are summarized in Table 4.1.

	Analytic form
$\nu_r\,(e,\mu,a,Q)$	$\frac{c^3 F\left(\frac{\pi}{2},\frac{z_-^2}{z_+^2}\right)}{GM\left\{\left[I_2\left(\frac{\pi}{2},e,\mu,a,Q\right)+2EI_8\left(\frac{\pi}{2},e,\mu,a,Q\right)\right]F\left(\frac{\pi}{2},\frac{z_-^2}{z_+^2}\right)-2a^2z_+^2EI_8\left(\frac{\pi}{2},e,\mu,a,Q\right)K\left(\frac{\pi}{2},\frac{z_-^2}{z_+^2}\right)\right\}}$
$\nu_\theta\,(e,\mu,a,Q)$	$\frac{c^3a\sqrt{1-E^2}z_+I_8\left(\frac{\pi}{2},e,\mu,a,Q\right)}{2GM\left\{\left[I_2\left(\frac{\pi}{2},e,\mu,a,Q\right)+2EI_8\left(\frac{\pi}{2},e,\mu,a,Q\right)\right]F\left(\frac{\pi}{2},\frac{z_-^2}{z_+^2}\right)-2a^2z_+^2EI_8\left(\frac{\pi}{2},e,\mu,a,Q\right)K\left(\frac{\pi}{2},\frac{z_-^2}{z_+^2}\right)\right\}}$
$\nu_\phi\,(e,\mu,a,Q)$	$\frac{c^3\left\{\left[-I_1\left(\frac{\pi}{2},e,\mu,a,Q\right)-2LI_8\left(\frac{\pi}{2},e,\mu,a,Q\right)\right]F\left(\frac{\pi}{2},\frac{z_-^2}{z_+^2}\right)+2LI_8\left(\frac{\pi}{2},e,\mu,a,Q\right)\Pi\left(z_-^2,\frac{\pi}{2},\frac{z_-^2}{z_+^2}\right)\right\}}{2\pi GM\left\{\left[I_2\left(\frac{\pi}{2},e,\mu,a,Q\right)+2EI_8\left(\frac{\pi}{2},e,\mu,a,Q\right)\right]F\left(\frac{\pi}{2},\frac{z_-^2}{z_+^2}\right)-2a^2z_+^2EI_8\left(\frac{\pi}{2},e,\mu,a,Q\right)K\left(\frac{\pi}{2},\frac{z_-^2}{z_+^2}\right)\right\}}$

which gives

$$A\,(1+x_1)\,(1+x_2)=A-B+C=\mu\left(1-e^2\right)^2\left[1-\mu^2x^2\left(3-e^2-2e\right)\right], \quad (4.12b)$$

where the translation equation given by Eq. (3.17a) for $Q=0$ is used to substitute for E^2. Also, m^2 and n^2 reduce to

$$m^2=\frac{2B}{B-C}=\frac{4\mu^2ex^2}{\left[1-\mu^2x^2\left(3-e^2-2e\right)\right]}, \quad n^2=\frac{4AB^2}{2B^2\left(A-B\right)+2AC}=0. \quad (4.12c)$$

The substitution of these reduced expressions of m^2 and n^2 further simplifies the integrals I_3, I_4, I_5, and I_6, as shown in Appendix A.2, which finally yields the expressions for azimuthal angle and time coordinate for equatorial trajectories to

be given by

$$\phi - \phi_0 = -\frac{1}{2} I_1 = a_1 \Pi\left(-p_2^2, \psi, m^2\right) + b_1 \Pi\left(-p_3^2, \psi, m^2\right), \tag{4.13a}$$

$$\begin{aligned} t - t_0 = \frac{1}{2} I_2 &= a_2 I_5 + b_2 I_6 + c_2 I_3 + d_2 I_4, \\ &= a_2 \left[\frac{p_1^4 \sin\psi \cos\psi \sqrt{1 - m^2 \sin^2\psi}}{2\left(1 + p_1^2\right)\left(m^2 + p_1^2\right)\left(1 + p_1^2 \sin^2\psi\right)} - \frac{F\left(\psi, m^2\right)}{2\left(1 + p_1^2\right)} + \frac{p_1^2 K\left(\psi, m^2\right)}{2\left(1 + p_1^2\right)\left(m^2 + p_1^2\right)} \right] \\ &+ \Pi\left(-p_1^2, \psi, m^2\right) \left\{ a_2 \frac{\left[p_1^4 + 2p_1^2\left(1 + m^2\right) + 3m^2\right]}{2\left(1 + p_1^2\right)\left(m^2 + p_1^2\right)} + b_2 \right\} + c_2 \Pi\left(-p_2^2, \psi, m^2\right) \\ &+ d_2 \Pi\left(-p_3^2, \psi, m^2\right), \end{aligned} \tag{4.13b}$$

where the substitution of Eq. (4.12b) into Eqs. (4.4a-4.4e) yields the reduced forms of the constants given by

$$a_1 = \frac{C_3}{2} = \frac{\mu^{1/2}\left[La^2 - 2xr_+\right]}{\sqrt{1 - a^2}\left(a^2\mu - a^2\mu e - r_+\right)\sqrt{1 - \mu^2 x^2\left(3 - e^2 - 2e\right)}}, \tag{4.13c}$$

$$b_1 = \frac{C_4}{2} = \frac{\mu^{1/2}\left[-La^2 + 2xr_-\right]}{\sqrt{1 - a^2}\left(a^2\mu - a^2\mu e - r_-\right)\sqrt{1 - \mu^2 x^2\left(3 - e^2 - 2e\right)}}, \tag{4.13d}$$

$$a_2 = \frac{C_5}{2} = \frac{2E}{\mu^{3/2}\left(1 - e\right)^2\sqrt{1 - \mu^2 x^2\left(3 - e^2 - 2e\right)}}, \tag{4.13e}$$

$$b_2 = \frac{C_6}{2} = \frac{4E}{\mu^{1/2}\left(1 - e\right)\sqrt{1 - \mu^2 x^2\left(3 - e^2 - 2e\right)}}, \tag{4.13f}$$

$$c_2 = \frac{C_7}{2} = \frac{2a^2\mu^{1/2}\left(-La + 2Er_-\right)}{r_-\sqrt{\left[1 - \mu^2 x^2\left(3 - e^2 - 2e\right)\right]\left(1 - a^2\right)}\left(a^2\mu - a^2\mu e - r_+\right)}, \tag{4.13g}$$

$$d_2 = \frac{C_8}{2} = \frac{2a\mu^{1/2}\left(-2Lr_-\sqrt{1 - a^2} - 2Er_-a + La^2\right)}{r_-\sqrt{\left[1 - \mu^2 x^2\left(3 - e^2 - 2e\right)\right]\left(1 - a^2\right)}\left(a^2\mu - a^2\mu e - r_-\right)}. \tag{4.13h}$$

The corresponding fundamental frequency formulae for the equatorial trajectories are

$$\nu_\phi\left(e, \mu, a\right) = \frac{c^3 \cdot \left[\phi\left(\psi = \pi/2\right) - \phi_0\right]}{2\pi GM \cdot \left[t\left(\psi = \pi/2\right) - t_0\right]}, \tag{4.14a}$$

$$\nu_r\left(e, \mu, a\right) = \frac{c^3}{GM \cdot t_r} = \frac{c^3}{2GM \cdot \left[t\left(\psi = \pi/2\right) - t_0\right]}, \tag{4.14b}$$

$$\nu_\theta\left(e, \mu, a\right) = \frac{2\nu_r\left(e, \mu, a\right)\mu^{1/2}\sqrt{\left(x^2 + a^2 + 2aEx\right)} \cdot F\left(\frac{\pi}{2}, m^2\right)}{\pi\left[1 - \mu^2 x^2\left(3 - e^2 - 2e\right)\right]^{1/2}}, \tag{4.14c}$$

TABLE 4.3: This table summarizes the trajectory formulae and fundamental frequency formulae for the equatorial and eccentric bound orbits in the Kerr geometry.

	Analytic form
$\phi-\phi_0$	$-\frac{1}{2}I_1 = a_1\Pi\left(-p_2^2,\psi,m^2\right)+b_1\Pi\left(-p_3^2,\psi,m^2\right)$
$t-t_0$	$= \frac{1}{2}I_2 = a_2 I_5 + b_2 I_6 + c_2 I_3 + d_2 I_4,$ $= a_2\left[\frac{p_1^4\sin\psi\cos\psi\sqrt{1-m^2\sin^2\psi}}{2\left(1+p_1^2\right)\left(m^2+p_1^2\right)\left(1+p_1^2\sin^2\psi\right)} - \frac{F\left(\psi,m^2\right)}{2\left(1+p_1^2\right)} + \frac{p_1^2 K\left(\psi,m^2\right)}{2\left(1+p_1^2\right)\left(m^2+p_1^2\right)}\right] + d_2\Pi\left(-p_3^2,\psi,m^2\right)$ $+\Pi\left(-p_1^2,\psi,m^2\right)\left\{a_2\frac{\left[p_1^4+2p_1^2\left(1+m^2\right)+3m^2\right]}{2\left(1+p_1^2\right)\left(m^2+p_1^2\right)}+b_2\right\}+c_2\Pi\left(-p_2^2,\psi,m^2\right)$
$\nu_\phi\left(e,\mu,a\right)$	$= \frac{c^3\cdot[\phi(\psi=\pi/2)-\phi_0]}{2\pi GM\cdot[t(\psi=\pi/2)-t_0]}$
$\nu_r\left(e,\mu,a\right)$	$= \frac{c^3}{GM\cdot t_r} = \frac{c^3}{2GM\cdot[t(\psi=\pi/2)-t_0]}$
$\nu_\theta\left(e,\mu,a\right)$	$= \frac{2\nu_r(e,\mu,a)\mu^{1/2}\sqrt{(x^2+a^2+2aEx)}\cdot F\left(\frac{\pi}{2},m^2\right)}{\pi[1-\mu^2x^2(3-e^2-2e)]^{1/2}}$

where $\nu_r\left(e,\mu,a\right)$ is given by Eq. (4.14b) and m^2 is given by Eq. (4.12c). See Appendix A.2 for the derivation of $\nu_\theta\left(e,\mu,a\right)$ for the equatorial and eccentric bound orbits.

These compact expressions, Eqs. (4.13, 4.14), for the equatorial eccentric trajectories have their importance in various astrophysical studies, in addition to, gyroscope precession and phase space studies. The trajectory and fundamental frequency formulae derived in this section are summarized in Table 4.3.

4.5 Spherical orbits ($e = 0$, $Q \neq 0$)

Spherical orbits are the non-equatorial counterparts of circular orbits and set a crucial signpost in the dynamical study of non-equatorial and separatrix trajectories. In this section, we first deduce the expressions of E and L for the spherical orbits as functions of the radius of the spherical orbit, r_s, and (a, Q). We then reduce the general trajectory solution, Eq. (4.6), to the spherical orbit case, and also write the analytic form of the fundamental frequencies for spherical trajectories.

4.5.1 Energy and angular momentum of spherical orbits

The exact expressions for energy and angular momentum for the spherical orbits can be derived by substituting $e = 0$ and $\mu = 1/r_s$, where r_s is the radius of the orbit, in the expressions for E, L, and x given by Eqs. (3.17a-3.17e), which yields

$$E = \frac{\left\{ \begin{array}{r} 2a^4 Q + (r_s - 3)(r_s - 2)^2 r_s^4 - a^2 r_s \left[r_s^2 (3r_s - 5) + Q (r_s (r_s - 4) + 5) \right] \\ - 2a \left[r_s (r_s - 2) + a^2 \right] \sqrt{a^2 Q^2 - r_s^3 Q (r_s - 3) + r_s^5} \end{array} \right\}^{1/2}}{r_s^2 \left[r_s (r_s - 3)^2 - 4a^2 \right]^{1/2}}, \tag{4.15a}$$

$$x = \frac{\left\{ \begin{array}{r} -2a^4 Q + r_s^2 (r_s - 3) \left[r_s^2 - (r_s - 3) Q \right] + a^2 r_s (r_s^3 + r_s^2 - 2Q r_s + 8Q) \\ - 2a \left[r_s (r_s - 2) + a^2 \right] \sqrt{a^2 Q^2 - r_s^3 Q (r_s - 3) + r_s^5} \end{array} \right\}^{1/2}}{r_s^{1/2} \left[r_s (r_s - 3)^2 - 4a^2 \right]^{1/2}}, \tag{4.15b}$$

and

$$L = x + aE. \tag{4.15c}$$

Similar formulae were derived in terms of inclination angle using an approximation in Grossman *et al.* (2012), whereas we have written the exact form in terms of the fundamental parameters and constant of motion Q. These formulae reduce to the energy and angular momentum formulae for circular orbits when $Q = 0$ is

substituted (Bardeen *et al.* 1972):

$$E = \frac{r_c^2 - 2r_c + a\sqrt{r_c}}{r_c\left(r_c^2 - 3r_c + 2a\sqrt{r_c}\right)^{1/2}}, \quad L = \frac{\sqrt{r_c}\left(r_c^2 - 2a\sqrt{r_c} + a^2\right)}{r_c\left(r_c^2 - 3r_c + 2a\sqrt{r_c}\right)^{1/2}}. \tag{4.16}$$

4.5.2 Trajectory solution for spherical orbits

Here, we derive the reduced form of the integrals of motion for the spherical trajectories. Rewriting the integral form of the trajectory solution (r, ϕ, θ, t), Eq. (4.1b-4.1d),

$$\phi - \phi_0 = -\frac{1}{2}\int_{r_0}^{r} \frac{1}{\Delta\sqrt{R}}\frac{\partial R}{\partial L}\mathrm{d}r^{'} - \frac{1}{2}\int_{\theta_0}^{\theta} \frac{1}{\sqrt{\Theta}}\frac{\partial \Theta}{\partial L}\mathrm{d}\theta^{'} = -\frac{1}{2}I_1 - \frac{1}{2}H_1, \tag{4.17a}$$

$$t - t_0 = \frac{1}{2}\int_{r_0}^{r} \frac{1}{\Delta\sqrt{R}}\frac{\partial R}{\partial E}\mathrm{d}r^{'} + \frac{1}{2}\int_{\theta_0}^{\theta} \frac{1}{\sqrt{\Theta}}\frac{\partial \Theta}{\partial E}\mathrm{d}\theta^{'} = \frac{1}{2}I_2 + \frac{1}{2}H_2, \tag{4.17b}$$

$$\int_{r_0}^{r} \frac{\mathrm{d}r^{'}}{\sqrt{R}} = \int_{\theta_0}^{\theta} \frac{\mathrm{d}\theta^{'}}{\sqrt{\Theta}} \Rightarrow I_8 = H_3, \tag{4.17c}$$

where R and Θ are defined by Eqs. (4.1e) and (4.1f) respectively.

From Eq. (4.17c), we have

$$\frac{\mathrm{d}r^{'}}{\sqrt{R}} = \frac{\mathrm{d}\theta^{'}}{\sqrt{\Theta}}; \tag{4.18}$$

the substitution of the above equation into Eqs. (4.17a, 4.17b) for the spherical orbits reduces the expressions of the azimuthal angle and coordinate time to

$$\phi - \phi_0 = -\frac{1}{2}\left[\frac{1}{\Delta}\frac{\partial R}{\partial L}H_3 + H_1\right], \quad t - t_0 = \frac{1}{2}\left[\frac{1}{\Delta}\frac{\partial R}{\partial E}H_3 + H_2\right]. \tag{4.19}$$

Since, $r = r_s$ is a constant for the spherical orbits, the expressions of $\frac{1}{\Delta}\frac{\partial R}{\partial L}$ and $\frac{1}{\Delta}\frac{\partial R}{\partial E}$ can be written as

$$\frac{1}{\Delta}\frac{\partial R}{\partial L} = \frac{2\left(2Lr_s - Lr_s^2 - 2r_s aE\right)}{\Delta}, \quad \frac{1}{\Delta}\frac{\partial R}{\partial E} = \frac{2\left[E\left(a^2r_s^2 + r_s^4 + 2a^2r_s\right) - 2Lar_s\right]}{\Delta}, \tag{4.20}$$

where the θ integrals H_1, H_2, and H_3 have been previously derived, and they are given by Eq. (4.5) (Fujita and Hikida 2009). Hence, the substitution of Eqs. (4.20, 4.5) into Eq. (4.19) yields the expressions of $(\phi-\phi_0,\, t-t_0)$ for the spherical orbits, given by

$$\begin{aligned}\phi-\phi_0 = \quad & \frac{1}{a\sqrt{1-E^2}z_+}\left\{\frac{(a^2L-2aEr_s)}{\Delta}\left[F\left(\arcsin\left(\frac{\cos\theta}{z_-}\right),\frac{z_-^2}{z_+^2}\right)\right.\right. \\ & \left.-F\left(\arcsin\left(\frac{\cos\theta_0}{z_-}\right),\frac{z_-^2}{z_+^2}\right)\right]-L\left[\Pi\left(z_-^2,\arcsin\left(\frac{\cos\theta}{z_-}\right),\frac{z_-^2}{z_+^2}\right)\right. \\ & \left.\left.-\Pi\left(z_-^2,\arcsin\left(\frac{\cos\theta_0}{z_-}\right),\frac{z_-^2}{z_+^2}\right)\right]\right\}, \qquad (4.21a)\end{aligned}$$

$$\begin{aligned}t-t_0 = \quad & \frac{1}{a\sqrt{1-E^2}z_+}\left\{Ea^2z_+^2\left[K\left(\arcsin\left(\frac{\cos\theta}{z_-}\right),\frac{z_-^2}{z_+^2}\right)-K\left(\arcsin\left(\frac{\cos\theta_0}{z_-}\right),\frac{z_-^2}{z_+^2}\right)\right]\right. \\ & +\left[F\left(\arcsin\left(\frac{\cos\theta_0}{z_-}\right),\frac{z_-^2}{z_+^2}\right)-F\left(\arcsin\left(\frac{\cos\theta}{z_-}\right),\frac{z_-^2}{z_+^2}\right)\right]\cdot \\ & \left.\left[Ea^2z_+^2+\frac{E\left(a^2r_s^2+r_s^4+2a^2r_s\right)-2Lar_s}{\Delta}\right]\right\}. \qquad (4.21b)\end{aligned}$$

4.5.3 Fundamental frequencies of spherical trajectories

The closed forms for fundamental frequencies associated with the non-equatorial eccentric bound trajectories have been previously derived, and they are given by Eq. (4.11) (Schmidt 2002). We first reduce the common denominator of these expressions to the case of spherical orbits. If we take $I_8\left(e,\mu,a,Q\right)$ outside from the denominator of Eqs. (4.11a-4.11c), it gives

$$\begin{aligned}\left[\left(I_2+2a^2z_+^2EI_8\right)F\left(\frac{\pi}{2},\frac{z_-^2}{z_+^2}\right)-2a^2z_+^2EI_8K\left(\frac{\pi}{2},\frac{z_-^2}{z_+^2}\right)\right] = I_8\left[\left(\frac{I_2}{I_8}+2a^2z_+^2E\right)\cdot\right. \\ \left.F\left(\frac{\pi}{2},\frac{z_-^2}{z_+^2}\right)-2a^2z_+^2EK\left(\frac{\pi}{2},\frac{z_-^2}{z_+^2}\right)\right], \qquad (4.22)\end{aligned}$$

where by definition $I_2/I_8 = \frac{1}{\Delta}\frac{\partial R}{\partial E}$ for spherical orbits which is given by Eq. (4.20). Hence, Eqs. (4.22), (4.20) and (4.11b) combine to give the vertical oscillation frequency for the spherical orbits

$$\nu_\theta\left(r_s,a,Q\right)=\frac{a\sqrt{1-E^2}z_+}{4\left\{\left[\frac{\left[E\left(a^2r_s^2+r_s^4+2a^2r_s\right)-2Lar_s\right]}{\Delta}+a^2z_+^2E\right]F\left(\frac{\pi}{2},\frac{z_-^2}{z_+^2}\right)-a^2z_+^2EK\left(\frac{\pi}{2},\frac{z_-^2}{z_+^2}\right)\right\}}. \tag{4.23}$$

Next using Eq. (4.22), the azimuthal frequency, Eq. (4.11c), can be written as

$$\nu_\phi\left(r_s,a,Q\right)=\frac{\left\{\left[-\frac{I_1}{I_8}-2L\right]F\left(\frac{\pi}{2},\frac{z_-^2}{z_+^2}\right)+2L\cdot\Pi\left(z_-^2,\frac{\pi}{2},\frac{z_-^2}{z_+^2}\right)\right\}}{4\pi\left\{\left[\frac{\left[E\left(a^2r_s^2+r_s^4+2a^2r_s\right)-2Lar_s\right]}{\Delta}+a^2z_+^2E\right]F\left(\frac{\pi}{2},\frac{z_-^2}{z_+^2}\right)-a^2z_+^2EK\left(\frac{\pi}{2},\frac{z_-^2}{z_+^2}\right)\right\}}, \tag{4.24a}$$

where $I_1/I_8 = \frac{1}{\Delta}\frac{\partial R}{\partial L}$, which is given by Eq. (4.20). Hence, the azimuthal frequency for the spherical orbits is given by

$$\nu_\phi\left(r_s,a,Q\right)=\frac{\left\{\left[-\frac{\left(2Lr_s-Lr_s^2-2r_saE\right)}{\Delta}-L\right]F\left(\frac{\pi}{2},\frac{z_-^2}{z_+^2}\right)+L\cdot\Pi\left(z_-^2,\frac{\pi}{2},\frac{z_-^2}{z_+^2}\right)\right\}}{2\pi\left\{\left[\frac{\left[E\left(a^2r_s^2+r_s^4+2a^2r_s\right)-2Lar_s\right]}{\Delta}+a^2z_+^2E\right]F\left(\frac{\pi}{2},\frac{z_-^2}{z_+^2}\right)-a^2z_+^2EK\left(\frac{\pi}{2},\frac{z_-^2}{z_+^2}\right)\right\}}. \tag{4.24b}$$

Similarly, the radial oscillation frequency, Eq. (4.11a), can be written for the spherical orbits by using Eq. (4.22) as

$$\nu_r\left(r_s,a,Q\right)=\frac{F\left(\frac{\pi}{2},\frac{z_-^2}{z_+^2}\right)}{2I_8\left\{\left[\frac{\left[E\left(a^2r_s^2+r_s^4+2a^2r_s\right)-2Lar_s\right]}{\Delta}+a^2z_+^2E\right]F\left(\frac{\pi}{2},\frac{z_-^2}{z_+^2}\right)-a^2z_+^2EK\left(\frac{\pi}{2},\frac{z_-^2}{z_+^2}\right)\right\}}, \tag{4.25a}$$

where for spherical orbits integral I_8 reduces to a constant as shown below.

We see that the expression for k^2, Eq. (4.4j), reduces to zero for spherical orbits ($e = 0$), because we see from Eq. (6.8c,6.8e) that $A = B = 0$. Hence, from Eq.

(4.3h), $I_8\left(\alpha=\pi/2, e=0, \mu=1/r_s, a, Q\right)$ reduces to

$$I_8 = \frac{2\mu}{\sqrt{C}} F\left(\frac{\pi}{2}, k^2=0\right) = \frac{\pi r_s}{\sqrt{r_s^4\left(1-E^2\right)+\left(3Qa^2-2x^2r_s-2Qr_s\right)}}. \tag{4.25b}$$

Hence, the radial oscillation frequency, Eq. (4.25a), for spherical orbits reduces to

$$\nu_r\left(r_s, a, Q\right) = \frac{\sqrt{r_s^4\left(1-E^2\right)+\left(3Qa^2-2x^2r_s-2Qr_s\right)}\cdot F\left(\frac{\pi}{2}, \frac{z_-^2}{z_+^2}\right)}{2\pi r_s\left\{\left[\frac{\left[E\left(a^2r_s^2+r_s^4+2a^2r_s\right)-2Lar_s\right]}{\Delta}+a^2z_+^2E\right]F\left(\frac{\pi}{2}, \frac{z_-^2}{z_+^2}\right)-a^2z_+^2EK\left(\frac{\pi}{2}, \frac{z_-^2}{z_+^2}\right)\right\}}. \tag{4.25c}$$

The analytic formulae of (E, L), the trajectory solution, and the fundamental frequencies for the spherical orbits are together summarized in Table 4.4.

4.6 Non-equatorial separatrix trajectories

The separatrix orbits have been studied for the equatorial plane around a Kerr black hole (Perez-Giz and Levin 2009; Levin and Perez-Giz 2009). They have been shown as homoclinic orbits that asymptote to an energetically bound and unstable circular orbit. Here, we discuss the non-equatorial counterpart of these separatrix trajectories where these orbits asymptote to an energetically bound, unstable spherical orbit. These non-equatorial homoclinic trajectories are critical in calculating the evolution of test objects transiting from inspiral to plunge, which is not always confined to the equatorial plane, as in EMRIs emitting gravitational radiation.

In this section, we derive the exact expressions for the conic parameters (e, μ) for non-equatorial separatrix orbits as a function of the radius of the corresponding

TABLE 4.4: This table summarizes (E, L) formulae, the trajectory formulae, and the fundamental frequency formulae for the spherical orbits in the Kerr geometry.

	Analytic form
E	$\frac{\left\{\begin{array}{r} 2a^4Q+(r_s-3)(r_s-2)^2 r_s^4-a^2r_s\left[r_s^2(3r_s-5)+Q(r_s(r_s-4)+5)\right] \\ -2a\left[r_s(r_s-2)+a^2\right]\sqrt{a^2Q^2-r_s^3Q(r_s-3)+r_s^5}\end{array}\right\}^{1/2}}{r_s^2\left[r_s(r_s-3)^2-4a^2\right]^{1/2}}$
L	$x=\frac{\left\{\begin{array}{r} -2a^4Q+r_s^2(r_s-3)\left[r_s^2-(r_s-3)Q\right]+a^2r_s(r_s^3+r_s^2-2Qr_s+8Q) \\ -2a\left[r_s(r_s-2)+a^2\right]\sqrt{a^2Q^2-r_s^3Q(r_s-3)+r_s^5}\end{array}\right\}^{1/2}}{r_s^{1/2}\left[r_s(r_s-3)^2-4a^2\right]^{1/2}}$, $L=x+aE$
$\phi-\phi_0$	$\frac{1}{a\sqrt{1-E^2}z_+}\left\{\frac{(a^2L-2aEr_s)}{\Delta}\left[F\left(\arcsin\left(\frac{\cos\theta}{z_-}\right),\frac{z_-^2}{z_+^2}\right)-F\left(\arcsin\left(\frac{\cos\theta_0}{z_-}\right),\frac{z_-^2}{z_+^2}\right)\right]\right.$ $\left.-L\left[\Pi\left(z_-^2,\arcsin\left(\frac{\cos\theta}{z_-}\right),\frac{z_-^2}{z_+^2}\right)-\Pi\left(z_-^2,\arcsin\left(\frac{\cos\theta_0}{z_-}\right),\frac{z_-^2}{z_+^2}\right)\right]\right\}$
$t-t_0$	$\frac{1}{a\sqrt{1-E^2}z_+}\left\{Ea^2z_+^2\left[K\left(\arcsin\left(\frac{\cos\theta}{z_-}\right),\frac{z_-^2}{z_+^2}\right)-K\left(\arcsin\left(\frac{\cos\theta_0}{z_-}\right),\frac{z_-^2}{z_+^2}\right)\right]\right.$ $\left.+\left[F\left(\arcsin\left(\frac{\cos\theta_0}{z_-}\right),\frac{z_-^2}{z_+^2}\right)-F\left(\arcsin\left(\frac{\cos\theta}{z_-}\right),\frac{z_-^2}{z_+^2}\right)\right]\left[Ea^2z_+^2+\frac{E(a^2r_s^2+r_s^4+2a^2r_s)-2Lar_s}{\Delta}\right]\right\}$,
$\nu_\phi(r_s,a,Q)$	$\frac{\left\{\left[-\frac{(2Lr_s-Lr_s^2-2r_saE)}{\Delta}-L\right]F\left(\frac{\pi}{2},\frac{z_-^2}{z_+^2}\right)+L\cdot\Pi\left(z_-^2,\frac{\pi}{2},\frac{z_-^2}{z_+^2}\right)\right\}}{2\pi\left\{\left[\frac{\left[E(a^2r_s^2+r_s^4+2a^2r_s)-2Lar_s\right]}{\Delta}+a^2z_+^2E\right]F\left(\frac{\pi}{2},\frac{z_-^2}{z_+^2}\right)-a^2z_+^2EK\left(\frac{\pi}{2},\frac{z_-^2}{z_+^2}\right)\right\}}$
$\nu_r(r_s,a,Q)$	$\frac{\sqrt{r_s^4(1-E^2)+(3Qa^2-2x^2r_s-2Qr_s)}\cdot F\left(\frac{\pi}{2},\frac{z_-^2}{z_+^2}\right)}{2\pi r_s\left\{\left[\frac{\left[E(a^2r_s^2+r_s^4+2a^2r_s)-2Lar_s\right]}{\Delta}+a^2z_+^2E\right]F\left(\frac{\pi}{2},\frac{z_-^2}{z_+^2}\right)-a^2z_+^2EK\left(\frac{\pi}{2},\frac{z_-^2}{z_+^2}\right)\right\}}$
$\nu_\theta(r_s,a,Q)$	$\frac{a\sqrt{1-E^2}z_+}{4\left\{\left[\frac{\left[E(a^2r_s^2+r_s^4+2a^2r_s)-2Lar_s\right]}{\Delta}+a^2z_+^2E\right]F\left(\frac{\pi}{2},\frac{z_-^2}{z_+^2}\right)-a^2z_+^2EK\left(\frac{\pi}{2},\frac{z_-^2}{z_+^2}\right)\right\}}$

spherical orbit, r_s, and (a, Q). We also show that these formulae reduce to the equatorial case, previously derived in Levin and Perez-Giz (2009), when $Q \to 0$ is applied. Next, we derive the exact analytic expressions for the non-equatorial separatrix trajectories by reducing it from the general trajectory formulae, Eqs. (4.6a-4.6c). We find that in this case, the radial part of the solutions can be reduced to a form that involves only logarithmic and trigonometric functions.

4.6.1 Exact expressions of conic variables for non-equatorial separatrix orbits

Similar to the case of the equatorial plane, the non-equatorial separatrix trajectories can be parametrized by the radius of unstable spherical orbits, r_s, for a given combination of a and Q, where r_s varies from MBSO to ISSO. The energy and angular momentum of the separatrix orbits can be determined by Eqs. (4.15a-4.15c) by varying r_s between the extrema MBSO and ISSO radii. In the (e, μ) plane, these homoclinic orbits forms the boundary (other than $e = 0$ and $e = 1$ curves) of the allowed bound orbit region defined by Eq. (4.8) for a fixed a and Q; see red curve in Fig. 4.1(a). The locus of this boundary in the (e, μ) plane is obtained when equality is applied to the inequality Eq. (4.8a), which results in

$$\left[\mu^3 a^2 Q\,(1+e)^2 + \mu^2\left(\mu a^2 Q - x^2 - Q\right)(3-e)\,(1+e) + 1\right] = 0. \tag{4.26}$$

ISSO is a homoclinic orbit with $e = 0$ and MBSO is a homoclinic orbit with $e = 1$; hence the endpoints of the separatrix curve (red curve in Fig. 4.1(a)) represents the ISSO and MBSO radii. At these endpoints, the parameter μ takes values as described below:

For ISSO, $e = 0$ for the homoclinic orbit gives $\mu = \dfrac{2r_a}{2r_p r_a} = \dfrac{1}{r_p} = \dfrac{1}{r_s}$.

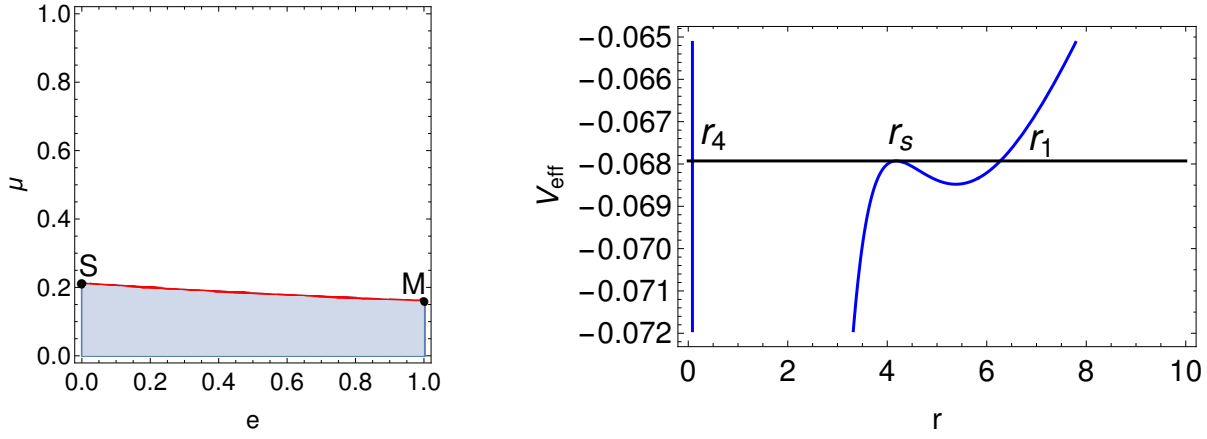

(a) (b)

FIGURE 4.1: (a) The shaded region depicts bound orbit region in the $(e,\ \mu)$ plane determined by Eqs. (4.8) for $a = 0.5$ and $Q = 5$. The red boundary of the region represents non-equatorial separatrix orbits with eccentricity of the orbit varying along the curve. The black dot represented by S corresponds to the ISSO with $(e = 0,\ \mu = 1/r_s)$, whereas M represents the MBSO with $(e = 1,\ \mu = 1/2r_s)$; (b) The effective potential, Eq. (3.3b), is shown for a non-equatorial separatrix orbit with $E = 0.92959309$, $L = 2.15349738$, $a = 0.5$, and $Q = 5$, where the horizontal line represents the total energy given by $\left(E^2 - 1\right)/2$.

For MBSO, $e = 1$ for the homoclinic orbit gives $\mu = \dfrac{1 + r_p/r_a}{2r_p} = \dfrac{1}{2r_p} = \dfrac{1}{2r_s}$.

The equations for ISSO and MBSO radii can be obtained using the equation of separatrix curve, Eq. (4.26), by plugging in $(e = 0,\ \mu = 1/r_s)$ and $(e = 1,\ \mu = 1/2r_s)$ to derive ISSO and MBSO respectively (as shown in Appendix A.3). Hence, the equations for these radii are given by

$$r_s^9 - 12r_s^8 - 6a^2r_s^7 + 36r_s^7 + 8a^2Qr_s^6 - 28a^2r_s^6 - 24a^2Qr_s^5 + 9a^4r_s^5 - 24a^4Qr_s^4 + 48a^2Qr_s^4 + 16a^4Q^2r_s^3 - 8a^4Qr_s^3 - 48a^4Q^2r_s^2 + 48a^4Q^2r_s - 16a^6Q^2 = 0, \quad (4.28)$$

for ISSO and

$$r_s^8 - 8r_s^7 - 2a^2r_s^6 + 16r_s^6 + 2a^2Qr_s^5 - 8a^2r_s^5 - 6a^2Qr_s^4 + a^4r_s^4 - 2a^4Qr_s^3 + 8a^2Qr_s^3 + a^4Q^2r_s^2 - 2a^4Qr_s^2 - 2a^4Q^2r_s + a^4Q^2 = 0. \quad (4.29)$$

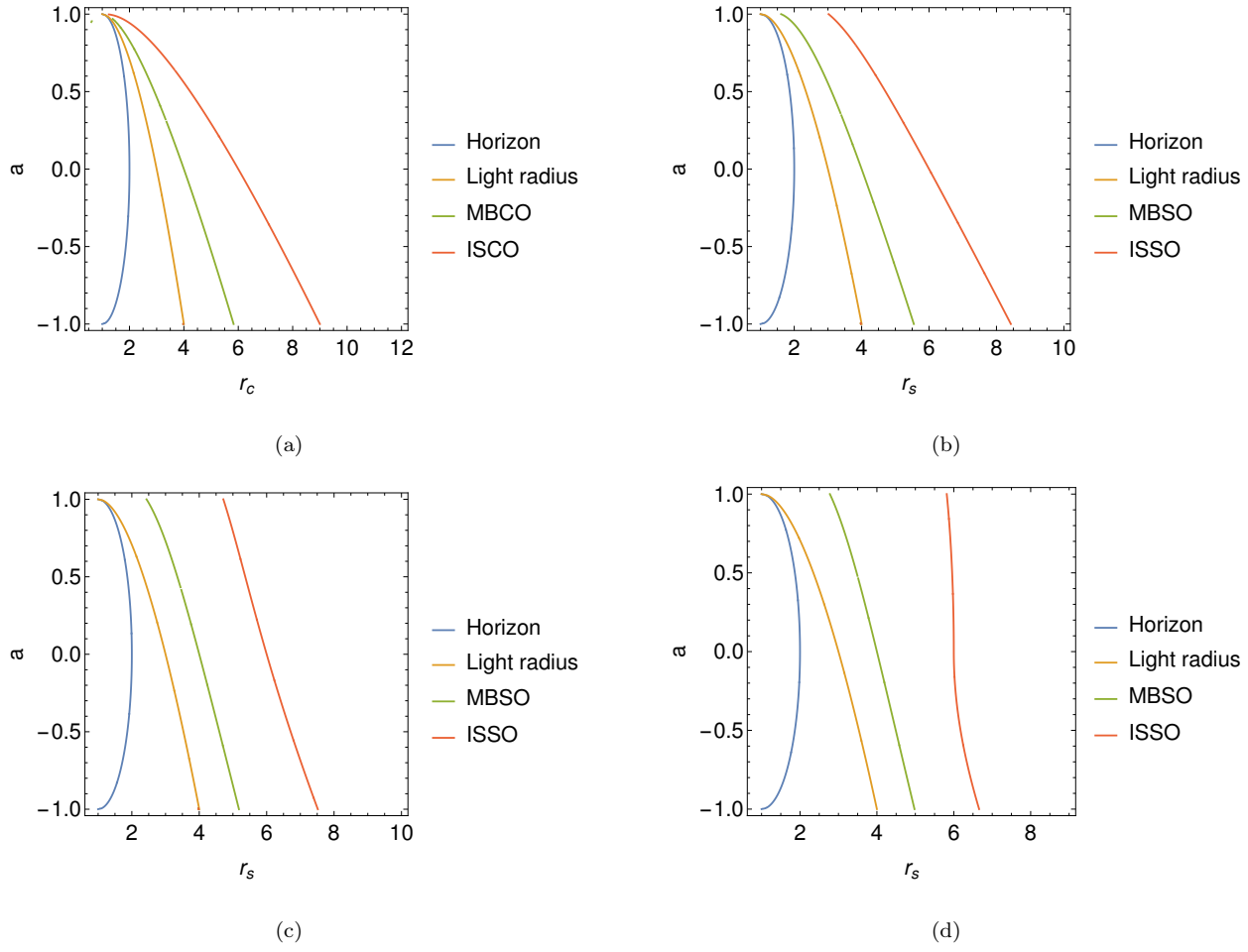

FIGURE 4.2: The contours of different important radii around the Kerr black hole in the (r_s, a) plane for (a) $Q = 0$, (b) $Q = 5$, (c) $Q = 10$, and (d) $Q = 12$.

for MBSO. The light radius for the spherical orbits can be obtained by equating the denominator of Eq. (4.15a) to zero, so that $E \to \infty$, which has the well known form for the equatorial light radius (Bardeen *et al.* 1972) given by

$$X = 2\left\{1 + \cos\left[\frac{2}{3}\arccos\left(-a\right)\right]\right\}. \tag{4.30}$$

Fig. 4.2 shows the contours of these radii in the (r_s, a) plane for various Q values.

The effective potential diagram for the non-equatorial separatrix orbits shows double roots $(r_2 = r_3)$ of $R(r)$ at the periastron of the eccentric orbit and it also represents the spherical orbit radius, r_s (see Fig 4.1(b)). One of the remaining two roots of $R(r)$ represents the apastron $(= r_1 > r_s)$ of the eccentric orbit and the

other inner root ($= r_4 < r_s$) is not the part of the bound trajectory.

Now, following a similar method used in Levin and Perez-Giz (2009), we derive the expressions for e and μ for separatrix orbits with $Q \neq 0$. We write $R(r) = 0$ in the form

$$u^4 + a^{'} u^3 + b^{'} u^2 + c^{'} u + d^{'} = 0, \tag{4.31a}$$

where $u = 1/r$ and

$$a^{'} = -\frac{2\left[x^2 + Q\right]}{a^2 Q}, \quad b^{'} = \frac{(x^2 + 2aEx + a^2 + Q)}{a^2 Q}, \quad c^{'} = -\frac{2}{a^2 Q}, \quad d^{'} = \frac{1 - E^2}{a^2 Q}. \tag{4.31b}$$

For the separatrix orbits, Eq. (4.31a) can be written as

$$(u - u_s)^2 \cdot \left[u^2 - (u_1 + u_4)\, u + u_1 u_4\right] = 0, \tag{4.32}$$

where $u_s = 1/r_s$, $u_1 = 1/r_1$ apastron of the orbit, and $u_4 = 1/r_4$ corresponds to the inner most root of $R(r)$. The comparison of u^3 and constant term of the above equation with those of Eq. (4.31a) further gives the expression

$$u_1 = \frac{1}{2}\left[-\left(a^{'} + 2u_s\right) - \sqrt{(a^{'} + 2u_s)^2 - \frac{4d^{'}}{u_s^2}}\right]. \tag{4.33}$$

The conic parameters for such an orbit are given by

$$e_s = \frac{u_s - u_1}{u_s + u_1}, \qquad \mu_s = \frac{u_s + u_1}{2}, \tag{4.34}$$

where the substitution of u_1 and $u_s = 1/r_s$ yields

$$e_s = \frac{4 + a^{'} r_s + \sqrt{(r_s a^{'} + 2)^2 - 4d^{'} r_s^4}}{-a^{'} r_s - \sqrt{(r_s a^{'} + 2)^2 - 4d^{'} r_s^4}}, \tag{4.35a}$$

$$\mu_s = \frac{1}{4r_s}\left[-a^{'} r_s - \sqrt{(r_s a^{'} + 2)^2 - 4d^{'} r_s^4}\right]; \tag{4.35b}$$

since a homoclinic orbit has the same energy and angular momentum of the unstable spherical orbit, as shown in Fig. 4.1(b); hence $a^{'}$ and $d^{'}$ can be rewritten using the formulae of E and L for the spherical orbits, Eqs. (4.15a-4.15c), to be

$$a^{'} = \frac{2\left\{\begin{array}{l} 2a^4Q - r_s^2\left(r_s-3\right)\left[r_s^2-\left(r_s-3\right)Q\right] - a^2 r_s\left(r_s^3+r_s^2-2Qr_s+8Q\right) \\ \quad + 2a\left[r_s\left(r_s-2\right)+a^2\right]\sqrt{a^2Q^2-r_s^3Q\left(r_s-3\right)+r_s^5} - Qr_s\left[r_s\left(r_s-3\right)^2-4a^2\right] \end{array}\right\}}{a^2Qr_s\left[r_s\left(r_s-3\right)^2-4a^2\right]}, \tag{4.35c}$$

$$d^{'} = \frac{\left\{\begin{array}{l} -2a^4Q - \left(r_s-3\right)\left(r_s-2\right)^2 r_s^4 + a^2 r_s\left[r_s^2\left(3r_s-5\right)+Q\left(r_s\left(r_s-4\right)+5\right)\right] \\ \quad + r_s^4\left[r_s\left(r_s-3\right)^2-4a^2\right] + 2a\left[r_s\left(r_s-2\right)+a^2\right]\sqrt{a^2Q^2-r_s^3Q\left(r_s-3\right)+r_s^5} \end{array}\right\}}{a^2Qr_s^4\left[r_s\left(r_s-3\right)^2-4a^2\right]}. \tag{4.35d}$$

These expressions reduce to the $(e,\,\mu)$ formulae for the equatorial separatrix orbits (see Appendix A.4 for the details) when the limit $Q \to 0$ is implemented, to the forms previously derived by Levin and Perez-Giz (2009):

$$e_s = -\frac{r_c^2-6r_c-3a^2+8a\sqrt{r_c}}{r_c^2+a^2-2r_c}, \quad \mu_s = \frac{r_c^2+a^2-2r_c}{4r_c\left(\sqrt{r_c}-a\right)^2}. \tag{4.36}$$

4.6.2 Exact forms for the non-equatorial separatrix trajectories

In this section, we show the reduction of our general trajectory solutions, Eqs. (4.6), for the case of separatrix orbits with $Q \neq 0$ to simple expressions. The separatrix or homoclinic orbits represent a curve in the $(e,\,\mu)$ plane for a fixed a and Q combination, Fig. 4.1, which is also the boundary of the bound orbit region defined by Eqs. (4.8). This separatrix curve is defined by Eq. (4.26), which gives us the relation

$$x^2 + Q = \frac{1+4\mu^3a^2Q\left(1+e\right)}{\mu^2\left(3-e\right)\left(1+e\right)}; \tag{4.37}$$

this further reduces the expressions of A, B, C (Eqs. (6.8c-4.4h)) and correspondingly the expressions of n^2 and m^2 to

$$n^2 = 1 \quad \text{or} \quad k^2 = 1, \tag{4.38a}$$

$$m^2 = \frac{a^2 Q\mu^3 e\,(1+e)\,(3-e)}{\left[1+2a^2\,(-1+e^2)\,Q\mu^3\right]}. \tag{4.38b}$$

The integrals governing the vertical motion (θ integrals) given by Eqs. (4.5a, 4.5b, 4.5c) retain their same form as they do not involve $k^2 = 1$, whereas, the radial integrals given by Eqs. (4.3a-4.3h) reduce further, when $k^2 = 1$ is substituted. The elliptic integrals reduce to forms involving trigonometric and logarithmic functions using the following identities given here

$$\Pi\left(q^2, \alpha, 1\right) = \frac{1}{1-q^2}\left[\ln\left(\tan\alpha + \sec\alpha\right) - q\,\ln\sqrt{\frac{1+q\sin\alpha}{1-q\sin\alpha}}\right], \text{where } q^2 > 0,\ q^2 \neq 1,$$

$$= \frac{1}{1-q^2}\left[\ln\left(\tan\alpha + \sec\alpha\right) + \mid q \mid \tan^{-1}\left(\mid q \mid \sin\alpha\right)\right], \text{ where } q^2 < 0, \tag{4.39a}$$

$$F\left(\alpha, 1\right) \quad = \ln\left(\tan\alpha + \sec\alpha\right), \tag{4.39b}$$

$$K\left(\alpha, 1\right) \quad = \sin\alpha. \tag{4.39c}$$

The final and simple expressions for the azimuthal angle, $(\phi - \phi_0)$, $(t - t_0)$, and the equation relating $r - \theta$ motion for the non-equatorial separatrix trajectories (see Appendix A.5 for the derivation) are given by

$$\phi - \phi_0 = \quad \frac{1}{2}\left\{\frac{\sqrt{\mu\,(1+e)\,(3-e)}}{\sqrt{e\left[1+2a^2\,(-1+e^2)\,Q\mu^3\right](1-a^2)}}\left[\frac{\left[La^2 - 2xr_+\right]}{\left(a^2\mu - a^2\mu e - r_+\right)}S_3\right.\right.$$
$$\left.\left. + \frac{\left[-La^2 + 2xr_-\right]}{\left(a^2\mu - a^2\mu e - r_-\right)}S_4\right] - H_1\right\}, \tag{4.40a}$$

$$t-t_0 = \frac{\sqrt{(1+e)(3-e)}}{\sqrt{e\mu\left[1+2a^2\left(-1+e^2\right)Q\mu^3\right]}}\left\{\frac{E}{\mu\left(1-e\right)^2}S_5+\frac{a^2\mu\left(-La+2Er_-\right)}{r_-\sqrt{\left(1-a^2\right)}\left(a^2\mu-a^2\mu e-r_+\right)}S_3\right.$$
$$\left.+\frac{2E}{(1-e)}S_6+\frac{a\mu\left(-2Lr_-\sqrt{1-a^2}-2Ear_-+La^2\right)}{r_-\sqrt{\left(1-a^2\right)}\left(a^2\mu-a^2\mu e-r_-\right)}S_4\right\}+\frac{1}{2}H_2, \tag{4.40b}$$

$$\frac{2\mu\left(1-e^2\right)az_+\sqrt{1-E^2}}{\sqrt{C-A+\sqrt{B^2-4AC}}}\ln\left(\tan\alpha+\sec\alpha\right) = \left\{F\left(\arcsin\left(\frac{\cos\theta_0}{z_-}\right),\frac{z_-^2}{z_+^2}\right)\right.$$
$$\left.-F\left(\arcsin\left(\frac{\cos\theta}{z_-}\right),\frac{z_-^2}{z_+^2}\right)\right\}. \tag{4.40c}$$

where integrals $S_3 - S_7$ are summarized in Table 4.5, and $H_1\left(\theta,\theta_0,e,\mu,a,Q\right)$, $H_2\left(\theta,\theta_0,e,\mu,a,Q\right)$ are given by Eq. (4.5a), (4.5b) respectively. These expressions have their utility in evaluating the trajectory evolution of inspiralling objects near the separatrix, and just before plunging, for extreme mass-ratio inspirals (EMRIs) in gravitational wave astronomy (Glampedakis *et al.* 2002; Drasco *et al.* 2005; Drasco 2006). The analytic formulae for (e_s, μ_s) and the trajectory solution for the non-equatorial separatrix trajectories are together summarized in Table 4.5.

4.7 Consistency check with previous results

To verify our results, we have reduced our analytic formulae to various known results:

1. *Equatorial separatrix orbits*: We reduce the non-equatorial separatrix trajectories, Eqs. (4.40) (Table 4.5), to the case of equatorial separatrix orbits, and found that they are consistent with earlier results derived in Levin and Perez-Giz (2009).

TABLE 4.5: This table summarizes the analytic form for the expressions of (e_s, μ_s) and the trajectory solution for the non-equatorial separatrix orbits.

	Analytic solutions
(e_s, μ_s)	$e_s = \frac{4+a^{'}r_s+\sqrt{\left(r_s a^{'}+2\right)^2-4d^{'}r_s^4}}{-a^{'}r_s-\sqrt{\left(r_s a^{'}+2\right)^2-4d^{'}r_s^4}}$, $\quad \mu_s = \frac{1}{4r_s}\left[-a^{'}r_s-\sqrt{\left(r_s a^{'}+2\right)^2-4d^{'}r_s^4}\right]$, where $a^{'} = \frac{2\left\{\begin{array}{l} 2a^4Q-r_s^2\left(r_s-3\right)\left[r_s^2-\left(r_s-3\right)Q\right]-a^2r_s\left(r_s^3+r_s^2-2Qr_s+8Q\right) \\ +2a\left[r_s\left(r_s-2\right)+a^2\right]\sqrt{a^2Q^2-r_s^3Q\left(r_s-3\right)+r_s^5}-Qr_s\left[r_s\left(r_s-3\right)^2-4a^2\right] \end{array}\right\}}{a^2Qr_s\left[r_s\left(r_s-3\right)^2-4a^2\right]}$, and $d^{'} = \frac{\left\{\begin{array}{l} -2a^4Q-\left(r_s-3\right)\left(r_s-2\right)^2r_s^4+a^2r_s\left[r_s^2\left(3r_s-5\right)+Q\left(r_s\left(r_s-4\right)+5\right)\right] \\ +r_s^4\left[r_s\left(r_s-3\right)^2-4a^2\right]+2a\left[r_s\left(r_s-2\right)+a^2\right]\sqrt{a^2Q^2-r_s^3Q\left(r_s-3\right)+r_s^5} \end{array}\right\}}{a^2Qr_s^4\left[r_s\left(r_s-3\right)^2-4a^2\right]}$.
$\phi-\phi_0$	$\frac{1}{2}\left\{\frac{\sqrt{\mu(1+e)(3-e)}}{\sqrt{e[1+2a^2(-1+e^2)Q\mu^3](1-a^2)}}\left[\frac{\left[La^2-2xr_+\right]}{(a^2\mu-a^2\mu e-r_+)}S_3+\frac{\left[-La^2+2xr_-\right]}{(a^2\mu-a^2\mu e-r_-)}S_4\right]-H_1\right\}$
$t-t_0$	$\frac{\sqrt{(1+e)(3-e)}}{\sqrt{e\mu[1+2a^2(-1+e^2)Q\mu^3]}}\left\{\frac{E}{\mu(1-e)^2}S_5+\frac{a^2\mu(-La+2Er_-)}{r_-\sqrt{(1-a^2)(a^2\mu-a^2\mu e-r_+)}}S_3+\frac{2E}{(1-e)}S_6+\frac{a\mu\left(-2Lr_-\sqrt{1-a^2}-2Ear_-+La^2\right)}{r_-\sqrt{(1-a^2)(a^2\mu-a^2\mu e-r_-)}}S_4\right\}+\frac{1}{2}H_2$
$r-\theta$ coupling equation	$\frac{2\mu\left(1-e^2\right)az_+\sqrt{1-E^2}}{\sqrt{C-A+\sqrt{B^2-4AC}}}\ln\left(\tan\alpha+\sec\alpha\right)=\left\{F\left(\arcsin\left(\frac{\cos\theta_0}{z_-}\right),\frac{z_-^2}{z_+^2}\right)-F\left(\arcsin\left(\frac{\cos\theta}{z_-}\right),\frac{z_-^2}{z_+^2}\right)\right\}$.
S_3	$=\frac{1}{(1+p_2^2)}\left[\frac{p_2^2}{\sqrt{-\left(p_2^2+m^2\right)}}\ln\sqrt{\frac{\sqrt{1-m^2}+\sqrt{-\left(p_2^2+m^2\right)}\sin\alpha}{\sqrt{1-m^2}-\sqrt{-\left(p_2^2+m^2\right)}\sin\alpha}}+\frac{\ln\left(\tan\alpha+\sec\alpha\right)}{\sqrt{1-m^2}}\right]$
S_4	$=\frac{1}{(1+p_3^2)}\left[\frac{p_3^2}{\sqrt{-\left(p_3^2+m^2\right)}}\ln\sqrt{\frac{\sqrt{1-m^2}+\sqrt{-\left(p_3^2+m^2\right)}\sin\alpha}{\sqrt{1-m^2}-\sqrt{-\left(p_3^2+m^2\right)}\sin\alpha}}+\frac{\ln\left(\tan\alpha+\sec\alpha\right)}{\sqrt{1-m^2}}\right]$
S_5	$=\frac{1}{\sqrt{1-m^2}\left(m^2+p_1^2\right)^2}\left[\frac{m^2\left(m^2-p_1^2m^2+2p_1^2\right)}{\left(1+p_1^2\right)}\ln\left(\tan\alpha+\sec\alpha\right)+p_1^4S_7+\frac{2p_1^2m^2\left(1-m^2\right)}{\left(1+p_1^2\right)}\mid s\mid\tan^{-1}\left[\mid s\mid\sin\alpha\right]\right]$
S_6	$=\frac{\ln\left(\tan\alpha+\sec\alpha\right)}{\sqrt{1-m^2}\left(1+p_1^2\right)}+\frac{p_1^2\sqrt{1-m^2}}{\left(m^2+p_1^2\right)\left(1+p_1^2\right)}\mid s\mid\tan^{-1}\left[\mid s\mid\sin\alpha\right]$
S_7	$=\frac{1}{2\left(1-s^2\right)^2}\left[\frac{s^4\sin\alpha\cos^2\alpha}{\left(1-s^2\sin^2\alpha\right)}+2\ln\left(\tan\alpha+\sec\alpha\right)-s^2\sin\alpha+\left(3-s^2\right)\mid s\mid\tan^{-1}\left(\mid s\mid\sin\alpha\right)\right]$

2. *Spherical orbits*: We also found that the frequency ratio, ν_ϕ/ν_θ, from Eqs. (4.11b, 4.11c) (Table 4.2), reduce to the case of maximally rotating black hole, $a = 1$, for spherical orbits previously derived in Wilkins (1972).

3. *Equatorial circular orbits*: We also show the reduction of our frequency formulae to the standard case of equatorial circular orbits ($e = 0$, $Q = 0$), where the frequency formulae are given by (Bardeen *et al.* 1972; Wilkins 1972)

$$\nu_\phi\left(r,a\right) = \frac{c^3}{2\pi GM_\bullet}\frac{1}{\left(r^{3/2}+a\right)}, \tag{4.41a}$$

$$\nu_r\left(r,a\right) = \nu_\phi\left(1-\frac{6}{r}-\frac{3a^2}{r^2}+\frac{8a}{r^{3/2}}\right)^{1/2}, \tag{4.41b}$$

$$\nu_\theta\left(r,a\right) = \nu_\phi\left(1+\frac{3a^2}{r^2}-\frac{4a}{r^{3/2}}\right)^{1/2}. \tag{4.41c}$$

This is derivable from both equatorial eccentric orbits ($e \neq 0$, $Q = 0$), Eq. (4.14) (Table 4.3), and spherical orbits ($e = 0$, $Q \neq 0$), Eqs. (4.23, 4.24b, 4.25c) (Table 4.4), formulae.

See Appendix A.6 for these derivations.

4.8 Trajectories

The analytic solution of the integrals of motion presented in this paper in §4.2.1 provides a direct and exact recipe to study bound trajectories without involving numerical integrations. These expressions have their utility in calculating extreme mass ratio inspirals (EMRIs) in gravitational wave astronomy, where numerical models consider an adiabatic progression through series of geodesics around a Kerr black hole (Glampedakis *et al.* 2002; Drasco *et al.* 2005; Drasco 2006). We now discuss various kinds of bound geodesics around Kerr black hole using our analytic solution for the integrals of motion. We use the translation formulae, Eqs.

(3.17), to obtain the integrals of motion only in terms of (e, μ, a, Q) parameters. To sketch the trajectories, we have chosen the starting point for the trajectories to be ($\beta_0 = \pi/2$, $\alpha = 0$) as it follows from Eq. (4.1d). We use Eq. (4.6c) to calculate corresponding small change in θ or β with the small change in r or α and substitute corresponding (r, θ) or (α, β) values in Eqs. (4.6a) and (4.6b) to calculate (ϕ, t).

There are various possible kinds of bound orbits. Here, we take up the each case and sketch these trajectories for different combinations of (a, Q), where the parameters values are tabulated in the Table 4.6. We take up slow rotating ($a = 0.2$) and fast rotating black hole situations ($a = 0.5$ or $a = 0.8$), with both prograde and retrograde cases, for various Q values. The various features of these orbits are enumerated below:

1. *Eccentric orbits*: Figs. 4.4 and 4.5 represent eccentric bound prograde and retrograde trajectories respectively, where the parameter values are depicted in the Table 4.6. The particle periodically oscillates between the periastron and the apastron, and is also bound between $\theta = \arccos(z_-)$ and $\theta = \arccos(-z_-)$ as shown in (t-r) and (t-θ) plots in Figs. 4.4 and 4.5, whereas (t-ϕ) plots depict that ϕ varies between 0 to 2π. We have fixed (e, μ) of the plotted trajectories and show the variation with change in a and Q parameters. The motion of the trajectory increases in the vertical direction with increase in Q parameter.

2. *Homoclinic/Separatrix orbits*: Homoclinic orbits are the separatrices between eccentric bound and plunge orbits, where the particle asymptotically approaches the unstable spherical/circular orbit in both the distant past and the distant future. The energy and angular momentum of the orbiting particle simultaneously correspond to a stable eccentric bound orbit and an unstable spherical/circular orbit. Separatrix orbits in the equatorial plane of a Kerr black hole are well studied (Levin and Perez-Giz 2009; Perez-Giz

TABLE 4.6: The following table summarizes the values of conic parameters (e, μ) chosen in the listed orbit simulations to study eccentric, homoclinic and spherical orbits for different (a, Q) combinations for both prograde and retrograde cases constructed using Eqs. (4.6).

Type of orbit	Orbit #	Inverse latus-rectum of the orbit μ	Eccentricity of the orbit e	Spin of the black hole a	Carter's constant Q	Varying parameter
Eccentric orbits	E1	0.1	0.6	0.2	3	a
	E2	0.1	0.6	0.8	3	
	E3	0.1	0.6	0.2	8	a
	E4	0.1	0.6	0.8	8	
	E5	0.1	0.6	-0.2	3	a
	E6	0.1	0.6	-0.8	3	
	E7	0.1	0.6	-0.2	8	a
	E8	0.1	0.6	-0.8	8	
Homoclinic orbits	H1	0.153	0.6	0.2	3	a and e
	H2	0.208	0.2	0.5	3	
	H3	0.153	0.5	0.2	8	a
	H4	0.172	0.5	0.5	8	
	H5	0.127	0.5	-0.2	3	a and e
	H6	0.127	0.2	-0.5	3	
	H7	0.134	0.5	-0.2	8	a
	H8	0.123	0.5	-0.5	8	
Spherical orbits	S1	0.222	0	0.5	3	a and Q
	S2	0.144	0	-0.5	8	
Zoom-whirl	Z1	0.155	0.5	0.2	5	a
	Z2	0.226	0.5	0.8	5	
	Z3	0.142	0.8	0.2	5	a
	Z4	0.212	0.8	0.8	5	
	Z5	0.162	0.5	0.5	10	a
	Z6	0.179	0.5	0.8	10	

and Levin 2009; O'Shaughnessy 2003). The homoclinic orbits form an important group in Kerr dynamics as they represent the transition between inspiral and plunge orbits and hence, have their significance in the study of the gravitational wave spectrum under the adiabatic approximation. The homoclinic or separatrix orbits correspond to the boundary of the region in (e, μ, a, Q) space, defined by Eq. (4.26). Separatrix orbits with $Q \neq 0$ also have similar features as the equatorial separatrix orbits, where the particle asymptotically approaches the unstable spherical orbit. Figs. 4.6 and 4.7 show prograde and retrograde non-equatorial homoclinic/separatrix orbits respectively (see Table 4.6 for parameter values). We see from H3 and H4 trajectories that an increase in spin parameter, a, increases the range of θ. The orbit initially follows an eccentric path and asymptotically approaches the periastron radius which also corresponds to the unstable spherical orbit radius as shown in (t-r) plots of Figs. 4.6 and 4.7.

3. *Spherical orbits*: Fig. 4.8 shows prograde and retrograde innermost stable spherical orbits (ISSO), which are also the homoclinic orbits with $e = 0$. All the spherical stable orbits exist outside ISSO, whereas unstable spherical orbits are found between ISSO and MBSO.

4. *Zoom-whirl orbits*: Zoom whirl orbits are orbits where the particle takes a finite number of revolutions at the periastron before going back to the apastron, which is an extreme form of the periastron precession. Their significance in gravitational astronomy has been studied for the case of equatorial Kerr orbits (Glampedakis and Kennefick 2002). Here, we discuss zoom-whirl orbits with $Q \neq 0$ as shown in Fig. 4.9, where the particle takes finite revolutions with varying θ at the periastron before turning back to the apastron. We have chosen the value of μ very near to the separatrix, where usually the zoom whirl behavior is seen, for different values of (e, a, Q) combinations. As expected, the particle spends more time at the periastron, compared to the time taken at apastron, to take a finite number of revolutions which is

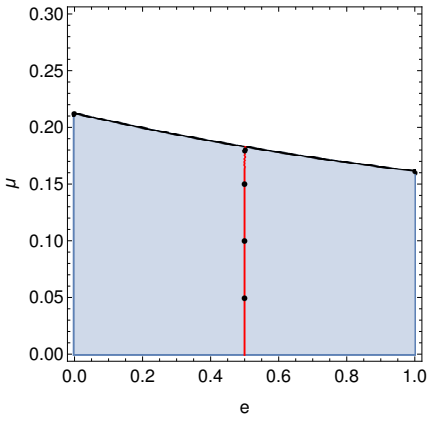

FIGURE 4.3: The shaded region depicts the bound orbit region defined by Eq. (4.7c) in the (e, μ) plane for $a = 0.5$ and $Q = 5$. The black curve represents the homoclinic orbits where the endpoints depict $e = 0$ and $e = 1$ homoclinic orbits corresponding to the ISSO and MBSO respectively. The red curve represents $e = 0.5$ and we study orbits with different μ values as depicted by the dots on this curve.

making the $t - r$ plots appear flatter near the periastron, (see Fig. 4.9). We again see that the increase in a increases the range of vertical motion of the orbit like for the eccentric orbits case. Homoclinic/Separatrix orbit family is the limiting case of the zoom-whirl orbit family where the particle takes infinite revolutions as it asymptotes to the unstable spherical orbit.

Now, we discuss how different kinds of orbits are distributed in the bound orbit region in the (e, μ) plane defined by the Eq. (4.8) for a fixed combination of (a, Q). We fix $a = 0.5$ and $Q = 5$ and show the shaded bound orbit region in Fig. 4.3, that represents the eccentric orbits allowed. The black curve which is the boundary of the shaded region represents homoclinic or separatrix orbits. The curve defined by $e = 0$ represents all the spherical orbits with its endpoint at ISSO, which intersects with the separatrix line. We fix $e = 0.5$ depicted by the red curve in Fig. 4.3 and take different values of μ, as depicted by the black dots on the red curve, and plot the corresponding trajectories and study their corresponding behavior.

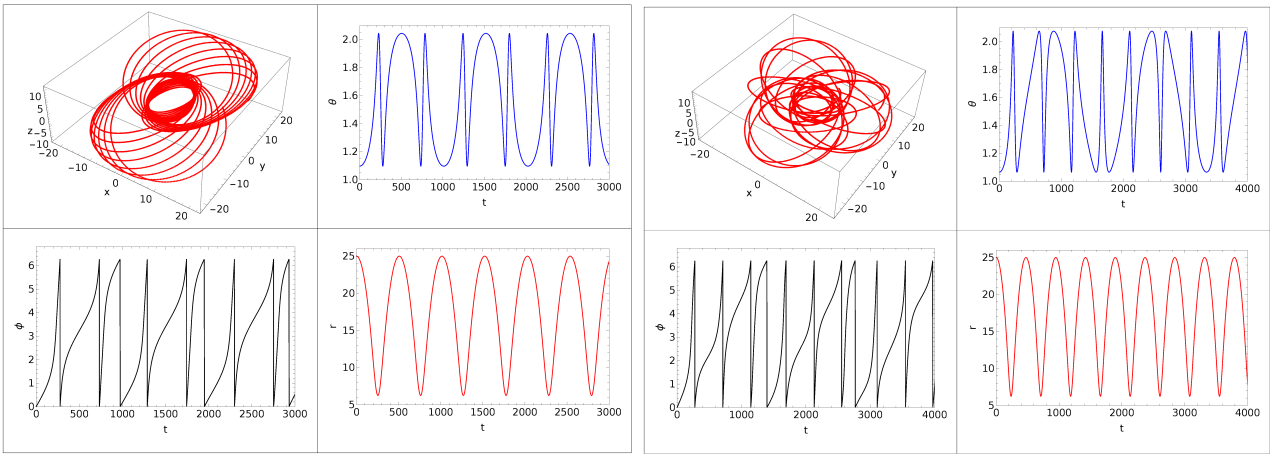

(a) (b)

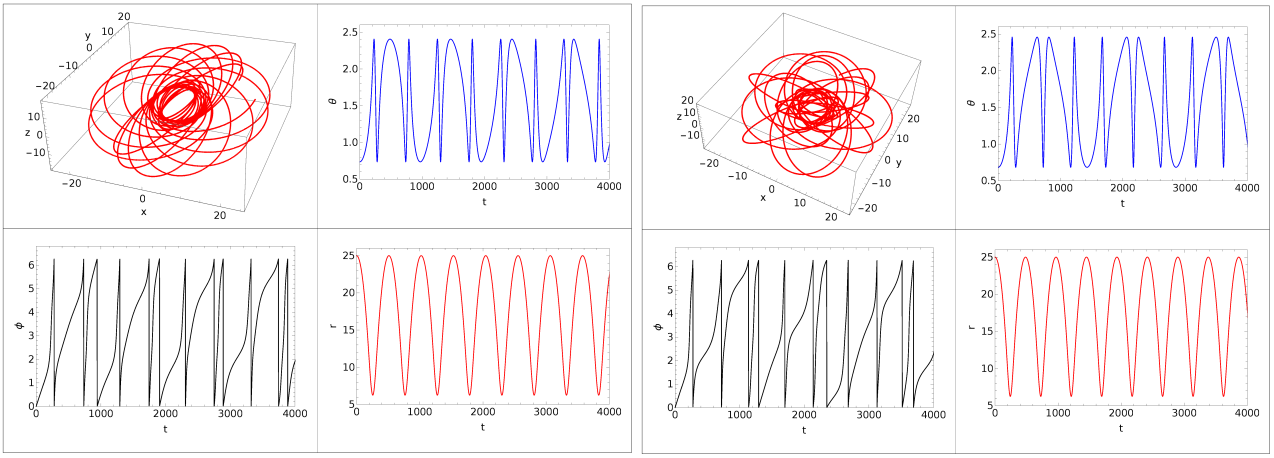

(c) (d)

FIGURE 4.4: The figure shows prograde eccentric bound orbits (a) E1, (b) E2, (c) E3, and (d) E4 in the Table 4.6, for various combinations of (e, μ, a, Q) satisfying Eq. (4.7c) and also presents the evolution of corresponding θ, ϕ and r with coordinate time, t.

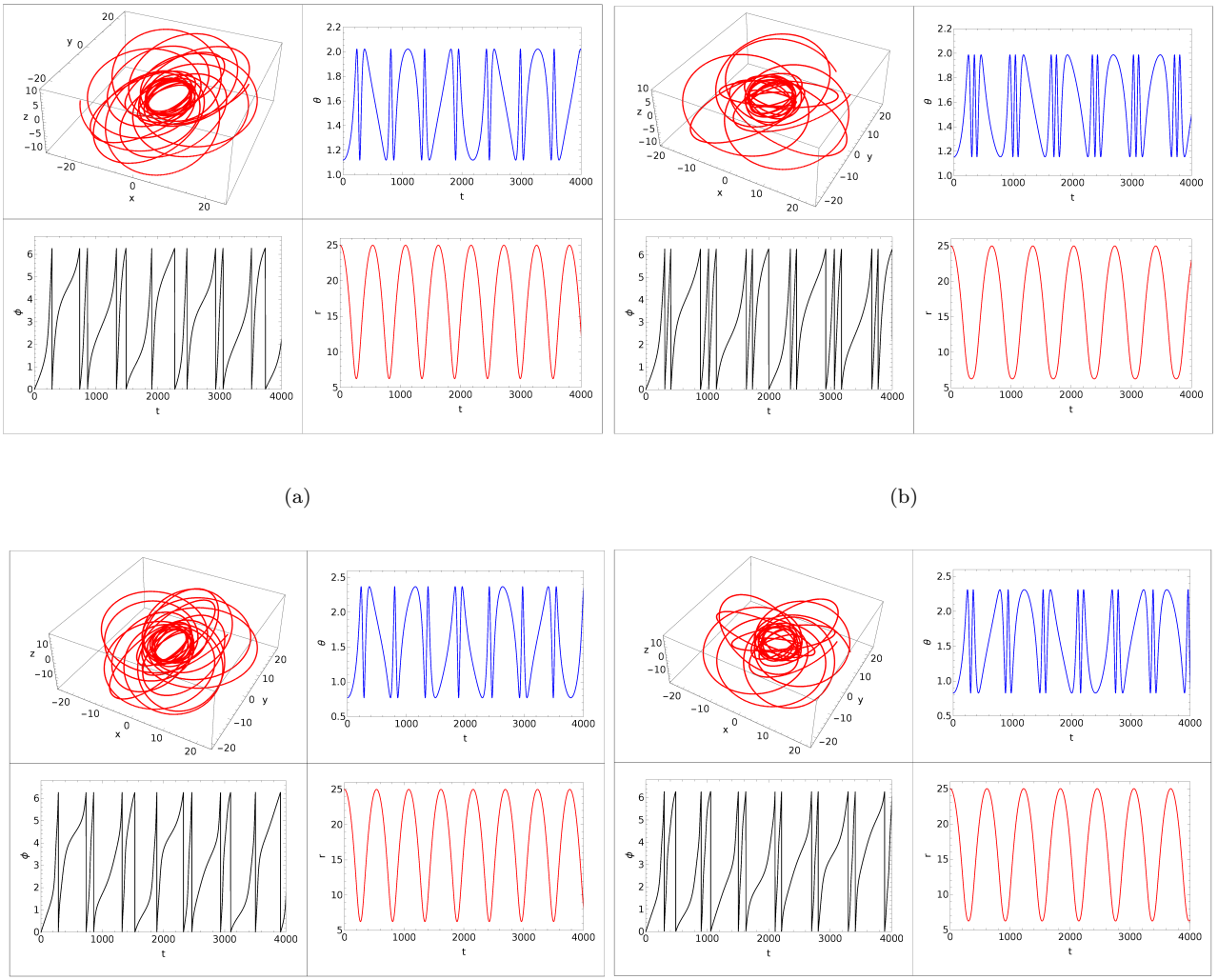

(a) (b)

(c) (d)

FIGURE 4.5: The figure shows retrograde eccentric bound orbits (a) E5, (b) E6, (c) E7, and (d) E8 in the Table 4.6, for various combinations of (e, μ, a, Q) satisfying Eq. (4.7c) and also presents the evolution of corresponding θ, ϕ and r with coordinate time, t.

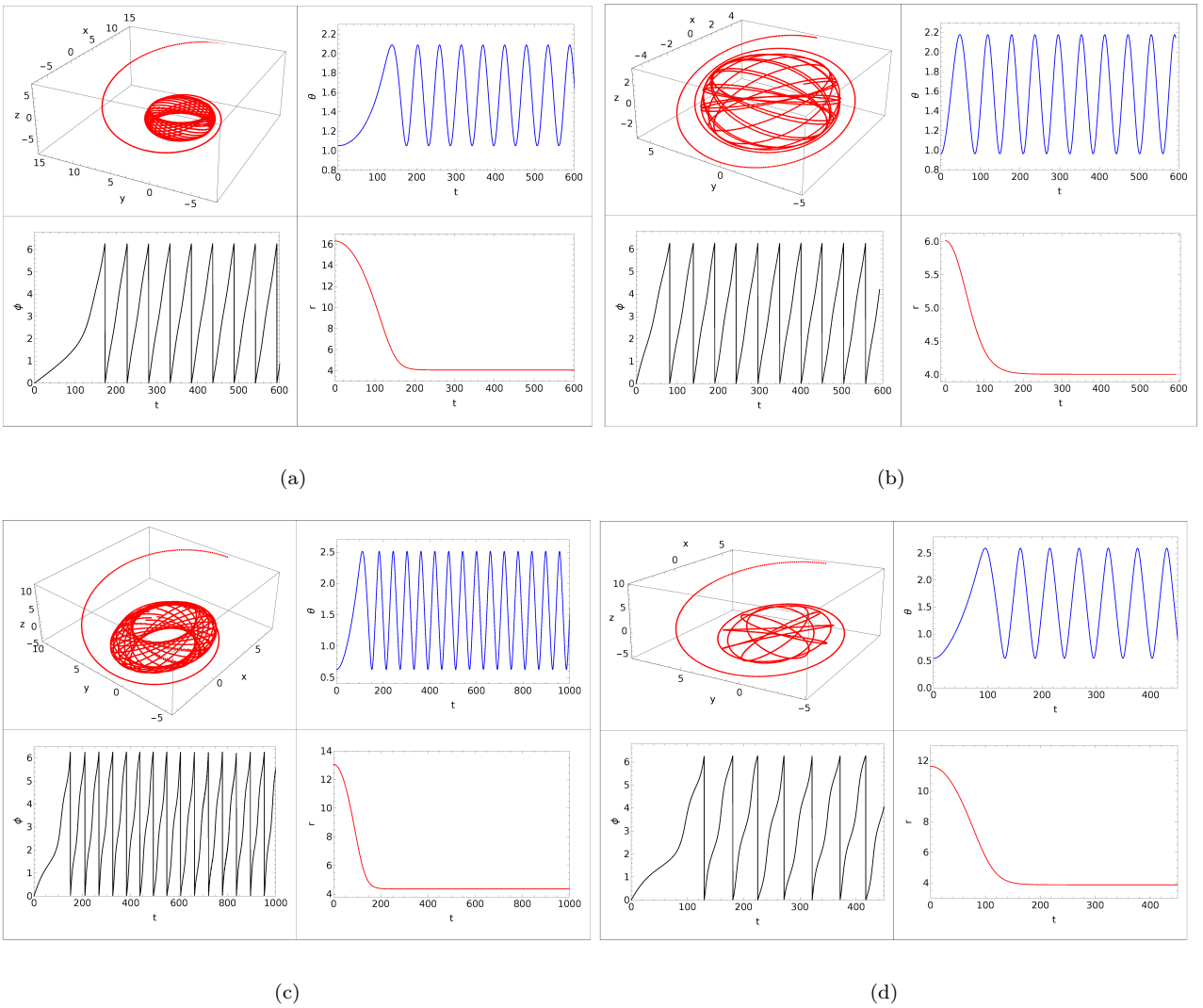

(a) (b)

(c) (d)

FIGURE 4.6: The figure shows the prograde homoclinic orbits (a) H1, (b) H2, (c) H3, and (d) H4 in the Table 4.6, for various combinations of (e, μ, a, Q) and also presents the evolution of corresponding θ, ϕ and r with coordinate time, t.

We see from Figs. 4.10 and 4.11, that for a fixed $e = 0.5$, as μ is increased, the trajectory shows zoom-whirl behavior as it gets closer to the separatrix or homoclinic orbit for the corresponding e value. It can be seen in the t-r plot of Fig. 4.11(b) that the particle spends some time at the periastron which depicts the zoom-whirl behavior. Hence, it can be said that zoom-whirl behavior is a near separatrix phenomenon and can occur at any eccentricity.

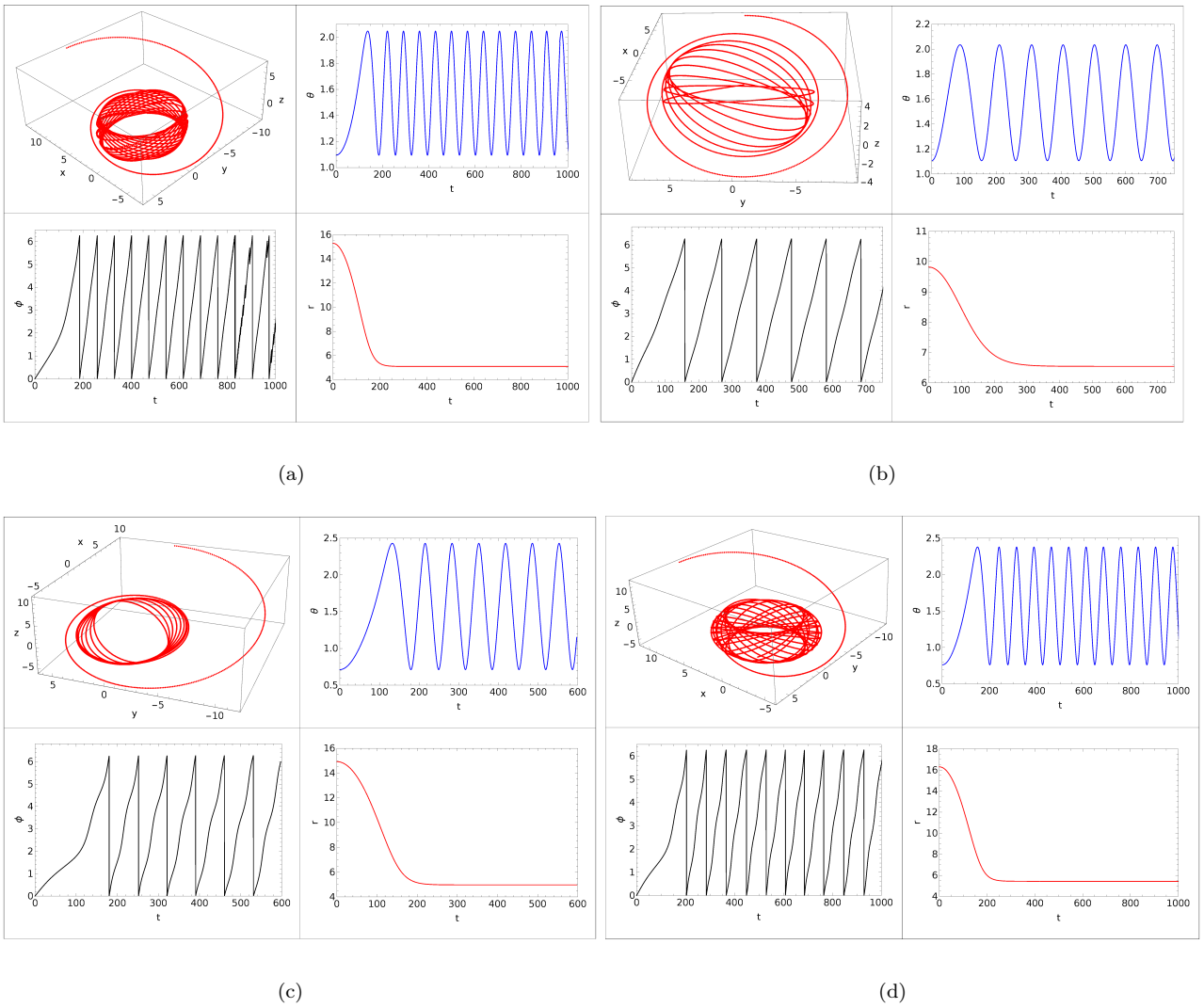

(a) (b)

(c) (d)

FIGURE 4.7: The figure shows the retrograde homoclinic orbits (a) H5, (b) H6, (c) H7, and (d) H8 in the Table 4.6, for various combinations of (e, μ, a, Q) and also presents the evolution of corresponding θ, ϕ and r with coordinate time, t.

4.9 Applications

There are various important applications of our analytic solutions of the general non-equatorial trajectories and the fundamental frequencies for astrophysical studies as discussed below:

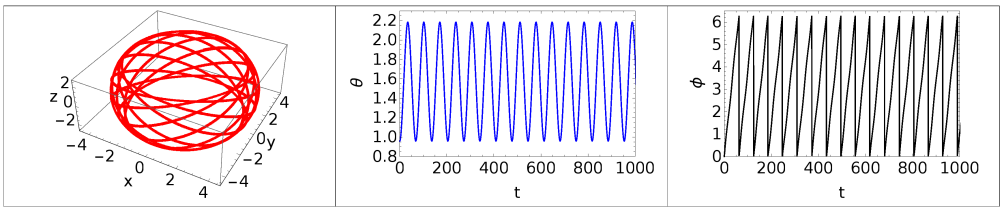

(a)

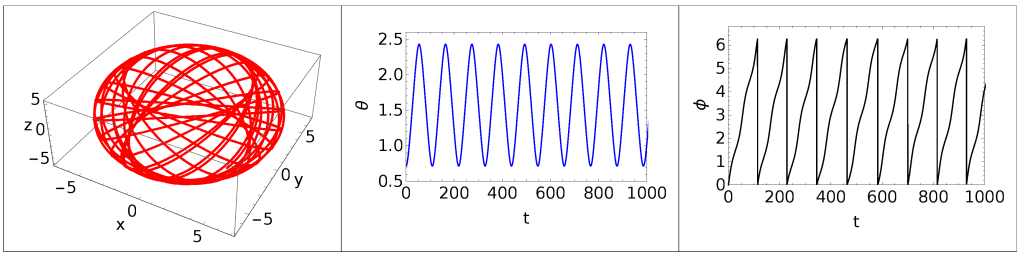

(b)

FIGURE 4.8: The figure shows the spherical orbits for (a) prograde, S1, (b) retrograde, S2, in the Table 4.6 along with the corresponding evolution of θ, ϕ and r with coordinate time, t.

1. *Gravitational waves*: One of the crucial applications of our trajectory solution is the case of gravitational waves from the extreme-mass ratio inspirals (EMRIs). Our analytic formulae are directly applicable for the frequency domain calculation of the gravitational waves using the Teukolsky formalism (Teukolsky 1973), or Kludge scheme (Sopuerta and Yunes 2011), and the orbits can be computed more accurately than the numerical calculations (Drasco and Hughes 2006). Also, the homoclinic orbits, which are the separatrix between plunge and bound geodesics (Levin and Perez-Giz 2008; Perez-Giz and Levin 2009), have their importance to study the zoom-whirl behavior of inspirals near separatrix (Glampedakis and Kennefick 2002; Healy *et al.* 2009). In this paper, we provide the analytic formulae for eccentricity and inverse-latus rectum, (e, μ), for non-equatorial separatrix orbits which are crucial for the selection of these orbits for the study of gravitational waveforms in the Kerr geometry.

2. *Relativistic precession*: The exact analytic formula for the azimuthal angle,

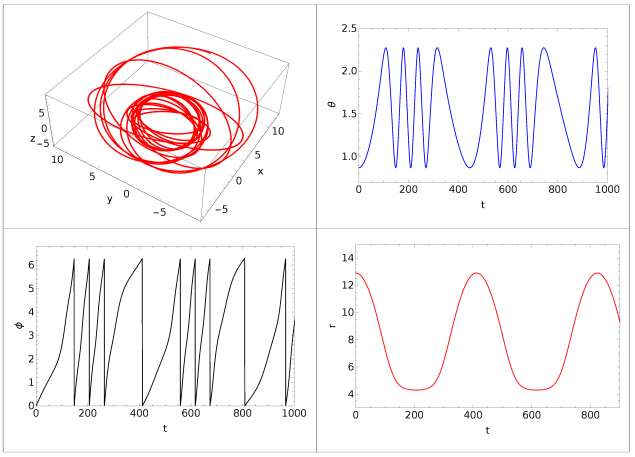

(a)

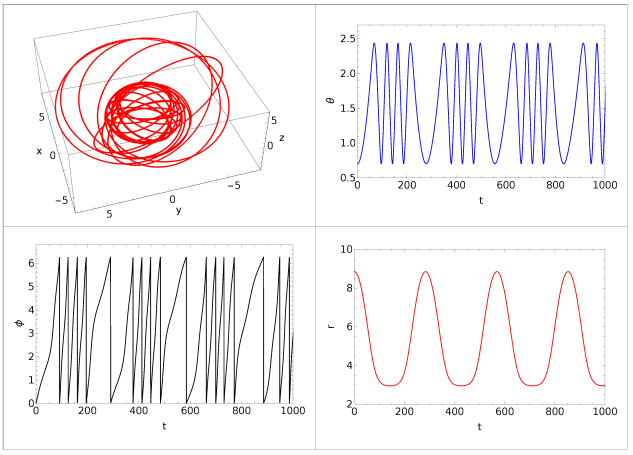

(b)

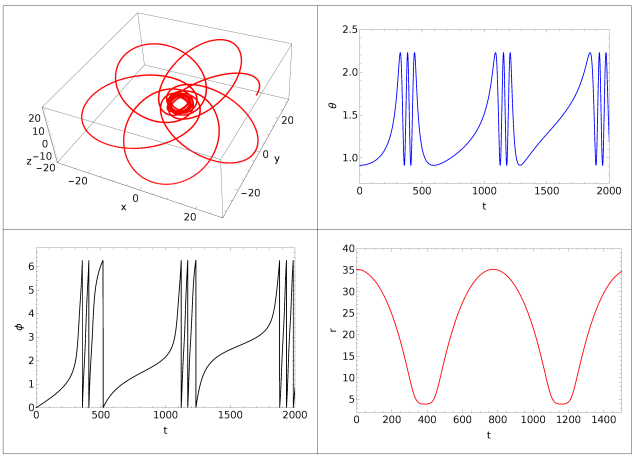

(c)

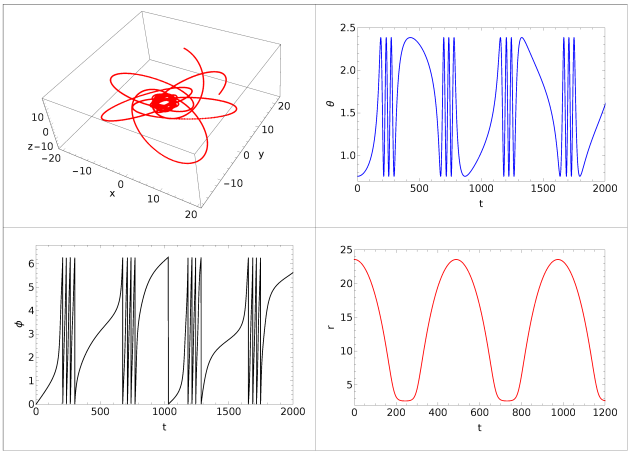

(d)

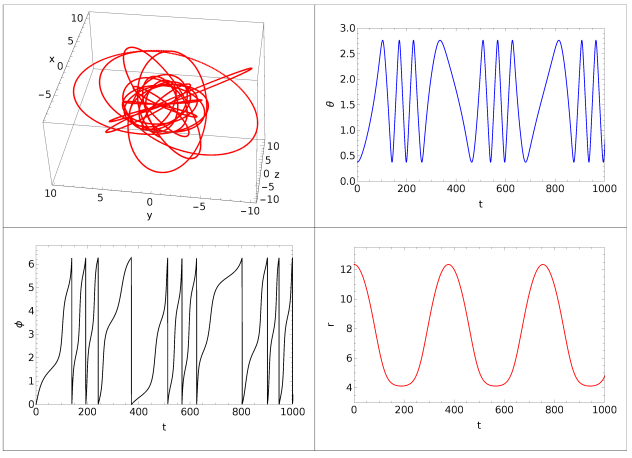

(e)

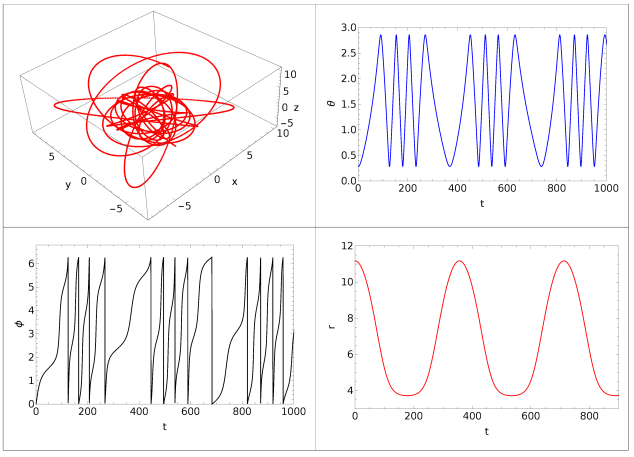

(f)

FIGURE 4.9: The figure shows zoom whirl orbits (a) Z1, (b) Z2, (c) Z3, (d) Z4, (e) Z5, and (f) Z6 in the Table 4.6, for various combinations of (e, μ, a, Q) satisfying Eq. (4.7c) and also presents the evolution of corresponding θ, ϕ and r with coordinate time, t.

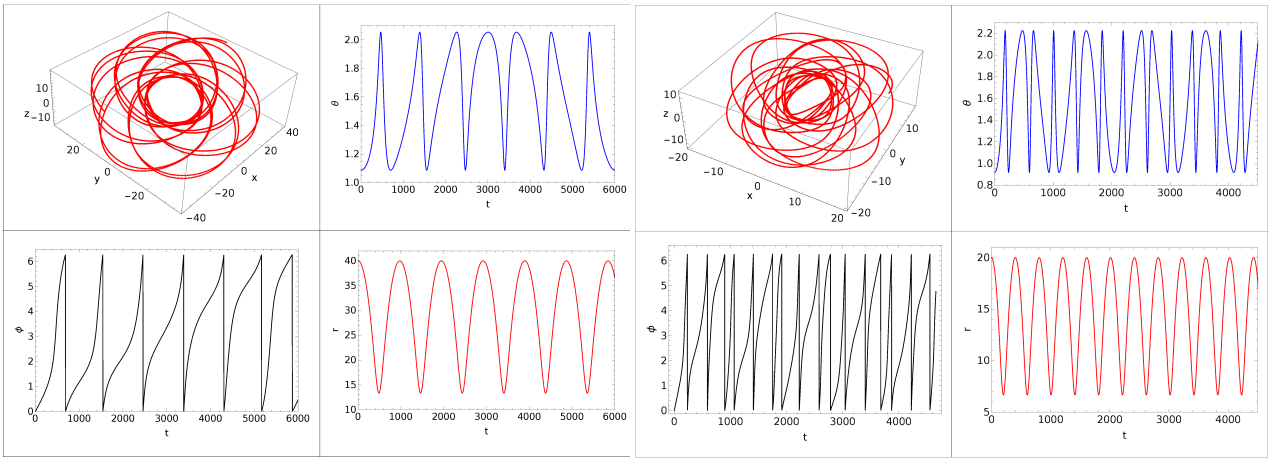

(a) (b)

FIGURE 4.10: The figure shows the eccentric trajectories on the red curve of Fig. 4.3 ($e = 0.5$, $a = 0.5$, $Q = 5$) for (a) $\mu = 0.05$, and (b) $\mu = 0.1$.

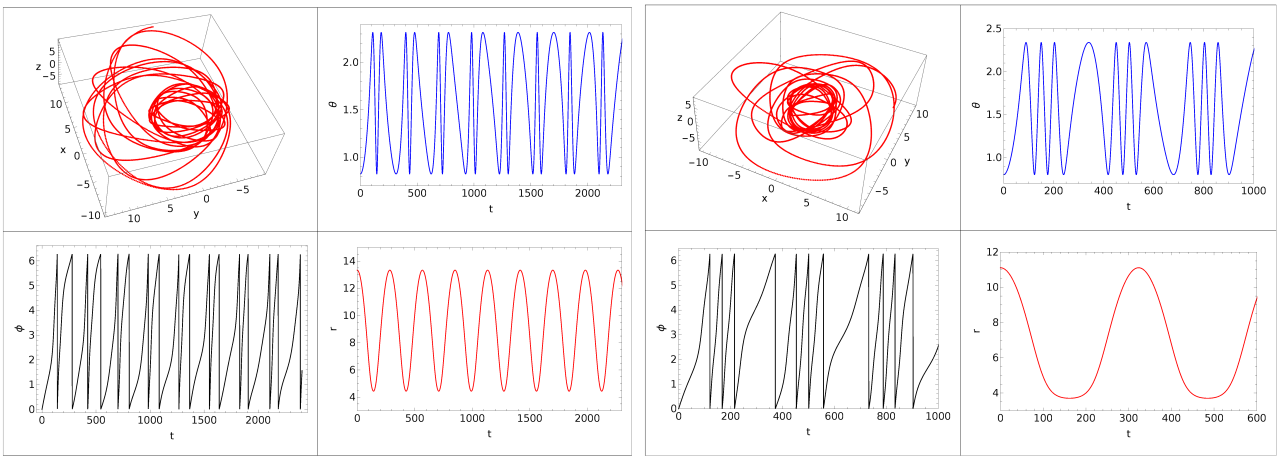

(a) (b)

FIGURE 4.11: The figure shows the eccentric trajectories on the red curve of Fig. 4.3 ($e = 0.5$, $a = 0.5$, $Q = 5$) for (a) $\mu = 0.15$, and (b) $\mu = 0.18$. We see that the trajectory shown in (b) represent a zoom-whirl orbit.

$\phi - \phi_0$, is useful to find the precession of the orbits in the astrophysical systems like planets, black hole, and double pulsar systems. PSR J0737-3039 is one example of a double pulsar system having two pulsars, PSR J0737-3039A and PSR J0737-3039B having 23 ms (Burgay *et al.* 2003) and 2.8 s (Lyne *et al.* 2004) period respectively, which is useful to study the relativistic precession phenomenon valid in a strong gravitational field. The periastron advance was estimated in this source using the first PK parameter, $\dot{\omega}$ (Kramer *et al.* 2006). Our exact analytic results can be used to make a more accurate estimation of the relativistic advance of the periastron in pulsar systems where one component is having a major spin contribution.

3. *Quasi-periodic oscillations (QPOs)*: QPOs are broad peaks seen in the Fourier power spectrum of the Neutron star X-ray binaries (NSXRB) and black hole X-ray binaries (BHXRB). The relativistic precession (RP) model was introduced (Stella and Vietri 1999) to explain the kHz QPOs in NSXRB and later applied to BHXRB (Stella *et al.* 1999). The RP model can be used to calculate the black hole parameters assuming a circular or eccentric orbit is giving rise to a pair of observed high-frequency QPOs and a singular and nearly simultaneous corresponding Type-C QPO (Motta *et al.* 2014a,b), where our exact formulae for the fundamental frequencies are applicable. We generalize the RP model, which we call the generalized RP (GRP) model, to associate QPO frequencies with the fundamental frequencies of the non-equatorial and equatorial eccentric trajectories, and the spherical orbits.

4. *Gyroscope precession*: The calculation of the precession of the spin of a test gyroscope is another application for the test of general relativity. In previous studies, approximate expressions were used for the fundamental frequencies as a series expansion in terms of eccentricity up to order e^2 around a Kerr black hole for the stable bound orbits in the equatorial plane (Bini *et al.* 2016a). Our exact analytic results are useful to estimate more accurate results which are useful to explain the reported results of geodetic drift rate

and frame-dragging drift rate by the Gravity Probe B (GP-B) (Everitt *et al.* 2015).

5. *Phase space study*: The study of dynamics of Kerr orbits by Poincaré maps is also well-discussed (Levin and Perez-Giz 2008). Our closed-form solutions are directly applicable to the study of the extreme chaotic behavior of orbits like Zoom-whirl orbits, which are extreme forms of perihelion precession (Glampedakis and Kennefick 2002), and their phase space structures.

4.10 Summary

The summary of this chapter is given below:

1. We first translate the parameters (E, L, a, Q) to (e, μ, a, Q) using the translation formulae, Eqs. (3.17) to completely describe the trajectory solution in the (e, μ, a, Q) space. We then select the allowed bound orbit by choosing the parameters (e, μ, a, Q) using the bound orbit conditions, Eqs. (4.8).

2. We have derived the closed-form analytic solutions of the general eccentric trajectory in the Kerr geometry as function of elliptic integrals, $\{\phi(r,\theta), t(r,\theta), r(\theta)\}$, Eqs. (4.6a-4.6c). These trajectories around a Kerr black hole were previously derived in terms of Mino time (Fujita and Hikida 2009), λ, subject to the initial conditions on $\mathrm{d}r(0)/\mathrm{d}\lambda$ and $\mathrm{d}\theta(0)/\mathrm{d}\lambda$. The application of our trajectory solution to the various possible studies is numerically faster and does not require any selection of initial conditions. We choose the starting point of the trajectory as the apastron of the orbit, r_a or $\alpha = 0$, and the initial polar angle, θ_0 or β_0, is an extra parameter which can be arbitrarily chosen between maximum and minimum allowed θ range for a given Q. The input variables for plotting the trajectories are α and β which define the

range of r and θ for a fixed combination of (e, μ, a, Q). These results are summarized in Table 4.1.

3. We derived the closed-form expressions for the fundamental frequencies in terms of elliptic integrals, Eqs. (4.11), using the long time average method and without using Mino time, λ. We show that these expressions match with those derived in Schmidt (2002) using Hamilton-Jacobi formulation, which were left in the quadrature form, and we have obtained a closed-form using elliptic integrals. These expressions are summarized in Table 4.2. We present the consistency of our trajectory solution by reducing it to the equatorial separatrix case and also show that the frequency ratio, ν_ϕ/ν_θ, matches with the standard expression derived Wilkins (1972) for the spherical orbits (see Appendix A.6).

4. We reduce our trajectory solution for the equatorial and eccentric orbits, Eq. (4.13), and derive the expressions for their fundamental frequencies, Eq. (4.14). These results are summarized in Table 4.3.

5. We have derived the formulae for E and L for the spherical orbits as functions of radius r_s, a, and Q, given by Eq. (4.15). We also derived the reduced form of the trajectory solution $\{\phi\left(r_s,\theta\right), t\left(r_s,\theta\right)\}$, Eq. (4.21), and the expressions of fundamental frequencies for the spherical orbits, Eqs. (4.23, 4.24b, 4.25c). These results are summarized in Table 4.4.

6. We have derived the equations for ISSO, MBSO, and spherical light radius, Eqs. (4.28-4.30). The light radius derived is the same as that for the equatorial case.

7. We discussed the non-equatorial separatrix orbits, which asymptote to the unstable spherical radius sharing the same E and L values with the eccentric bound orbit. The radius of this unstable spherical radius for the separatrix orbit exists between $MBSO$ and $ISSO$. We write the exact forms for the

eccentricity and inverse-latus rectum (e_s, μ_s) for the non-equatorial separatrix orbits as functions of r_s, a, and Q, given by Eqs. (4.35). We use our general trajectory solutions to derive the equations of motions for non-equatorial separatrix orbits, given by Eqs. (4.40), and find that the radial part of the solutions can be completely reduced to the form containing only trigonometric and logarithmic functions. We also show the reduction of these trajectories to the equatorial case which is also a new and useful form and match the solutions with the previously known result derived in Levin and Perez-Giz (2009) (see Appendix A.6). Separatrix trajectories are essential in the study of gravitational waves from EMRIs, where our analytic solutions are directly applicable. These results are summarized in Table 4.5.

8. We discuss families of allowed bound orbit trajectories like non-equatorial eccentric, non-equatorial separatrix, zoom whirl, and spherical orbits around a rotating black hole using our analytic solution for the trajectories. Homoclinic trajectories have their applications in the gravitational wave astronomy as these trajectories are the boundaries between bound eccentric and plunge orbits. Separatrix/homoclinic orbits were studied for the equatorial case in Levin and Perez-Giz (2009); Perez-Giz and Levin (2009). In this paper, we describe non-equatorial homoclinic and zoom-whirl trajectories, which is the more generalized case for the application to gravitational astronomy.

9. We sketch various types of trajectories, using our analytic formulae discussed above, in §4.8, and discuss their astrophysical applications in §4.9.

10. By using the set of equations in Fujita and Hikida (2009) and comparing them with our expressions, it is found that our calculation is easier to implement and numerically faster by ~ 20, in the equatorial case, for example.

The results include novel aspects, listed above, and alternate and more useful new forms of the known formulae, given in the points (2) and (3) above. The equations and Tables providing these results are indicated in the points above.

4.11 Discussion and Conclusions

There are several notable results in the vast literature discussing various aspects of dynamics in Kerr geometry such as the quadrature formulae for the trajectories (Chandrasekhar 1983; Carter 1968)), circular orbit formulae Bardeen *et al.* (1972), conditions for spherical orbits Wilkins (1972), expressions in terms of quadratures for the oscillation frequencies (Schmidt 2002), formulae for trajectories in terms of quadratures for spherical polar motion (Kraniotis 2004), trajectories for non-spherical polar motion Kraniotis (2007), and expressions for the trajectories and oscillation frequencies (Fujita and Hikida 2009) in terms of Mino time (Mino 2003). Besides these key results there are other useful expressions reported for example on separatrix orbits (Levin and Perez-Giz 2009), and on eccentric equatorial bound orbits (Chandrasekhar (1983); Bini *et al.* (2016a)).

We discuss below the utility of the results in this chapter:

The recipe for calculating frequencies and trajectories by Fujita and Hikida (2009) is as follows: The operative equations are $\{\phi(\lambda), t(\lambda), r(\lambda)\}$, Eqs. (6), (23)-(33), (35)-(45), which require linear combinations of many other equations. The analogy to $r(\chi)$ or $\chi(r)$ is $r(\lambda)$ or $\lambda(r)$ (Eqs. (26, 27)); the latter is non-trivial, whereas the former is simple. Given λ, (ϕ, t) are calculated subsequently inverting linear combinations of many other elliptic integrals. We have numerically matched our frequency formulae with that given in Fujita and Hikida (2009) and we find that there is a minor typo in their expression of Γ below Eq. (20) in section 3.3, where there is a factor of $E/2$ missing in the term $(r_1 - r_3)(r_2 - r_4)E(k_r)$. However, the correct factor has been applied to calculate the numbers in their Tables (1, 2, 3) given in Fujita and Hikida (2009). By using the set of equations in Fujita and Hikida (2009) and comparing with our expressions, it is found that our calculation is easier to implement and numerically faster by ~ 20, in the equatorial case, for example.

The novel results listed in given in (1) and (3)-(8) of the summary: translation conditions of $\{E, L\} \to \{e, \mu\}$, bound orbit conditions, $\{E(r_s), L(r_s)\}$, ISSO, MBSO, and light radius formulae, besides new form for equatorial trajectories, are useful for various applications and simulations related to astrophysical scenarios involving relativistic precession like QPOs and accretion disks. We have also derived the locus of the $Q \neq 0$ separatrix curve in the $e - \mu$ plane besides providing the form of the trajectories. Using this, further studies can be carried for chaotic motion and study of gravitational waves from zoom-whirl orbits which can be set-up by locating them near the separatrix locus, in the same spirit, as was done for the equatorial case (Levin and Perez-Giz 2009; Glampedakis and Kennefick 2002).

The analytic results presented in this paper have direct applications in astrophysics for example, the study of non-equatorial separatrix orbits which has not been discussed before. They also help in understanding the highly eccentric behaviour of trajectories seen in numerical simulations (Glampedakis *et al.* 2002) just before plunging onto the massive black hole in the case of EMRIs which is possibly related to the eccentric and inclined homoclinic orbits, besides relativistic precession in other astrophysical systems like binary pulsars and black holes, spin precession of gyroscopes around rotating black holes for the test of general relativity, and the study of chaotic orbits in the phase space.

Chapter 5

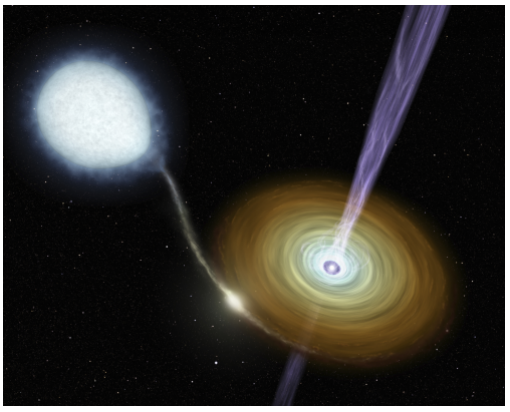

A cartoon picture of the BHXRB. Courtesy: NASA/ JPL-Caltech/R. Hurt (SSC)

A geometric origin for QPO frequencies in BHXRB*

5.1 Introduction

Quasi-periodic oscillations (QPOs) in BHXRBs are categorized as low-frequency QPOs (LFQPOs) with $\nu_0 < 30$Hz, which are again classified as type A, B, or C based on their various properties, and high-frequency QPOs (HFQPOs) with $\nu_0 > 30$Hz (Motta 2016). These different types of QPOs are also known to show a remarkable association with various spectral states during the outburst phase (Fender *et al.* 2004; Remillard *et al.* 2006; Fender and Belloni 2012; Motta 2016). The launch of the Rossi X-ray Timing Explorer (RXTE) in 1995 with its high sensitivity significantly increased the detection of BHXRBs, and made it possible

*This work is published in a paper: Rana and Mangalam (2020b).

to detect HFQPOs in their PDS in the late 1990s (Belloni and Stella 2014), for example, the detection of 300 Hz and 450 Hz QPOs in GRO J1655-40 (Remillard *et al.* 1999a; Strohmayer 2001a); QPOs in the range 102-284 Hz, at 188 Hz, 249-276 Hz and near 183 Hz, 283 Hz in XTE J1550-564 (Homan *et al.* 2001; Miller *et al.* 2001; Remillard *et al.* 2002); 67 Hz, 40 Hz, and 170 Hz in GRS 1915+105 (Morgan *et al.* 1997; Strohmayer 2001b; Belloni *et al.* 2006); 250 Hz in XTE J1650-500 (Homan *et al.* 2003); 240 Hz and 160 Hz in H1743-322 (Homan *et al.* 2005; Remillard *et al.* 2006); and more. Some of these HFQPOs have been detected simultaneously along with their peak frequencies showing nearly 3:2 or 5:3 ratios, indicating a resonance phenomenon (Remillard *et al.* 2006; Belloni and Stella 2014). There is also an interesting case of BHXRB GRO J1655-40 which showed three QPOs simultaneously−two HFQPOs and one type C LFQPO (Motta *et al.* 2014a). Understanding of the origin of HFQPOs and their simultaneity has been the prime focus of the observational studies as well as the theoretical models.

The study of general relativistic effects is important for a theoretical understanding of the origin of QPOs and their connection with various spectral states during the X-ray outburst, as these signals appear to emanate very close to the black hole. Several existing models, based on the instabilities in the accretion disk and other geometrical effects, which attempt to explain the origin of LFQPOs and HFQPOs. Most of these models assume that the disk inhomogeneities orbiting in the innermost regions of the accretion disk are the cause of high variability in the X-ray flux, resulting in QPOs in the PDS. A widely used model among them is the relativistic precession model (RPM) (Stella and Vietri 1999; Stella *et al.* 1999), which ascribes two simultaneous HFQPOs to the azimuthal, ν_ϕ, and periastron precession frequencies, $(\nu_\phi - \nu_r)$, and a third simultaneous type C LFQPO to the nodal precession frequency, $(\nu_\phi - \nu_\theta)$, of a self-emitting blob of matter in the accretion disk. The RPM has been applied to the cases of BHXRBs GRO J1655-40 (Motta *et al.* 2014a) and XTE J1550-564 (Motta *et al.* 2014b) to estimate the spin parameter and mass of the black hole, where they assumed the precession

frequencies of nearly circular particle trajectories in the accretion disk around a Kerr black hole. Recently, in contrast with the localized assumption of the RPM, the most frequently detected type C QPOs in BHXRBs have been modeled as the Lense−Thirring frequency of a radially extended thick torus precessing as a rigid body (Ingram *et al.* 2009; Ingram and Done 2011, 2012). This model describes the increase in type C QPO frequency with the hard to soft spectral transition during outburst as coincident with the decrease in outer radius of the torus and also shows that the maximum type C QPO frequency should be close to 10−30 Hz (Motta *et al.* 2018). Other models which concentrate on the 3:2 or 5:3 resonance phenomena of simultaneous HFQPOs under the regime of particle approach; for instance, the nonlinear resonance models (Kato 2004, 2008; Török *et al.* 2005, 2011) which explain the phenomenon of simultaneous HFQPOs as an excitation due to the nonlinear resonant coupling between the oscillations within the accretion disk. One such nonlinear resonance phenomenon is the parametric resonance between radial, ν_r, and vertical, ν_θ, oscillation frequencies of particles in the accretion disk (Abramowicz *et al.* 2003). Another explanation of HFQPOs is based on the Keplerian and radial frequencies of the deformation of the clumps of matter that is due to the simulated tidal interactions in the accretion disk (Germanà *et al.* 2009). A recent model involves the study of (magneto)hydrodynamic instabilities, for example, in particular, to understand the 3:2 resonance of HFQPOs using the general relativistic and ray-tracing simulations (Tagger and Varnière 2006; Varniere *et al.* 2019).

The RPM takes into account of the fundamental phenomenon of relativistic precession, which is dominant and inevitable in the strong-field regime around a black hole. Although the emission mechanism for the production of QPOs with strong rms (~ 20 %) is hitherto unknown, it explains some important observational relations, for example, the Psaltis−Belloni−Klis (PBK) (Psaltis *et al.* 1999), which is a positive correlation between the HFQPOs and the LFQPOs in different BHXRBs. In a few other BHXRBs, the characteristic frequency of a broad feature (not a

QPO) in the PDS during the hard state shows the same correlation with the LFQPOs. This correlation has been explained using the RPM as a variation of the radius of origin around the Kerr black hole, tracing the QPO frequency.

In this chapter, we expand the RPM from a restricted study of circular orbits and explore the fundamental frequency range of the nonequatorial eccentric, equatorial eccentric, and spherical particle trajectories around a Kerr black hole and associate them with the properties of QPOs. We call this the generalized RPM (GRPM). The general trajectory solutions around a Kerr black hole and their corresponding fundamental frequencies have been extensively studied before (Schmidt 2002; Fujita and Hikida 2009; Rana and Mangalam 2019a,b). The existence of nonequatorial eccentric, equatorial eccentric, and spherical orbits near a rotating black hole is tangible, and hence the relativistic precession of these orbits can also be included in the model for the emission of QPOs. The quadrature form of the general trajectory solution $\{\phi, \theta, r, t\}$ around a Kerr black hole (Carter 1968) and the corresponding fundamental frequencies $\{\nu_\phi, \nu_r, \nu_\theta\}$ (Schmidt 2002) are well known. Later, the complete analytic form for the trajectories and the fundamental frequencies was derived in terms of the Mino time (Mino 2003) and the standard elliptic integrals (Fujita and Hikida 2009). More recently, a more compact, analytic, and numerically faster form was derived, in terms of the standard elliptic integrals, for the particle trajectory solutions and their fundamental frequencies was derived (Rana and Mangalam 2019a,b). We use these analytic formulae for the fundamental frequencies via the GRPM for the periastron and nodal precession of nonequatorial eccentric, equatorial eccentric, and spherical trajectories around a Kerr black hole to associate them with the detected QPO frequencies. The RPM was previously described for circular $\{e = 0, Q = 0\}$ orbits (Stella and Vietri 1999; Stella *et al.* 1999). We now include $\{e \neq 0, Q \neq 0\}$ orbits in this paradigm and test the more general model in this paper. Finally, we show that the eccentric trajectory solution also satisfies the PBK correlation for the case of BHXRB GRO J1655-40.

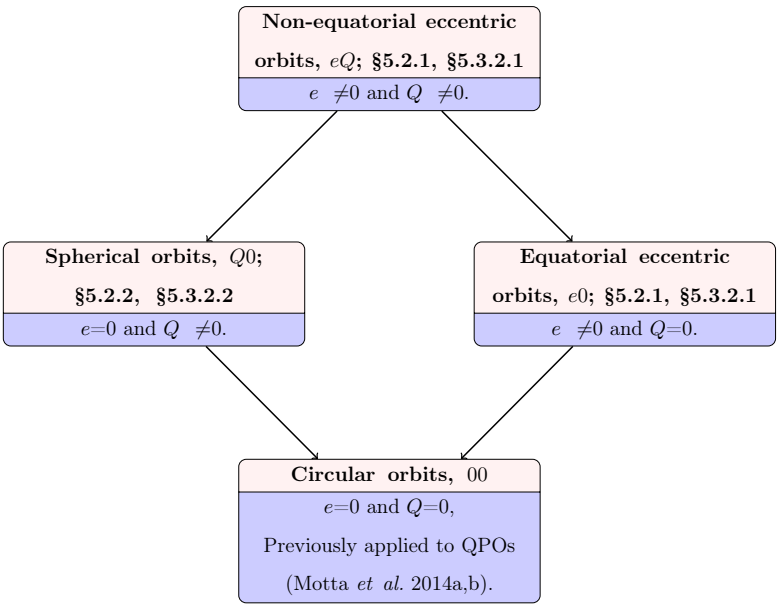

FIGURE 5.1: Flowchart of various Kerr orbits (with the nomenclature used here of nonequatorial eccentric (eQ), spherical ($Q0$), eccentric equatorial ($e0$), and circular (00) orbits) studied to explore QPO frequencies using the GRPM in various sections of this paper, where the most specialized case of circular orbits was previously studied (Motta *et al.* 2014a,b). Clearly, the GRPM is valid strictly only when $e \neq 0$.

This chapter is structured as follows. We first motivate the association of fundamental frequencies of the general eccentric and spherical trajectories with the QPOs in BHXRBs assuming the GRPM in §5.2.1 and §5.2.2; see Figure 5.1 for the terminology used for eQ (general case), $Q0$ (spherical), $e0$ (eccentric equatorial), and 00 (circular orbits). We then take up the cases of BHXRBs M82 X-1, GRO J1655-40, XTE J1550-564, 4U 1630-47, and GRS 1915+105, where HFQPOs have been discovered before. We discuss their observation history in Appendix B.1, and we discuss observations of each BHXRB that we use for our analysis in §5.3.1. Using the observed QPO frequencies in these BHXRBs, we calculate the corresponding orbital parameters. The method for the parameter estimation and its corresponding errors are discussed in §5.3.2 and in Appendix **??**. We discuss the results for general eccentric trajectories in §5.3.2.1, and those corresponding to the spherical orbit in §5.3.2.2. We also show in §5.4 that the PBK correlation is well explained by the eccentric trajectory solutions found in the case of BHXRB GRO

J1655-40. In §5.5, we compare our model with another model for the fluid flow in the general-relativistic thin accretion disk. We finally discuss and conclude our results in §5.6.

5.2 Generalized Relativistic Precession model (GRPM)

The relativistic precession is a phenomenon that is due to strong gravity near a rotating black hole, and its consequence for QPOs originating very close to the black hole is studied. We motivate the association of QPOs in BHXRBs with the fundamental frequencies of general nonequatorial bound particle trajectories around a Kerr black hole through the GRPM. Figure 5.2 shows the periastron and nodal precession of an eccentric particle trajectory near the equatorial plane of a rotating black hole. We suggest that the instabilities in the inner region close to the rotating black hole might provide a radiating plasma cloud (it could be a blob or a torus with the collection of such trajectories degenerate in the parameter space) with enough energy and angular momentum to attain an eccentric ($e \neq 0$) trajectory, or a nonequatorial trajectory ($Q \neq 0$, Carter's constant, Carter (1968)), or both simultaneously ($e \neq 0$, $Q \neq 0$). The Carter's constant can be roughly interpreted as representative of the residual of the angular momentum in the $x-y$ plane, $Q \propto L^2 - L_z^2$, so we have $Q = 0$ for the equatorial orbits where $L = L_z$. We first try to find the suitable range for the parameters, $\{e, r_p, a, Q\}$, of these orbits that produce the fundamental frequencies to compare with the observed range of QPO frequencies in BHXRBs, where r_p represents the periastron point of the orbit and a represents the spin of the black hole. We divide our study of the trajectories into three categories (see Figure 5.1), where a particle follows one of these:

1. A nonequatorial eccentric trajectory ($e \neq 0$, $Q \neq 0$) called eQ.

2. An equatorial eccentric trajectory ($e \neq 0$, $Q = 0$) called $e0$.

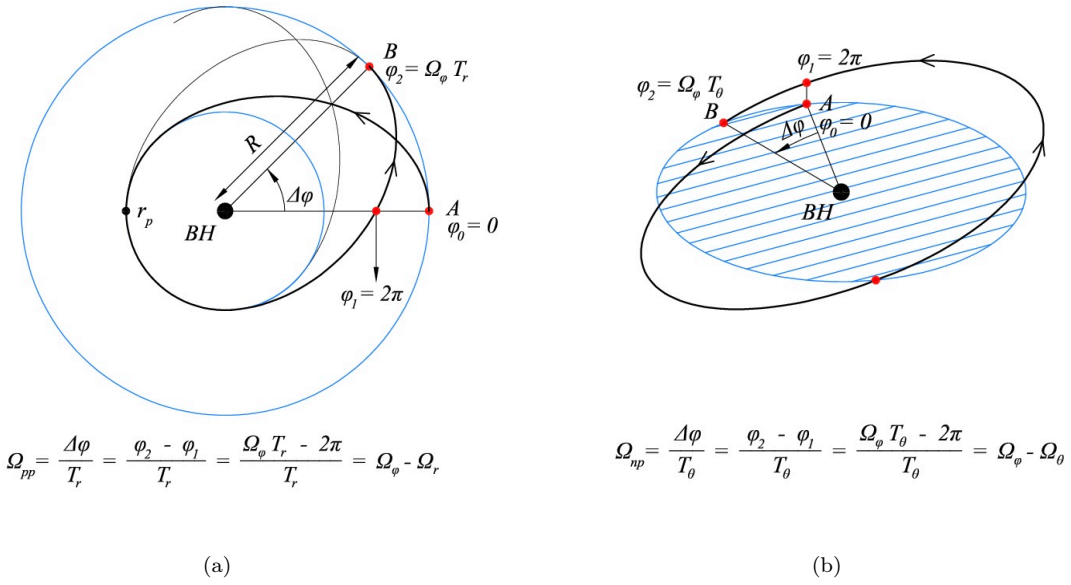

FIGURE 5.2: Generalized relativistic precession phenomenon for $Q \neq 0$, near a black hole (BH) at the center, rotating anticlockwise, where $\Omega_{\rm pp}$ represents the periastron precession and $\Omega_{\rm np}$ represents the nodal precession frequency. The initial point of the trajectory is indicated by point A, from where the particle follows an eccentric trajectory before completing one (a) radial or (b) vertical oscillation to reach point B. The particle sweeps an extra $\Delta\phi$ azimuthal angle during one (a) radial or (b) vertical oscillation because the azimuthal motion is faster than the radial or vertical motion causing the periastron or nodal precession.

3. A nonequatorial and noneccentric, also called a spherical trajectory ($e = 0$, $Q \neq 0$), called $Q0$.

We are using dimensionless parameters ($G = c = M_\bullet = 1$) as the convention in this article for simplicity, so that $r_p \to r_p/\left(GM_\bullet/c^2\right)$, $r_a \to r_a/\left(GM_\bullet/c^2\right)$, $a \to J/\left(GM_\bullet^2/c\right)$, and $Q \to Q/\left(GM_\bullet^2/c\right)^2$, where J is the angular momentum and $M_\bullet$ is the mass of the black hole, and r_a is the apastron point of the bound orbit, while $e = \left(r_a - r_p\right)/\left(r_a + r_p\right)$, the eccentricity parameter, is dimensionless by definition. We also define another mass parameter $\mathcal{M} = M_\bullet/M_\odot$ scaled by solar mass for convenience. The most general nonequatorial trajectory (eQ) around a Kerr black

hole comprises of periastron precession in the orbital plane, superimposed on the precession of the orbital plane about the spin axis of the rotating black hole. Figure 5.3 shows one such trajectory around a Kerr black hole centered at the origin.

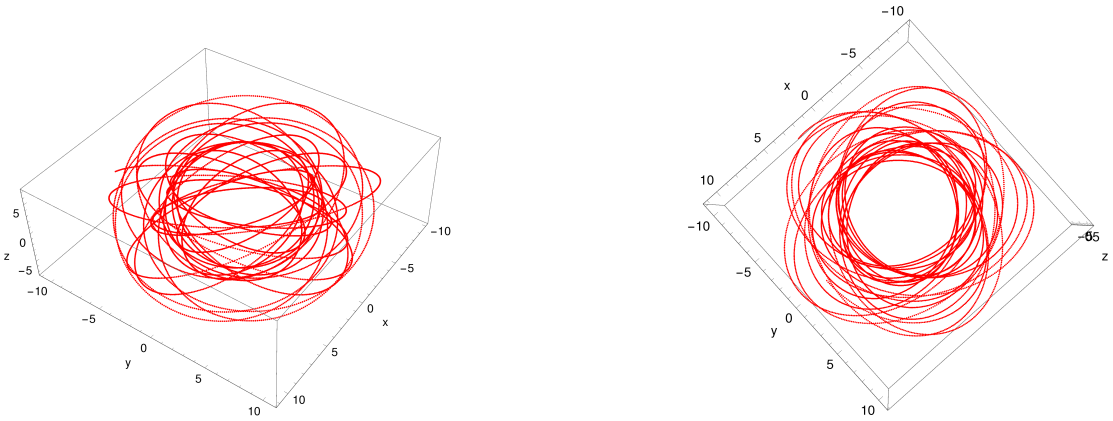

(a) (b)

FIGURE 5.3: Example of eQ trajectory with parameters $\{e = 0.3,\ r_p = 5.917,\ a = 0.5,\ Q = 5\}$ around a Kerr black hole at the origin, with its spin pointing in the positive z-direction: (a) shows the side view of the orbit representing the nodal precession phenomenon of the orbital plane about the spin axis of the black hole; (b) top view of the orbit showing the periastron precession phenomenon.

There are a variety of bound Kerr orbits, for example, nonequatorial eccentric, separatrix, zoom-whirl, and spherical orbits, that have been systematically studied before (chapter 4). Hence, here we first discuss the distribution of these orbits in the parameter space and then isolate the most plausible type of orbits, which should give us the observed range of QPO frequencies assuming the GRPM. These bound orbits are distributed in particular regions in the parameter space and into different parameter ranges for different types of orbits. In Figure 5.4, we show how this distribution belongs in different regions in the $(r,\ a)$ plane, where $r = R/R_g$ represents distance from the black hole, and $R_g = (GM_\bullet/c^2)$. These regions are separated by important radii, which are shown as various curves for the equatorial $(Q = 0)$ and nonequatorial $(Q = 4)$ trajectories in Figure 5.4, where we see that the (un)stable bound orbits are found in regions 1, 2, and 3. Region 4 is beyond the light radius, which extends down to the horizon radius $[r_+ = \left(1 + \sqrt{1 - a^2}\right)]$,

where bound particle orbits are not present, which means any particle in this region would plunge into the black hole, and region 5 is inside the horizon surface. We summarize the distribution of various trajectories in the (r, a) plane (Fig. 5.4) below:

- *Eccentric orbits*: Region 1 and 2.
- *Separatrix orbits*: Region 2.
- *Zoom-whirl orbits*: Region 1 and 2.
- *Stable spherical (circular) orbits*: Region 1.
- *Unstable spherical (circular) orbits*: Region 2 and 3,

where the regions are represented for equatorial orbits in Fig. 5.4(a) and for non-equatorial orbits in Fig. 5.4(b). Hence, we restrict our exploration search of suitable parameters for required QPO frequencies to the regions 1 and 2, where stable circular (spherical), equatorial (nonequatorial) eccentric, zoom-whirl, and separatrix orbits are found. These bound orbits can also be shown as a region

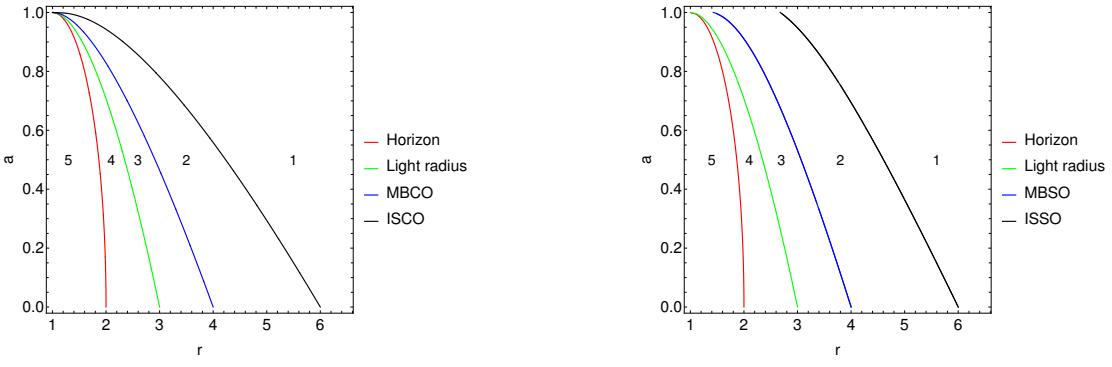

(a) (b)

FIGURE 5.4: Important radii: the ISCO (ISSO), MBCO (MBSO), light radius, and the horizon. These radii separate various kinds of orbits outside a Kerr black hole in the (r, a) plane, indicated by different regions that are depicted by numbers, for (a) the equatorial orbits with $Q = 0$, and (b) nonequatorial orbits with $Q = 4$.

in the (e, μ) space defined by Eq. (3.1). This bound orbit region is shown as a

shaded region in Fig. 5.5 which only includes regions 1 and 2 of the $(r_p,\, a)$ plane shown in Fig. 5.4, where the condition for these bound orbits is given by Eq. (4.8). The RPM has been applied to two cases of BHXRBs, assuming the precession of

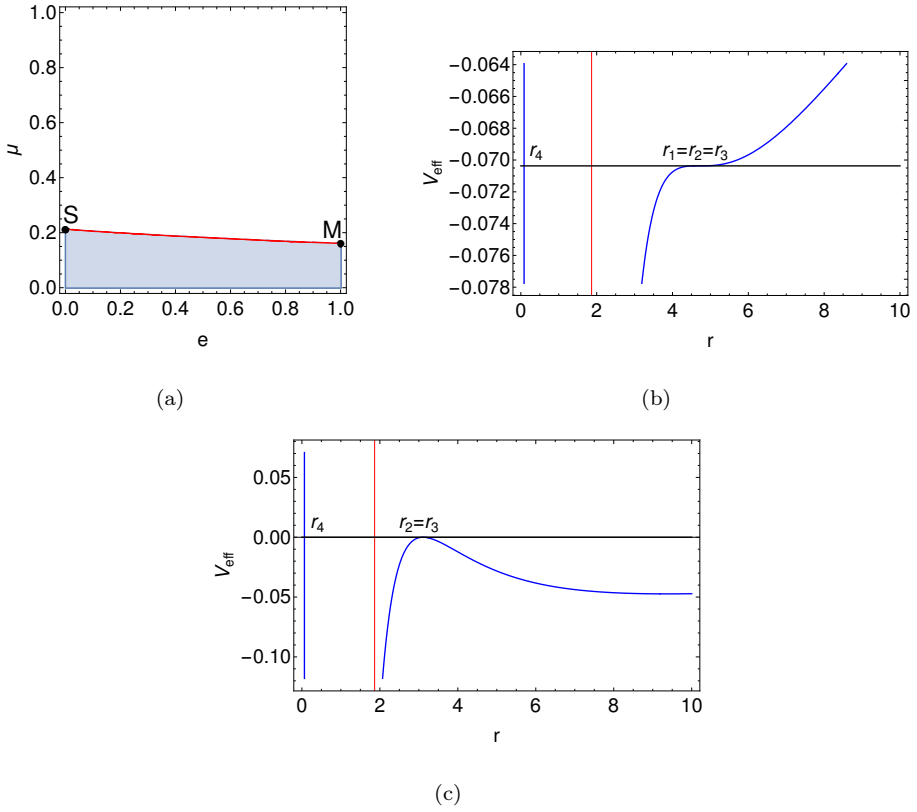

FIGURE 5.5: (a) The shaded region represents all possible bound orbits in the $(e,\, \mu)$ plane for $\{a = 0.5,\, Q = 5\}$, where S depicts the ISSO and M depicts the MBSO radius, and the red curve represents separatrix orbits [see Fig. 4.1]; the corresponding effective potential diagrams are shown as a function of r for (b) ISSO and (c) MBSO, where the horizontal black curve represents $\left(E^2 - 1\right)/2$ and the vertical red curve represents the horizon radius, and $\{r_1,\, r_2,\, r_3,\, r_4\}$ are four roots of the effective potential, which are also the turning points of a trajectory, and where $r_1 = \infty$ for MBSO.

nearly circular orbits (negligible eccentricity [†]) in the equatorial plane of a Kerr black hole (Motta *et al.* 2014a,b). In general, the observed range of HFQPOs in BHXRBs is 40-500 Hz, whereas that of type C LFQPOs is 10 mHz to 30 Hz (Remillard *et al.* 2006; Belloni and Stella 2014). The formulae for fundamental particle frequencies of nearly circular and equatorial orbits are given by Bardeen

[†]as there is no periastron precession for $e = 0$.

et al. (1972) and Wilkins (1972); see Appendix A.6 for the derivation of these formulae from the general frequency formulae of $e0$ and $Q0$ orbits:

$$\nu_\phi(r,a) = \frac{c^3}{2\pi G M_\bullet}\frac{1}{(r^{3/2}+a)}, \quad \bar{\nu}_\phi(r,a) = \frac{\nu_\phi}{(c^3/GM_\bullet)} = \frac{1}{2\pi\,(r^{3/2}+a)}, \tag{5.1a}$$

$$\nu_r(r,a) = \nu_\phi\left(1-\frac{6}{r}-\frac{3a^2}{r^2}+\frac{8a}{r^{3/2}}\right)^{1/2}, \quad \bar{\nu}_r(r,a) = \frac{\nu_r}{(c^3/GM_\bullet)}, \tag{5.1b}$$

$$\nu_\theta(r,a) = \nu_\phi\left(1+\frac{3a^2}{r^2}-\frac{4a}{r^{3/2}}\right)^{1/2}, \quad \bar{\nu}_\theta(r,a) = \frac{\nu_\theta}{(c^3/GM_\bullet)}, \tag{5.1c}$$

where $\{\bar{\nu}_\phi,\ \bar{\nu}_r,\ \bar{\nu}_\theta\}$ are the dimensionless frequencies, where we use the convention $a > 0$ for the prograde and $a < 0$ for the retrograde orbits in this article. Using these formulae and assuming the RPM, it was retrodicted for BHXRB GRO J1655-40 and XTE J1550-564 that these signals originated very close to and outside the ISCO radius, at nearly $r = 5.677 \pm 0.035$ for GRO J1655-40 and $r = 5.47 \pm 0.12$ for XTE J1550-564 (Motta *et al.* 2014a,b). We show that the expected QPO frequency range associated with the 00 orbits in the RPM $\{\nu_\phi,\ \nu_{\rm pp} \equiv (\nu_\phi - \nu_r),\ \nu_{\rm np} \equiv (\nu_\phi - \nu_\theta)\}$ is valid for a wide range of r, where ν_ϕ, $\nu_{\rm pp}$, and $\nu_{\rm np}$ correspond to the HFQPO-1, HFQPO-2, and type C LFQPO, respectively [‡]. To illustrate this, we present a mass-independent model of these frequencies. In Table 5.1, we have shown the observed range of the HFQPO and LFQPO frequencies in BHXRBs along with a typical range in dimensionless values $\{\bar{\nu}_\phi,\ \bar{\nu}_{\rm pp},\ \bar{\nu}_{\rm np}\}$, obtained by scaling the observed frequencies of HFQPOs in BHXRBs using the corresponding known value of the black hole mass $\mathcal{M} \sim 5 - 10$ (given in Table 5.3). For a BHXRB, the typical frequency range of the type C QPOs is 10 mHz to 30 Hz, and we have scaled this frequency range with $\mathcal{M} = 10$ (a typical mass value for BHXRB) to obtain the dimensionless frequency range. This provides an expected range of the geometrical orbital parameters independent of the black hole mass that implies largely a range of r_p. Figure 5.6 shows the contours of $\bar{\nu}_\phi$, $\bar{\nu}_{\rm pp}$, and $\bar{\nu}_{\rm np}$ for the 00 orbits, using Equations (5.1a–5.1c), in the $(r,\ a)$ plane outside the ISCO radius (region 1 of Figure 5.4(a)). We find the following:

[‡]where pp and np represent the periastron and nodal precession frequencies, respectively.

TABLE 5.1: Summary of the Observed QPO Frequency Range in BHXRBs and Their Corresponding Dimensionless Values Derived from Data Given in Table 5.3.

Type of QPO	QPOs in the RPM and GRPM	Observed QPO frequency range in Hz	Dimensionless frequency range $\bar{\nu} = \nu \cdot 10^{-3}/\left(c^3/GM_\bullet\right)$
HFQPO-1	ν_ϕ	$100 - 500$	$2 - 15$
HFQPO-2	ν_{pp}	$40 - 300$	$1 - 9$
Type-C LFQPO	ν_{np}	$10^{-2} - 30$	$10^{-5} - 1$

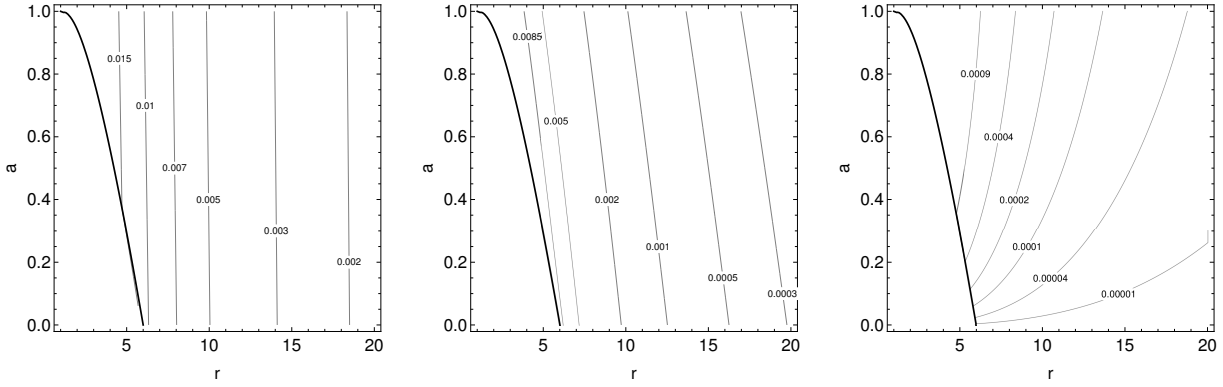

(a) (b) (c)

FIGURE 5.6: Dimensionless frequency contours are shown for circular and equatorial trajectories (00), using Equations (5.1a–5.1c), in the (r, a) plane outside the ISCO radius, which is indicated by a thick black contour as also depicted in Figure 5.4, for HFQPOs (a) $\bar{\nu}_\phi$, (b) $\bar{\nu}_{\rm pp}$, and type C LFQPO (c) $\bar{\nu}_{\rm np}$ assuming the RPM.

1. The expected range of simultaneous QPO frequencies corresponds to a wide range of $r \sim 5 - 15$ for the 00 orbits, which is typically the inner region of the accretion disk.

2. The simultaneous QPOs, if associated with the 00 orbits, should originate very near to the ISCO radius.

3. We expect much higher QPO frequency values $\{\bar{\nu}_\phi \gtrsim 0.015,\ \bar{\nu}_{\rm pp} \gtrsim 0.009,\ \bar{\nu}_{\rm np} \gtrsim 0.001\}$ for the 00 orbits near the ISCO radius for $a \gtrsim 0.5$, as seen in Figure 5.6, which are outside the observed QPO frequency range.

Now, with this, we can explore the frequency range of the nonequatorial eccentric, equatorial eccentric, and spherical orbits using a similar approach assuming the GRPM in the regions 1 and 2 of Figure 5.4 (shaded region of Figure 5.5).

5.2.1 Non-equatorial and equatorial eccentric orbits: eQ and $e0$

Here, we use the formulae of the fundamental frequencies for the non-equatorial and equatorial eccentric particle trajectories to explore the required frequency range for QPOs in BHXRBs, based on the GRPM, and determine the corresponding parameter range $\{e,\, r_p,\, a,\, Q\}$ associated with these trajectories.

As shown in Figure 5.3, the orbital plane of a nonequatorial eccentric trajectory oscillates with respect to the spin axis of the black hole, along with the phenomenon of periastron precession taking place in the orbital plane. A complete analytic trajectory solution and the fundamental frequencies for such trajectories around a Kerr black hole were derived in terms of $\{e,\, \mu,\, a,\, Q\}$ parameters, where the inverse latus rectum can be written in terms of $\{e, r_p\}$ as $\mu = 1/\left[r_p\,(1+e)\right]$. The expressions of dimensionless fundamental frequencies for these trajectories are given by Eq. (4.11).

Next, in the case of equatorial eccentric orbits ($e0$), the expressions for the fundamental frequencies can be further reduced to a simpler form given by Eq. (4.14).

Now, we use these frequency formulae, Eq. (4.11), to deduce the suitable parameter range of parameters $\{e,\, r_p,\, a,\, Q\}$ for eQ and Eq. (4.14) for $e0$ trajectories to find $\{e,\, r_p,\, a\}$ to retrodict the observed range of QPOs in BHXRBs, which is provided in Table 5.1. In Figures 5.7−5.9, we have shown the variation of the

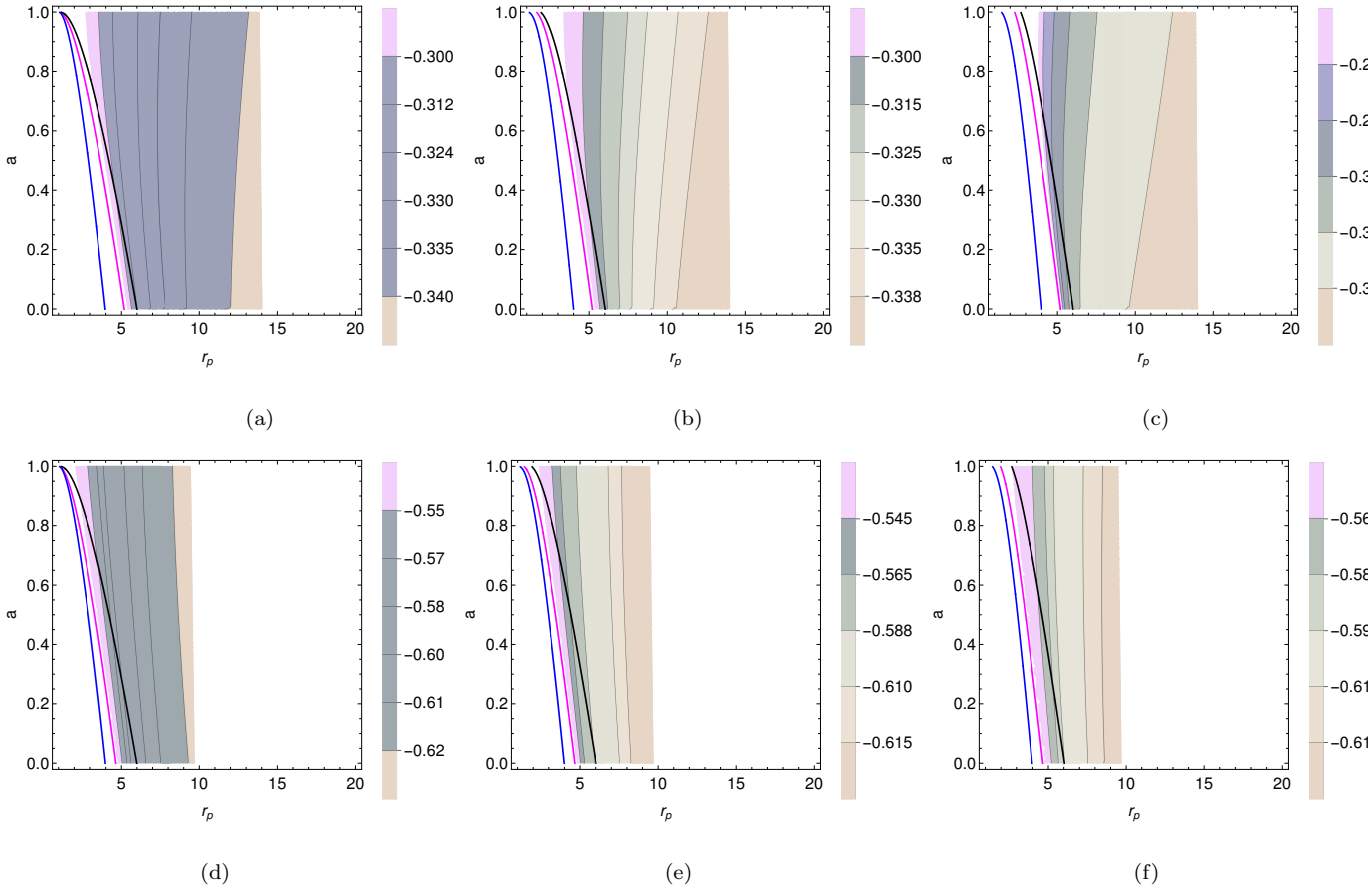

FIGURE 5.7: The contours of $\delta_\phi\,(e, r_p, a, Q)$ are shown in the $(r_p,\, a)$ plane for eccentric orbits around a Kerr black hole, where the parameter combinations are (a) $\{e = 0.25, Q = 0\}$, (b) $\{e = 0.25, Q = 2\}$, (c) $\{e = 0.25, Q = 4\}$, (d) $\{e = 0.5, Q = 0\}$, (e) $\{e = 0.5, Q = 2\}$, and (f) $\{e = 0.5, Q = 4\}$.

quantities

$$\delta_\phi\,(e, r_p, a, Q) = \frac{[\bar{\nu}_\phi\,(e, r_p, a, Q) - \bar{\nu}_\phi\,(e = 0, r_p, a, Q = 0)]}{\bar{\nu}_\phi\,(e = 0, r_p, a, Q = 0)}, \tag{5.2a}$$

$$\delta_{\rm pp}\,(e, r_p, a, Q) = \frac{[\bar{\nu}_{\rm pp}\,(e, r_p, a, Q) - \bar{\nu}_{\rm pp}\,(e = 0, r_p, a, Q = 0)]}{\bar{\nu}_{\rm pp}\,(e = 0, r_p, a, Q = 0)}, \tag{5.2b}$$

$$\delta_{\rm np}\,(e, r_p, a, Q) = \frac{[\bar{\nu}_{\rm np}\,(e, r_p, a, Q) - \bar{\nu}_{\rm np}\,(e = 0, r_p, a, Q = 0)]}{\bar{\nu}_{\rm np}\,(e = 0, r_p, a, Q = 0)}, \tag{5.2c}$$

in the $(r_p,\, a)$ plane for combinations of e ={0.25, 0.5} and Q ={0, 2, 4}. These quantities provide a fractional deviation between frequencies of general eccentric orbits and circular orbits for the same spin and periastron radius. For this comparison, we have calculated the frequency corresponding to a circular orbit at

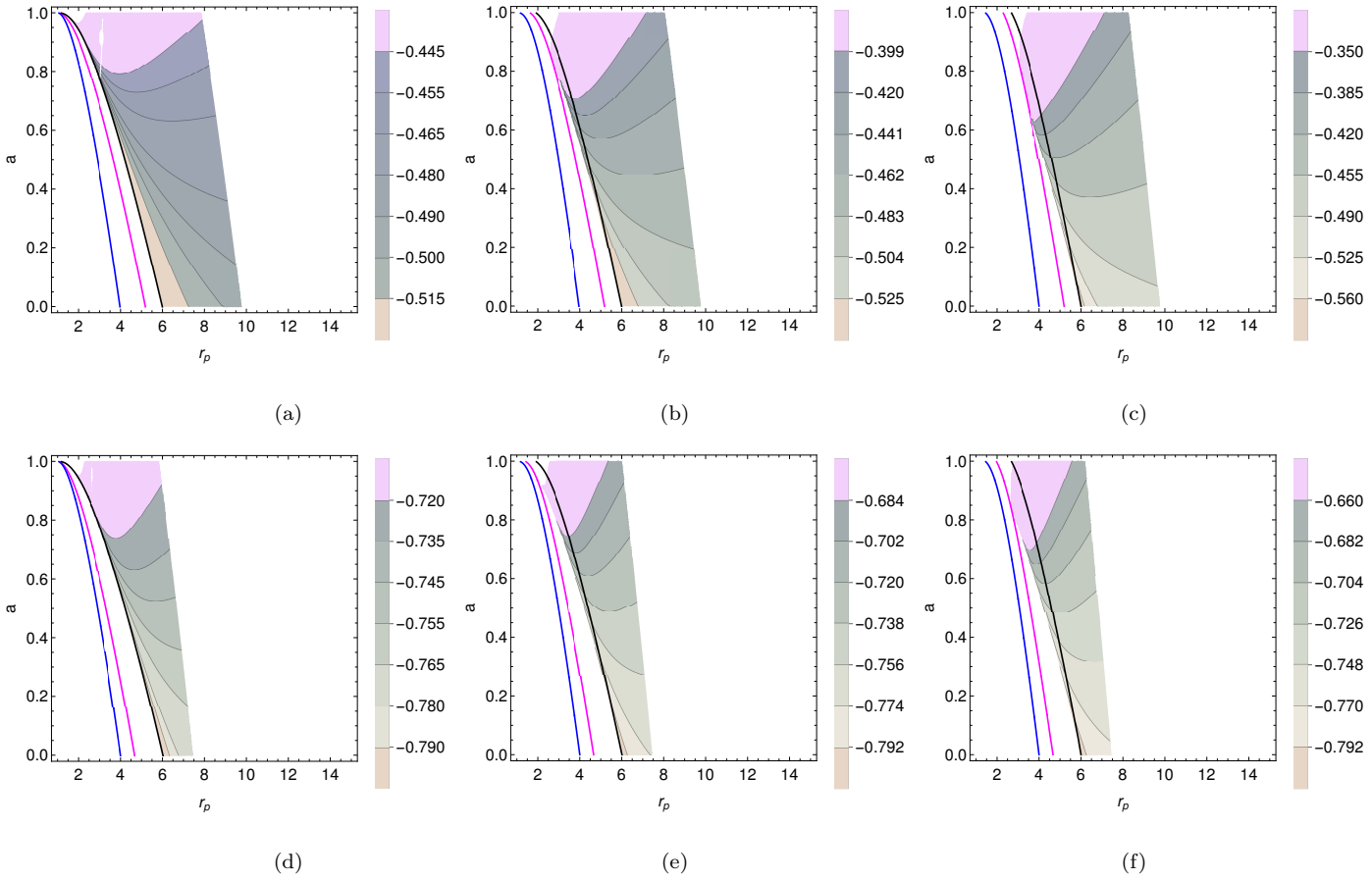

(a) (b) (c)

(d) (e) (f)

FIGURE 5.8: The contours of $\delta_{\rm pp}\,(e, r_p, a, Q)$ are shown in the $(r_p,\, a)$ plane for eccentric orbits around a Kerr black hole, where the parameter combinations are (a) $\{e = 0.25, Q = 0\}$, (b) $\{e = 0.25, Q = 2\}$, (c) $\{e = 0.25, Q = 4\}$, (d) $\{e = 0.5, Q = 0\}$, (e) $\{e = 0.5, Q = 2\}$, and (f) $\{e = 0.5, Q = 4\}$.

the same radius, $r_p = r$, for a fixed value of parameter a. Hence, the deviation, δ, between frequencies defined in this manner is dominated by the parameters e and Q. Also, these deviations are shown only in the region where $\bar{\nu}_\phi\,(e, r_p, a, Q)$, $\bar{\nu}_{\rm pp}\,(e, r_p, a, Q)$, and $\bar{\nu}_{\rm np}\,(e, r_p, a, Q)$ are in the range of QPO frequencies allowed by the observations, as provided in Table 5.1. Hence, these plots together give us the information of deviation of frequencies from circularity, as the e and Q parameters are varied, along with information on the range of (e, r_p, a, Q) for general eccentric orbits allowed by the observed range of QPO frequency. The 3:2 and 5:3 ratios of the simultaneous HFQPOs, seen in a few BHXRBs, are also a remarkable phenomenon that we need to fathom; for example, 300 Hz and 450 Hz HFQPOs

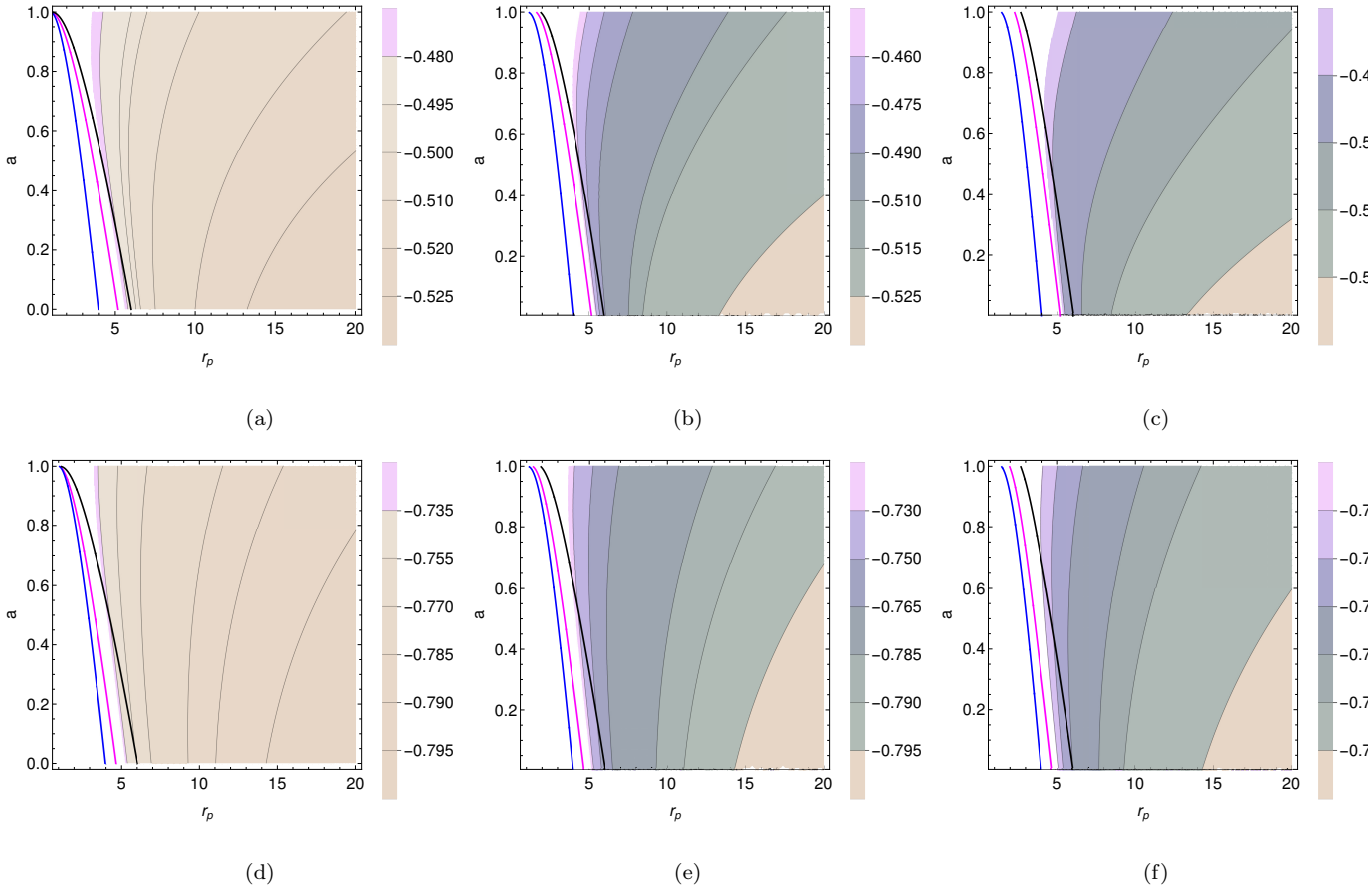

FIGURE 5.9: The contours of $\delta_{\rm np}\,(e, r_p, a, Q)$ are shown in the $(r_p,\ a)$ plane for eccentric orbits around a Kerr black hole, where the parameter combinations are (a) $\{e = 0.25, Q = 0\}$, (b) $\{e = 0.25, Q = 2\}$, (c) $\{e = 0.25, Q = 4\}$, (d) $\{e = 0.5, Q = 0\}$, (e) $\{e = 0.5, Q = 2\}$, and (f) $\{e = 0.5, Q = 4\}$.

were seen in GRO J1655-40 (Remillard *et al.* 1999a; Strohmayer 2001a), and 240 Hz and 160 Hz HFQPOs in H1743-322 (Homan *et al.* 2005; Remillard *et al.* 2006). Assuming the GRPM, this ratio is given by $\nu_\phi/\nu_{pp} = \bar{\nu}_\phi/\bar{\nu}_{\rm pp}$, which is a dimensionless quantity. The contours of this ratio are shown in Figure 5.10 for the six combinations from the set $e = \{0.25,\ 0.5\}$, $Q = \{0,\ 2,\ 4\}$. The blue contours in Figures 5.7−5.10 represent the ISSO radius, and black contours represent the MBSO radius as also indicated in Figure 5.4, whereas the magenta color contours represent the separatrix orbits, given by Eq. (4.26), defining the innermost limit for r_p of an eccentric orbit with a given e.

A summary of the results is given below:

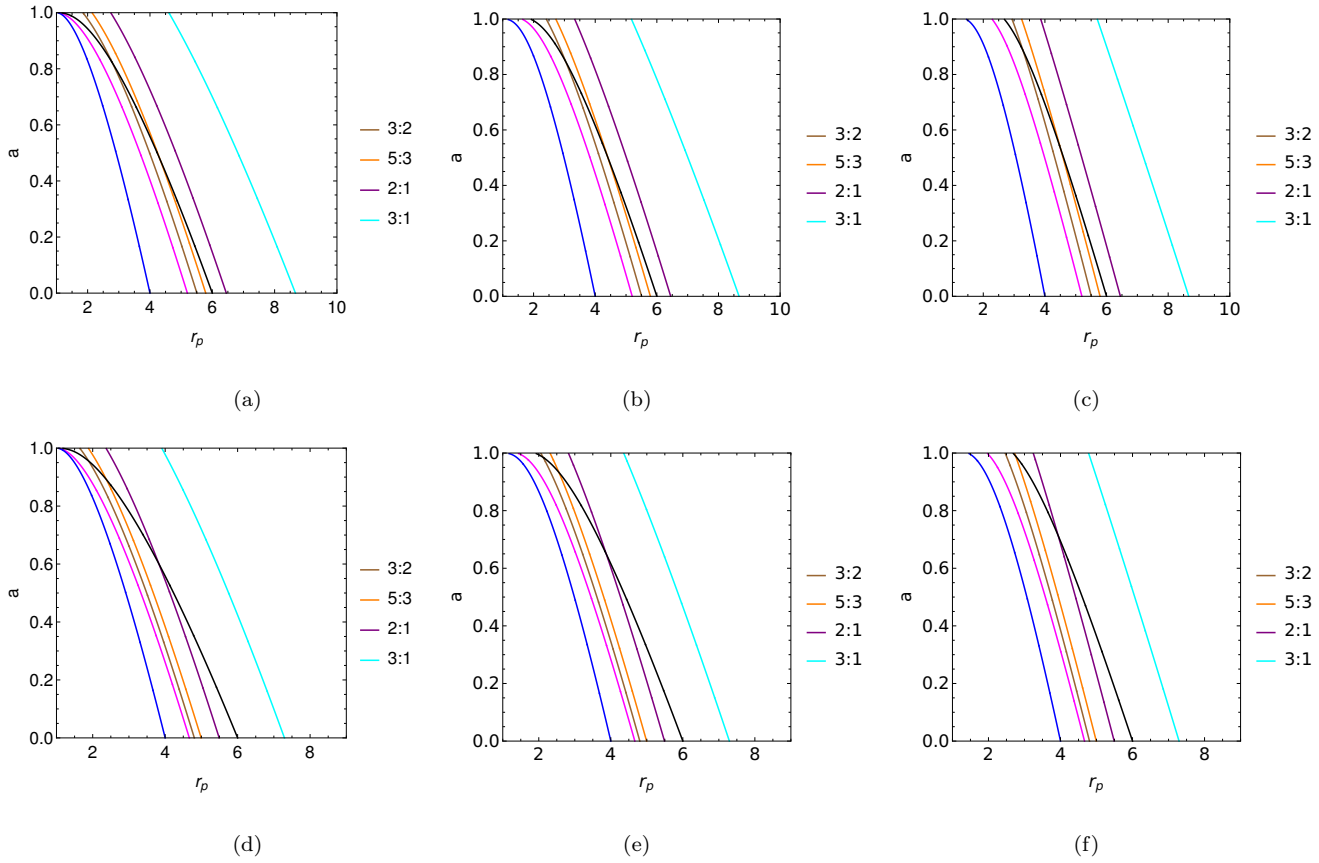

FIGURE 5.10: The HFQPO frequency ratio, $\bar{\nu}_\phi/\bar{\nu}_{\rm pp}$, contours are shown for eccentric orbits around a Kerr black hole in the $(r_p,\ a)$ plane, assuming the GRPM, where the parameter combinations are (a) $\{e = 0.25,\ Q = 0\}$, (b) $\{e = 0.25,\ Q = 2\}$, (c) $\{e = 0.25,\ Q = 4\}$, (d) $\{e = 0.5,\ Q = 0\}$, (e) $\{e = 0.5,\ Q = 2\}$, and (f) $\{e = 0.5,\ Q = 4\}$.

1. Assuming the GRPM, (non)equatorial eccentric trajectories with small to moderate eccentricities, $e \lesssim 0.5$, with $Q \sim 0 - 4$ also generate the expected range of QPO frequencies, $\{\bar{\nu}_\phi,\ \bar{\nu}_{\rm pp},\ \bar{\nu}_{\rm np}\}$, in BHXRBs, as shown in Table 5.1. We have not taken very high values for the Q parameter, as the particle oscillation is expected to be close to the equatorial plane in typical BHXRB scenarios.
2. The effective r_p ranges that produce the required QPO frequency ranges are $\Delta r_p \sim 2 - 15$ for $\bar{\nu}_\phi$, $\Delta r_p \sim 2 - 10$ for $\bar{\nu}_{\rm pp}$, and $\Delta r_p \sim 4 - 20$ for $\bar{\nu}_{\rm np}$, where a varies from 0 to 1. While these Δr_p values are strongly dependent on e, they are only weakly dependent on the Q parameter. The frequency $\bar{\nu}_{\rm np}$ (see

Figure 5.9) increases with a, which implies that we expect to find high type C LFQPO values (nearly $\bar{\nu}_{\rm np} \sim 0.001$) for the black holes with high spin.

3. As e increases, the allowed region shifts close to the black hole. In other words, we expect (non)equatorial eccentric orbits close to the black hole to create the allowed frequency range, whereas circular orbits at comparatively larger radius cater to the same frequency range (see Figure 5.6). This is consistent with the finding that the GRPM favors slightly eccentric and strongly relativistic orbits. We also see that as e increases, the frequencies deviate and decrease from corresponding circular orbit frequencies; for example, $\bar{\nu}_{\phi}$ decreases by 30% for $e = 0.25$ to 60% for $e = 0.5$ (see Figure 5.7), $\bar{\nu}_{\rm pp}$ decreases by 40% for $e = 0.25$ to 79% for $e = 0.5$ (see Figure 5.8), and $\bar{\nu}_{\rm np}$ decreases by 40% for $e = 0.25$ to 80% for $e = 0.5$ (see Figure 5.9).
4. The dependence of these frequencies on Q is very weak. Although the change is comparatively small, we see that these frequencies increase with Q. For example, the maximum increase in $\bar{\nu}_{\phi}$ is ∼3% (see Figure 5.7) and ∼10% for $\bar{\nu}_{\rm pp}$ (see Figure 5.8), whereas it is ∼3% for $\bar{\nu}_{\rm np}$ (see Figure 5.9) as Q changes from 0 to 4. Even for high Q values, say $Q \sim 10$, the change in frequencies is of the same order.
5. Expectedly, the associated frequencies increase as the r_p of a trajectory decreases for a given $\{e,\ a,\ Q\}$, where r_p of an eccentric trajectory is limited by the corresponding separatrix orbit, having the same $\{e, a, Q\}$ values.
6. As shown in Figure 5.10, the 3:2 or 5:3 ratios of HFQPOs originate in the region very close to the separatrix orbits, which is between MBSO and ISSO radii corresponding to typically $\Delta r_p \sim 2 - 6$; this range is dependent on a since r_p decreases as a increases. The frequency ratio contours shift close to the black hole as e is increased, whereas these contours move toward large r_p as Q is increased. This indicates that nonequatorial orbits show a 3:2 or 5:3 ratio of HFQPO frequencies farther away from the black hole than the equatorial orbits, and eccentric orbits have such ratios comparatively closer to the black hole than the circular orbits. Therefore, eQ and 00 orbits close

to the black hole can account for these ratios, as e and Q have canceling effects.

5.2.2 Spherical orbits: $Q0$

Similar to the eQ trajectories, the spherical orbits ($Q0$) are also specific to the rotating black holes. They are the orbits with a constant radius, r_s, where the orbital plane precesses on a sphere about the spin axis of the black hole. Similar to the ISCO and MBCO radii for circular orbits, ISSO and MBSO radii exist for the spherical orbits that are functions of the a and Q parameters. We explore the ranges of parameters, $\{r_s,\, a,\, Q\}$, for spherical orbits allowed by the observed frequency range of QPOs (see Table 5.1). The fundamental frequency formulae for the spherical orbits reduce to the form given by Eqs. (4.23-4.25c).

In Figure 5.11, we show the contours of the quantities

$$\delta_{\phi}\left(r_s, a, Q\right) = \frac{\left[\bar{\nu}_{\phi}\left(r_s, a, Q\right) - \bar{\nu}_{\phi}\left(r_s, a, Q=0\right)\right]}{\bar{\nu}_{\phi}\left(r_s, a, Q=0\right)}, \tag{5.3a}$$

$$\delta_{\rm pp}\left(r_s, a, Q\right) = \frac{\left[\bar{\nu}_{\rm pp}\left(r_s, a, Q\right) - \bar{\nu}_{\rm pp}\left(r_s, a, Q=0\right)\right]}{\bar{\nu}_{\rm pp}\left(r_s, a, Q=0\right)}, \tag{5.3b}$$

$$\delta_{\rm np}\left(r_s, a, Q\right) = \frac{\left[\bar{\nu}_{\rm np}\left(r_s, a, Q\right) - \bar{\nu}_{\rm np}\left(r_s, a, Q=0\right)\right]}{\bar{\nu}_{\rm np}\left(r_s, a, Q=0\right)}, \tag{5.3c}$$

for QPOs in the $(r_s,\, a)$ plane for spherical orbits with $Q = \{2,\, 4\}$ assuming the GRPM, using Eqs. (4.23-4.25c). The blue contours in Figures 5.11 and 5.12 represent the ISSO radii, and the black contours represent the MBSO radii. The results for spherical orbits are enumerated below:

1. Assuming the GRPM, we see that the spherical orbits with $Q \sim 0 - 4$ are in the expected range of QPO frequencies for BHXRBs. The allowed range of r_s to source the QPOs is typically $\sim 3 - 18$ for $\bar{\nu}_{\phi}$ (see Figures 5.11(a) and

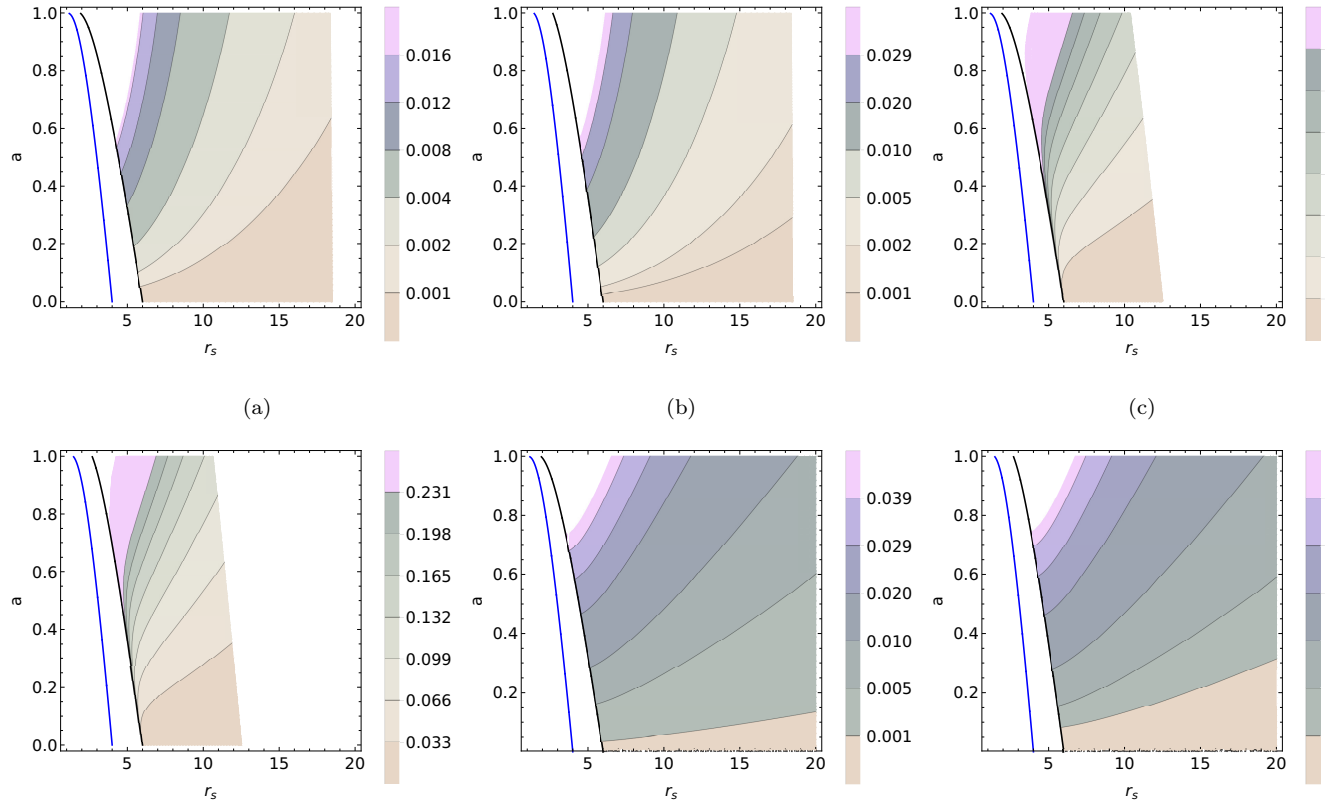

FIGURE 5.11: The contours of $\delta_\phi\,(r_s, a, Q)$ are shown for (a) Q=2, (b) Q=4; $\delta_{\rm pp}\,(r_s, a, Q)$ for (c) Q=2, (d) Q=4; and $\delta_{\rm np}\,(r_s, a, Q)$ for (e) Q=2, (f) Q=4 in the (r_s, a) plane for the spherical orbits around a Kerr black hole.

5.11(b)), $\sim 3-12$ for $\bar{\nu}_{\rm pp}$ (see Figures 5.11(c) and 5.11(d)), and $\sim 3-20$ for $\bar{\nu}_{\rm np}$ (see Figures 5.11(e) and 5.11(f)), where a varies from 0 to 1.

2. The frequencies change weakly with Q. The maximum changes in frequencies are ∼2−3% for $\bar{\nu}_\phi$, ∼11−23% for $\bar{\nu}_{\rm pp}$, and ∼4−8% for $\bar{\nu}_{\rm np}$ as Q changes from 2 to 4 for the spherical orbits. The associated frequencies increase as r_s decreases for a given $\{a, Q\}$.

3. We see from Figure 5.12 that the 3:2 or 5:3 ratio of HFQPOs, $\bar{\nu}_\phi/\bar{\nu}_{\rm pp}$, for spherical orbits should emanate in the region $r_s \sim 3-7$ for Q=2 and $r_s \sim 3.5-7.5$ for Q=4. The ranges of r_s are also dependent on a, where r_s for a given ratio contour decreases as a increases.

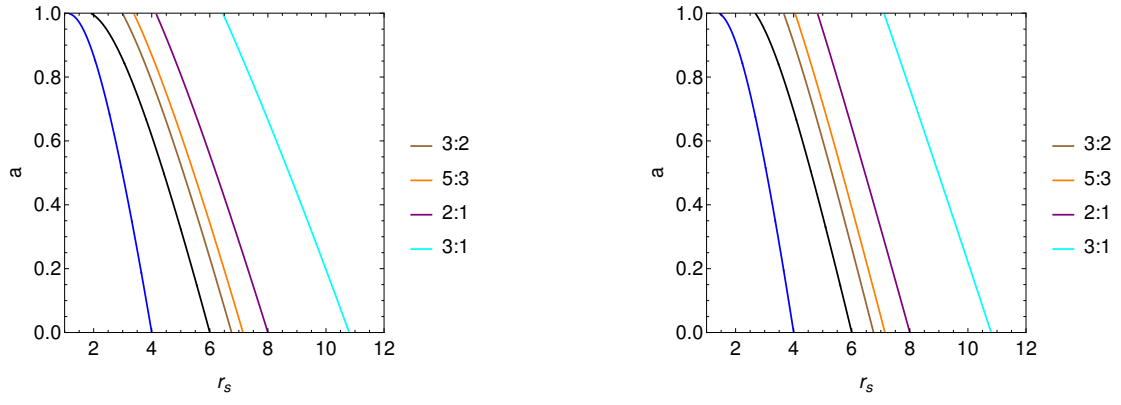

(a) (b)

FIGURE 5.12: The HFQPO frequency ratio, $\bar{\nu}_\phi/\bar{\nu}_{\rm pp}$, contours are shown for the spherical orbits around a Kerr black hole in the $(r_s,\, a)$ plane, assuming the GRPM for (a) $Q = 2$ and (b) $Q = 4$.

5.3 Parameter estimation of orbits in black hole systems with observed QPOs

Next, we take up a few cases of black hole systems that are known to have shown either two or three simultaneous QPOs in their PDS, and we extract the parameter values of the nonequatorial eccentric (eQ), equatorial eccentric ($e0$), and the spherical orbits ($Q0$) corresponding to the observed QPO frequencies using our GRPM. The solution for a given GRPM class (eQ, $Q0$, $e0$) being attempted here is based on balancing the knowns (number of simultaneous frequencies, two or three) with the number of unknown parameters $\{e, r_p, a, Q\}$ (see Table 5.2 illustrating this criterion). For the three frequency cases (M82 X-1 and GRO J1655-40), we have to either supply a from available data or deduce this using a procedure that involves minimizing χ^2 in the unknown parameter volume. For the geometric study of orbits that is of importance here, we have taken the view that the best approximation to a is to be determined first, and then the solution vector $\{e, r_p, Q\}$ (which is crucial for the orbital shape) for the peak probability is found. We have taken slightly different approaches for the two sources as exact solutions are found only in one of the two sources (M82 X-1), where we minimize χ^2 in the a

TABLE 5.2: Various GRPMs, Their Corresponding Unknown Parameters, and Underlying Assumptions for BHXRBs with Three and Two Simultaneous QPOs.
*need to supply a from the best fit of χ^2;
†a is fixed from the available data (see Table 5.3).

BHXRB with 3 QPOs			
GRPM	Model parameters	Number of parameters	Number of observed QPOs
eQ	$\{e,\, r_p,\, a,\, Q\}$	4	3*
$e0$	$\{e,\, r_p,\, a\}$	3	3
$Q0$	$\{a,\, r_s,\, Q\}$	3	3
BHXRB with 2 QPOs			
$e0$	$\{e,\, r_p\}$	2	2†
$Q0$	$\{r_s,\, Q\}$	2	2†

dimension to isolate a. In the other case where no exact solution vector is found (GRO J1655-40), and where it is computationally expensive to explore the full four-dimensional parameter volume of $\{e, r_p, Q, a\}$ in a fine-grained manner, we have only done a primary coarse-grained search to find a sufficiently accurately and then proceeded to determine the unknown parameters $\{e, r_p, Q\}$ by a fine-grid search. The two QPO frequency cases (XTE J1550-564, 4U 1630-47, and GRS 1915+105) are searched by direct fine-grid computations assuming a from available data (see Table 5.2 and 5.3).

We describe our parameter search criteria below:

1. For BHXRBs with three simultaneous QPOs, that is, M82 X-1 and GRO J1655-40 (see Table 5.3), since a type C LFQPO is also present, which corresponds to the nodal oscillation frequency ($\nu_{\rm np}$), we search for all eQ, $e0$, and $Q0$ orbit solutions. We use Eqs. (4.11) and (4.14) to equate the QPO frequencies to $\{\nu_\phi,\, \nu_{\rm pp},\, \nu_{\rm np}\}$ and find the parameters $\{e,\, r_p,\, a\}$ of eQ and $e0$ orbits for M82 X-1 and GRO J1655-40. Next, we calculate the most probable spin of the black hole to estimate $\{e,\, r_p,\, Q\}$ of the orbit. Similarly, we study

the $Q0$ orbits as solutions to the QPOs using Eqs. (4.23-4.25c) and find the parameters $\{r_s,\, a,\, Q\}$ for these BHXRBs. Hence, the parameters searched for these cases are

$$\text{3QPOs} \quad = \begin{cases} eQ \text{ and } e0, & \{\mathcal{M} = \text{fixed from observations}, e, r_p, a, Q = \{0,1,2,3,4\}\}, \\ Q0, & \{\mathcal{M} = \text{fixed from observations}, e = 0, r_s, a, Q\}. \end{cases} \tag{5.4a}$$

2. For BHXRBs with two simultaneous QPOs, that is, XTE J1550-564, 4U 1630-47, and GRS 1915+105 (see Table 5.3), we expect that the solutions are likely to be equatorial as the LFQPO, or $\nu_{\rm np}$ oscillation, is absent (this is consistent with no large-amplitude nodal oscillations and strictly equatorial orbits). Hence, we search for $e0$ solutions using Eqs. (4.14) for $\{\nu_\phi,\, \nu_{\rm pp}\}$ to find $\{e,\, r_p\}$ of the orbit. However, we also check for the $Q0$ orbital solution in these systems and estimate the parameters $\{r_s,\, Q\}$ using $\{\nu_\phi,\, \nu_{\rm pp}\}$. Hence, the parameters searched for in these cases are

$$\text{2QPOs} \quad = \begin{cases} e0, & \{(\mathcal{M}, a) = \text{fixed from observations}, e, r_p, Q = 0\}, \\ Q0, & \{(\mathcal{M}, a) = \text{fixed from observations}, e = 0, r_s, Q\}. \end{cases} \tag{5.4b}$$

We have summarized the history of black hole systems considered here in Appendix B.1. In §5.3.1, we summarize the observations related to QPO detection, mass, and spin estimation and the parameters we estimated for each source. In §5.3.2, we explain the method used to estimate the parameters of these orbits and corresponding errors and then present the results for the (non)equatorial eccentric orbits in §5.3.2.1, and spherical orbits in §5.3.2.2.

5.3.1 Source selection

Here we summarize the QPO observations of the black hole systems that we have selected to implement the GRPM for the general eccentric and spherical trajectories. We have chosen cases where either two or three simultaneous QPOs have been detected, which are as follows:

1. M82 X-1: We use the HF-analog QPOs of M82 X-1 along with the other detected LFQPOs (Pasham and Strohmayer 2013b) to estimate the parameters $\{e,\, r_p,\, a\}$ of the eQ and $e0$ trajectories, where the QPOs are created, by varying Q in the range $0-4$ using the GRPM. Next, using these results, we calculate the most probable value of a to estimate the remaining parameters $\{e,\, r_p,\, Q\}$, using three simultaneous QPO frequencies, in §5.3.2.1. In our analysis, we have assumed the mass of the black hole to be $\mathcal{M} = 428$ (Pasham *et al.* 2014). We also search for the $Q0$ orbit solution and estimate the corresponding parameters $\{r_s,\, a,\, Q\}$ assuming the GRPM in §5.3.2.2. In this paper, we have assumed that the LFQPOs are simultaneous with 3.32±0.06 Hz and 5.07±0.06 Hz QPOs, because these HF-analog QPOs were found to be stable over a few years (Pasham *et al.* 2014), and during this period LFQPOs were also detected; see Table 5.3. Hence, we explore the parameter space of $\{\mathcal{M} = 428,\, e,\, r_p,\, a,\, Q\}$ (see Equation (5.4a)).

2. GRO J1655-40: We use three simultaneous frequencies detected, 441±2 Hz, 298±4 Hz, and 17.3±0.1 Hz (Motta *et al.* 2014a), to associate them with the general eQ and $e0$ trajectories assuming the GRPM in §5.3.2.1. We also explore a $Q0$ trajectory solution. For this BHXRB, we fixed the mass of the black hole to the previously known value, $\mathcal{M} = 5.4$ (Beer and Podsiadlowski 2002). We did not find any $Q0$ orbit solution for this BHXRB. Hence, we explore the parameter space of $\{\mathcal{M} = 5.4,\, e,\, r_p,\, a,\, Q\}$ (see Equation (5.4a)).

TABLE 5.3: Summary of existing BHXRBs that exhibit either three or two simultaneous QPOs. The first two rows represent the cases having twin HFQPOs with simultaneous type-C QPO. The remaining rows show the cases of BHXRB having only twin HFQPOs. The columns show the source name, QPO frequencies, and previously measured mass through optical, infra-red or X-ray observations, previously known spin of the black hole measured by fit to the Fe Kα line or to the continuum spectrum (for 1 and 2 we calculate the parameter a from our method), and the class of GRPM applied to estimate the parameters. The references are indicated by lower case letters (a-m).
References: (a) Pasham *et al.* (2014), (b) Pasham and Strohmayer (2013b), (c) Motta *et al.* (2014a), (d) Beer and Podsiadlowski (2002), (e) Miller *et al.* (2001), (f) Orosz *et al.* (2011), (g) Miller and Miller (2015), (h) Klein-Wolt *et al.* (2004), (i) Seifina *et al.* (2014), (j) King *et al.* (2014), (k) Strohmayer (2001b), (l) Steeghs *et al.* (2013), (m) Miller *et al.* (2013).

S.No	**BHXRB**	ν_1 **(Hz)**	ν_2 **(Hz)**	ν_3 **(Hz)**	$\mathcal{M}$	a	**Model classes**
1.	M82 X-1	$5.07\pm0.06^{(a)}$	$3.32\pm0.06^{(a)}$	$(204.8 \pm 6.3 \times 10^{-3})^{(b)}$	$428\pm105^{(a)}$	-	eQ, $e0$, $Q0$
2.	GRO J1655-40	$441\pm2^{(c)}$	$298\pm4^{(c)}$	$17.3\pm0.1^{(c)}$	$5.4\pm0.3^{(d)}$	-	eQ, $e0$, $Q0$
3.	XTE J1550-564	$268\pm3^{(e)}$	$188\pm3^{(e)}$	-	$9.1\pm0.61^{(f)}$	$0.34^{+0.37}_{-0.45}$ (g)	$e0$, $Q0$
4.	4U 1630-47	$179.3\pm5.7^{(h)}$	$38.06\pm7.3^{(h)}$	-	$10\pm0.1^{(i)}$	$0.985^{+0.005}_{-0.014}$ (j)	$e0$, $Q0$
5.	GRS 1915+105	$69.2\pm0.15^{(k)}$	$41.5\pm0.4^{(k)}$	-	$10.1\pm0.6^{(l)}$	$0.98\pm0.01^{(m)}$	$e0$, $Q0$

3. XTE J1550-564: We use the simultaneous frequencies, 268±3 Hz and 188±3 Hz (Miller *et al.* 2001), in our GRPM and calculate $\{e,\ r_p\}$ of the orbit assuming the $e0$ orbit in §5.3.2.1. We also estimate the parameters $\{r_s,\ Q\}$ of the $Q0$ orbit using these QPO frequencies in §5.3.2.2. We assumed that the mass of the black hole is $\mathcal{M} = 9.1$, as estimated using the optical spectro-photometric observations (Orosz *et al.* 2011), and that the spin of the black hole is $a = 0.34$ (Miller and Miller 2015), estimated from the disk continuum spectrum. Hence, we explore the parameter space of $\{\mathcal{M} = 9.1,\ a = 0.34,\ e,\ r_p\}$ for $e0$ orbits and $\{\mathcal{M} = 9.1,\ a = 0.34,\ r_s,\ Q\}$ for $Q0$ orbits (see Equation (5.4b)).

4. 4U 1630-47: We use the twin HFQPOs at 179.3±5.7 Hz and 38.06±7.3 Hz (Klein-Wolt *et al.* 2004) and associate them with the fundamental frequencies

of the $e0$ orbits to find the parameters $\{e,\, r_p\}$ in §5.3.2.1. We assumed the mass of the black hole to be $\mathcal{M} = 10$, calculated from the scaling of the photon index of the Comptonized spectral component with the LFQPOs (Seifina *et al.* 2014). We fixed the spin of the black hole to $a = 0.985$, as previously estimated from the fit to the reflection spectrum using NuSTAR observations (King *et al.* 2014). We did not find a $Q0$ orbit solution for this BHXRB. Hence, we explore the solution space of $\{\mathcal{M} = 10,\, a = 0.985,\, e,\, r_p\}$ for the $e0$ orbit (see Equation (5.4b)).

5. GRS 1915+105: We take simultaneous HFQPOs at 69.2±0.15 Hz and 41.5±0.4 Hz (Strohmayer 2001b) to study the $e0$ orbits using the GRPM and calculate the corresponding parameters $\{e,\, r_p\}$ in §5.3.2.1. We fixed the mass of the black hole to $\mathcal{M} = 10.1$, estimated using the near-infrared spectroscopic observations (Steeghs *et al.* 2013). We assumed the spin of the black hole to be $a = 0.98$, calculated by fitting to the disk reflection spectrum using NuSTAR observations (Miller *et al.* 2013). We did not find a $Q0$ orbit solution for this BHXRB. Hence, we explore the solution space of $\{\mathcal{M} = 10.1,\, a = 0.98,\, e,\, r_p\}$ for the $e0$ orbit (see Equation (5.4b)).

We have summarized the BHXRB data in the Table 5.3 along with the frequencies of detected QPOs, and previously known values of mass and spin of the black hole, along with their references.

5.3.2 Method used and results

We apply the GRPM to associate the fundamental frequencies of eQ, $e0$, and $Q0$ orbits with QPOs. Here, we describe a generic procedure that we have used to estimate errors in the orbital parameters. A flowchart of this method is provided in Fig. 5.13.

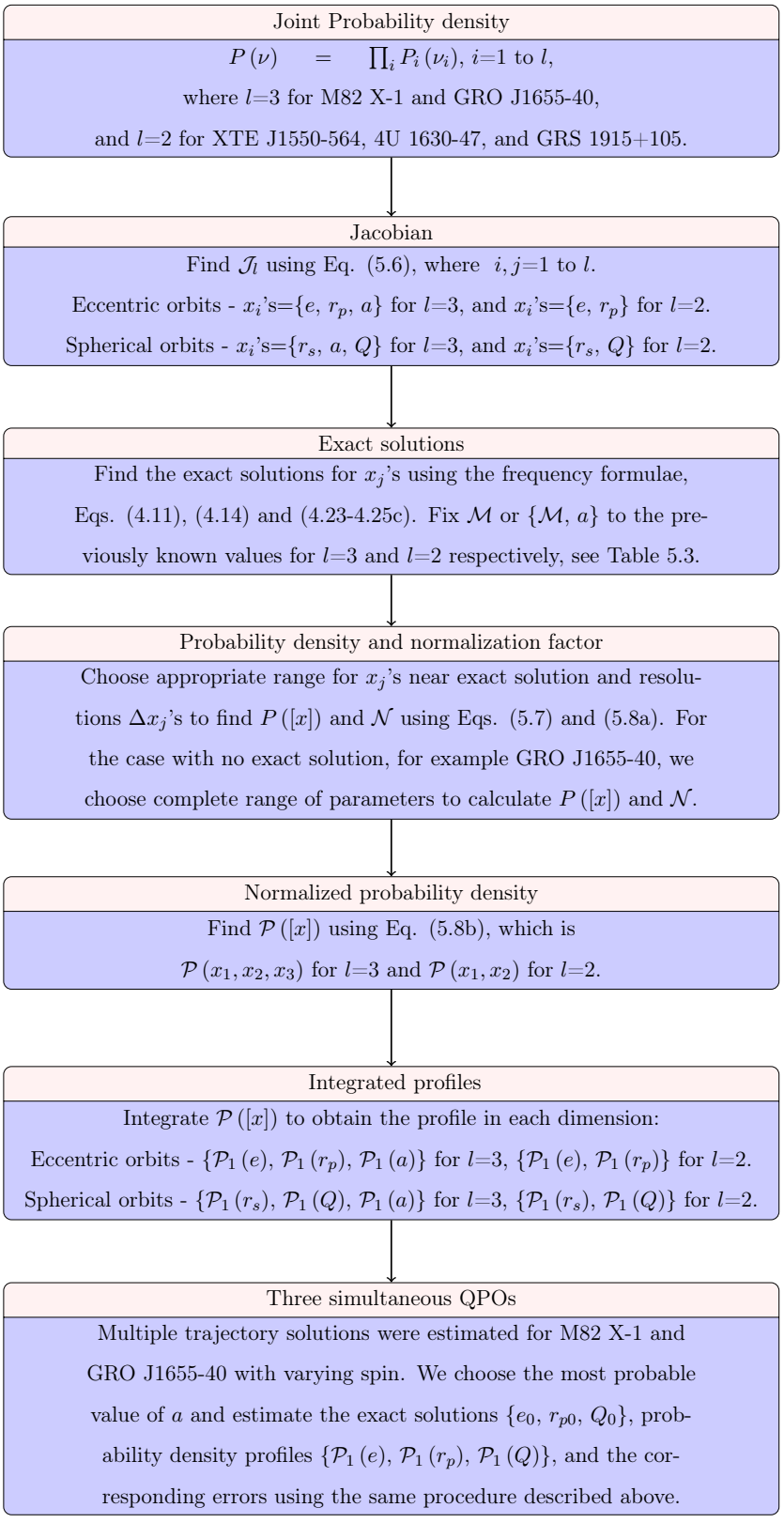

FIGURE 5.13: Flowchart of the method used to estimate the orbital solutions for QPOs and corresponding errors.

1. We assume that the QPO frequencies, ν_1, ν_2 and ν_3, are Gaussian distributed with mean values at ν_{10}, ν_{20}, and ν_{30} (with $\nu_{10} > \nu_{20} > \nu_{30}$), which are equal to the observed QPO centroid frequencies (see Table 5.3). For BHXRBs with two simultaneous QPOs, we only have ν_1 and ν_2. The joint probability density distribution of these frequencies will be given by

$$P(\nu) = \prod_{i=1}^{l} P_i(\nu_i), \tag{5.5a}$$

where $l = 3$ and $l = 2$ for BHXRBs with three and two simultaneous QPOs, respectively. Here, $P_i(\nu_i)$ represents the Gaussian distribution of the ith QPO frequency, given by

$$P_i(\nu_i) = \frac{1}{\sqrt{2\pi\sigma_i^2}} \exp\left[-\frac{(\nu_i - \nu_{i0})^2}{2\sigma_i^2}\right]. \tag{5.5b}$$

2. We find the Jacobian of the transformation from frequency to orbital parameter space using the formulae of fundamental frequencies, which are given by

$$\mathcal{J}_l = \frac{\partial \nu_i}{\partial x_j}; \quad \mathcal{J}_l = \begin{cases} \mathcal{J}_2, & \text{2 simultaneous QPOs,} \\ \mathcal{J}_3, & \text{3 simultaneous QPOs,} \end{cases} \tag{5.6a}$$

where $\{i, j\}$=1 to l and x_j represent the orbital parameters, and $\mathcal{J}$ is given by

$$\mathcal{J}_3 = \begin{bmatrix} \frac{\partial \nu_1}{\partial x_1} & \frac{\partial \nu_1}{\partial x_2} & \frac{\partial \nu_1}{\partial x_3} \\ \frac{\partial \nu_2}{\partial x_1} & \frac{\partial \nu_2}{\partial x_2} & \frac{\partial \nu_2}{\partial x_3} \\ \frac{\partial \nu_3}{\partial x_1} & \frac{\partial \nu_3}{\partial x_2} & \frac{\partial \nu_3}{\partial x_3} \end{bmatrix} \quad \text{and} \quad \mathcal{J}_2 = \begin{bmatrix} \frac{\partial \nu_1}{\partial x_1} & \frac{\partial \nu_1}{\partial x_2} \\ \frac{\partial \nu_2}{\partial x_1} & \frac{\partial \nu_2}{\partial x_2} \end{bmatrix}. \tag{5.6b}$$

For general eccentric trajectories ($Q \neq 0$), which are implemented for BHXRBs with three QPOs, we have $\{x_1, x_2, x_3\}$=$\{e, r_p, a\}$, whereas for equatorial eccentric trajectories ($Q = 0$), implemented for BHXRBs with two QPOs, we have $\{x_1, x_2\}$=$\{e, r_p\}$. Similarly, for the spherical orbit case,

these parameters are $\{x_1, x_2, x_3\}=\{r_s, Q, a\}$ or $\{x_1, x_2\}=\{r_s, Q\}$. The Jacobian is completely expressible in terms of the standard elliptic integrals and can be easily evaluated from Equation (5.6) and using the frequency formulae, Eqs. (4.11), (4.14), and (4.23-4.25c), where $\nu_1 = \nu_\phi$, $\nu_2 = (\nu_\phi - \nu_r)$, and $\nu_3 = (\nu_\phi - \nu_\theta)$ according to the RPM and GRPM. The analytic expressions for the elements of the Jacobian are too long to reproduce here, but they are used to make our computations faster.

3. Next, we write the probability density distribution in the parameter space given by

$$P([x]) = P(\nu)\,|\mathcal{J}_l|, \tag{5.7}$$

where $[x]$ represent the set of parameters $\{x_1, x_2, x_3\}$ for $l = 3$ and $\{x_1, x_2\}$ for $l = 2$, and $\{\nu_1, \nu_2, \nu_3\}$ or $\{\nu_1, \nu_2\}$ are substituted in terms of parameters using our analytic formulae.

We take $Q = \{0, 1, 2, 3, 4\}$ for the general $\{e, Q\}$ trajectory solutions that are implemented for the sources M82 X-1 and GRO J1655-40. For each fixed value of Q, we find the corresponding probability density distribution in the parameter space using Equation (5.7).

4. We calculate the exact solutions for parameters by solving $\nu_\phi = \nu_{10}$, $\nu_{\rm pp} = \nu_{20}$, and $\nu_{\rm np} = \nu_{30}$ using Eqs. (4.11) for non-equatorial eccentric trajectories, Eqs. (4.14) for equatorial eccentric, and Eqs. (4.23-4.25c) for the spherical trajectories. We fix $\mathcal{M}$ for $l = 3$, and both $\mathcal{M}$ and a for $l = 2$ to the previous values; see Table 5.3. We find 1σ errors in the parameters by taking an appropriate parameter volume around the exact solution, and we generate sets of parameter combinations with resolution Δx_j in this volume. The chosen parameter range, exact solutions, and corresponding resolutions are summarized in Tables 5.4, 5.6, and 5.7. We then calculate the probability density using Equation (5.7), for all of the generated parameter combinations

and normalize the probability density by the normalization factor

$$\mathcal{N} = \frac{\sum_k P\left([x]_k\right) \Delta V_k}{V}, \quad \Delta V_k = \prod_{j=1}^{l} \Delta x_{j,k}, \quad V = \sum_k \Delta V_k, \tag{5.8a}$$

where k varies from 1 to the number of total parameter combinations taken in the parameter volume, and $[x]_k$ is the kth combination of the parameters in the parameter volume. Hence, the normalized probability density is given by

$$\mathcal{P}\left([x]\right) = \frac{P\left([x]\right)}{\mathcal{N}}. \tag{5.8b}$$

5. The allowed parameter combinations for the bound orbits are governed by the condition, Eq. (4.8). For a spherical orbit, we have $e = 0$. Hence, we ensure that the parameters (e, r_p, a, Q) for eccentric and (r_s, a, Q) for spherical trajectories follow the bound orbit condition. If any parameter combination does not obey the bound orbit condition, then $\mathcal{P}\left([x]\right)$ is taken to be zero at that point in the parameter volume.

6. Next, we integrate the normalized probability density, $\mathcal{P}\left([x]\right)$, Equation (5.8b), in two dimensions to obtain the profile in the remaining third dimension of the parameters for BHXRBs with three simultaneous QPOs, and similarly by integrating in one dimension for the two QPO cases, we obtain the profile in the other dimension. So we finally obtain the one-dimensional distributions $\mathcal{P}_1\left(e\right)$, $\mathcal{P}_1\left(r_p\right)$, and $\mathcal{P}_1\left(a\right)$.

7. Finally, we fit the normalized probability density profiles in each of the parameter dimensions to find the corresponding mean values, and quoted errors are obtained such that they contain a probability of 68.2% about the peak value of the probability density. The results of these fits are given in Tables 5.4, 5.6, and 5.7.

8. For BHXRBs M82 X-1 and GRO J1655-40, we find various orbital solutions showing varying $\{a,\ Q\}$ values. As the spin of the black hole should be

fixed, we choose the most probable value of a, and then we estimate the remaining parameters $\{e,\, r_p,\, Q\}$, their profiles $\{\mathcal{P}_1\,(e),\, \mathcal{P}_1\,(r_p),\, \mathcal{P}_1\,(Q)\}$, and the corresponding errors using the same procedure given above in steps 1 to 6, where the orbital parameters are now given by $\{x_1,\, x_2,\, x_3\}$=$\{e,\, r_p,\, Q\}$.

9. Although we have made accurate calculations described above, to obtain a rough and quick estimate of the errors, we may use the following procedure. Assuming that the probability density is Gaussian distributed independently in e, r_p and a parameters, the normalized joint probability density distribution is given by

$$\mathcal{P}\,(e, r_p, a) = \frac{1}{(2\pi)^{3/2}\,\sigma_e \sigma_{r_p} \sigma_a} \exp\left\{-\frac{1}{2}\left[\left(\frac{e-e_0}{\sigma_e}\right)^2 + \left(\frac{r_p - r_{p0}}{\sigma_{r_p}}\right)^2 + \left(\frac{a-a_0}{\sigma_a}\right)^2\right]\right\}, \tag{5.9a}$$

where the distribution is centered at the exact solution (e_0, r_{p0}, a_0), and σ_e, σ_{r_p}, and σ_a are the corresponding 1σ errors, derived using the method described above. The total probability contained in a volume $\mathcal{V}$ in (e, r_p, a) space is given by

$$p = \frac{\int\int\int_{\mathcal{V}} \exp\left\{-\frac{1}{2}\left[\left(\frac{e-e_0}{\sigma_e}\right)^2 + \left(\frac{r_p - r_{p0}}{\sigma_{r_p}}\right)^2 + \left(\frac{a-a_0}{\sigma_a}\right)^2\right]\right\} \mathrm{d}e \cdot \mathrm{d}r_p \cdot \mathrm{d}a}{(2\pi)^{3/2}\,\sigma_e \sigma_{r_p} \sigma_a}; \tag{5.9b}$$

so that the total probability p inside an ellipsoid in $(e,\, r_p,\, a)$ space specified by

$$\left[\left(\frac{e-e_0}{\sigma_e}\right)^2 + \left(\frac{r_p - r_{p0}}{\sigma_{r_p}}\right)^2 + \left(\frac{a-a_0}{\sigma_a}\right)^2\right] = s_3^2, \tag{5.9c}$$

is given by

$$p = \sqrt{\frac{2}{\pi}} \int_0^{s_3} \exp\left(\frac{-s^2}{2}\right) s^2\, \mathrm{d}s = \frac{2}{\sqrt{\pi}} \gamma\left(\frac{3}{2}, \frac{s_3^2}{2}\right), \tag{5.9d}$$

where $\gamma\left(\frac{3}{2}, \frac{s_3^2}{2}\right)$ is the incomplete gamma function.

Similarly, for two QPO cases, the joint probability density distribution can be written as

$$\mathcal{P}\left(e, r_p\right) = \frac{1}{2\pi\sigma_e\sigma_{r_p}} \exp\left\{-\frac{1}{2}\left[\left(\frac{e-e_0}{\sigma_e}\right)^2 + \left(\frac{r_p - r_{p0}}{\sigma_{r_p}}\right)^2\right]\right\}. \tag{5.10a}$$

The total probability contained in a surface $\mathcal{S}$ in (e, r_p) space is given by

$$p = \frac{1}{2\pi\sigma_e\sigma_{r_p}} \int\int_{\mathcal{S}} \exp\left\{-\frac{1}{2}\left[\left(\frac{e-e_0}{\sigma_e}\right)^2 + \left(\frac{r_p - r_{p0}}{\sigma_{r_p}}\right)^2\right]\right\} \mathrm{d}e \cdot \mathrm{d}r_p. \tag{5.10b}$$

The total probability inside an ellipse, specified by

$$\left[\left(\frac{e-e_0}{\sigma_e}\right)^2 + \left(\frac{r_p - r_{p0}}{\sigma_{r_p}}\right)^2\right] = s_2^2, \tag{5.10c}$$

is given by

$$p = \int_0^{s_2} \exp\left(\frac{-s^2}{2}\right) s \, \mathrm{d}s = 1 - \exp\left(\frac{-s_2^2}{2}\right). \tag{5.10d}$$

For a given p, we can calculate s_3^2 and s_2^2, and hence evaluate the error

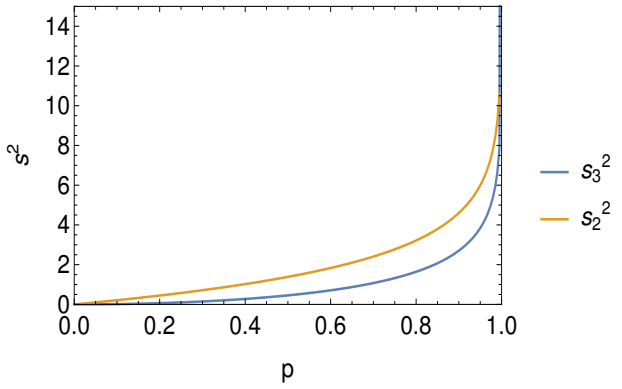

FIGURE 5.14: Figure showing s_3^2 and s_2^2 as a function of probability p given by Equations (5.9d) and (5.10d).

ellipsoid corresponding to p. ${s_2}^2$ and ${s_3}^2$ are shown as a functions of p in Figure 5.14. This can be used to get rough estimates of the error distribution of the parameters. However, we calculate them exactly in §5.3.2.

Next, we summarize the results corresponding to eQ and $e0$ models in §5.3.2.1 and $Q0$ model in §5.3.2.2.

5.3.2.1 Non-equatorial and equatorial eccentric orbits (eQ and $e0$)

We have taken the cases of five BHXRBs, known to have either three or two simultaneous detections of QPOs in their observations, to study the eccentric and nonequatorial trajectories as solutions to the QPOs assuming the GRPM. Here we summarize the results for the cases of three and two simultaneous QPOs separately, as discussed below:

1. *Three simultaneous QPOs*: In our analysis, varying the dimensionless parameter $Q = \{0, 1, 2, 3, 4\} \propto (L^2 - L_z^2)$ gives us various trajectory solutions having different $\{e,\, r_p,\, a,\, Q\}$ combinations. We first find the exact solutions for the parameters $\{e,\, r_p,\, a\}$, given in the Table 5.4, by equating the centroid frequencies of three simultaneous QPOs (see Table 5.3) to $\{\nu_\phi,\, \nu_{\rm pp},\, \nu_{\rm np}\}$ for each value of $Q = \{0, 1, 2, 3, 4\}$ using our analytic formulae (Eqs. (4.11)). We estimate errors for the parameters $\{e,\, r_p,\, a\}$ using the method discussed in §5.3.2 (see Figure 5.13) for each value of Q. The results of fits to the integrated profiles $\{\mathcal{P}_1\,(e),\, \mathcal{P}_1\,(r_p),\, \mathcal{P}_1\,(a)\}$ are summarized in the Table 5.4. Since the spin of the black hole is not expected to vary, we estimate the most probable spin value for these black holes and then estimate the orbital parameters $\{e,\, r_p,\, Q\}$ and their corresponding errors again using the same method discussed in §5.3.2 (see Figure 5.13). The results for each case are as follows:

   - *M82 X-1*: In this case, we find that the (non)equatorial trajectories with small to moderate eccentricities $e \sim 0.18-0.28$ with $r_p = 4.6-5.07$ and $a = 0.28-0.31$ (see Table 5.4) are possible exact solutions for the

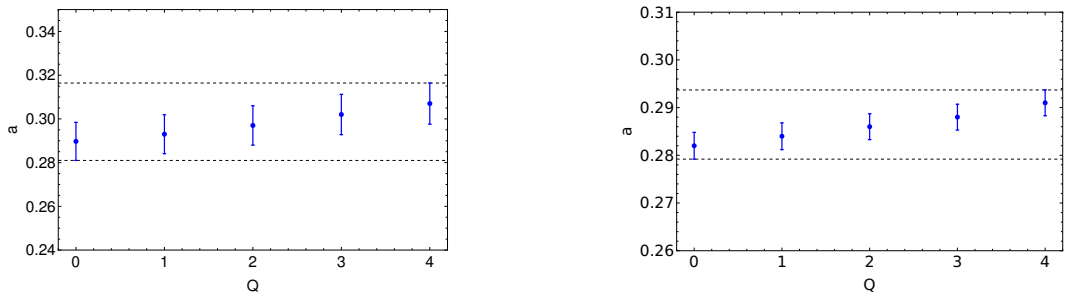

(a) (b)

FIGURE 5.15: The figures show 1σ errors in the spin parameters for various Q values for exact solutions of (a) M82 X-1, and corresponding to the peak of the probability distributions for (b) GRO J1655-40, as given in the Table 5.4. The upper and lower dashed curves correspond to the limits of the calculated errors. Although each Q value corresponds to a different spin of the black hole, the calculated values, and corresponding errors are within a narrow band which puts a sharp and reasonable constraint on the spin of the black hole.

observed QPO frequencies in M82 X-1, for Q between 0 and 4. Starting with these exact solutions, the most probable value of the spin is found first. In Fig 5.15(a), we show the spin variation in the parameter solutions for QPOs as a function of Q. Next, to estimate the most probable value of the spin, we minimize the function

$$\chi^2_a = \sum_i \frac{(a - a_i)^2}{\sigma^2_{a_i}}, \tag{5.11a}$$

which gives

$$a = \frac{\sum_i \left(a_i/\sigma^2_{a_i}\right)}{\sum_i \left(1/\sigma^2_{a_i}\right)}, \tag{5.11b}$$

where $i = 1 - 6$ corresponds to six probable solutions for a, and the σ_i values are the corresponding 1 σ errors, where five of these are given in Table 5.4, and the remaining one corresponds to the spherical orbit solution found for M82 X-1 given in Table 5.7. By including these six solutions, we have spanned the complete (e, Q) parameter space, which is bounded by $e0$ and $Q0$ solutions. This gives us the most probable spin value of $a = 0.2994$.

Hence, we fix the spin of the black hole to this most probable estimate

and then calculate the remaining parameters $\{e,\, r_p,\, Q\}$ and corresponding errors using the method given in §5.3.2 and Figure 5.13. We find the exact solution for QPOs at $\{e = 0.2302,\, r_p = 4.834,\, Q = 2.362\}$ calculated by equating centroid QPO frequencies to $\{\nu_\phi,\, \nu_{\rm pp},\, \nu_{\rm np}\}$ while fixing $a = 0.2994$. The probability density distribution profiles $\{\mathcal{P}_1\,(e),\, \mathcal{P}_1\,(r_p),\, \mathcal{P}_1\,(Q)\}$, along with their model fit, and the probability contours in the parameter plane $\{e,\, Q\}$, $\{r_p,\, e\}$, and $\{Q,\, r_p\}$ are shown in Figure 5.16. The results of the model fit to the integrated profiles are summarized in Table 5.5. The corresponding errors are quoted with respect to the exact solution of the parameters, which slightly differ from the peak of the integrated profiles $\{\mathcal{P}_1\,(e),\, \mathcal{P}_1\,(r_p),\, \mathcal{P}_1\,(Q)\}$, as expected (see Figure 5.16).

- *GRO J1655-40*: For this case, we did not find the exact solution for the parameters $\{e,\, r_p,\, a\}$ when the centroid frequencies of QPOs, Table 5.3, are equated to $\{\nu_\phi,\, \nu_{\rm pp},\, \nu_{\rm np}\}$. However, we generate the probability density profiles $\mathcal{P}_1\,(e)$, $\mathcal{P}_1\,(r_p)$, and $\mathcal{P}_1\,(a)$ for each value of Q between 0 and 4. The results of fits for these profiles are summarized in Table 5.4. We found that the probability density peaks near very small eccentricities $e \sim 0.05 - 0.07$ for various values of Q, whereas r_p ranges between 5.24 and 5.43 and a ranges between 0.282 and 0.291; see Table 5.4. The change in the value of the spin of the black hole as a function of Q is shown in Figure 5.15(b) for GRO J1655-40. Next, we find the most probable value of the spin for this BHXRB. Since we did not find any exact solution for the parameters by equating centroid frequencies of QPOs to the frequency formulae, we calculated the χ^2 function given by

$$\chi^2 = \frac{\left(\nu_\phi - \nu_{10}\right)^2}{\sigma_1^2} + \frac{\left(\nu_{\rm pp} - \nu_{20}\right)^2}{\sigma_2^2} + \frac{\left(\nu_{\rm np} - \nu_{30}\right)^2}{\sigma_3^2}, \qquad (5.12)$$

in the four-dimensional parameter space $\{e,\, r_p,\, a,\, Q\}$ using Eqs. (4.11) for $\{\nu_\phi,\, \nu_{\rm pp},\, \nu_{\rm np}\}$, and we numerically found the minimum $\chi^2 = 2.814$ for the parameter combination $\{e = 0.021,\, r_p = 5.51,\, a = 0.283,\, Q =$

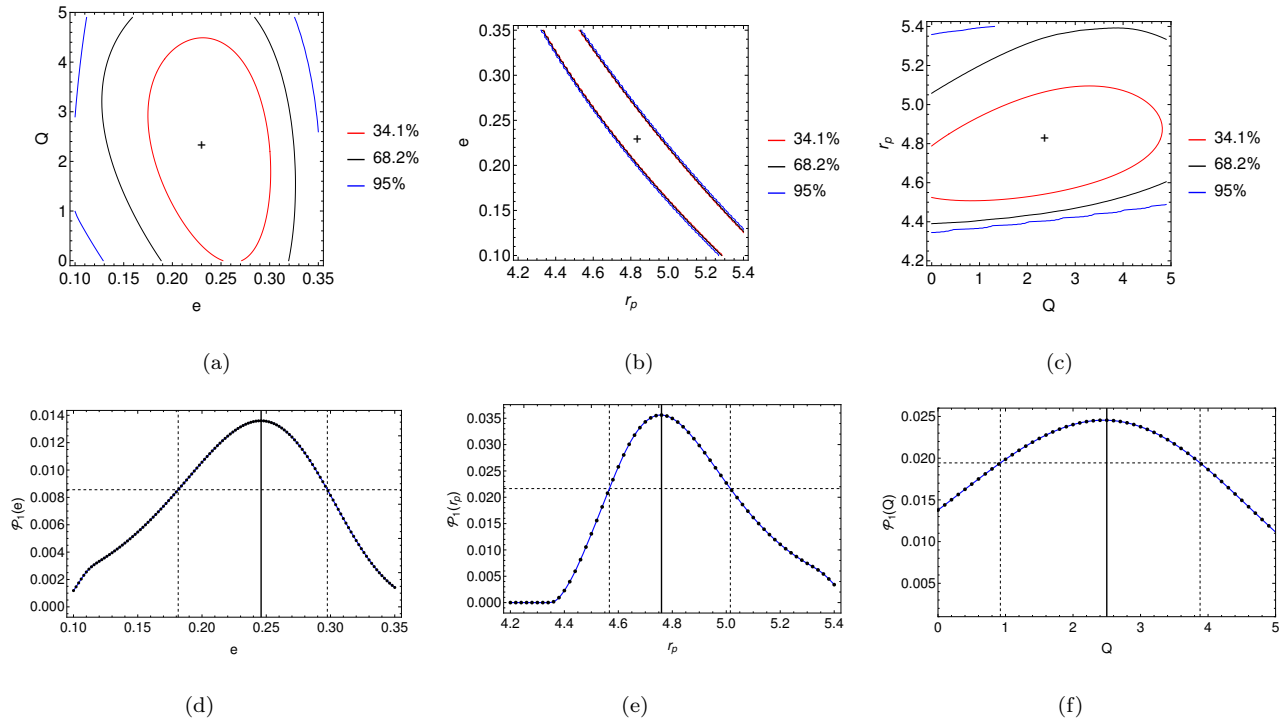

FIGURE 5.16: The probability contours in the parameter planes are shown in (a) $\{e, Q\}$, (b) $\{r_p, e\}$, and (c) $\{Q, r_p\}$, where the + sign marks the exact solution for the parameters for QPOs in M82 X-1 with $a = 0.2994$. The probability density profiles are shown in (d) $\mathcal{P}_1(e)$, (e) $\mathcal{P}_1(r_p)$, and (f) $\mathcal{P}_1(Q)$, where the black points represent integrated probability densities and the blue curves are their model fit. The dashed vertical lines enclose a region with 68.2% probability, and the solid vertical line marks the peak of the profiles.

0}. This is a primary coarse-grained search to find a viable solution of a. Next, we assume $a = 0.283$ corresponding to the minimum χ^2 to calculate the final solution for the parameters $\{e, r_p, Q\}$, which are the key parameters for the geometric study, using the more accurate fine-grid method described in §5.3.2 and Figure 5.13. We find that the probability density peaks near $\{e = 0.071, r_p = 5.25, Q = 0\}$. The results of fitting to the $\{\mathcal{P}_1(e), \mathcal{P}_1(r_p), \mathcal{P}_1(Q)\}$ profiles are summarized in the Table 5.5, whereas these profiles with their model fit and the probability contours in the parameter plane $\{e, Q\}$, $\{r_p, e\}$, and $\{Q, r_p\}$ are shown in Figure 5.17.

Hence, we conclude for both M82 X-1 and GRO J1655-40 that (non)equatorial

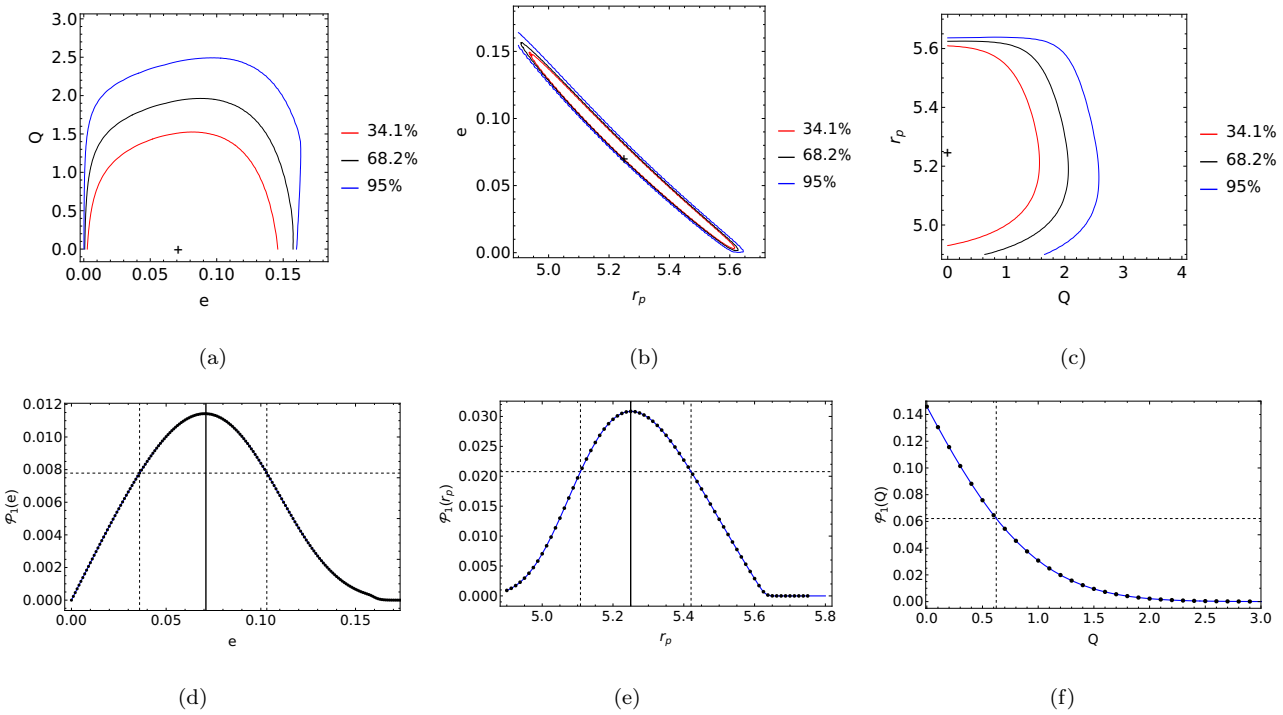

FIGURE 5.17: The probability contours in the parameter planes are shown in (a) $\{e, Q\}$, (b) $\{r_p, e\}$, and (c) $\{Q, r_p\}$, where the + sign marks the peak of the probability density for GRO J1655-40 with $a = 0.283$. The probability density profiles are shown in (d) $\mathcal{P}_1(e)$, (e) $\mathcal{P}_1(r_p)$, and (f) $\mathcal{P}_1(Q)$, where the dashed vertical lines enclose a region with 68.2% probability and the solid vertical line marks the peak of the profiles.

trajectories (both eQ and $e0$) with small or moderate eccentricities in the region very close to the black hole are the solutions for the observed QPOs assuming our GRPM. A self-emitting blob of matter close to a Kerr black hole can have enough energy and angular momentum to attain an eccentric and nonequatorial trajectory. These results are also consistent with the conclusions made in §5.2.1 that the trajectories having small to moderate eccentricities with $Q = 0 - 4$ are also possible solutions for the observed range of QPO frequencies in BHXRBs.

The errors in QPO frequencies cause to a distribution in the solution space $\{e, r_p, Q\}$ as solutions using our GRPM, as shown in Figures 5.16 and 5.17. We take various combinations of these parameters within the range of 1σ errors, as summarized in Table 5.5, as any such parameter combination is a

probable solution for the frequencies within the width of QPOs observed in the power spectrum. In Figure 5.18, we have plotted together the trajectories for these parameter combinations for both BHXRBs M82 X-1 and GRO J1655-40. Each trajectory has different parameter values $\{e,\ r_p,\ Q\}$ and is indicated by a different color, where we fixed the spin of the black hole to $a = 0.2994$ for M82 X-1 and $a = 0.283$ for GRO J1655-40. Hence, these trajectories, having fundamental frequencies very close to each other and within the width of the QPO, together simulate the strong rms of the observed QPOs. The trajectories together span a torus in the region $4.7 - 9.08$ for M82 X-1 and $5.11 - 6.67$ for GRO J1655-40, which should be the emission region for QPOs, where we expect precession frequencies of both the eQ and $e0$ trajectories. The ISCO radius is ~ 5 for both the cases of BHXRB. We suggest that the simultaneous HFQPO and LFQPO emission should be from a region that is close to the inner edge of the accretion disk ($r_{\rm in}$), where both eQ and $e0$ trajectories span a torus; the disk edge could be a source of blobs that are generating QPOs, as we will argue later in §5.5. In contrast, a rigid body precession model is invoked by some authors (Ingram *et al.* 2009; Ingram and Done 2011, 2012), where Lense−Thirring precession of a rigid torus is suggested as the origin of the type C QPOs. Here, instead of the rigid precession of a solid torus, we propose that a collective precession of various trajectories, spanning a torus region, explains the origin of HFQPOs and LFQPOs simultaneously. We argue that HFQPOs originate when $r_{\rm in}$ comes in very close to the black hole at some point during the outburst (the soft state). In the hard state, $r_{\rm in}$ is farther out, and the type C QPO is more frequent and it is more prone to the vertical oscillations ($\nu_{\rm np}$). This scenario explains the increase in the frequency of type C QPOs with a decrease in $r_{\rm in}$, while the spectrum transits from the hard to soft state.

2. *Two simultaneous QPOs*: We have considered only equatorial eccentric trajectories, Q=0, for these BHXRBs, as we can estimate only two parameters of the orbit corresponding to two simultaneous QPOs. First, we find the exact

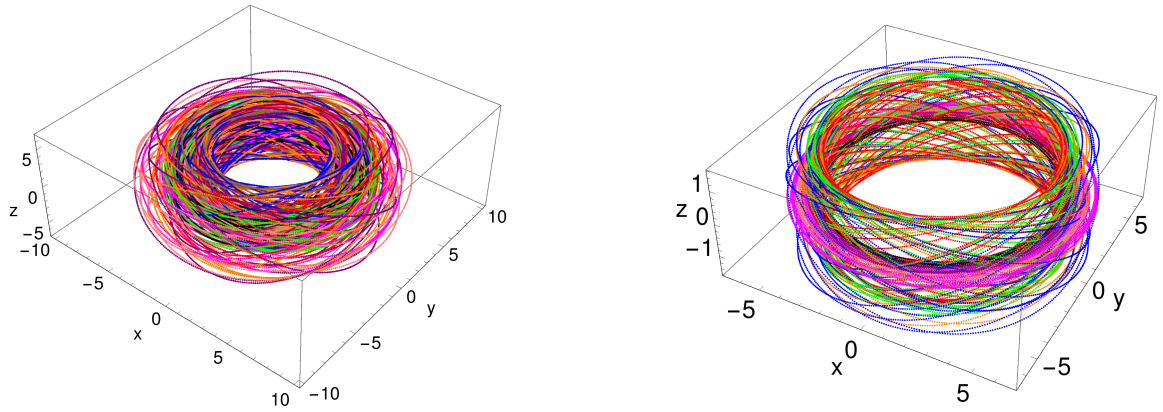

(a) (b)

FIGURE 5.18: The figures show various trajectories together having parameter combinations $\{e,\, r_p,\, Q\}$ within the estimated range of 1σ errors, as tabulated in the Table 5.5, for (a) M82 X-1 and (b) GRO J1655-40. The spin of the black hole is fixed to the most probable estimates, which are $a = 0.2994$ for M82 X-1 and $a = 0.283$ for GRO J1655-40. Each color corresponds to a different parameter combination, where $\{e = 0.18 - 0.29;\, r_p = 4.7 - 5;\, Q = 1 - 4\}$ for M82 X-1 and $\{e = 0.035 - 0.103;\, r_p = 5.11 - 5.42;\, Q = 0 - 0.6234\}$ for GRO J1655-40.

solutions for the parameters $\{e,\, r_p\}$, summarized in Table 5.6, by equating the centroid frequencies of two simultaneous QPOs (see Table 5.3) to $\{\nu_\phi,\, \nu_{\rm pp}\}$ using our analytic formulae for Q=0, Eqs. (4.14). Then we calculate the errors in the parameters $\{e,\, r_p\}$ using the method discussed in §5.3.2 (see Figure 5.13). The results are summarized in Table 5.6. These results are described below:

- *XTE J1550-564*: We find that an equatorial trajectory with eccentricity $e = 0.262$ with $r_p = 4.365$ (see Table 5.6) as a solution for the observed QPO frequencies in XTE J1550-564. The calculated probability density profiles in e and r_p dimensions, $\mathcal{P}_1\,(e)$ and $\mathcal{P}_1\,(r_p)$, were found to be skew symmetric and were fit by an interpolating function. The corresponding errors were obtained by taking the integrated probability of 68.2% about the peak value of the probability density distributions. The quoted errors are calculated with respect to the exact solution of the parameters, which slightly deviates from the peak of the integrated

profiles $\{\mathcal{P}_1(e)$ and $\mathcal{P}_1(r_p)\}$; see Figure 5.19 and Table 5.6. These profiles, corresponding model fit, and the probability contours in the (e, r_p) plane are shown in Figure 5.19.

- *4U 1630-47*: We found an exact solution at $\{e = 0.734,\ r_p = 2.249\}$ (see Table 5.6) by equating $\{\nu_\phi,\ \nu_{\rm np}\}$ instead of $\{\nu_\phi,\ \nu_{\rm pp}\}$ to the centroid QPO frequencies. This might be because the QPO with a lower frequency of $\sim$ 38Hz (see Table 5.3) is too small to be an HFQPO. The calculated probability density profiles in the e and r_p dimensions, the corresponding model fit, and the probability contours in the (e, r_p) plane are shown in Figure 5.20. In this case, too, we see that $\mathcal{P}_1(e)$ and $\mathcal{P}_1(r_p)$ profiles are skew, such that the integrated probability is 68.2% about the peak value of the probability density distributions, and the errors are quoted with respect to the exact solution of the parameters, which slightly deviates from the peak of the integrated profiles $\mathcal{P}_1(e)$ and $\mathcal{P}_1(r_p)$ (see Figure 5.20 and Table 5.6). We see that a highly eccentric orbit is found as the most probable solution.

- *GRS 1915+105*: We found an exact solution at $\{e = 0.918,\ r_p = 1.744\}$; see Table 5.6. We find a highly eccentric equatorial trajectory as the most probable solution that can give the observed QPO frequencies in GRS 1915+105. This result is similar to the case of 4U 1630-47, which leads us to observe that a black hole with a high spin value prefers a highly eccentric orbit solution to simultaneous QPOs. The calculated probability density profiles $\mathcal{P}_1(e)$ and $\mathcal{P}_1(r_p)$ are well fit by the Gaussian. The corresponding model fit and the probability contours in the (e, r_p) plane are shown in Figure 5.21.

Hence, we conclude that for XTE J1550-564, 4U 1630-47, and GRS 1915+105, the $e0$ model in the region $r_p = 1.74 - 4.36$ are the probable cause of the observed QPOs in the power spectrum. We found high eccentricity values for the orbits as solutions for QPOs in the cases of BHXRB 4U 1630-47

TABLE 5.4: Summary of results corresponding to (Non)equatorial eccentric solutions (eQ and $e0$) for BHXRBs M82 X-1 and GRO J1655-40. The columns describe the range of parameter volume considered for $\{e,\, r_p,\, a\}$ with a chosen resolution to calculate the normalized probability density at each point inside the parameter volume using Equation (5.8b), the exact solutions for $\{e,\, r_p,\, a\}$ calculated using Eqs. (4.11), and the results of the model fit to $\mathcal{P}_1\,(e)$, $\mathcal{P}_1\,(r_p)$, and $\mathcal{P}_1\,(a)$, for each value of Q between 0 and 4.

BHXRB	Q	e **range**	**Resolution** Δe	**Exact solution** e_0	**Model fit to** $\mathcal{P}_1\,(e)$	r_p **range**	**Resolution** Δr_p	**Exact solution** r_{p0}	**Model fit to** $\mathcal{P}_1\,(r_p)$	a **range**	**Resolution** Δa	**Exact solution** a_0	**Model fit to** $\mathcal{P}_1\,(a)$
M82 X-1	0	$0.23 - 0.32$	0.001	0.277	$0.277^{+0.066}_{-0.045}$	$4.4 - 4.85$	0.005	4.616	$4.616^{+0.069}_{-0.126}$	$0.26 - 0.32$	0.001	0.290	0.290 ± 0.009
	1	$0.21 - 0.31$	0.001	0.259	$0.259^{+0.072}_{-0.045}$	$4.3 - 5$	0.01	4.698	$4.698^{+0.068}_{-0.154}$	$0.265 - 0.315$	0.001	0.294	0.294 ± 0.009
	2	$0.19 - 0.29$	0.001	0.239	$0.239^{+0.080}_{-0.046}$	$4.45 - 5.1$	0.01	4.795	$4.795^{+0.066}_{-0.166}$	$0.27 - 0.32$	0.001	0.298	0.298 ± 0.009
	3	$0.16 - 0.26$	0.001	0.214	$0.214^{+0.090}_{-0.045}$	$4.55 - 5.25$	0.01	4.913	$4.913^{+0.081}_{-0.163}$	$0.28 - 0.33$	0.001	0.302	0.302 ± 0.009
	4	$0.12 - 0.24$	0.001	0.187	$0.187^{+0.113}_{-0.047}$	$4.65 - 5.35$	0.01	5.067	$5.067^{+0.076}_{-0.221}$	$0.285 - 0.335$	0.001	0.308	0.308 ± 0.009
GRO J1655-40	0	$0 - 0.22$	0.002	-	$0.07^{+0.042}_{-0.038}$	$4.6 - 5.7$	0.01	-	$5.24^{+0.191}_{-0.186}$	$0.265 - 0.3$	0.001	-	0.282 ± 0.003
	1	$0 - 0.22$	0.002	-	$0.062^{+0.040}_{-0.034}$	$4.6 - 5.8$	0.015	-	$5.305^{+0.170}_{-0.185}$	$0.24 - 0.32$	0.002	-	0.284 ± 0.003
	2	$0 - 0.2$	0.002	-	$0.056^{+0.038}_{-0.031}$	$4.7 - 5.85$	0.015	-	$5.345^{+0.167}_{-0.169}$	$0.27 - 0.31$	0.001	-	0.286 ± 0.003
	3	$0 - 0.2$	0.002	-	$0.052^{+0.036}_{-0.029}$	$4.75 - 5.9$	0.015	-	$5.395^{+0.151}_{-0.170}$	$0.275 - 0.32$	0.001	-	0.288 ± 0.003
	4	$0 - 0.2$	0.002	-	$0.05^{+0.034}_{-0.028}$	$4.8 - 5.95$	0.015	-	$5.43^{+0.147}_{-0.162}$	$0.278 - 0.31$	0.001	-	0.291 ± 0.003

TABLE 5.5: Summary of results for $\{e, r_p, Q\}$ parameter solutions and corresponding errors for QPOs in BHXRBs M82 X-1 and GRO J1655-40. The columns describe the range of parameter volume taken for $\{e, r_p, Q\}$, and the chosen resolution to calculate the normalized probability density at each point inside the parameter volume, the exact solutions, and the results of the model fit to the integrated profiles. The spin of the black hole is fixed to the most probable estimates, which are $a = 0.2994$ for M82 X-1 and $a = 0.283$ for GRO J1655-40.

BHXRB	e **range**	**Resolution** Δe	**Exact solution** e_0	**Model fit to** $\mathcal{P}_1(e)$	r_p **range**	**Resolution** Δr_p	**Exact solution** r_{p0}	**Model fit to** $\mathcal{P}_1(r_p)$	Q **range**	**Resolution** ΔQ	**Exact solution** Q_0	**Model fit to** $\mathcal{P}_1(Q)$
M82 X-1	$0.1 - 0.35$	0.002	0.230	$0.230^{+0.067}_{-0.049}$	$4.2 - 5.4$	0.02	4.834	$4.834^{+0.181}_{-0.268}$	$0 - 5$	0.1	2.362	$2.362^{+1.519}_{-1.439}$
GRO J1655-40	$0 - 0.18$	0.001	-	$0.071^{+0.031}_{-0.035}$	$4.9 - 5.75$	0.0125	-	$5.25^{+0.171}_{-0.142}$	$0 - 3$	0.1	-	$0^{+0.623}$

TABLE 5.6: Summary of results corresponding to the equatorial eccentric orbit solutions for BHXRBs XTE J1550-564, 4U 1630-47, and GRS 1915+105. The columns describe the parameter range considered for $\{e,\, r_p\}$, its resolution, the exact solutions for $\{e,\, r_p\}$ calculated using $\{\nu_\phi,\, \nu_{\rm pp}\}$ for XTE J1550-564 and GRS 1915+105, and using $\{\nu_\phi,\, \nu_{\rm np}\}$ for 4U 1630-47 using Eqs. (4.14), and results of the model fit to $\mathcal{P}_1\,(e)$ and $\mathcal{P}_1\,(r_p)$.

BHXRB	e **range**	**Resolution** Δe	**Exact solution** e_0	**Model fit to** $\mathcal{P}_e\,(e)$	r_p **range**	**Resolution** Δr_p	**Exact solution** r_{p0}	**Model fit to** $\mathcal{P}_{r_p}\,(r_p)$
XTE J1550-564	$0.01 - 0.7$	0.0005	0.262	$0.262^{+0.090}_{-0.062}$	$2.5 - 6.5$	0.005	4.365	$4.365^{+0.169}_{-0.279}$
4U 1630-47	$0.4 - 0.99$	0.0005	0.734	$0.734^{+0.066}_{-0.048}$	$1 - 4.5$	0.005	2.249	$2.249^{+0.249}_{-0.353}$
GRS 1915+105	$0.6 - 0.999$	0.0005	0.918	0.918 ± 0.002	$0.3 - 4$	0.005	1.744	$1.744^{+0.025}_{-0.011}$

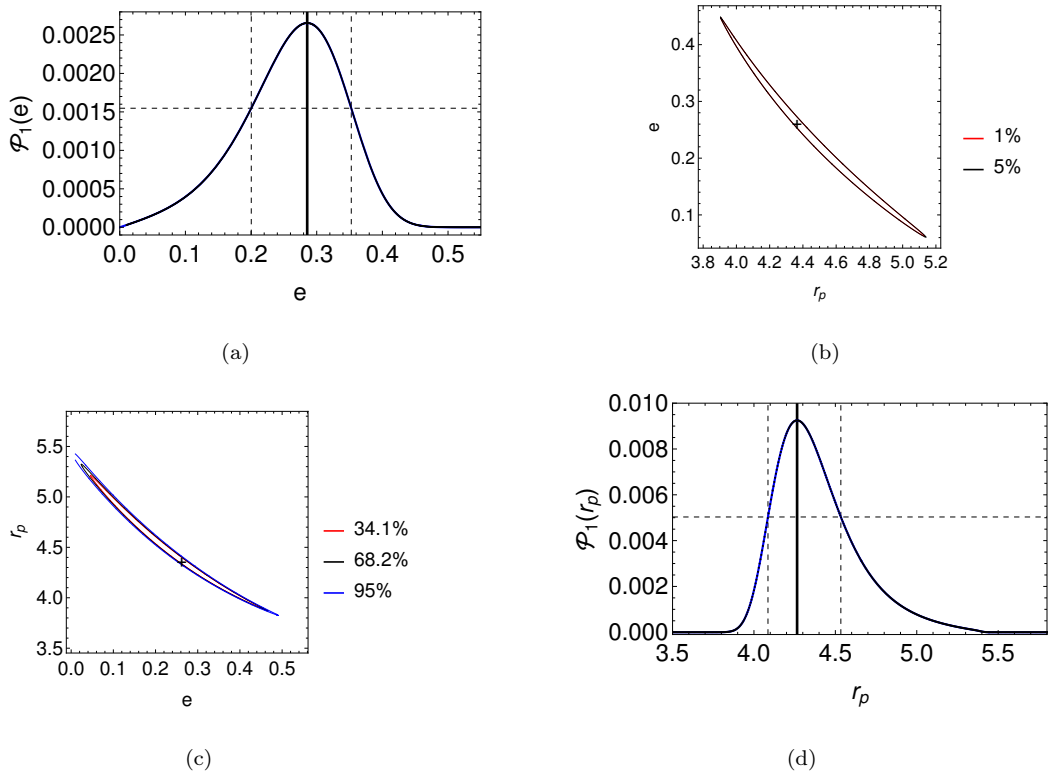

FIGURE 5.19: The integrated density profiles of BHXRB XTE J1550-564 are shown in (a) $\mathcal{P}_1\,(e)$ and (d) $\mathcal{P}_1\,(r_p)$, where the dashed vertical lines enclose a region with 68.2% probability, and the solid vertical line corresponds to the peak of the profiles. The probability contours of the parameter solution are shown in the (b) $(r_p,\, e)$ and (c) $(e,\, r_p)$ planes, where the + sign marks the exact solution.

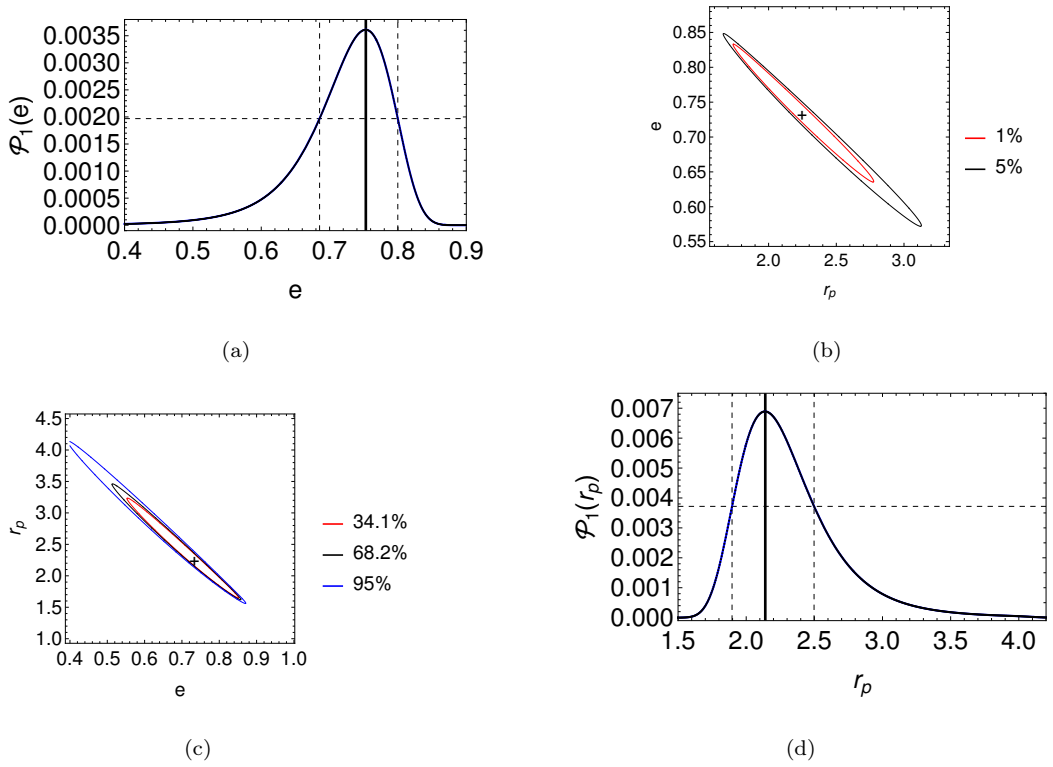

FIGURE 5.20: The integrated density profiles are shown in (a) $\mathcal{P}_1(e)$ and (d) $\mathcal{P}_1(r_p)$ for BHXRB 4U 1630-47, where the dashed vertical lines enclose a region with 68.2% probability, and the solid vertical line corresponds to the peak of the profiles. The probability contours of the parameter solution are shown in the (b) (r_p, e) and (c) (e, r_p) planes, where the + sign marks the exact solution.

and GRS 1915+105, and this indicates that black holes with very high spin values prefer highly eccentric orbits in the QPO solutions.

We show all of the eccentric trajectory solutions together for both $Q = 0$ and $Q \neq 0$ in Figure 5.22 in the (r_p, a) plane along with the radii ISCO (ISSO), MBCO (MBSO), light radius, and the horizon. We see that the calculated eccentric orbit solutions are found in region 1 of the (r_p, a) plane (as defined in Figure 5.4) and near ISCO for $Q = 0$ in the cases of BHXRB 4U 1630-47, GRO J1655-40, and GRS 1915+105. The trajectory solutions are found in region 2 near ISCO for XTE J1550-564 ($Q = 0$) and near ISSO for M82 X-1 ($Q = 2.362$; as defined in Figure 5.4). These results are also consistent with the results discussed in §5.2.1, except that very high e values are found for trajectories in BHXRB 4U 1630-47 and GRS

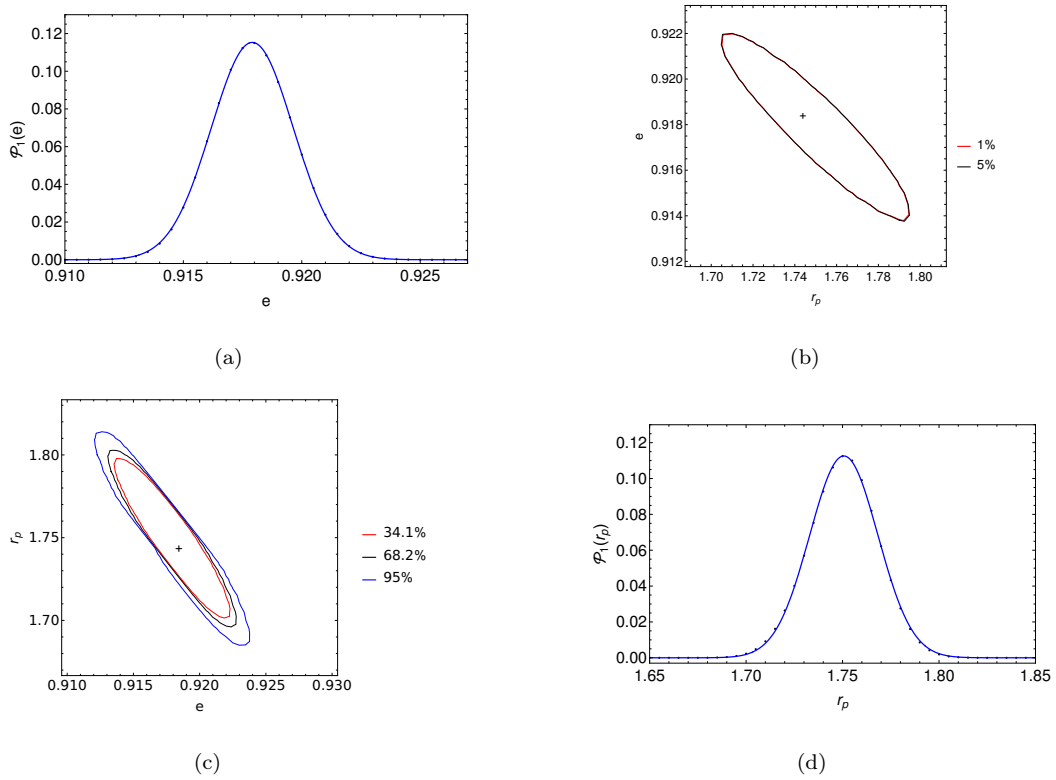

FIGURE 5.21: The integrated density profiles are shown in (a) $\mathcal{P}_1(e)$ and (d) $\mathcal{P}_1(r_p)$ for BHXRB GRS 1915+105, where the dashed vertical lines enclose a region with 68.2% probability, and the solid vertical line corresponds to the peak of the profiles. The probability contours of the parameter solution are shown in the (b) (r_p, e) and (c) (e, r_p) planes, where the + sign marks the exact solution.

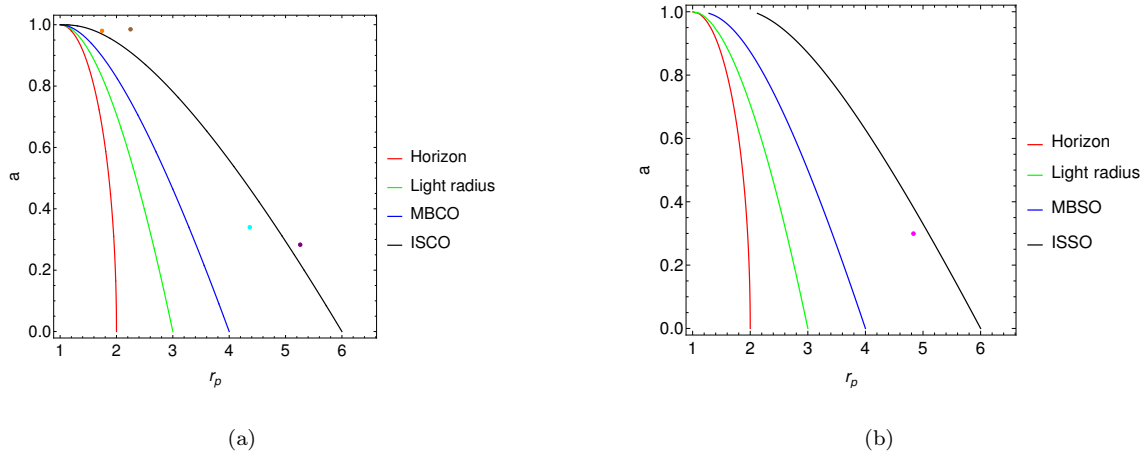

FIGURE 5.22: Equatorial eccentric orbit solutions for QPOs observed in BHXRBs GRO J1655-40 (purple), XTE J1550-564 (cyan), 4U 1630-47 (brown), and GRS 1915+105 (orange) for (a) $Q = 0$; and (b) the nonequatorial eccentric orbit solution for BHXRB M82 X-1 (magenta) for $Q = 2.362$.

1915+105. Hence, we conclude that the eccentric trajectory solutions with $Q = 0$ and $Q \neq 0$ for the observed QPOs in BHXRBs are found either in the region 1 or region 2 of the (r_p, a) plane but close to the ISCO (ISSO) curve; we call this radius as R_0. As all these orbit solutions are distributed near R_0, it is expected that this radius is very close to the inner edge radius, $r_{\rm in}$, of the circular accretion disk, which could also be a source of blobs that are generating these QPOs. The torus region, shown in Figure 5.18, spans a part of regions 1 and 2 near R_0, which can be represented as $\left(R_0{}^{+\Delta_1}_{-\Delta_2}\right)$, where Δ_i represents a small deviation from R_0 (which need not be the center point of the torus in this scenario). This means that the orbits near R_0 are induced by the instabilities in the inner flow to be (non)equatorial and eccentric.

5.3.2.2 Spherical Orbits

Here we summarize the results of associating the spherical orbits around a Kerr black hole with QPOs in BHXRBs. We limited this study to the cases of BHXRBs M82 X-1 and XTE J1550-564, as we found the exact solutions for the parameters $\{r_s,\ a,\ Q\}$ or $\{r_s,\ a\}$ for only these two BHXRBs when we solved $\{\nu_\phi = \nu_{10},\ \nu_{\rm pp} = \nu_{20},\ \nu_{\rm np} = \nu_{30}\}$ for M82 X-1 and $\{\nu_\phi = \nu_{10},\ \nu_{\rm pp} = \nu_{20}\}$ for XTE J1550-564 using Equations (4.23-4.25c). We calculated errors for the parameters using the method discussed in §5.3.2 (also see Figure 5.13); these results are summarized in the Table 5.7 and are presented below:

- *M82 X-1*: We found the exact solution for a spherical orbit at $\{r_s = 6.044,\ a = 0.321,\ Q = 6.113\}$ for M82 X-1. The spherical trajectory with these parameter values is shown in Figure 5.23(a). The calculated probability density profiles and the model fit are shown in Figure 5.24. The $\mathcal{P}_1\left(r_s\right)$ and $\mathcal{P}_1\left(Q\right)$ profiles were found to be skew symmetric, and the integrated probability is 68.2% about the peak of the probability density distribution

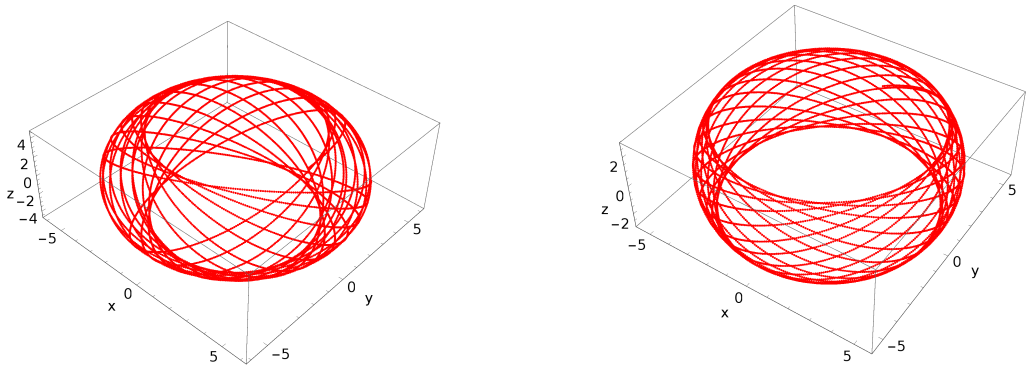

(a) (b)

FIGURE 5.23: Spherical trajectories corresponding to the exact solutions calculated for (a) M82 X-1 at $\{r_s = 6.044,\ a = 0.321,\ Q = 6.113\}$ and for (b) XTE J1550-564 at $\{r_s = 5.538,\ a = 0.34,\ Q = 2.697\}$, as also provided in Table 5.7.

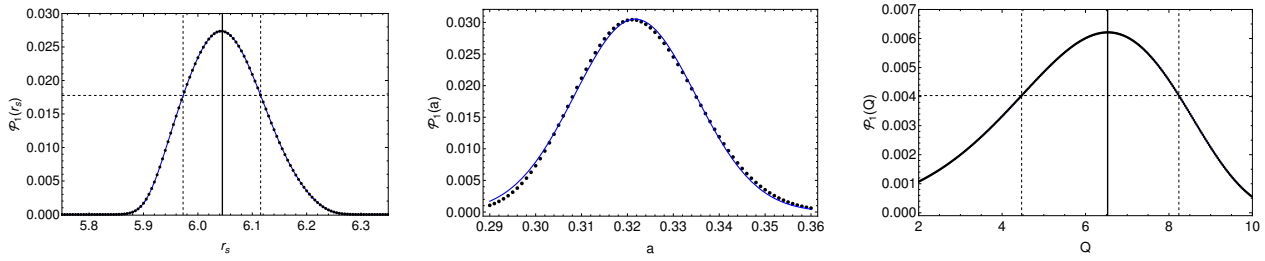

(a) (b) (c)

FIGURE 5.24: Probability density profiles in $\{r_s, a, Q\}$ dimensions for M82 X-1: (a) $\mathcal{P}_1(r_s)$, (b) $\mathcal{P}_1(a)$, and (c) $\mathcal{P}_1(Q)$. The black points represent normalized probability density profiles generated using the method described in §5.3.2, and the blue curves are the model fit, and the results are summarized in Table 5.7. The errors for the $\mathcal{P}_1(r_s)$ and $\mathcal{P}_1(Q)$ profiles are obtained such that the integrated probability between the vertical dashed curves is 68.2%, whereas the vertical thick curves correspond to the peak value of the reduced probability density distributions.

between the error bars, while $\mathcal{P}_1(a)$ is well fit by a Gaussian. We see that the spin of the black hole is also found very close to the spin solutions estimated in §5.3.2.1. We conclude that along with the eQ trajectories having moderate eccentricities, as discussed in §5.3.2.1, a spherical trajectory ($Q0$) at $r_s = 6.044$ with $Q = 6.113$ is also a viable solution that can produce the observed QPO frequencies in M82 X-1. The corresponding spin estimate $a = 0.321 \pm 0.0132$ was utilized in §5.3.2.1 using Equation (5.11b) to calculate

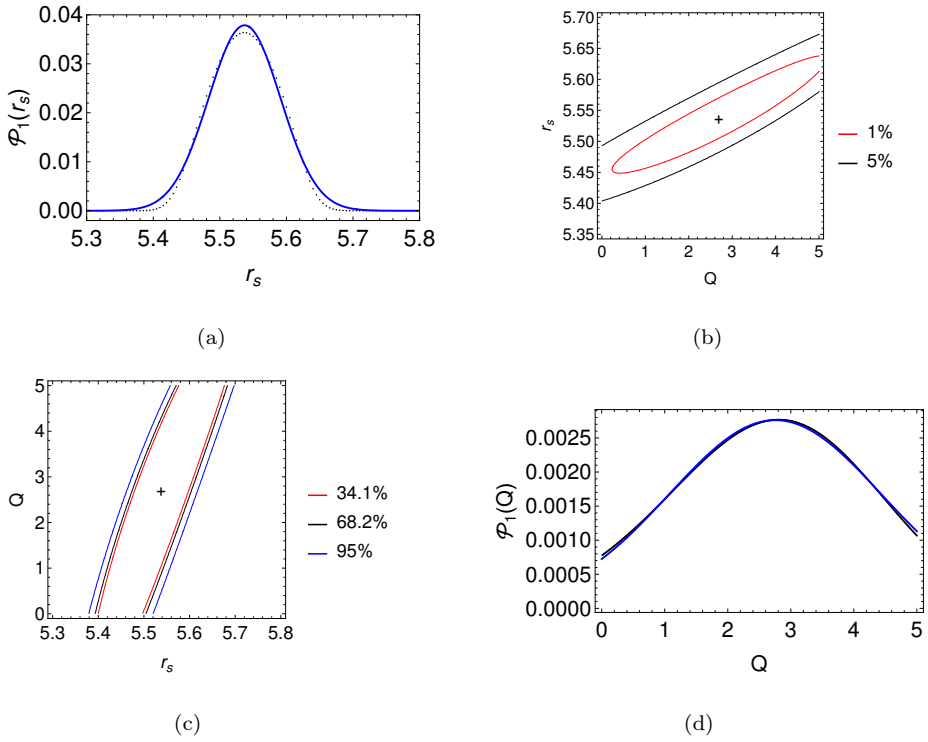

FIGURE 5.25: The integrated density profiles are shown in (a) $\mathcal{P}_1(r_s)$ and (d) $\mathcal{P}_1(Q)$ for the spherical orbit solution of BHXRB XTE J1550-564, where the dashed vertical lines enclose a region with 68.2% probability, and the solid vertical line corresponds to the peak of the profiles. The probability contours of the parameter solution are shown in the (b) (Q, r_s) and (c) (r_s, Q) planes, where the + sign marks the exact solution.

the most probable value of the spin for M82 X-1.

- *XTE J1550-564*: A spherical trajectory solution was found at $r_s = 5.538$ and $Q = 2.697$ for BHXRB XTE J1550-564 that is shown in Figure 5.23(b), and the calculated probability density profiles, the Gaussian model fit, and the probability contours in the $\{r_s, Q\}$ plane are shown in Figure 5.25. So, along with an $e0$ trajectory, as discussed in §5.3.2.1, a $Q0$ orbit is also a viable candidate for the observed QPOs in the temporal power spectrum of XTE J1550-564.

We found that the spherical trajectories are also possible solutions for QPOs in BHXRBs M82 X-1 ($a = 0.321$, $Q = 6.113$, $r_s = 6.044$, $r_I = 5.258$) and XTE

TABLE 5.7: Summary of results corresponding to the spherical orbit solutions for BHXRBs M82 X-1 and XTE J1550-564. The columns describe the range of parameter volume considered for $\{r_s, a, Q\}$ and its resolution to calculate the normalized probability density using Equation (5.8b), the exact solutions for $\{r_s, a, Q\}$ calculated using Equations (4.23-4.25c), the value of parameters corresponding to the peak of the integrated profiles in $\{r_s, a, Q\}$, and results of the model fit to $\mathcal{P}_1(r_s)$, $\mathcal{P}_1(Q)$, and $\mathcal{P}_1(a)$.

BHXRB	r_s **Range**	**Resolution** Δr_s	**Exact Solution** r_{s0}	**Model Fit to** $\mathcal{P}_1(r_s)$	Q **Range**	**Resolution** ΔQ	**Exact Solution** Q_0	**Model Fit to** $\mathcal{P}_1(Q)$	a **Range**	**Resolution** Δa	**Exact Solution** a_0	**Model Fit to** $\mathcal{P}_1(a)$
M82 X-1	$5.75-6.35$	0.005	6.044	$6.044^{+0.071}_{-0.072}$	$2-10$	0.03	6.113	$6.113^{+2.124}_{-1.645}$	$0.29-0.36$	0.001	0.321	0.321 ± 0.013
XTE J1550-564	$3-8$	0.005	5.538	5.538 ± 0.054	$0.01-5$	0.01	2.697	$2.697^{+1.738}_{-1.627}$	-	-	-	-

J1550-564 (a = 0.34, Q = 2.697, r_s = 5.538, r_I = 4.988). This indicates that the spherical trajectory solutions are in region 1 of the (r, a) plane, as defined in Figure 5.4; for both BHXRBs, and they are very close to the ISSO radius, r_I. These results are also consistent with the results discussed in §5.2.2, where the QPO-generating region is close to the ISSO curve in the (r, a) plane. For the case of M82 X-1, the spherical trajectory solution has a different value of spin compared to the ones estimated in §5.3.2.1, but it is very close to the other estimates given in Table 5.4. This value of spin, together with other results in Table 5.4, is used to estimate the most probable value of spin of the black hole for M82 X-1, which is $a = 0.2994$. We also see that a low eccentric trajectory prefers a high Q value and vice versa, as seen from the results shown in Table 5.4. As the Q value of the orbit is increased, the eccentricity of the trajectory solution decreases for both BHXRBs M82 X-1 and GRO J1655-40. This trend is also followed here: for the spherical orbit ($e = 0$), $Q \sim 6$ is found as a solution for M82 X-1 and $Q \sim 2.7$ for XTE J1550-564, whereas a moderately eccentric trajectory solution was found with $Q = 0$ for XTE J1550-564; see Table 5.6.

We conclude that various kinds of Kerr orbits, for example, spherical $\{e = 0, Q \neq 0\}$, equatorial eccentric $\{e \neq 0, Q = 0\}$, and nonequatorial eccentric $\{e \neq 0, Q \neq 0\}$, are also viable solutions for QPOs in BHXRBs. Hence, such trajectories with similar fundamental frequencies can together give a strong QPO signal in the temporal power spectrum.

5.4 The PBK correlation

A tight correlation between the frequencies of two components in the PDS of various sources, including black hole and neutron star X-ray binaries, was discovered (Psaltis *et al.* 1999). Such a correlation among various variability components

of the PDS in both types of sources suggests a common and important emission mechanism for these signals. This correlation is either between two QPOs, an LFQPO and either of the two HFQPOs, or it is between an LFQPO and high-frequency broadband noise components. We adopt the definition of Belloni *et al.* (2002) for these variability components: $L_{\rm LF}$ for LFQPO, and L_l and L_u for lower and upper HFQPOs or broad noise components. A systematic study of 571 RXTE observations was carried out for BHXRB GRO J1655-40 between 1996 March and 2005 October (Motta *et al.* 2014a), and they also found such correlation between the type C QPOs and high-frequency QPOs and broadband components (either L_l or L_u; see Tables 1 and 2 and Figure 5 of Motta *et al.* (2014a)). In this study, they calculated mass, spin of the black hole, and the radius at which QPOs originated $\{\mathcal{M} = 5.31,\ a = 0.29,\ r = 5.68\}$ (Motta *et al.* 2014a) using $\{L_u = \nu_\phi,\ L_l = \nu_{\rm pp},\ L_{\rm LF} = \nu_{\rm np}\}$, assuming that circular equatorial orbits are the origin of three simultaneous QPOs in the RPM (00 model as defined in Figure 5.1). Using the estimated values of $\mathcal{M}$ and a, they fit the PBK correlation of variability components in GRO J1655-40 by varying r.

Here we apply the $e0$ model solution calculated in §5.3.2.1 assuming $\{L_u = \nu_\phi,\ L_l = \nu_{\rm pp},\ L_{\rm LF} = \nu_{\rm np}\}$, using the observation ID having three simultaneous QPOs detected in GRO J1655-40 (shown in Table 5.3), to fit the PBK correlation. We fix the mass of the black hole to $\mathcal{M} = 5.4$ (Beer and Podsiadlowski 2002) and the spin of the black hole to the most probable value, $a = 0.283$, estimated by minimizing the χ^2 function, given by Equation (5.12). We fix e and Q to the values estimated by the fine-grid method $\{e = 0.071,\ Q = 0\}$ and vary r_p to calculate the frequencies. In Figure 5.26, we show the correlations of the frequencies corresponding to the parameters $\{e = 0.071,\ a = 0.283,\ Q = 0\}$, which are in good agreement with the PBK correlation. In Figure 5.27, these frequencies are shown as functions of r_p. We see that the data points for L_u components fit very well (see Figure 5.26(a)), whereas the L_l components show a good fit in the high-frequency range [see Figures 5.26(b),5.26(c)]. The $L_{\rm LF}$ components also show good agreement with

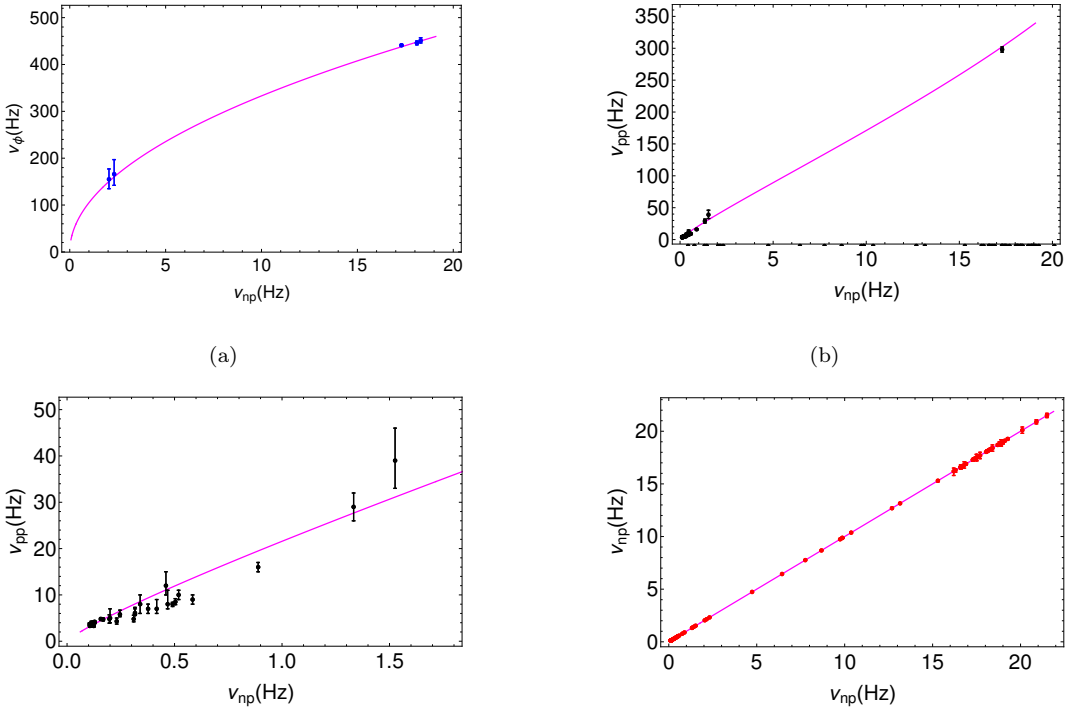

FIGURE 5.26: The PBK correlation is shown for BHXRB GRO J1655-40 as previously observed [data points are from Motta *et al.* (2014a)]. The observed correlation is in good agreement with the frequencies of the $e0$ solution estimated, where $\{e = 0.071,\ a = 0.283,\ Q = 0,\ \mathcal{M} = 5.4\}$, for GRO J1655-40 in §5.3.2.1, where (a) ν_ϕ, (b) $\nu_{\rm pp}$ in the high-frequency range, (c) $\nu_{\rm pp}$ in the low-frequency range, and (d) $\nu_{\rm np}$ are shown. The blue, black, and red data points represent the L_u, L_l, and $L_{\rm LF}$ components of the PDS, respectively. The magenta curves show the theoretical values of frequencies.

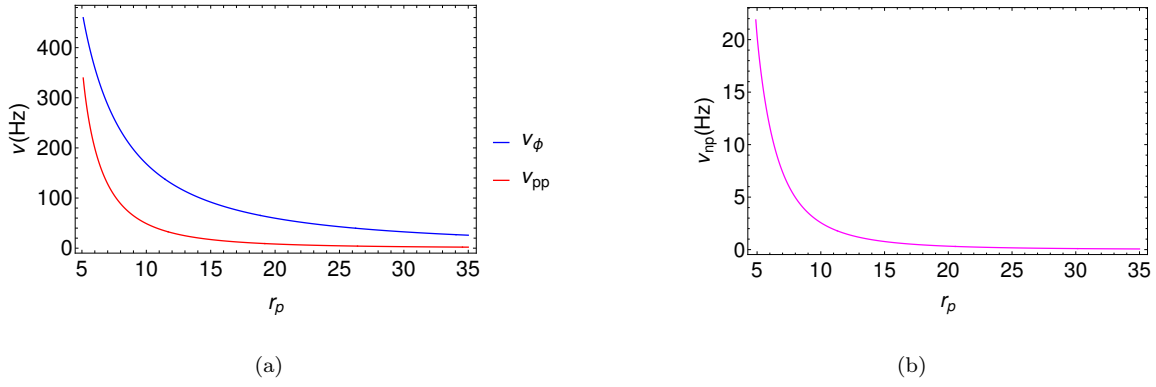

FIGURE 5.27: The frequencies (a) ν_ϕ and $\nu_{\rm pp}$, (b) $\nu_{\rm np}$ are shown as function of r_p, for the $e0$ solution vector $\{e = 0.071,\ a = 0.283,\ Q = 0,\ \mathcal{M} = 5.4\}$.

TABLE 5.8: Nonequatorial eccentric Orbit (eQ) solutions for L_l and $L_{\rm LF}$ components detected in RXTE observations of GRO J1655-40 (Motta *et al.* 2014a), where the first row corresponds to the observation ID with three simultaneous QPOs. The mass of the black hole was fixed to $\mathcal{M} = 5.4$ and spin was fixed to $a = 0.283$.

L_{LF} (Hz)	L_l (Hz)	r_p	e	Q
17.3	298	5.25	0.071	0
0.106	3.3	29.179	0.077	24.423
0.117	3.9	28.228	0.083	33.903
0.123	4	27.758	0.083	33.392
0.128	4	27.389	0.083	32.642
0.11	3.5	28.818	0.082	33.622
0.115	3.7	28.392	0.083	34.028
0.128	4.2	27.389	0.083	33.010
0.157	4.8	25.576	0.083	30.964
1.333	29	12.464	0.079	10.921
0.46	12	17.826	0.085	22.343

the eccentric orbit solution (see Figure 5.26(d)).

Thirty-four L_l and $L_{\rm LF}$ components which were detected simultaneously in the same observation ID [see Table 1 of Motta *et al.* (2014a)]. To calculate r_p, we first solve for $L_{\rm LF} = \nu_{\rm np}$ for the solution vector $\{e = 0.071, Q = 0, a = 0.283, \mathcal{M} = 5.4\}$; this locates the r_p, where oscillations are present, to a good approximation. Using these r_p values, we simultaneously solve $\{\nu_{\rm pp} = L_l, \nu_{\rm np} = L_{\rm LF}\}$ using the centroid frequencies of these components and estimate the exact solutions for parameters $\{e, Q\}$ with $\{a = 0.283, \mathcal{M} = 5.4\}$. In 10 out of 34 cases, we found low-eccentricity eQ solutions for these PDS components, where the calculated parameters are shown in Table 5.8. We find orbits with high Q values at large r_p (this is expected as $Q \propto L^2 - L_z^2$) as solutions for these PDS components. This exercise confirms the existence of eQ in addition to $e0$ solutions for QPOs.

5.5 Gas flow near ISSO (ISCO)

2012MNRAS.420..684P 2014ApJ...791...74M In this section, we discuss our torus picture of eccentric trajectories, and we examine the model of fluid flow in the general-relativistic thin disk around a Kerr black hole (Penna *et al.* 2012; Mohan and Mangalam 2014) with the aim of finding a source of the $e0$, eQ, and $Q0$ trajectories. In this model, the region around the rotating black hole was divided into various regimes: (1) the plunge region between the ISCO radius and black hole horizon dominated by gas pressure and electron scattering based opacity, (2) the edge region at and very near to the ISCO radius dominated by gas pressure and electron scattering based opacity, (3) the inner region outside the edge region with small radii comparable to ISCO dominated by radiation pressure and electron scattering based opacity, (4) the middle region outside the inner region where gas pressure again dominates over the radiation pressure and electron scattering based opacity, (5) the outer region far from the black hole horizon and outside the middle region dominated by gas pressure and electron scattering based opacity. The analytic forms for the important quantities like flux of radiant energy, F, temperature, T, and radial velocity in the locally nonrotating frame, β_r, were given for these different regions (as functions of r, a, viscosity, α, accretion rate, $\dot{m} = \dot{M}_\bullet/\dot{M}_{Edd}$, and $M_\bullet$) where nonzero stresses were incorporated at the inner edge of the disk in this model (Penna *et al.* 2012). Also, the expression for quality factor $Q_\phi\left(r, a, \beta_r\right)$ was derived for ν_ϕ QPO frequencies in the equatorial plane, which is given by [Mohan and Mangalam (2014), typo fixed in Equation (10)]

$$Q_\phi\left(r, a, \beta_r\right) = \frac{-\sqrt{A}}{3\pi\beta_r\Delta r^{1/2}}\left[1 - \frac{\left(A\Omega - 2ar\right)^2}{\Sigma^2\Delta}\right]^{-1/2}, \tag{5.13}$$

where $A = \left(r^2 + a^2\right)^2 - a^2\Delta\sin^2\theta$, $\Delta = r^2 + a^2 - 2r$, $\Sigma = r^2 + a^2\cos^2\theta$, and $\Omega = 1/\left(r^{3/2} + a\right)$, and where $\theta = \pi/2$ is assumed in Equation (5.13). Using this formula, one can obtain the quality factor of the QPO in various regions close to

the black hole by substituting the β_r of the corresponding region as defined above. The expressions for β_r in the edge and inner regions are given by (Equations (12), (13) of Mohan and Mangalam (2014))

$$\beta_{r,edge} = -7.1 \times 10^{-5} \alpha^{4/5} m_1^{-1/5} \dot{m}^{2/5} r^{-2/5} \mathcal{B}^{4/5} \mathcal{C}^{-1/2} \mathcal{D}^{3/10} \Phi^{-3/5}, \quad (5.14a)$$

$$\beta_{r,inner} = -124.416\ \alpha\ \dot{m}^2 r^{-5/2} \mathcal{A}^2 \mathcal{B}^{-3} \mathcal{C}^{-1/2} \mathcal{D}^{-1/2} \mathcal{S}^{-1} \Phi, \quad (5.14b)$$

where $m_1 = M_\bullet/10M_\odot$, $\mathcal{C} = 1 - 3r^{-1} + 2ar^{-3/2}$ [there is a typo in the expression of $\mathcal{C}$, Equation (A4c), in Penna *et al.* (2012)]; and $\mathcal{A}$, $\mathcal{B}$, $\mathcal{D}$, $\mathcal{S}$, and Φ are given in Penna *et al.* (2012) (Equations A4(a), (b), (d), (o) and (3.6)).

In Figure 5.28(a) and 5.28(b), we have shown the contours for β_r and Q_ϕ for the edge region in the (r, a) plane, and the $p^{\rm gas}/p^{\rm rad}$ ratio as a function of r in Figure 5.28(c). One can discern the transition from the inner to edge region by the sudden increase of the $p^{\rm gas}/p^{\rm rad}$ ratio, as seen in Figure 5.28(c), which is given by [Penna *et al.* (2012), Equation (3.7g)]

$$\frac{p^{\rm gas}}{p^{\rm rad}} = 1.983 \times 10^{-8} m_1^{-1/4} \alpha^{-1/4} \dot{m}^{-2} r^{21/8} \mathcal{A}^{-5/2} \mathcal{B}^{9/2} \mathcal{D} \mathcal{S}^{5/4} \Phi^{-2}. \quad (5.15)$$

In Table 5.9, we give the range of $\{r,\ Q_\phi,\ \beta_r,\ p^{\rm gas}/p^{\rm rad}\}$ for the edge and inner regions for different combinations of a and $\dot{m}$, fixing $\{m_1 = 1,\ \alpha = 0.1\}$ for BHXRBs, with a low accretion rate ($\dot{m} \simeq 0.1$) corresponding to the hard spectral state and a high accretion rate ($\dot{m} \simeq 0.3$) corresponding to the soft spectral state of BHXRBs. We see a sharp rise in p^{gas}/p^{rad} values in the edge region in Figure 5.28(c). The ranges of Q_ϕ in both the edge and inner regions are very high compared to those observed in BHXRBs ($Q_\phi = 5 - 40$). We, therefore, suggest that the QPOs are coming from a region very close to and inside ISCO; we identify this with the torus region, consisting of geodesics (Penna *et al.* 2012), and hence Q_ϕ is different. This

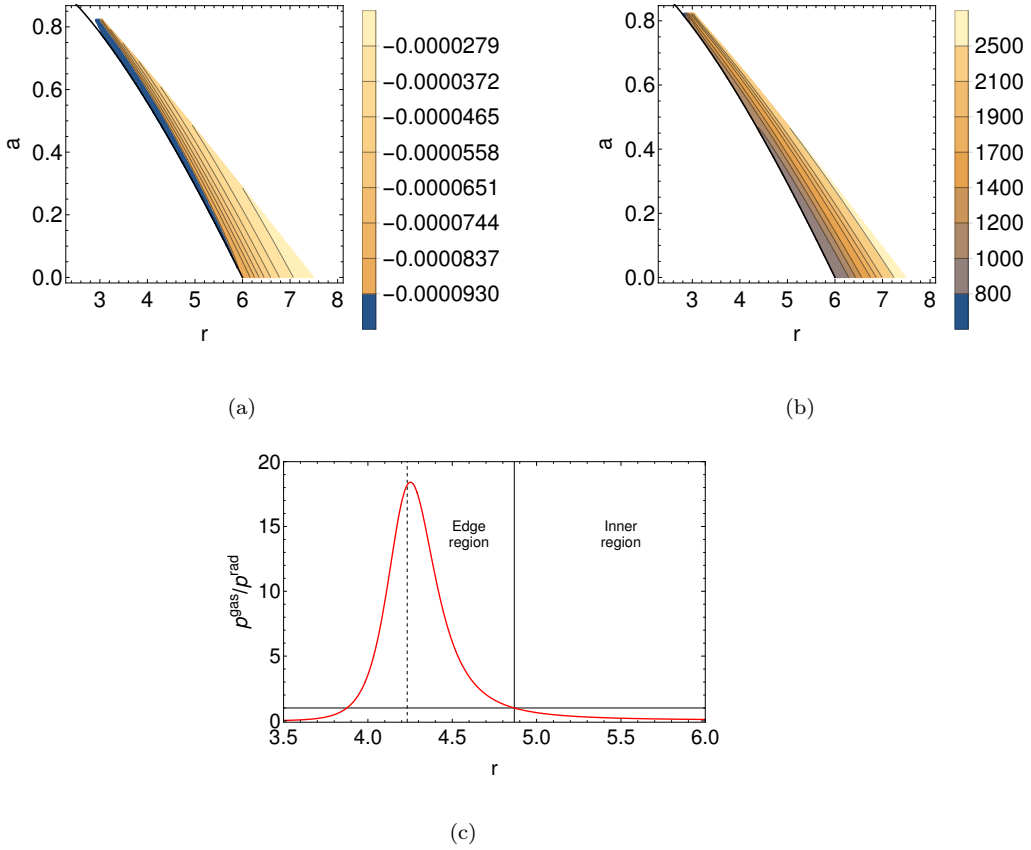

(a) (b)

(c)

FIGURE 5.28: Contours of (a) β_r and (b) Q_ϕ in the $(r,\, a)$ plane in the edge region of the general-relativistic thin disk, and (c) $p^{\rm gas}/p^{\rm rad}$ as a function of r with $a = 0.5$ (where the dotted vertical curve corresponds to ISCO and the solid vertical curve corresponds to r when $p^{\rm gas}/p^{\rm rad} = 1$). We have fixed $\{\alpha = 0.1,\, m_1 = 1,\, \dot{m} = 0.1\}$.

is also supported by the observation that the edge-flow-sourced geodesics populate the torus region obtained here for M82 X-1 ($r = 4.7 - 9.08$) and GRO J1655-40 ($r = 5.1 - 6.67$); see Figure 5.18. Specifically, the sharp pressure ratio gradient suggests that the edge region can be a launchpad for the instabilities that then oscillate with fundamental frequencies, causing geodesic flows in the torus region inside ISCO ($r < r_{\rm ISCO}$), where the fluid motion is close to Hamiltonian flow. A further understanding of this proposal (or conjecture) can be gained by carrying out a detailed model or simulation of the GRMHD flow in the edge region.

TABLE 5.9: Ranges of r, pressure ratio, $p^{\rm gas}/p^{\rm rad}$, quality factor, Q_ϕ, and radial velocity, β_r, in the edge and inner regions of fluid flow in the relativistic thin accretion disk around a Kerr black hole (Penna *et al.* 2012; Mohan and Mangalam 2014), where we have fixed $\{m_1 = 1,\, \alpha = 0.1\}$ for BHXRBs.

Region	$(a = 0.3, \dot{m} = 0.1)$	$(a = 0.5, \dot{m} = 0.1)$	$(a = 0.3, \dot{m} = 0.3)$	$(a = 0.5, \dot{m} = 0.3)$
	$(r, p^{\rm gas}/p^{\rm rad}, \beta_r, Q_\phi)$	$(r, p^{\rm gas}/p^{\rm rad}, \beta_r, Q_\phi)$	$(r, p^{\rm gas}/p^{\rm rad}, \beta_r, Q_\phi)$	$(r, p^{\rm gas}/p^{\rm rad}, \beta_r, Q_\phi)$
Edge	$4.98 - 5.93$	$4.23 - 4.87$	$4.98 - 5.25$	$4.23 - 4.35$
	$1.002 - 29.84$	$1.003 - 18.41$	$1.026 - 1.921$	$1.003 - 1.186$
	$-(2.84 - 10.2) \times 10^{-5}$	$-(3.81 - 11.37) \times 10^{-5}$	$-(1.03 - 1.34) \times 10^{-4}$	$-(1.36 - 1.49) \times 10^{-4}$
	$914.46 - 2624.12$	$1019.24 - 2473.07$	$694.29 - 844.59$	$773.62 - 814.27$
Inner	$5.93 - 85.22$	$4.87 - 87.81$	$5.25 - 226.2$	$4.35 - 229.45$
	$0.0589 - 0.998$	$0.0373 - 0.999$	$0.0065 - 0.998$	$0.0041 - 0.998$
	$-(1.2052 - 69.28) \times 10^{-6}$	$-(1.1601 - 110.71) \times 10^{-6}$	$-(1.127 - 626.95) \times 10^{-6}$	$-(1.107 - 1001.39) \times 10^{-6}$
	$688.09 - 9830.85$	$501.112 - 10046.3$	$76.21 - 6333.26$	$55.52 - 6397.35$

5.6 Discussion, caveats, and conclusions

The QPOs in BHXRBs have been an important probe for comprehending the inner accretion flow close to the rotating black hole. Many theoretical models have been proposed in the past to explain its origin and in particular LFQPOs and HFQPOs (Kato 2004; Török *et al.* 2005; Tagger and Varnière 2006; Germanà *et al.* 2009; Ingram *et al.* 2009; Ingram and Done 2011, 2012). These various models have been able to explain different properties of QPOs. For example, one of these models attributes the HFQPOs to the Rossby instability under the general relativistic regime (Tagger and Varnière 2006), whereas another model attributes type C QPOs to the Lense−Thirring precession of a rigid torus of matter around a Kerr black hole (Ingram *et al.* 2009; Ingram and Done 2011, 2012). Although these models can explain either LFQPOs or HFQPOs, they do not explain the simultaneity of these QPOs, as previously observed in BHXRB GRO J1655-40 (Motta *et al.* 2014a). The RPM, which is based on the geometric phenomenon of the relativistic precession of particle trajectories, explains these simultaneous QPOs as $\{\nu_\phi, (\nu_\phi - \nu_r), (\nu_\phi - \nu_\theta)\}$ of a self-emitting blob of matter (or instability)

in a bound orbit near a Kerr black hole. We have extended the RPM for QPOs in BHXRBs to study and associate the fundamental frequencies of the bound particle trajectories near a Kerr black hole, which are eQ, $e0$, and $Q0$ solutions with the frequencies of QPOs. We call this as the generalized RPM (GRPM). Recently, novel and compact analytic forms for the trajectories around a Kerr black hole and their fundamental frequencies were derived (Rana and Mangalam 2019a,b). We applied these formulae to the GRPM to extract the QPO frequencies. Graphical examples of these trajectories around a Kerr black hole are shown in Figures 5.18, 5.23, and 5.29. A summary of these results is given in Table 5.10.

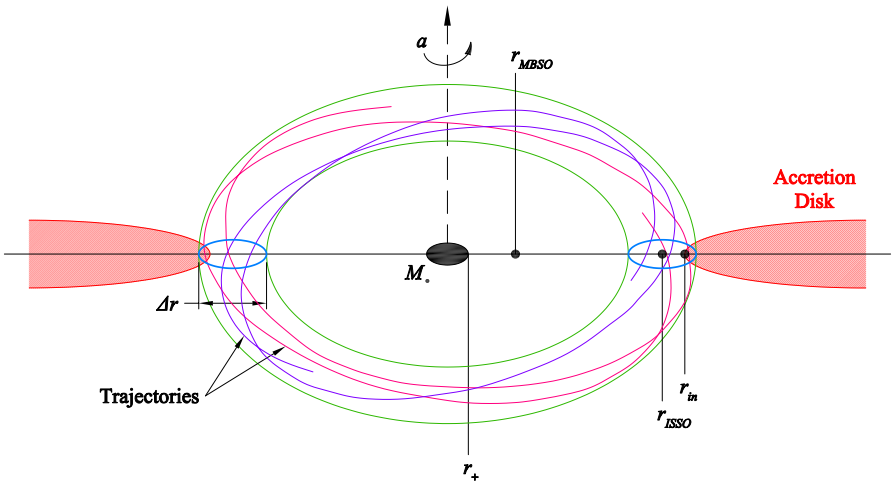

FIGURE 5.29: The cartoon shows a geometric model explaining the region of origin of QPOs assuming the more general nonequatorial eccentric trajectories in the GRPM, where the torus extent is $R_0{}^{+\Delta_1}_{-\Delta_2}$ (and torus width $\Delta r = \Delta_1 + \Delta_2$).

We add the following caveats and conclusions:

1. *Orbital solutions*: The fundamental frequencies of the eQ, $e0$, and $Q0$ trajectories are in the range of QPO signals observed in BHXRBs, so these

TABLE 5.10: Summary of orbital solutions found for QPOs observed in five BHXRBs using the GRPM in this article, and the corresponding region of the (r_p, a) plane where QPOs originate.

BHXRB	**Number of QPOs**	**Model class**	e	r_p	a	Q	**MBSO**	**ISCO**	**ISSO**	**Region in (r_p, a) plane**
M82 X-1	3	eQ	$0.230^{+0.067}_{-0.049}$	$4.834^{+0.181}_{-0.268}$	0.299	$2.362^{+1.519}_{-1.439}$	3.424	4.981	5.096	2
		$Q0$	0	$6.044^{+0.071}_{-0.072}$	0.321±0.013	$6.113^{+2.124}_{-1.645}$	3.475	4.903	5.258	1
GRO J1655-40	3	eQ	$0.071^{+0.031}_{-0.035}$	$5.25^{+0.171}_{-0.142}$	0.283	$0^{+0.623}$	-	5.039	-	1
XTE J1550-564	2	$e0$	$0.262^{+0.090}_{-0.062}$	$4.365^{+0.169}_{-0.279}$	0.34	0	-	4.835	-	2
		$Q0$	0	5.538±0.054	0.34	$2.697^{+1.738}_{-1.627}$	3.35	4.835	4.988	1
4U 1630-47	2	$e0$	$0.734^{+0.066}_{-0.048}$	$2.249^{+0.249}_{-0.353}$	0.985	0	-	1.541	-	1
										1
GRS 1915+105	2	$e0$	0.918±0.002	$1.744^{+0.025}_{-0.011}$	0.98	0	-	1.614	-	1

are viable solutions for explaining the observed QPOs in BHXRBs M82 X-1, GRO J1655-40, XTE J1550-564, 4U 1630-47, and GRS 1915+105 in the GRPM paradigm. We see that these trajectory solutions are found in either region 1 or 2 of the (r, a) plane, as defined in Figure 5.4, and shown in Figure 5.22. The values of the black hole spin for BHXRBs M82 X-1 and GRO J1655-40 were fixed to their most probable values calculated in §5.3.2.1, and to the previously observed values for the other BHXRBs for eccentric orbit solutions. For BHXRBs with two QPOs, fixing the spin to previously known values increases the uncertainty in the estimated orbital parameters, because the spin values assumed have uncertainties associated with the X-ray spectroscopic methods that are influenced by systematics, with the general finding that the solution lies near ISCO. However, our exercise still supports the GRPM. A spin value was also calculated for M82 X-1 for a $Q0$ solution. A summary of these parameter solutions and corresponding MBSO, ISCO, and ISSO radii for all BHXRBs is given in Table 5.10.

2. *Trajectories in the torus*: We found trajectories, having different parameter combinations within the estimated range of errors in the orbital parameters and having fundamental frequencies within the width of the observed QPOs,

as solutions for QPOs in BHXRBs M82 X-1 and GRO J1655-40. We also found that the distinct parameter solutions found for these cases follow a trend that, as the eccentricity of the orbit decreases, the Q value increases for a given QPO frequency pair. This behavior can also be understood from Figures 5.7−5.9, where the frequencies increase as Q increases, but decrease as e increases for a given r_p. This implies that to obtain the degenerate parameter solutions for the same set of frequencies, a low eccentricity $\Longleftrightarrow$ high Q trend is expected. We also found that these trajectories span a torus region near the Kerr black hole, as shown in Figure 5.18, which together give rise to the same peaks in the power spectrum. This should also explain the strong rms seen for the HFQPOs and type C LFQPOs. Another possibility of a rigidly precessing torus was suggested (Ingram *et al.* 2009; Ingram and Done 2011, 2012); our proposal consists of a nonprecessing torus, which includes all viable solutions of the GRPM: eQ, $e0$, and $Q0$ trajectories.

3. *Torus region*: The emission of simultaneous QPOs is expected from a region where different trajectories having similar fundamental frequencies span a torus, as shown in Figure 5.18 and they can together show a strong peak in the power spectrum. The inner radius of the circular accretion disk is expected to be close to this torus region in such a scenario. In Figure 5.29, we depict this geometric model where the emission region of the simultaneous QPOs is shown as a torus region close to the inner edge of the accretion disk. This torus region is expected to be outside the MBSO radius, and the ISSO radius is expected to be in between the torus region for the eccentric orbit solutions, as observed in the case of M82 X-1. The torus region can be represented as $R_0{}^{+\Delta_1}_{-\Delta_2}$, where R_0 is an $e = 0$ orbit (ISCO or ISSO) and Δ_i represents the region very close to R_0. The width of the torus region in this model is given by $\Delta r = (\Delta_1 + \Delta_2)$. All of the orbit solutions are found to be distributed near R_0; hence, it is expected that this radius corresponds to the inner edge radius, $r_{\rm in}$, of the circular accretion disk. This torus region exists in region 1 and(or) 2 near the R_0 radius. Due to the instabilities in the inner

flow, we argue that the nearly $e0$ orbits near the R_0 radius transcend to eQ orbits. Based on the geometry of the orbits and the emission region, we plan to build a detailed GRMHD-based model to expand on the GRPM paradigm. More cases of BHXRBs with three simultaneous QPOs, if detected in the future, will help us test our models.

4. *Highly eccentric solutions*: For QPOs in BHXRBs 4U 1630-47 and GRS 1915+105, we found highly eccentric $e0$ solutions. This indicates that black holes with high spin values prefer highly eccentric trajectories as solutions to the QPOs. This behavior can also be understood from Figures 5.7−5.9, where we see that for black holes with very high spins, the QPOs originate very close to the black hole, and the solution contours move close to the black hole as e increases. This implies that more eccentric orbits are preferred for a given frequency pair of QPOs for a black hole with very high spin. We do not find any spherical orbit solution for QPOs in these two BHXRBs, which confirms that the orbital solution is purely equatorial, but such highly eccentric solutions are unlikely. We expect more and better estimates of the orbital solutions in the future if a more precise estimate of the spin is available, or if three simultaneous QPOs are discovered in BHXRBs 4U 1630-47 and GRS 1915+105. For the case that we studied in this paper of 4U 1630-47, the lower frequency of the QPO pair probably has a different origin than the high-frequency feature suggested by Klein-Wolt *et al.* (2004). However, even in such a scenario, the frequency range of this QPO still implies an origin near the torus region in our model. There was also another pair of QPOs observed in 4U 1630-47 (Klein-Wolt *et al.* 2004), for which there was no exact solution found in the orbital parameter space.

5. *Nonequatorial solutions*: In the case of BHXRBs M82 X-1 and XTE 1550-564, we found both eQ ($e0$ for XTE 1550-564) and $Q0$ solutions, and the spin determinations are slightly different for the two different types of trajectory solutions. These solutions were found close to and outside their corresponding ISSO radii. The mass of the black hole in case of M82 X-1 was fixed to the

intermediate-mass black hole (IMBH) range, $\mathcal{M} = 428$, because the QPOs observed in the low-frequency range (3−5 Hz) were found to be very stable, unlike LFQPOs, implying that they are HFQPO counterparts of BHXRBs, and hence indicating an IMBH (Pasham *et al.* 2014). Although this mass estimation stems from the mass-scaling relation of QPOs, which is not very reliable, a more accurate estimate of $\mathcal{M}$, if found in the IMBH range, will not significantly change the result. However, if, in the future, a more reliable and precise estimate places it in the stellar-mass range, then the outcome from the GRPM will be dramatically different. The QPOs observed in XTE 1550-564 by Miller *et al.* (2001) were later shown to be the result of the data averaging by Motta *et al.* (2014b), where the same QPO moved up in the frequency, appearing as a distinct QPO. As in the case of 4U 1630-47, the range of this QPO frequency still implies an origin near the torus region.

6. *Spectral states*: We suggest that HFQPOs originate when $r_{\rm in}$ comes very close (near ISCO/ISSO) to the black hole during the soft spectral state of the outburst. When $r_{\rm in}$ is farther out as in the hard state, the resulting type C QPO frequency is of the order of millihertz. As a type C QPO occurs more frequently and is prone to the vertical oscillations, the increase in its frequency is explained as an increase in $\nu_{\rm np}$ when $r_{\rm in}$ decreases, with the spectral transition from the hard to soft state.

7. *Circularity*: The RPM was previously applied to understand the QPOs observed in BHXRBs GRO J1655-40 and XTE J1550-564 (Motta *et al.* 2014a,b) using the fundamental frequencies of 00 orbits. We have found an eQ solution for GRO J1655-40 very close to an equatorial orbit having a very small eccentricity $e \sim 0.071$ (see Table 5.10), which is in a very close agreement with the solution found by Motta *et al.* (2014a), where their estimated mass of the black hole, $\mathcal{M} = 5.307$, is also very close to our assumption, $\mathcal{M} = 5.4$ (see Table 5.3). Our most probable spin estimated for GRO J1655-40, $a = 0.283$, is almost the same as found by Motta *et al.* (2014a), $a \sim 0.286$, but our solution provides a more precise estimation of e and Q values while confirming

a near 00 orbit solution as assumed by Motta *et al.* (2014a). For the case of XTE J1550-564, the mass of the black hole was assumed to be $\mathcal{M} = 9.1$ by Motta *et al.* (2014b) as also in our model. Our assumption for the spin, $a = 0.34^{+0.37}_{-0.45}$ (Orosz *et al.* 2011), is also nearly the same as the value estimated by Motta *et al.* (2014b); but our model gives the $e0$ and $Q0$ solutions for XTE J1550-564, having moderate $e = 0.262^{+0.090}_{-0.062}$ and $Q = 2.697^{+1.738}_{-1.627}$ values, respectively (see Table 5.10). This indicates that the assumption of circularity is not always valid.

8. *Solution degeneracy*: To study the impact of the GRPM (with nonzero e and Q), we have explored the behavior of $\{\delta_\phi, \delta_{\rm pp}, \delta_{\rm np}\}(e, r_p, a, Q)$ as defined in Equation (5.2) as deviations from the 00 behavior (circularity). We find that the frequencies are strongly dependent on e but not so much on Q (see Figures 5.7−5.9). This is elaborated upon in points 3 and 4 in §5.2.1, and in points 2 and 3 in §5.2.2 for spherical orbits. The GRPM has a built-in degeneracy in the parameter space $\{e, r_p, a, Q\}$, called the isofrequency pairs, for a given combination of QPO frequencies. This degeneracy is a known behavior of trajectories around a Kerr black hole (Warburton *et al.* 2013), where different combinations of $\{E, L_z, Q\}$ can have the same set $\{\nu_\phi, \nu_r, \nu_\theta\}$ for a fixed a. An evidence of this degeneracy is also seen in Figures 5.7−5.9, where the contours of $\{\delta_\phi, \delta_{\rm pp}, \delta_{\rm np}\}(e, r_p, a, Q)$ have multiple solutions; that is, for a given δ value, there are different combinations of $\{e, Q\}$ that have distinct contours on the (r_p, a) plane. Unlike RPM, the mass of the black hole is always assumed from the previous estimates in the GRPM, which is a valid assumption because the underlying physics or behavior of the Kerr orbits is independent of $M_\bullet$. The GRPM, along with the statistical method (Figure 5.13, §5.3.2) that is applied, provides a more precise estimation of the spin of the black hole.

9. *Frequency ratio*: The 3:2 and 5:3 ratios of the simultaneous HFQPOs are a phenomenon observed in a few cases of BHXRBs: 300 and 450 Hz HFQPOs in GRO J1655-40 (Remillard *et al.* 1999a; Strohmayer 2001a), 240 and 160

Hz HFQPOs in H1743-322 (Homan *et al.* 2005; Remillard *et al.* 2006). Such claims, other than the case of GRO J1655-40, are probably not real (Belloni *et al.* 2012). Hence, the possibility of such ratios is still causes skepticism. However, if true, the GRPM suggests that the origin of these ratios is very close to the torus region and $r_{\rm in}$.

10. *The PBK correlation*: In §5.4, we show that the $e0$ solution $\{e = 0.071,\ a = 0.283,\ Q = 0,\ \mathcal{M} = 5.4\}$, estimated using a fine-grid method in §5.3.2.1, fits the PBK correlation that was previously observed in BHXRB GRO J1655-40 (Motta *et al.* 2014a). This fit is shown in Figure 5.26. We also found that 10 observation IDs, where L_l and $L_{\rm LF}$ (broad frequency components) were detected simultaneously (Motta *et al.* 2014a), show low-eccentricity eQ solutions, where the calculated parameters are shown in Table 5.8. The calculated Q values are consistent with large r_p and small e values. This exercise suggests that eQ solutions for QPOs are viable.

11. *Probing the disk edge with a GR fluid model*: We study a model of fluid flow in the general-relativistic thin accretion disk (Penna *et al.* 2012; Mohan and Mangalam 2014). We find that the disk edge flows into a torus region containing Hamiltonian geodesics that was obtained for M82 X-1 ($r = 4.7-9.08$) and GRO J1655-40 ($r = 5.11 - 6.67$). Specifically, the sharp gradient of the $p^{\rm gas}/p^{\rm rad}$ pressure ratio, seen in Figure 5.28(c), suggests that the edge region is a launch pad for the instabilities that orbit with fundamental frequencies of the geodesics in the edge and geodesic regions, which then follow the geodesics inside the torus region and also close to the edge region, where Hamiltonian dynamics is applicable, that is built into the GRPM. The range of $\{r,\ Q_\phi,\ \beta_r,\ p^{\rm gas}/p^{\rm rad}\}$ for the edge and inner regions for different combinations of a and $\dot{m}$, fixing $\{m_1 = 1,\ \alpha = 0.1\}$, is given in Table 5.9, and the contours of β_r and Q_ϕ in the $(r,\ a)$ plane for the edge region are shown in Figures 5.28(a) and 5.28(b). The ranges of Q_ϕ (tuned to $\Delta\nu$, the width of the observed QPO), which is defined by orbits in the torus which was provided by observed frequency centroids, in both the edge and inner regions

are very high compared to those observed in BHXRBs ($Q_\phi = 5 - 40$). We are suggesting that the QPOs originate in the geodesic region. We also see that the edge is adjacent to the torus region (consisting of geodesics) found for M82 X-1 and GRO J1655-40, implying that the QPOs are originating from geodesics close to the edge region. Hence, the particle and gas dynamics models together justify the scenario sketched in Figure 5.29, of a unified fluid-particle picture that is the following: the source of the particles in the torus are dynamical instabilities of plasma blobs ejected from the edge region. These blobs have zero α and therefore obey the Hamiltonian dynamics. The clue that the torus region physically overlaps with the edge and geodesic regions is a subject of future detailed GRMHD models (and simulations).

12. *Isofrequency combinations*: In the cases with three simultaneous QPOs, once a is fixed (to the most probable value or the previously estimated value), it is easy to predict the remaining parameters $\{e,\, r_p,\, Q\}$ using three QPO frequencies. In the case of M82 X-1 and GRO J1655-40, when a was fixed to the most probable value (Table 5.5), we obtained a single solution for $\{e,\, r_p,\, Q\}$ and their errors $\{\Delta e,\, \Delta r_p,\, \Delta Q\}$, where this range of parameters spans the torus region based on the GRPM. However, there is a finite possibility (Warburton *et al.* 2013) that distinct solutions for the $\{e,\, r_p,\, Q\}$ triad are obtained for the same triple QPO frequency set, subject to the bound orbit conditions: $0 \leq e < 1$, $Q \geq 0$, and Equation (4.8). This completely depends on the values of the QPO frequency set that are further subject to the constraints of bound orbit conditions. In the cases where only two simultaneous QPOs exist, it is difficult to predict whether an $e = 0$ orbit will be preferred over an $e > 0$ orbit, or a $Q = 0$ orbit will be preferred over a $Q > 0$ orbit, or vice versa. This will be clear when more cases of three simultaneous QPOs are found and whether they yield distinct solution sets for $\{e,\, r_p,\, a,\, Q\}$, thereby indicating if the torus region at the disk edge is indeed the geometric origin of QPOs. From our numerical experiment, we find a distinct exact solution for $\{e,\, r_p,\, Q\}$ for the three simultaneous QPOs case, where a was

fixed to the most probable value. The RPM restricts the search to $\{e = 0,\ Q = 0\}$ orbital solutions, while the GRPM expands it to more general but astrophysically possible $\{e \neq 0,\ Q \neq 0\}$ solutions and thereby subsumes the RPM within its framework. Hence, the GRPM provides more realistic orbit solutions around a Kerr black hole that are outside the scope of the RPM, thus giving more impetus to probes of physical models of the origin of QPOs.

13. *Caveats*: The results predicted by the GRPM are subject to the veracity of the observed data that are inputs to our model. For example, in the case of 4U 1630-47 and GRS 1915+105, very highly eccentric orbit solutions obtained by the GRPM are unlikely; this implies that very high spin values in these cases are probably unreliable. Similarly, if M82 X-1 does not host an IMBH but a stellar-mass black hole or a neutron star, then the results predicted by the GRPM will change drastically. Also, for 4U 1630-47 and XTE J1550-564, where the input frequencies of QPOs are not very reliable (Klein-Wolt *et al.* 2004; Motta *et al.* 2014b), as discussed before, the results obtained by the GRPM might not be physically meaningful. As most of the measured frequencies do exist in a similar range, then their geometric origin in the torus region (as predicted by the GRPM) is valid.

14. *Future work*: In the near future, we expect suitable observational results from the currently operative Indian X-ray satellite, AstroSat, and from future missions, such as eXTP, which is proposed to have instruments with much higher sensitivity for fast variations and X-ray timing. If simultaneous QPO signals are observed from these missions, we expect to test our GRPM further.

Chapter 6

An image of a galaxy with an active galactic nucleus. Courtesy: arizona.edu

A relativistic orbit model for QPOs in AGN*

6.1 Introduction

Active galactic nuclei (AGN), at the center of most galaxies, are known to be powered by black holes of masses $M_\bullet = 10^5 - 10^9 M_\odot$ Rees (1984); Blandford and Rees (1992); Antonucci (1993). These systems are believed to be the scaled-up version of black hole X-ray binaries (BHXRB), possessing the same physical process of accretion McHardy (2010). The riveting evidence of this conjecture is the similarity between the X-ray variability in AGN and BHXRB McHardy *et al.* (2006); McHardy (2010). However, a complete understanding of the physical

*This work is published in a paper in the special issue on "X-ray Flux and Spectral Variability of Blazars" in Galaxies journal: Rana and Mangalam (2020a)

processes of accretion and the jet emission in AGN requires the variability analysis in various wavelength bands, from optical to γ ray.

X-ray Power spectral density (PSD) shape: The PSD of both BHXRB and AGN are known to show red noise, which decreases steeply at high frequencies (small timescales) following a power law, $P(\nu) \propto \nu^{-\alpha}$, where $\alpha \sim 2$ typically McHardy *et al.* (2004); Papadakis *et al.* (2010); Mangalam and Wiita (1993). At lower frequencies, below a characteristic frequency, called the break frequency (ν_b), the PSD flattens ($\alpha \sim 1$) McHardy *et al.* (2004); Papadakis *et al.* (2010); Mangalam and Wiita (1993). Such a characteristic PSD shape is well defined by a bending power-law model McHardy *et al.* (2004) and found in various types of AGN with ν_b ranging from $\sim 10^{-6}$-10^{-4} Hz Papadakis *et al.* (2010); González-Martín and Vaughan (2012). This break frequency is expected to approximately scale as an inverse of the black hole mass. However, the bending power-law shape of the PSD shape in BHXRB is known to be associated only with the soft spectral state Cui *et al.* (1997). Hence, the understanding of such a characteristic shape of the PSD is fundamental for probing the inner regions close to the black hole.

X-ray QPOs: The QPOs detected so far in the X-ray light curves of AGN are seen to be mostly associated with the Narrow-Line Seyfert 1 (NLSy1) galaxies, which are identified by the narrow width of their broad Hβ emission line with FWHM$<$ 2000 kms^{-1}, strong FeII lines, and weak forbidden lines Osterbrock and Pogge (1985); Goodrich (1989). NLSy1 galaxies are also known to show rapid X-ray variability and near Eddington accretion rates Komossa (2008). The first detection of a significant QPO in an X-ray light curve was reported in RE J1034+396 with timescale $\sim$ 3730 s using the XMM-Newton data Gierliński *et al.* (2008). Another significant QPO at $\sim$ 3.8 hour timescale was reported in an Ultrasoft Active Galactic Nucleus Candidate 2XMM J123103.2+110648 Lin *et al.* (2013) and many more. These X-ray QPOs were found in XMM-Newton data (0.3–10 keV).

Optical and γ ray QPOs: The optical and γ ray QPOs are also known to be discovered in a few BL Lacertae objects, also known as BL Lac. These objects are a class of AGN characterized by their large polarization, high variability, and weak emission lines Falomo *et al.* (2014); Padovani *et al.* (2017). These objects are interpreted as systems with a relativistic jet pointing directly towards the line of sight of the observer; hence, the jet emission dominates in these systems, and the discovered QPOs are thought to be associated with the jets. The γ ray QPOs are primarily discovered using the *FERMI*-LAT observations (100MeV-300GeV), for example, a γ ray QPO of timescale $T \sim 630$ days was reported in PKS2155-304 (Sandrinelli *et al.* 2014), where this timescale was found to be twice the optical period originally proposed by Zhang *et al.* (2014). Later, the presence of both these QPO timescales were confirmed (Sandrinelli *et al.* 2016a).

In this chapter, we present a model that unifies the origin of multiwavelength QPOs originating in the disk and the jet and also probes the genesis of the PSD shape of the X-ray light curve due to a corona. We study the association of X-ray QPOs discovered in NLSy1 type AGN with the relativistic circular and spherical orbits around a Kerr black hole using the generalized relativistic precession model (GRPM) [RPM: Stella and Vietri (1999), Stella *et al.* (1999); GRPM: chapter 5]. We also motivate that the non-equatorial trajectories (for example, spherical orbits), which are the consequence of axisymmetry of the Kerr spacetime, are also the viable solutions to the QPO frequencies using the GRPM (chapter 5). We also apply a relativistic jet model Mangalam (2018); Mohan and Mangalam (2015) to study the optical and γ ray QPO timescales in BL Lacertae objects. This model describes the simultaneous QPOs with 1:2 or 3:2 frequency ratio as the harmonics obtained in the Fourier series of the Doppler factor of the pulse profile from a blob rotating along with the jet. The Doppler factor includes the relativistic effects, such as Doppler boost, relativistic aberration, gravitational redshift, and light bending. We also present a model to describe the typical bending power-law profile of the PSD observed in AGN. Assuming the bending power-law profile

of the PSD shape, we find the intrinsic profile of the energy distribution of the particles orbiting in circular and spherical trajectories in the corona around a Kerr black hole, which results in a distribution in the fundamental frequency space. The X-ray flux gets modulated at this fundamental frequency, which is a function of distance from the black hole, and consequently also a function of E. A unified picture of these models of multiwavelength QPOs and PSD shape is shown in Figure 6.1, where r_M is the marginally bound spherical orbit (MBSO) radius, r_I is the innermost stable circular orbit (ISCO) radius, and r_X is the outer disk radius.

The structure of this chapter is as follows: In §6.2, we discuss the (G)RPM for the X-ray QPOs [RPM: Stella and Vietri (1999), Stella *et al.* (1999); GRPM: chapter 5]. In §6.2.1, we discuss the association of X-ray QPO frequencies with the equatorial circular orbits using the GRPM, whereas we study the spherical orbits as the origin of X-ray QPOs using the GRPM in §6.2.2. In §6.3, we apply a basic jet model (Mangalam 2018; Mohan and Mangalam 2015) to study the timescales of optical and γ ray QPOs in Blazars. We then study the genesis of the bending power-law shape of the PSD in AGN and derive the intrinsic energy distribution of the orbiting particles in §6.4. We summarize our results in §6.5, and draw conclusions in §6.6.

6.2 Relativistic circular and spherical orbits as solutions to X-ray QPOs

The X-ray emission from NLSy1 galaxies is believed to be originated from the inner region of the accretion disk in the context of the unification model of AGN (Antonucci 1993). We apply the (G)RPM [RPM: Stella and Vietri (1999), Stella *et al.* (1999); GRPM: chapter 5] to study the X-ray QPOs discovered in a few cases of NLSy1 type of AGN and one Type-2 AGN candidate, see Table 6.1. Using this

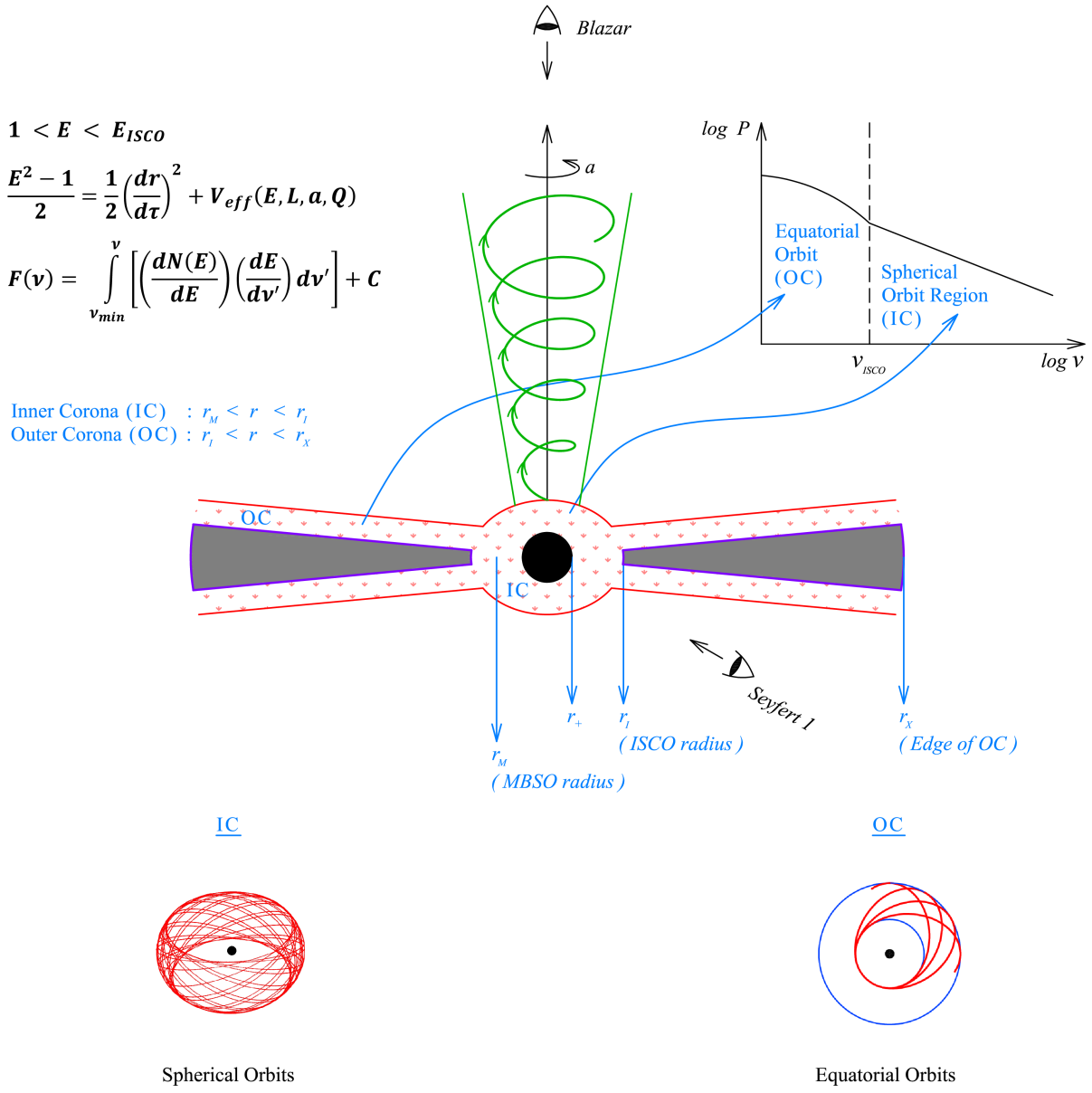

FIGURE 6.1: The figure shows a unified picture of the models for X-ray, optical, and γ ray QPOs and the origin of X-ray power spectral density (PSD) shape in AGN. The X-ray QPOs observed in NLSy1 galaxies are associated with the fundamental frequencies of the equatorial orbits in the accretion disk sandwiched by a corona region, which we call the outer corona (OC) region, $r_I < r < r_X$; the inner corona (IC) region, $r_M < r < r_I$, is associated with the fundamental frequencies of the spherical orbits around a Kerr black hole. The optical and γ ray QPOs in Blazars are shown as the harmonics of the timescale of a blob of matter moving along the jet. The shape of the PSD is studied using the fundamental frequency of matter which is governed by the radial effective potential, $V_{eff}(E, L, a, Q)$, providing the gravitational background responsible for the geodesic motion, in IC and OC regions to derive the energy distribution of the orbiting matter, $N(E)$, which is directly related to the observed intensity, $I(\nu)$, where ν is the temporal frequency.

model, we estimate the parameters: the spin of the black hole, a, and radius of an equatorial circular orbit, r, in the Kerr spacetime, where the QPO is originated. We also implement the GRPM to associate the frequencies of relativistic spherical orbits (non-equatorial) with the QPO frequencies to calculate the corresponding parameters (r_s, a, Q).

There are a few cases of BHXRB where a third low-frequency QPO (LFQPO) is also detected simultaneously to HFQPOs (Motta *et al.* 2014a,b), in such cases, this LFQPO is associated with the nodal precession frequency, $\nu_{np} = (\nu_\phi - \nu_\theta)$, in the GRPM. There is no such known case in AGN where three QPOs are detected simultaneously; however, the X-ray QPO detected in Type 2 AGN 2XMM J123103.2+110648 (see Table 6.1) was suggested as an LFQPO because of its large rms value (25-50%) (Lin *et al.* 2013), which is the typical characteristic of LFQPOs observed in BHXRB (Remillard *et al.* 2006).

Therefore, for AGN having a single QPO detection, we associate the QPO frequency with ν_ϕ, except for 2XMM J123103.2+110648 where we also analyze the ν_{np} frequency. For the cases of AGN with two simultaneous QPO detections, we use ν_ϕ and ν_{pp} frequencies in the GRPM. In Table 6.1, we have summarized the cases of AGN with either one or two simultaneous QPO detections in X-rays.

A generic procedure which we have used to estimate errors in the orbital parameters for NLSy1 AGN with two simultaneous X-ray QPOs, 1H 0707-495, see Table 6.1, is described in §5.3.2, chapter 5.

6.2.1 Circular orbits

In this section, we use the GRPM ($Q = 0$) for QPOs to estimate the (r, a) parameters of the circular orbits using their fundamental frequencies given by Eq.

TABLE 6.1: A list of statistically significant QPOs detected in the X-ray band (0.3-10KeV) by the XMM-Newton in AGN along with their black hole masses. **References**: [1]Zhou *et al.* (2010); [2]Gierliński *et al.* (2008); [3]Ho *et al.* (2012); [4]Lin *et al.* (2013); [5]Grupe *et al.* (2004); [6]Alston *et al.* (2015); [7]Pan *et al.* (2016); [8]Zhang *et al.* (2018); [9]Wang and Lu (2001); [10]Zhang *et al.* (2017); [11]Boller *et al.* (2001); [12]Hu *et al.* (2016); [13]Gupta *et al.* (2018).

Source	**Class of AGN**	$\mathcal{M}$ $(\times 10^6)$	**QPO period** **ks**	**QPO frequency** $(\times 10^{-4})$**Hz**
RE J1034+396	NLSy1	4[1]	3.73 ± 0.13	2.681 ± 0.093[2]
2XMM J123103.2+110648	Type-2 AGN	0.1[3]	13.71	0.729[4]
MS 2254.9-3712	NLSy1	4[5]	6.667	1.5[6]
1H 0707-495	NLSy1	5.2[7]	3.8 ± 0.17	2.632 ± 0.118[7,8]
			8.265 ± 1.366	1.21 ± 0.2[8]
Mrk 766	NLSy1	4.3[9]	6.452 ± 0.458	1.55 ± 0.11[10]
			4.2	2.38[11]
MCG-06-30-15	NLSy1	3.26[12]	3.6 ± 0.229	2.778 ± 0.177[13]

(5.1) [Bardeen *et al.* (1972), Wilkins (1972), Motta *et al.* (2014a)]. We discuss our results below:

1. We have computed the contours of $\nu_\phi\,(r, a)$, using Eq. (5.1a), for the QPO frequencies (given in Table 6.1) of RE J1034+396 (blue), MS 2254.9-3712 (red), and MCG-06-30-15 (magenta), shown in the (r, a) plane in Fig. 6.2(a). The masses of these black holes were assumed from the previous estimations (see Table 6.1). The model suggests that the QPO emission originates from a very narrow region of the accretion disk, where $r \sim (9.4 - 9.9)$ for RE J1034+396, $r \sim (10.4 - 11.4)$ for MS 2254.9-3712, and $r \sim 14.2$ for MCG-06-30-15 even though a ranges from 0 to 1. This implies that the QPO emission region is very close to the black hole, and this emission region remains very narrow and nearly independent of the spin of the black hole.

2. For the case of Mrk 766, two QPO frequencies were detected (see Table 6.1), but at different epochs. We have shown $\nu_\phi\,(r, a)$ contours for both these frequencies in Fig. 6.2(a), where $\nu_1 = 2.38 \times 10^{-4}$Hz (orange) and

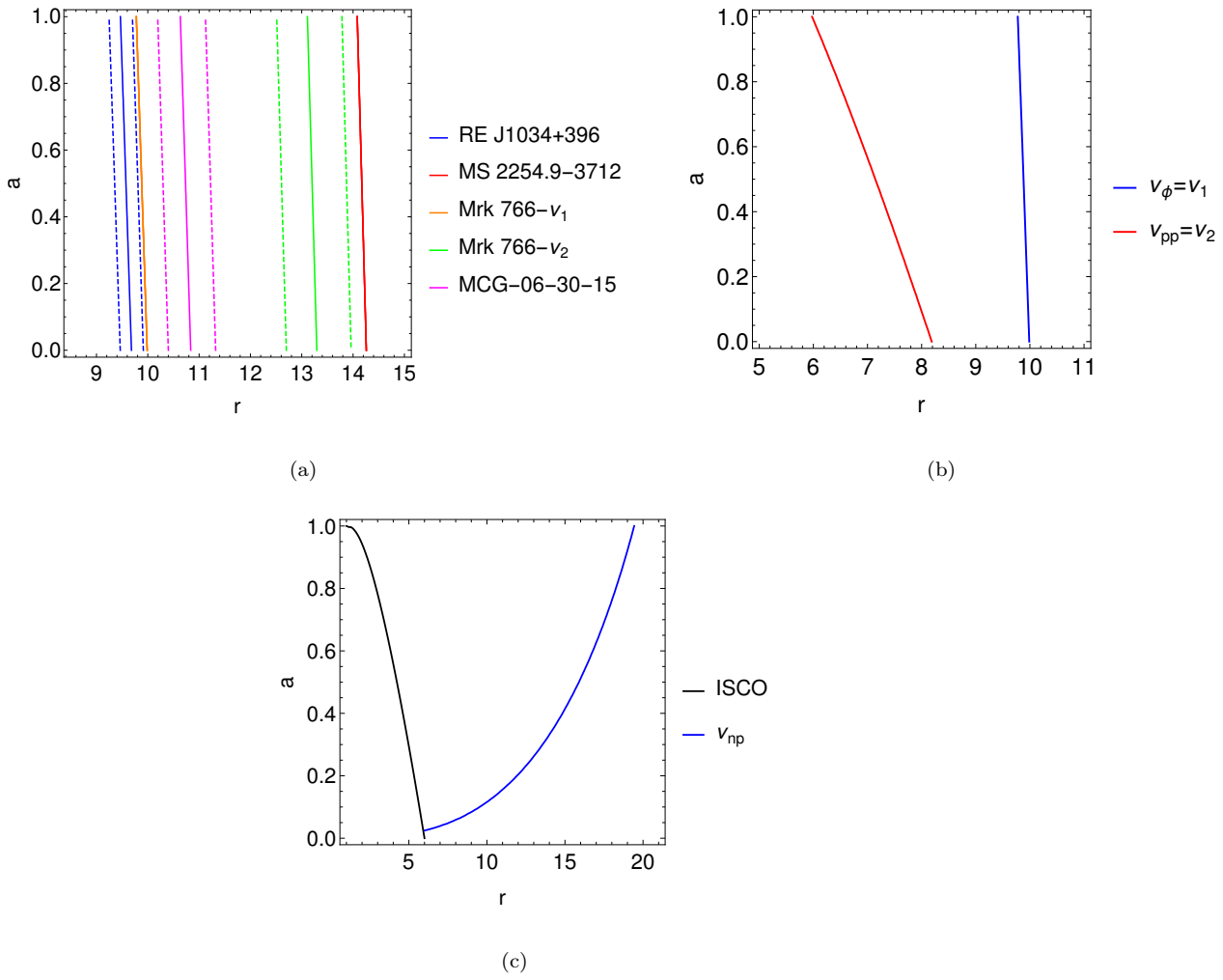

FIGURE 6.2: The figure shows the circular orbit frequency contours of (a) ν_ϕ, Eq. (5.1a), for the QPO frequencies of RE J1034+396, MS 2254.9-3712, Mrk 766, and MCG-06-30-15, given in Table 6.1; (b) ν_ϕ and ν_{pp} contours, Eq. (5.1b), for two QPO frequencies of Mrk 766; and (c) ν_{np} contour, Eq. (5.1c), for the QPO frequency of 2XMM J123103.2+110648.

$\nu_2 = 1.55 \times 10^{-4}$Hz (green). The mass of the black hole was fixed to $M_\bullet = 4.3 \times 10^6 M_\odot$ (Wang and Lu 2001). The QPO origin range is $r \sim 10$ for ν_1 and $r \sim (12.6 - 14)$ for ν_2, which is again found to be in a narrow range and very close to the black hole. Although these QPOs were not detected simultaneously, we tried to estimate a simultaneous solution for (r, a) by equating $\nu_\phi = \nu_1$ and $\nu_{pp} = \nu_2$ as per GRPM. We show them as curves in the (r, a) plane in Fig. 6.2(b) and we see that these contours do not cross each other, implying that there is no simultaneous solution for (r, a).

3. For the Type-2 AGN 2XMM J123103.2+110648, the detected QPO (see Table 6.1) was suggested as an LFQPO type because of its large rms value (Lin *et al.* 2013). If this QPO frequency is equated to the high-frequency component, $\nu_{\phi}(r, a)$, of the GRPM, we found that $r \sim 200$ which is far from the black hole to emit in X-rays. Hence, the GRPM predicts that this should be an LFQPO. We show the contours of the LFQPO component of the GRPM, $\nu_{np}(r, a)$, in the (r, a) plane for the QPO frequency of 2XMM J123103.2+110648 in Fig. 6.2(c), where we fixed $M_{\bullet} = 10^5 M_{\odot}$ (Ho *et al.* 2012). We see that the emission region for this LFQPO is $r \sim (6 - 20)$, for the whole range of a. Hence, the detected QPO of 2XMM J123103.2+110648 is suggested to be a LFQPO, in the context of the model, that originated very close to the black hole.

4. For the case having two simultaneous X-ray QPOs, 1H 0707-495 (see Table 6.1), we first solve the equations $\{\nu_{\phi}(r, a) = \nu_{10},\ \nu_{pp}(r, a) = \nu_{20}\}$ [using Eqs. (5.1a) and (5.1b)], assuming $M_{\bullet} = 5.2 \times 10^6 M_{\odot}$ (Pan *et al.* 2016), as per GRPM to estimate the exact solution for $(r,\ a)$, which is found to be $(r_0 = 8.214,\ a_0 = 0.0662)$. We then apply the method, described in §5.3.2, to estimate the errors in the parameters $(r,\ a)$ implied due to the errors of the QPO frequencies. The range of $(r,\ a)$ and corresponding resolutions used for our simulations are summarized in Table 6.2. Finally, we generate the probability density profiles in each parameter dimension $\{\mathcal{P}_1(r),\ \mathcal{P}_1(a)\}$, shown in Fig. 6.3, where we have also shown the probability contours in the parameter space. The results of the model fits to the probability density profiles are summarized in Table 6.2. The errors in the parameters are quoted with respect to the exact solution $(r_0,\ a_0)$, whereas the simulated $\{\mathcal{P}_1(r),\ \mathcal{P}_1(a)\}$ profiles peak at $(r = 8.092,\ a = 0.038)$, which slightly differs from the exact solution. Hence, our analysis assuming the circular orbit frequencies as the origin of QPOs, using the GRPM, in NLSy1 1H 0707-495, suggests that it harbors a slowly rotating black hole ($a \sim 0.0662$) at the center, and

TABLE 6.2: The table summarizes results of $\{r,\ a\}$ parameter solution, and corresponding errors for X-ray QPOs in NLSy1 1H 0707-495. The columns provide the range of parameter volume taken for $\{r,\ a\}$, the chosen resolution to calculate the normalized probability density at each point inside the parameter volume, the exact solutions, and the results of the model fit to the integrated profiles. The mass of the black hole is fixed to $M_\bullet = 5.2 \times 10^6 M_\odot$ (Pan *et al.* 2016).

Source	r **range**	**Resolution** Δr	**Exact solution** r_0	**Model fit**	a **range**	**Resolution** Δa	**Exact solution** a_0	**Model fit**
1H 0707-495	$7 - 9.5$	0.01	8.214	$8.214^{+0.116}_{-0.359}$	$0 - 0.9$	0.001	0.0662	$0.0662^{+0.2695}_{-0.0662}$

that the X-ray QPOs originate in the inner region of the accretion disk and very close to the black hole ($r \sim 8.214$).

6.2.2 Spherical orbits

In this section, we apply the GRPM for simultaneous QPOs of 1H 0707-495 to estimate the $(r_s,\ a,\ Q)$ parameters of the spherical orbits using their fundamental frequencies, given by Eqs. (4.24b, 4.25c). We discuss our results below:

1. We explore the parameter space $(r_s,\ a,\ Q)$ for the spherical orbits. Since there are two input QPO frequencies, we first vary the Q value to find various solutions of $\{r_s,\ a\}$ by solving equations $\{\nu_\phi = \nu_1,\ \nu_{pp} = \nu_2\}$ as per GRPM. $Q = 13$ is at the limit of astrophysically allowed bound orbits, Eq. (4.8); $Q < 13$ in the case of 1H 0707-495. The $Q = 13$ orbit is an unstable orbit very close to the separation of bound and unbound (called a separatrix orbit), and such an unstable orbit is not relevant to our study; hence, we fix our parameter exploration between $Q = 1$ and 12. In Figure 6.4, we have shown these solutions in the $(Q,\ a)$ and $(Q,\ r_s)$ planes.

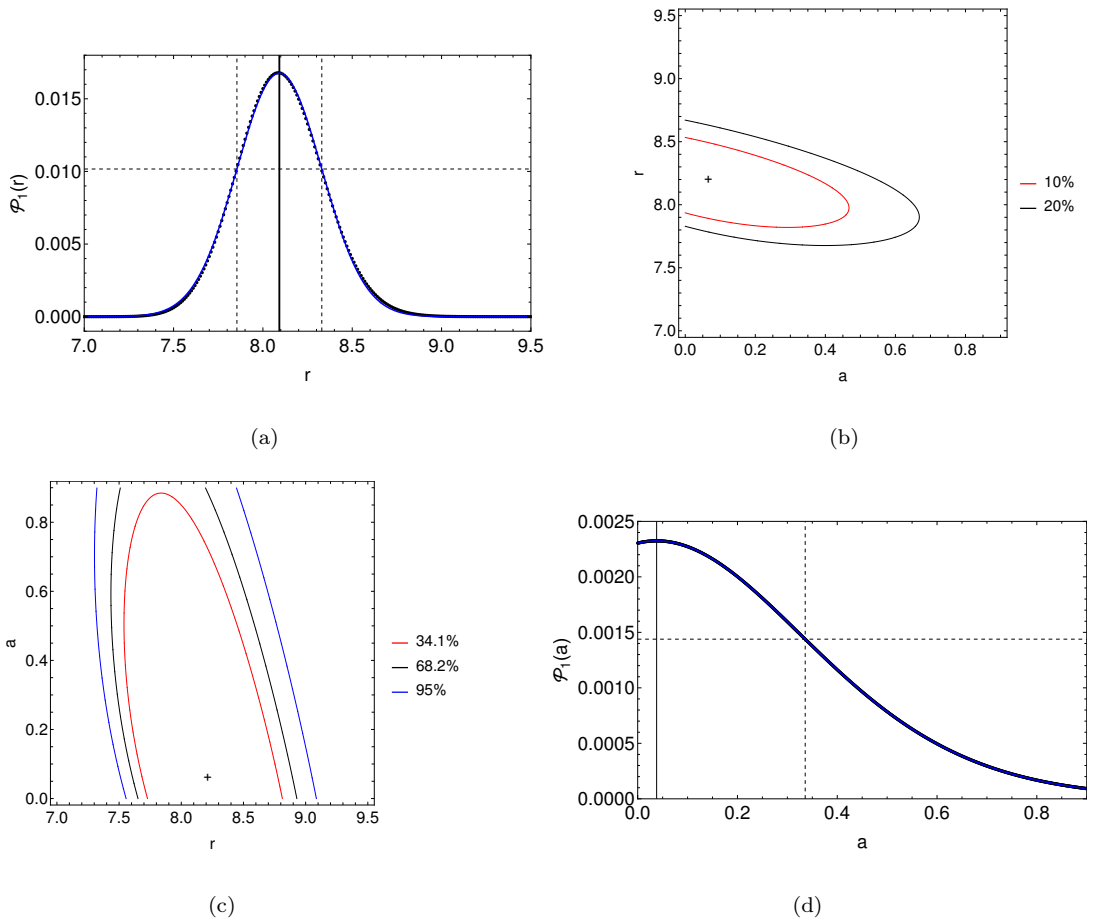

FIGURE 6.3: The integrated probability density profiles for 1H 0707-495 are shown in (a) $\mathcal{P}_1(r)$ and (d) $\mathcal{P}_1(a)$, where the dashed vertical lines enclose a region with 68.2% probability, and the solid vertical line corresponds to the peak of the profiles. The inner probability contours of the parameter solution are shown: (b) in the (a, r) plane, and (c) the outer contours in the (r, a) plane, where the + sign marks the exact solution.

2. Next, we fix $Q = \{1, 4, 8, 12\}$ and find the errors in the $\{r_s, a\}$ parameters using the method described in §5.3.2. The range of $\{r_s, a\}$, resolution taken in the simulations, along with the exact solutions and their errors obtained by fitting $\mathcal{P}_1(r_s)$ and $\mathcal{P}_1(a)$ are summarized in Table 6.3.

3. The ranges of $\{a, r_s, Q\}$, shown in Table 6.3 and Fig. 6.4, span the complete parameter volume for QPO frequencies of 1H 0707-495. As the spin of the black hole does not change in the timescale of a few months or years, we need to find the most probable value of spin. We first find the variance of

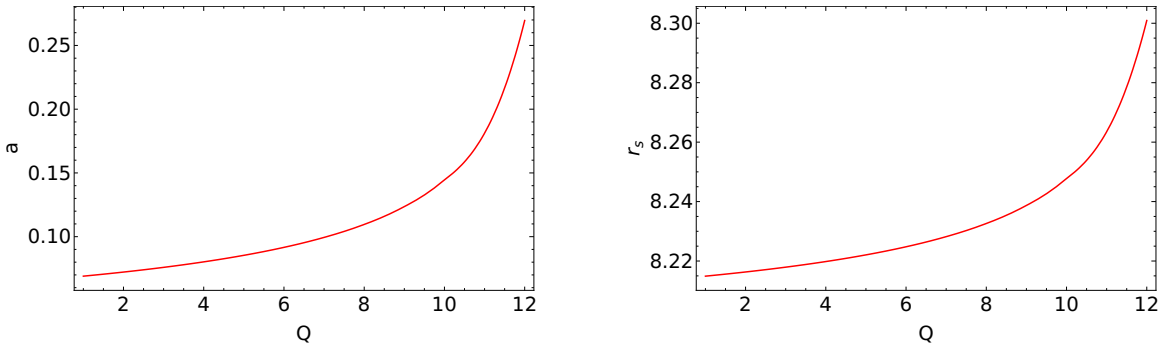

(a) (b)

FIGURE 6.4: The figure shows the solutions of spherical orbit parameters $\{r_{s0},\ a_0,\ Q_0\}$ for QPO frequencies of 1H 0707-495 in (a) $(Q,\ a)$, and in (b) $(Q,\ r_s)$ plane.

$\mathcal{P}_1(a)$ with respect to the exact solution of a for each Q, given in Table 6.3, which is given by

$$\sigma_{ai}{}^2 = \int_0^{0.9} (a - a_{0i})^2 \mathcal{P}_{1i}(a)\, da, \tag{6.1a}$$

where $\mathcal{P}_{1i}(a)$ is the probability density distribution in a parameter space for each value of Q. We have summarized the values of σ_a for each Q in Table 6.3. We then minimize the likelihood function

$$L(a) = \sum_i^4 \frac{(a - a_{0i})^2}{\sigma_{ai}{}^2}, \tag{6.1b}$$

to obtain the most probable value of the spin given by

$$a_p = \frac{\sum_i^4 (a_{01}/\sigma_{ai}{}^2)}{\sum_i^4 (1/\sigma_{ai}{}^2)}. \tag{6.1c}$$

We find the peak value to be $a_p = 0.139$ for 1H 0707-495, and corresponding solution of $\{r_s,\ Q\}$ for the QPO frequencies is $\{r_{sp} = 8.246,\ Q_p = 9.814\}$.

4. Next, we obtain the χ^2_a distribution function of a given by

$$\chi^2_a(a) = \exp[-L(a)]. \tag{6.2}$$

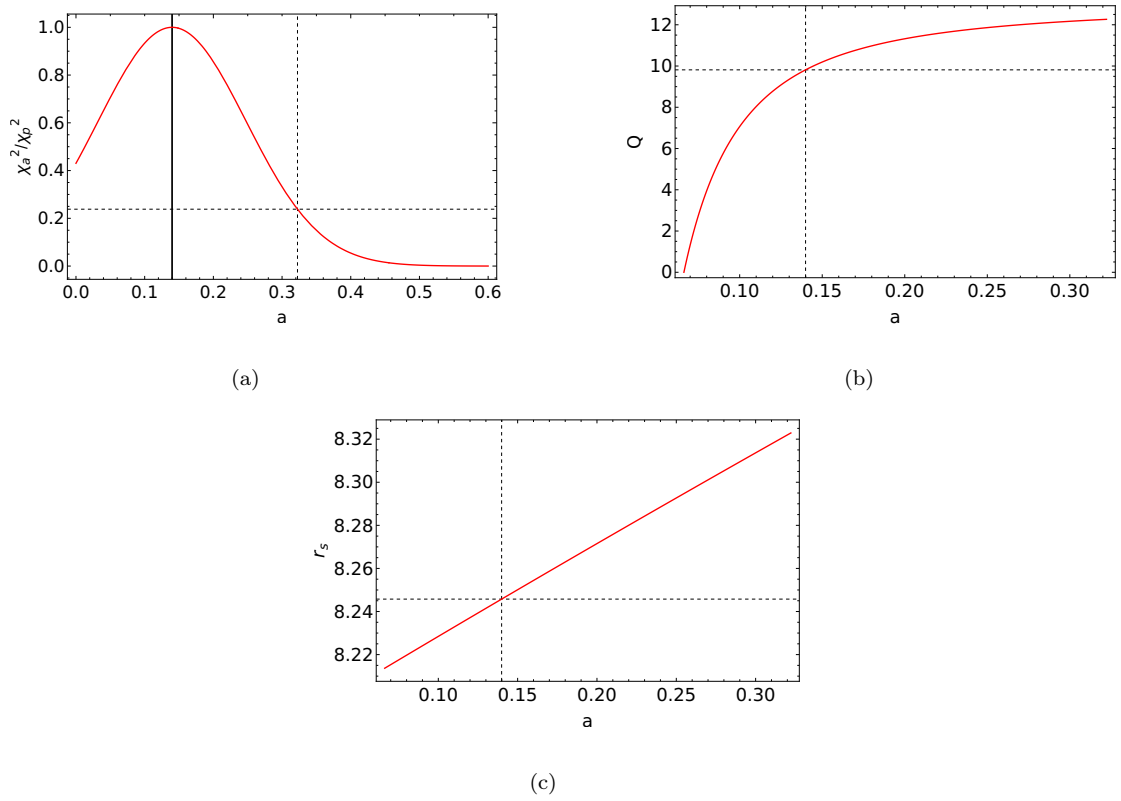

(a) (b)

(c)

FIGURE 6.5: The figure shows (a) χ_a^2/χ_p^2 function for a, where the vertical solid black curve depicts a_p and the vertical dashed black curve encloses the 95% probability region, (b) the range of Q and (c) r_s corresponding to the 2σ region of a, where the vertical dashed black curves mark $\{a_p\ ,r_{sp},\ Q_p\}$.

A plot of χ_a^2/χ_p^2 is shown in Fig. 6.5(a), where $\chi_p^2 = \chi_a^2\,(a_p)$. We obtain the 2σ errors with respect to a_p by normalizing the $\chi_a^2\,(a)$ function and obtain $0.139^{0.183}_{-0.139}$, where the region of 95% probability is indicated by the vertical dashed line in Fig. 6.5(a). We also show the range of r_s and Q in Figs. 6.5(b) and 6.5(c) within the 2σ region of a, as seen in Fig. 6.5(a), where the parameter ranges are $r_s = (8.214 - 8.323)$ and $Q = (0.0001 - 12.264)$.

5. Hence, we conclude that the spherical orbits, close to the black hole in the region, $r_s = (8.214 - 8.323)$ with Q values between $(0.0001 - 12.264)$, can explain the QPO frequencies observed in 1H 0707-495, while the most probable spin value to be $a_p = 0.139^{0.183}_{-0.139}$ with 2σ confidence.

TABLE 6.3: The table summarizes results of spherical orbit parameter solution, $\{r_s,\, a\}$, and corresponding errors for X-ray QPOs in NLSy1 1H 0707-495. The columns provide the range of parameter volume taken for $\{r_s,\, a\}$ by fixing $\{Q = 1, 4, 8, 12\}$, the chosen resolution to calculate the normalized probability density at each point inside the parameter volume, the exact solutions, the results of the model fit to the integrated profiles, and variance σ_a. The mass of the black hole is fixed to $M_\bullet = 5.2 \times 10^6 M_\odot$ (Pan *et al.* 2016).

Q	r_s **range**	**Resolution** Δr_s	**Exact solution** r_{s0}	**Model fit**	a **range**	**Resolution** Δa	**Exact solution** a_0	**Model fit**	σ_a
1	$6.5 - 9.5$	0.01	8.215	$8.215^{+0.118}_{-0.354}$	$0 - 0.9$	0.001	0.069	$0.069^{+0.28}_{-0.069}$	0.290
4	$6.5 - 9.5$	0.01	8.219	$8.219^{+0.127}_{-0.331}$	$0 - 0.9$	0.001	0.080	$0.080^{+0.316}_{-0.080}$	0.317
8	$6.5 - 10$	0.01	8.233	$8.233^{+0.157}_{-0.278}$	$0 - 0.9$	0.001	0.109	$0.109^{+0.366}_{-0.109}$	0.348
12	$6.5 - 10$	0.01	8.301	$8.301^{+0.231}_{-0.196}$	$0 - 0.9$	0.001	0.269	$0.269^{+0.127}_{-0.269}$	0.277

6.3 Relativistic jet model for the optical and γ ray QPOs

In a simple kinematic approach inspired by the lighthouse model (Camenzind and Krockenberger 1992; Mohan and Mangalam 2015; Mangalam 2018), the basic periodicity is set by

$$\begin{aligned} T_F = &\quad 30.93 \left(r_F^{3/2} + a\right)(1+z) m_6 \text{ s}, \\ \simeq &\quad 35.8 \left(\frac{r_F}{100}\right)^{3/2} (1+z)\, m_8 \text{ days}, \end{aligned} \tag{6.3}$$

where $m_6 = M_\bullet / (10^6 M_\odot)$ and $m_8 = M_\bullet / (10^8 M_\odot)$ and r_F is the radius of the footpoint of the magnetic field anchored in the equatorial plane. An important radius is the light cylinder radius, which given in geometrical units is $r_L = r_F^{3/2} + a$. The plasma is expected to relativistically follow the field lines upto the light cylinder rigidly beyond which the field lines would be bend. A reasonable estimate of the cylindrical radius of the plasma motion is expected to be typically $r_0 \equiv \chi r_L$ where $\chi = (0.1 - 10)$. Taking an angular momentum conservation beyond the Alfven radius, $r_A = x_A r_L$, where $x_A < 1$, will lead to $r_0^2 \Omega_0^2 = x_A^2 r_L^2 \Omega_F^2$, setting an observed periodicity of $T_0 = (\chi / x_A)\, T_F$. The value of (χ / x_A) depends on details

TABLE 6.4: A list of statistically significant QPOs detected in the γ ray and optical energy bands in BL Lacertae type of AGN, along with their redshifts and black hole masses. The theoretical timescales are calculated, using Eq. (6.3), such that the lower and upper limit correspond to $r_F = 30$ and $r_F = 80$ respectively.
References: [1]Ackermann *et al.* (2015b); [2]Chen (2018); [3]Sandrinelli *et al.* (2014); [4]Sandrinelli *et al.* (2016a); [5]Sandrinelli *et al.* (2018); [5]Tavani *et al.* (2018); [6]Ackermann *et al.* (2015a); [7]Sandrinelli *et al.* (2016b); [8](Sandrinelli *et al.* 2017)

Source	z	$\log\mathcal{M}$	**Energy band**	**QPO period** T_0 **(days)**	T_F **(days)**
PKS 2155-304	0.116[1]	8.7[2]	100MeV-300GeV	620±41[3,4,5]	33 − 143
			R (optical)	315±25[3,4,5]	
PG 1553+113	0.36[2]	~ 8[5]	100MeV-300GeV	780±63[5,6]	8 − 35
			R (optical)	810±52[5,6]	
PKS 0537-441	0.892[1]	8.56[2]	100MeV-300GeV	280±39[7]	40 − 176
			R (optical)	148±17[7]	
BL Lac	0.0686[1]	8.21[2]	100MeV-300GeV	680±35[5,8]	10 − 44
			R (optical)	670±40[5,8]	

of the relativistic MHD models and x_A is determined by the relativistic Bernoulli equation, but a range of $(\chi/x_A) = 1 - 20$ is reasonable (Mohan and Mangalam 2015). This is illustrated by estimating $T_F(r_F)$ for the range of $r_F = (30 - 80)$ (see Table 6.4); we see that the observed $\dfrac{T_0}{T_F(r_F = 50)}$ is in the range of $(1 - 20)$.

This agreement motivates the study of the plasma motion in the background of relativistic MHD models, and its comparison with fits to the light curves in the future. Another clue of the jet physics will come from polarization models, as evidenced by the promising but simplistic cylindrical relativistic polarization signatures of the EVPA, DOP, and Doppler boosted flux profiles, as predicted by Mangalam (2018); this will be an additional and useful tool to extract jet properties by doing detailed fits to polarization observations. There is an oscillatory behavior seen in both γ-ray and optical light curves (Sandrinelli *et al.* 2014, 2016a,b; Ackermann *et al.* 2015a; Sandrinelli *et al.* 2018, 2017; Bhatta 2019; Gupta *et al.* 2019) that

supports the above trend. There is also evidence of the radio structure that is supported by the basic model of Mohan and Mangalam (2015) as observed by An *et al.* (2020); Mohan *et al.* (2016).

6.4 Relativistic orbit model (ROM) and PSD shape

The X-ray timing analysis of NLSy1 galaxies has been proven to be an essential tool for probing the emission region and the underlying mechanism of the variability process of the X-ray flux in these sources. The shape of the power spectral density is found to have a shape which is well fit by a bending power-law model given by (McHardy *et al.* 2004)

$$\mathcal{P}_s(\nu) = P_0 \left(\frac{\nu}{\nu_b}\right)^{-\alpha_l} \left[1 + \left(\frac{\nu}{\nu_b}\right)^{(\alpha_h - \alpha_l)}\right]^{-1}, \tag{6.4}$$

where P_0 is the normalization constant, and α_l, α_h are the PSD slopes below and above the break frequency, ν_b. The power density spectrum shows that the low-frequency power spectrum is significantly flatter ($\alpha_l \sim 1$) than the high-frequency power spectrum ($\alpha_h > 2$). The break frequencies were found to be near $\nu_b \sim 6.7 \times 10^{-6}$Hz for PKS 0558-504 (Papadakis *et al.* 2010) and $\nu_b \sim 8 \times 10^{-4}$Hz for NGC 4051 (McHardy *et al.* 2004).

Here, we present a plausible relativistic orbit model to generate such a power density spectrum. As argued before, the non-equatorial orbits, such as spherical orbits, are the natural consequence of the axisymmetry of the Kerr space-time (Carter 1968; Rana and Mangalam 2019a). We assume that inside a spherical corona region of relativistic electrons (the inner corona, IC, $r_M < r < r_I$), existing inside the radius of innermost stable circular orbit (ISCO) (see Figure 6.1), the particles are in non-equatorial orbits. The thin accretion disk spans the region

outside ISCO, where the fluid motion is confined to the equatorial plane. We also assume that an outer corona region (OC, $r_I < r < r_X$) of relativistic particles envelopes this accretion disk, lying almost in the equatorial plane (see Figure 6.1). The energy per unit rest mass of these relativistic particles, E, orbiting in the equatorial circular trajectories, is given by (Bardeen *et al.* 1972)

$$E\left(r,a\right)=\frac{r^{2}-2r+a\sqrt{r}}{r\left(r^{2}-3r+2a\sqrt{r}\right)^{1/2}}. \tag{6.5}$$

We see that E increases with r outside ISCO, and it decreases with r inside ISCO, where it has minima at the ISCO radius; see Fig. 6.6(a). The stable circular orbits exist outside the ISCO radius, whereas the unstable circular orbits are found inside the ISCO radius. The mechanical energy per unit rest mass of the relativistic plasma, E, orbiting in the spherical trajectories, is given by [Eq. (4.15a)]

$$E\left(r_{s},a,Q\right)=\frac{\left\{\begin{array}{r}2a^{4}Q+\left(r_{s}-3\right)\left(r_{s}-2\right)^{2}r_{s}^{4}-a^{2}r_{s}\left[r_{s}^{2}\left(3r_{s}-5\right)+Q\left(r_{s}\left(r_{s}-4\right)+5\right)\right]\\ -2a\left[r_{s}\left(r_{s}-2\right)+a^{2}\right]\sqrt{a^{2}Q^{2}-r_{s}^{3}Q\left(r_{s}-3\right)+r_{s}^{5}}\end{array}\right\}^{1/2}}{r_{s}^{2}\left[r_{s}\left(r_{s}-3\right)^{2}-4a^{2}\right]^{1/2}}, \tag{6.6}$$

where E increases with r_s outside the innermost stable spherical orbit (ISSO), and it decreases with r_s inside ISSO, where it has minima at the ISSO radius; see Figure 6.6(b). The stable spherical orbits, for a fixed Q, exist outside the ISSO radius, whereas the unstable spherical orbits are found inside the ISSO radius.

A comparison of the ISCO and ISSO radii is shown in the (r, a) plane in Figure 6.7, where we see that these radii converge to $r = 6$ for the Schwarzschild black hole ($a = 0$), as the spherical orbits or ISSOs are possible only outside a Kerr black hole ($a \neq 0$) because of the axisymmetry of the Kerr space-time. Additionally, as the value of Q increases, the ISSO radii move further away from the black hole as compared to the ISCO radius. This implies that one will always find the unstable circular and the unstable spherical orbits inside the ISCO radius.

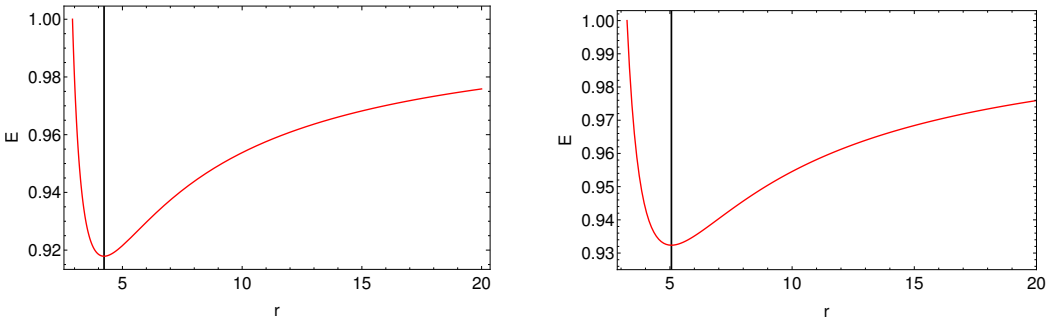

(a) (b)

FIGURE 6.6: The figure shows $E(r)$ as a function of r for (a) the equatorial circular orbits ($Q = 0$) and for (b) the spherical orbits with $Q = 8$, where $a = 0.5$. The vertical black curves correspond to the innermost stable circular orbit (ISCO) and to the innermost stable spherical orbit (ISSO) for $Q = 8$.

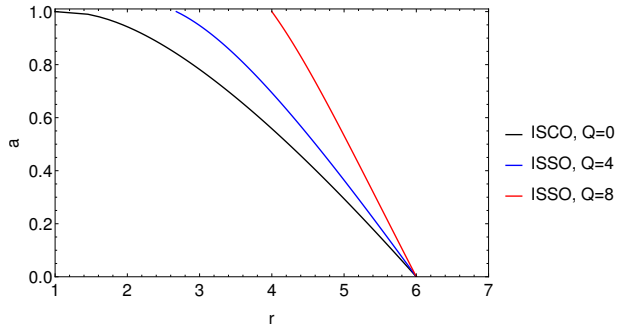

FIGURE 6.7: The figure shows a comparison of the ISCO and ISSO radii in the (r, a) plane. The ISSO radius moves outwards as Q increases.

6.4.1 The ROM

The underlying assumptions of our model are:

1. We associate the temporal frequency, ν, in the observed power spectral density with the fundamental azimuthal frequency of the particles orbiting in the circular orbits in the accretion disk outside ISCO, r_I, and both circular and spherical trajectories between r_I and marginally bound spherical orbit (MBSO) radius, r_M. These frequencies are functions of the orbital radius,

r or r_s, [Eqs. (5.1a) and (4.24b)], and hence they are also fundamentally related to the mechanical energy of the orbit through Eqs. (6.5, 6.6).

2. We assume a prior distribution of the energy of particles (or electrons) given by a power-law

$$N(E) = A\left(\frac{E}{E_I}\right)^{-\alpha_1}, \quad \text{IC}: \text{ radial range } r_M < r < r_I, \tag{6.7a}$$

$$= A\left(\frac{E}{E_I}\right)^{-\alpha_2}, \quad \text{OC}: \text{ radial range } r_I < r < r_X, \tag{6.7b}$$

where $N(E)$ represents the number of particles having energy E, α_1 and α_2 are the power-law indices inside and outside r_I respectively, E_I is the particle energy at r_I, and A is the normalization constant. The energy distribution, $N(E)$ (Eq. (6.7)), is constructed so that it is continous at r_I. Assuming that the total number of particles are N_0 (however, the PSD solution is independent of this), we have the normalization condition given by

$$\int N(E)\, dE = N_0, \tag{6.8a}$$

$$A\int_{E_I}^{1}\left(\frac{E}{E_I}\right)^{-\alpha_1} dE + A\int_{E_I}^{E_X}\left(\frac{E}{E_I}\right)^{-\alpha_2} dE = N_0, \tag{6.8b}$$

where the first and the second terms contribute for the regions inside and outside r_I respectively, and E_X corresponds to the energy of the particles at the outer radius of the equatorial circular accretion disk, r_X. Subsequently, we obtain

$$A(a,\alpha_1,\alpha_2) = N_0\left[\frac{\left(E_I(a)^{\alpha_1} - E_I(a)\right)}{(1-\alpha_1)} + \frac{\left(E_X(a)^{(1-\alpha_2)} E_I(a)^{\alpha_2} - E_I(a)\right)}{(1-\alpha_2)}\right]^{-1}. \tag{6.8c}$$

We redefine $A(a)$ such that

$$A(a,\alpha_1,\alpha_2) = N_0 B(a,\alpha_1,\alpha_2), \tag{6.8d}$$

where

$$B\left(a,\alpha_1,\alpha_2\right)=\left[\frac{\left(E_I\left(a\right)^{\alpha_1}-E_I\left(a\right)\right)}{\left(1-\alpha_1\right)}+\frac{\left(E_X\left(a\right)^{\left(1-\alpha_2\right)}E_I\left(a\right)^{\alpha_2}-E_I\left(a\right)\right)}{\left(1-\alpha_2\right)}\right]^{-1}. \tag{6.8e}$$

3. We assume that the break frequency of the PSD corresponds to the temporal frequency at the ISCO radius.

4. We also assume that the particle distribution in the temporal frequency space, $F\left(\bar{\nu}\right)$, directly translates to the observed intensity for a given temporal frequency, so that the power density is given by $P\left(\bar{\nu}\right)\propto F\left(\bar{\nu}\right)^2$.

Next, we derive the distribution of the temporal frequency, $F\left(\bar{\nu}\right)$, as follows:

$$\frac{dN\left(E\right)}{dE}=\frac{dF\left(\bar{\nu}\right)}{d\bar{\nu}}\frac{d\bar{\nu}}{dE}, \tag{6.9a}$$

$$\Rightarrow\frac{dF\left(\bar{\nu}\right)}{d\bar{\nu}}=\frac{dN\left(E\right)}{dE}\frac{dE\left(\bar{\nu}\right)}{d\bar{\nu}}. \tag{6.9b}$$

We obtain $\left(dN\left(E\right)/dE\right)$ from Eq. (6.7), and numerically obtain $E\left(\bar{\nu}\right)$ to derive $\left(dE\left(\bar{\nu}\right)/d\bar{\nu}\right)$, using Eqs. (5.1a, 6.5) for circular and Eqs. (4.24b, 6.6) for spherical orbits. In Fig. 6.8, we have shown $E(\bar{\nu}_\phi)$, where it is clear that the behaviour of $E(\bar{\nu}_\phi)$ changes inside and outside r_I. Outside r_I, Fig. 6.8(a), the radius of the circular orbits goes from r_I to $r_X\approx 50$ (1 keV$\approx\frac{GM_\bullet m_e}{r_X k_B}$), whereas inside r_I, Fig. 6.8(b), the radius of the circular orbits varies between r_I and marginally bound circular orbit (MBCO), r_M, which corresponds to $E=1$.

Next, we obtain the temporal frequency distribution given by

$$F_1\left(\alpha_1,\alpha_2,\bar{\nu},a,Q\right)=-\alpha_1 B\left(a,\alpha_1,\alpha_2\right)E_I\left(a\right)^{\alpha_1}\int_{\bar{\nu}_I(a)}^{\bar{\nu}}\Phi_1\left(\alpha_1,\bar{\nu}^{'},a,Q\right)d\bar{\nu}^{'}+N_I\left(\alpha_1,\alpha_2,a,Q\right),$$

inside ISCO, (6.10a)

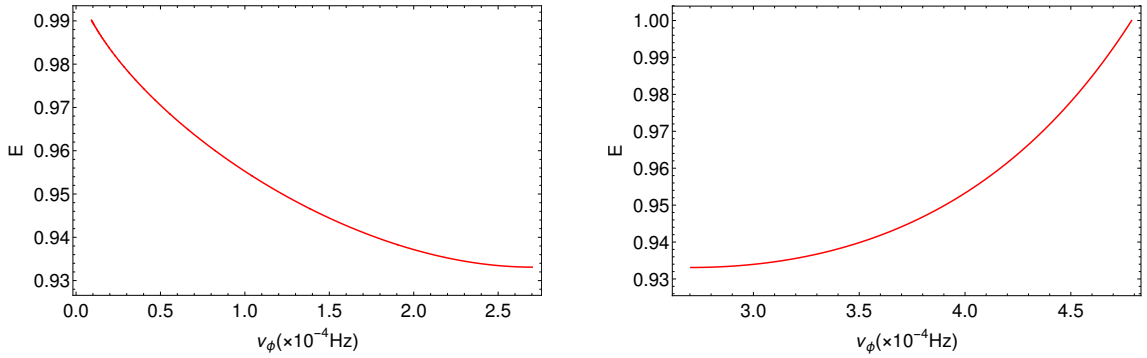

(a) (b)

FIGURE 6.8: The figure shows E as a function of ν_ϕ for the circular orbits (a) outside r_I, and (b) inside r_I for $a = 0.25$ and $M_\bullet = 10^7 M_\odot$. The minima of E is at r_I in both diagrams.

$$F_2\left(\alpha_1, \alpha_2, \bar{\nu}, a, Q\right) = -\alpha_2 B\left(a, \alpha_1, \alpha_2\right) E_I\left(a\right)^{\alpha_2} \int_{\bar{\nu}_X(a)}^{\bar{\nu}} \Phi_2\left(\alpha_2, \bar{\nu}^{'}, a\right) d\bar{\nu}^{'} + N_X\left(\alpha_1, \alpha_2, a, Q\right), \quad \text{outside ISCO,} \tag{6.10b}$$

where $\bar{\nu}_I\left(a\right)$ is frequency at r_I and $\bar{\nu}_X\left(a\right)$ is frequency at r_X [where the energy is E_X defined in Eq. (6.8c)]. $N_I\left(\alpha_1, \alpha_2, a, Q\right)$ and $N_X\left(\alpha_1, \alpha_2, a, Q\right)$ correspond to the number of particles having frequency at r_I and r_X respectively, where we have scaled the functions F_1, F_2, N_I, and N_X by N_0. The expressions for the functions $\Phi_1\left(\alpha_1, \bar{\nu}^{'}, a, Q\right)$ and $\Phi_2\left(\alpha_2, \bar{\nu}^{'}, a\right)$ are given by

$$\Phi_1\left(\alpha_1, \bar{\nu}^{'}, a, Q\right) = \frac{1}{E\left(\alpha_1, \bar{\nu}^{'}, a, Q\right)^{1+\alpha_1}} \frac{dE\left(\alpha_1, \bar{\nu}^{'}, a, Q\right)}{d\bar{\nu}^{'}}, \tag{6.11a}$$

$$\Phi_2\left(\alpha_2, \bar{\nu}^{'}, a\right) = \frac{1}{E\left(\alpha_2, \bar{\nu}^{'}, a\right)^{1+\alpha_2}} \frac{dE\left(\alpha_2, \bar{\nu}^{'}, a\right)}{d\bar{\nu}^{'}}. \tag{6.11b}$$

We scale the distribution functions, Eq. (6.10), by N_I for simplicity, which yields

$$f_1\left(\alpha_1,\alpha_2,\bar{\nu},a,Q\right) = \quad -\frac{V\left(a,\alpha_1,\alpha_2\right)}{N_I\left(\alpha_1,\alpha_2,a,Q\right)}C_{1Ik}\left(\alpha_1,\bar{\nu},a,Q\right)+1, \qquad \text{inside ISCO,} \tag{6.12a}$$

$$f_2\left(\alpha_1,\alpha_2,\bar{\nu},a,Q\right) = \quad -\frac{W\left(a,\alpha_1,\alpha_2\right)}{N_I\left(\alpha_1,\alpha_2,a,Q\right)}C_{2Xk}\left(\alpha_2,\bar{\nu},a\right)+n_X\left(\alpha_1,\alpha_2,a,Q\right), \qquad \text{outside ISCO,} \tag{6.12b}$$

where

$$C_{ijk}=\int_{\bar{\nu}_j}^{\bar{\nu}_k}\Phi_i\left(\bar{\nu}^{'}\right)d\bar{\nu}^{'}, \tag{6.12c}$$

$$V\left(a,\alpha_1,\alpha_2\right)=\alpha_1 B\left(a,\alpha_1,\alpha_2\right)E_I^{\alpha_1}, \qquad W\left(a,\alpha_1,\alpha_2\right)=\alpha_2 B\left(a,\alpha_1,\alpha_2\right)E_I^{\alpha_2}, \tag{6.12d}$$

and

$$f_i\left(\alpha_1,\alpha_2,\bar{\nu},a,Q\right)=\frac{F_i\left(\alpha_1,\alpha_2,\bar{\nu},a,Q\right)}{N_I\left(\alpha_1,\alpha_2,a,Q\right)}, \qquad n_X\left(\alpha_1,\alpha_2,a,Q\right)=\frac{N_X\left(\alpha_1,\alpha_2,a,Q\right)}{N_I\left(\alpha_1,\alpha_2,a,Q\right)}. \tag{6.12e}$$

We employ the condition that $f_1\left(\alpha_1,\alpha_2,\bar{\nu},a,Q\right)=f_2\left(\alpha_1,\alpha_2,\bar{\nu},a,Q\right)$ at the frequency corresponding to $\{r_I,\,\bar{\nu}_I\left(a\right)\}$, which gives

$$1=-\frac{W\left(a,\alpha_1,\alpha_2\right)}{N_I\left(\alpha_1,\alpha_2,a,Q\right)}C_{2XI}\left(\alpha_2,a\right)+n_X\left(\alpha_1,\alpha_2,a,Q\right), \tag{6.13a}$$

or

$$N_I\left(\alpha_1,\alpha_2,a,Q\right)=-W\left(a,\alpha_1,\alpha_2\right)C_{2XI}\left(\alpha_2,a\right)+N_X\left(\alpha_1,\alpha_2,a,Q\right). \tag{6.13b}$$

Next, we apply the normalization condition to the temporal frequency distribution given by

$$F_1\left(\alpha_1,\alpha_2,\bar{\nu}_M,a,Q\right)+F_2\left(\alpha_1,\alpha_2,\bar{\nu}_I,a,Q\right)=1, \tag{6.14a}$$

$$-V\left(a,\alpha_1,\alpha_2\right)C_{1IM}\left(\alpha_1,a,Q\right)-W\left(a,\alpha_1,\alpha_2\right)C_{2XI}\left(\alpha_2,a\right)+N_I\left(\alpha_1,\alpha_2,a,Q\right)+N_X\left(\alpha_1,\alpha_2,a,Q\right)=1 \tag{6.14b}$$

where $\bar{\nu}_M(a,Q)$ is the frequency at r_M. We solve Eqs. (6.14b) and (6.13b) together to obtain $N_I(\alpha_1,\alpha_2,a,Q)$ and $N_X(\alpha_1,\alpha_2,a,Q)$. Hence, the substitution of $N_I(\alpha_1,\alpha_2,a,Q)$ from Eq. (6.13b) into Eq. (6.14b) yields

$$N_X(\alpha_1,\alpha_2,a,Q)=\frac{1}{2}\left[1+V(a,\alpha_1,\alpha_2)\,C_{1IM}(\alpha_1,a,Q)+2W(a,\alpha_1,\alpha_2)\,C_{2XM}(\alpha_2,a)\right]. \tag{6.14c}$$

By substituting Eq. (6.14c) back in Eq. (6.13b), we find

$$N_I(\alpha_1,\alpha_2,a,Q)=\frac{1}{2}\left[1+V(a,\alpha_1,\alpha_2)\,C_{1IM}(\alpha_1,a,Q)\right]. \tag{6.15}$$

Hence, we obtain $N_X(\alpha_1,\alpha_2,a,Q)$ and $N_I(\alpha_1,\alpha_2,a,Q)$ using Eqs. (6.15) and (6.14c). Note that $\bar{\nu}_X<\bar{\nu}_I<\bar{\nu}_M$, where $\bar{\nu}_X<\bar{\nu}(r)<\bar{\nu}_I$ outside ISCO ($r_I<r<r_X$) and $\bar{\nu}_I<\bar{\nu}(r)<\bar{\nu}_M$ inside ISCO ($r_M<r<r_I$).

Now, we describe the procedure to obtain the model parameters α_1 and α_2 using observations:

1. If β_1 is the average slope of the observed PSD after the break frequency, $\bar{\nu}>\bar{\nu}_b$, given by

$$\frac{\Delta\log[P(\bar{\nu})]}{\Delta\log[\bar{\nu}]}=\beta_1 \quad\Rightarrow\quad 2\frac{\Delta\log[F_1(\bar{\nu})]}{\Delta\log[\bar{\nu}]}=\beta_1, \tag{6.16a}$$

where Δ represents the difference of values at the end points defined by MBSO and ISCO in our model: the end point of the PSD for $\bar{\nu}>\bar{\nu}_b$ (where $\bar{\nu}_b=\bar{\nu}_I(a)$) is at the MBSO radius ($\bar{\nu}_M(a)$), so that

$$2\log\left[\frac{f_1(\alpha_1,\alpha_2,\bar{\nu}_M(a),a,Q)}{f_1(\alpha_1,\alpha_2,\bar{\nu}_I(a),a,Q)}\right]=\beta_1\log\left[\frac{\bar{\nu}_M(a)}{\bar{\nu}_I(a)}\right], \tag{6.16b}$$

$$f_1(\alpha_1,\alpha_2,\bar{\nu}_M(a),a,Q)=u_1(a,\beta_1), \tag{6.16c}$$

$$\Rightarrow\left[1-\frac{C_{1IM}(\alpha_1,a,Q)\,V(a,\alpha_1,\alpha_2)}{N_I(\alpha_1,\alpha_2,a,Q)}\right]=u_1(a,\beta_1), \tag{6.16d}$$

where

$$u_1(a,\beta_1) = \left(\frac{\bar{\nu}_M(a)}{\bar{\nu}_I(a)}\right)^{\beta_1/2}, \tag{6.16e}$$

where $N_I(\alpha_1,\alpha_2,a,Q)$ can be substituted using Eq. (6.15), which yields

$$\frac{1-u_1(a,\beta_1)}{1+u_1(a,\beta_1)} = V(a,\alpha_1,\alpha_2)\,C_{1IM}(\alpha_1,a,Q). \tag{6.16f}$$

Hence, for a given combination of $\{a,\,Q\}$, we obtain a relation, given by Eq. (6.16f), where $\{\alpha_1,\,\alpha_2\}$ are unknowns.

2. Similarly, if β_2 is the average slope of the observed PSD before the break frequency, $\bar{\nu} < \bar{\nu}_b$, we have

$$2\frac{\Delta\log[F_2(\bar{\nu})]}{\Delta\log[\bar{\nu}]} = \beta_2. \tag{6.17a}$$

The lower extreme of the PSD at $r = r_X$, for $\bar{\nu} < \bar{\nu}_b$, is given by $\bar{\nu}_X(a)$, so that

$$2\log\left[\frac{f_2(\alpha_1,\alpha_2,\bar{\nu}_I(a),a,Q)}{f_2(\alpha_1,\alpha_2,\bar{\nu}_X(a),a,Q)}\right] = \beta_2\log\left[\frac{\bar{\nu}_I(a)}{\bar{\nu}_X(a)}\right], \tag{6.17b}$$

$$n_X(\alpha_1,\alpha_2,a,Q) = u_2(a,\beta_2), \tag{6.17c}$$

where

$$u_2(a,\beta_2) = \left(\frac{\bar{\nu}_I(a)}{\bar{\nu}_X(a)}\right)^{-\beta_2/2}. \tag{6.17d}$$

The substitution of $N_I(\alpha_1,\alpha_2,a,Q)$ and $N_X(\alpha_1,\alpha_2,a,Q)$ using Eqs. (6.15) and (6.14c) gives

$$\frac{u_2(a,\beta_2)-1}{1+u_1(a,\beta_1)} = W(a,\alpha_1,\alpha_2)\,C_{2XI}(\alpha_2,a). \tag{6.17e}$$

which is another relation to solve for $\{\alpha_1,\,\alpha_2\}$. Hence, Eqs. (6.12), (6.16f), and (6.17e) together give us values for $\{\alpha_1,\,\alpha_2\}$ for a fixed combination of $\{a,\,Q\}$.

3. We compute the slopes $\{\alpha_1,\,\alpha_2\}$ by the above mentioned criteria for different combinations of $(a,\,Q)$, which are shown in Table 6.5. We find that α_1 ranges

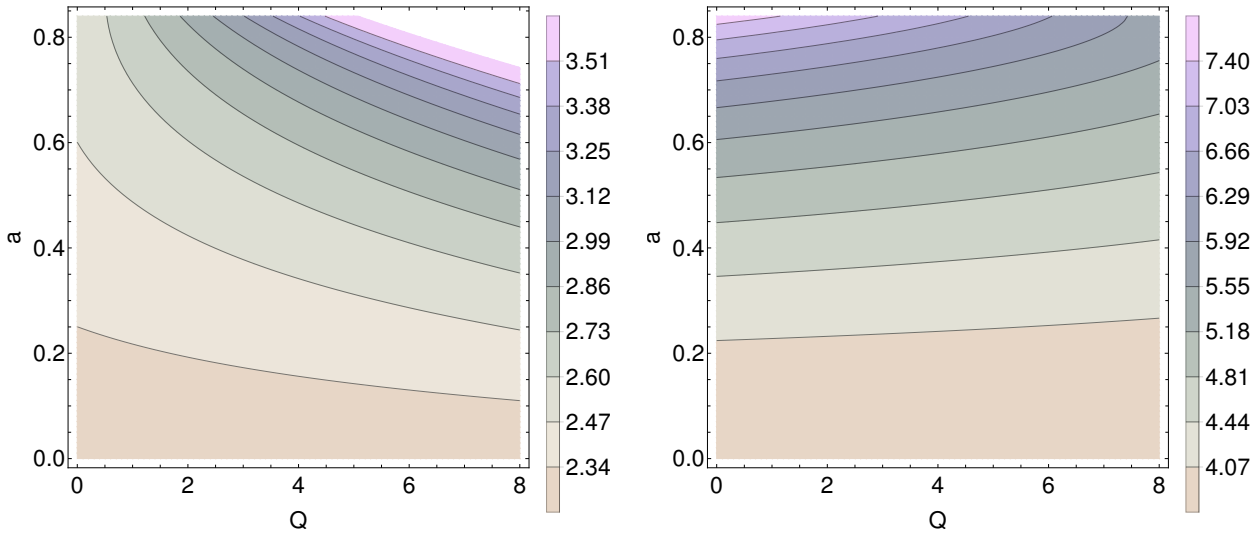

(a) (b)

FIGURE 6.9: The figure shows contours of (a) α_1, and (b) α_2 in the (Q, a) plane.

between $\sim[2.3 - 4]$ and α_2 is in the range $\sim[3.7 - 8.9]$, indicating that a power-law model for the intrinsic mechanical energy of the orbiting matter describes the shape of the observed PSD reasonably well. Additionally, if we reverse the analysis to estimate $\{\beta_1, \beta_2\}$ by fixing $\{\alpha_1 = 2.5, \alpha_2 = 3.5\}$ for $(a = 0.5, Q = 2)$, we find $\{\beta_1 = -1.97, \beta_2 = -0.77\}$ which are in good agreement with observations. We also show contours of α_1 and α_2 in the (Q, a) plane in Fig. 6.9, where the values of α_1 and α_2 increase with a. We also see that contours are independent of Q for small a, which is expected because the non-equatorial orbits do not exist in Schwarzschild spacetime.

4. The examples of PSD profile obtained in the scaled frequency space, $\bar{\nu}$, are shown in Fig. 6.10. We see that the PSD profiles for given parameter combinations in Table 6.5 show good fits to the expected bending power-law model, Eq. (6.4). The PSD represents a general power spectrum obtained independent of the mass of the black hole; hence, it applies to the stellar-mass black holes also. This validates the ROM as a plausible model for PSD observed in black holes.

TABLE 6.5: The table summarizes the computed values of $(\alpha_1,\ \alpha_2)$ and the parameter fits to the bending power-law, Eq. (6.4), for various combinations of $(a,\ Q)$, where we fixed $r_X = 10$ and $\{\beta_1 = -2,\ \beta_2 = -1\}$, and the frequencies were scaled by $(c^3/GM_\bullet)$.

#	$(a,\ Q)$	α_1	α_2	α_l	α_h	P_0
1	$(0.1, 0)$	2.286	3.753	0.282	2.74	0.866
2	$(0.5, 4)$	2.615	4.864	0.413	3.453	0.818
3	$(0.9, 0)$	2.462	8.873	0.488	5.561	1.112
4	$(0.9, 4)$	3.944	7.407	0.497	5.328	0.925

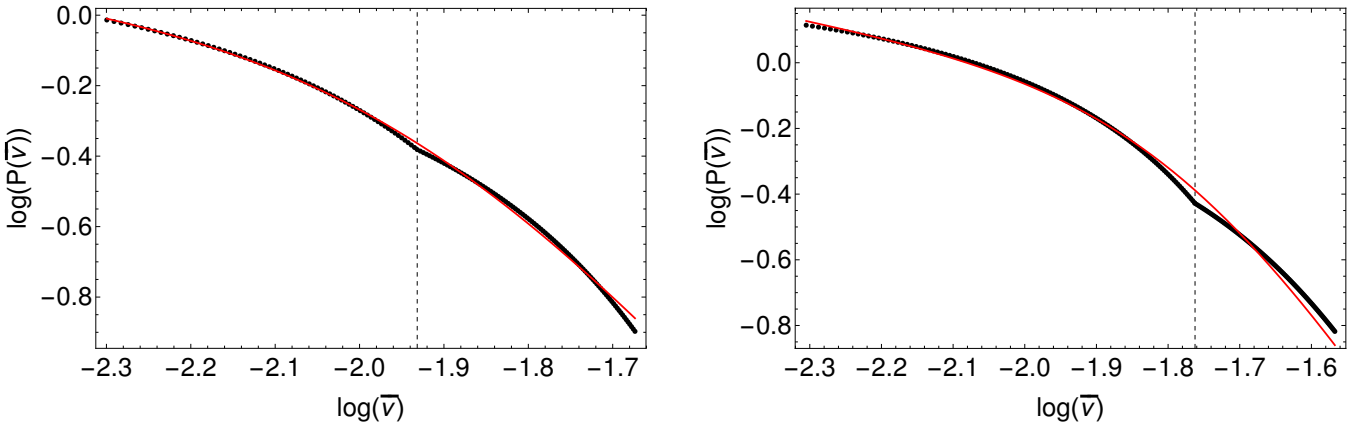

(a) (b)

FIGURE 6.10: The figure shows examples of PSD, $P(\bar{\nu}) \propto F(\bar{\nu})^2$, profile obtained using the ROM for the parameter combinations (a) #1, and (b) #2 given in Table 6.5. The red curve shows the bending power-law model fit, given by Eq. (6.4), where the fitting parameters are shown in Table 6.5. The vertical black dashed curve corresponds to the ISCO (break) frequency.

6.5 Summary

The results are summarized below:

- In §6.1, we summarized the observations for X-ray QPOs, which are traditionally associated with the accretion disk and corona, γ-ray QPOs normally

attributed to a jet, and the X-ray PSD usually connected with the inner and outer corona (see Fig. 6.1).

- In §6.2, we motivated the creation of (G)RPM models for X-ray QPOs and extracted the spins and radii for the sources, listed in Table 6.1, based on the model given in Stella and Vietri (1999); Stella *et al.* (1999); Rana and Mangalam (2020b). The GRPM model confirms that the detected QPO in Type-2 AGN 2XMM J123103.2+110648 is an LFQPO, as it was also suggested by Lin *et al.* (2013). In a statistical analysis, we were able to determine these parameters and their errors for 1H 0707-495, the case of two simultaneous QPOs, based on the observed QPO frequencies and their errors. The results are presented in Table 6.2 for circular orbits and in Table 6.3 for spherical orbits. We found non-planar orbits, with $Q \sim (1 - 12)$, which are very close to a Kerr black hole, that ($r_s \sim (8.2 - 8.3)$; $a \sim 0.14$) are the possible solutions for QPO frequencies of 1H 0707-495.

- Next, in §6.3, we applied the relativistic kinematic jet model to check its validity by comparing the basic frequency with the observed QPO periods in BL Lac objects, given in Table 6.4. The ratio T_0/T_F is typically in the range $1 - 20$, which is reasonable, given the range of footpoint radii of the field lines and typical location of the Alfvén point up to which the field line is rigid (Mohan and Mangalam 2015). It motivates detailed relativistic MHD models along with polarization profile predictions (as given in Mangalam (2018)) to compare with observations.

- In §6.4, we built a relativistic orbit model consisting of circular and spherical orbits that have a power-law distribution, and its mechanical energy is split into two parts (above and below the energy at ISCO). This formulation leads to unique results relating to the PSD slopes (before ($\bar{\nu} < \bar{\nu}_b$) and after ($\bar{\nu} > \bar{\nu}_b$) the break) with those of the energy spectrum for the given spin and mass of the black hole (Figs. 6.9 and 6.10). We plan to test this model against observations to extract $\{a, M_\bullet\}$.

6.6 Discussion, caveats, and conclusions

We add the following points of discussion of our results and conclusion:

1. The periastron and nodal precession of the particle orbits is an intrinsic phenomenon in Kerr geometry, which is a consequence of strong gravity and axisymmetry of the spacetime. We propose in the GRPM (chapter 5) that the precession frequencies of matter blobs orbiting in these trajectories, very close to the Kerr black hole, modulate the X-ray flux, from the thin accretion disk where the flow is hot. The origin of these non-equatorial orbits of blobs in a slim torus region having a single radius is motivated in chapter 5, where a model of fluid flow in the general relativistic thin accretion disk (Penna *et al.* 2012) is studied. In this study, we suggest that the edge region, defined in Penna *et al.* (2012), is a launchpad for plasma instabilities, where blobs orbit with fundamental frequencies of the geodesics near the edge and in the geodesic region (defined in Penna *et al.* (2012)), in which Hamiltonian dynamics is applicable. We also show in the GRPM that these geodesics span a torus region, which overlaps with the edge and geodesic region of Penna *et al.* (2012).

2. The QPOs in NLSy1s are usually observed when L/L_{Edd} is very high; for example, $L/L_{Edd} \sim 10$ in the case of RE J1034+396 (Gierliński *et al.* 2008) implies a high accretion rate, but the association of L/L_{Edd} with the QPO frequencies is not clear. Moreover, even if one assumes that the accretion process in AGN and BHXRB is the same and that both show similar characteristic $\mathcal{Q}$ shape in the hardness-intensity diagram (Remillard *et al.* 2006), over a timescale, T, this would be 10^5-10^6 times more than BHXRB timescales, as $T \propto M_\bullet$.

3. Our relativistic orbit model (ROM) is built on the formulation of the intrinsic mechanical energy distribution of the plasma in motion, where three

frequencies $\nu_X < \nu_I < \nu_M$ correspond to the low-frequency end, break frequency, and the high-frequency end of the PSD. However, there is a noise component to be added at higher frequencies of the PSD to obtain a more realistic PSD shape to the intrinsic energy distribution related to the frequencies of the unstable orbits inside MBSO. A more generalized approach will be to incorporate frequencies of the more general eccentric and non-planar orbits ($e \neq 0$, $Q \neq 0$) contributing to the PSD shape. This is planned as future work.

4. The fundamental frequencies of the spherical geodesics in the Kerr geometry seem to explain the PSD in the Inner Corona (IC) region, where $P\,(\nu_I < \nu < \nu_M)$; whereas the frequencies of the Outer Corona (OC) region are associated with the circular orbits, where $P\,(\nu_X < \nu < \nu_I)$. The results of this toy statistical model, ROM, seem promising. A detailed physical model is required to predict the power law indices in the energy spectrum. Furthermore, including a more ellaborate transfer function taking into account the GR effects like light bending and Doppler boosting, is in order for further study.

5. The paradigm of the ROM can be tested against observations by extracting $\{M_\bullet,\, a\}$ from observed $\{\nu_X, \nu_I, \nu_M, \beta_1, \beta_2\}$, and by exploring the parameter space $\{\alpha_1,\, \alpha_2\}$ which is the basis of the PSD for the ROM model. In the future, we plan to apply and test this model against several observed PSD of various AGN sources.

6. The total power of a PSD having a power-law profile is given by

$$\mathcal{P}_T \propto \int_0^{\nu_c} \left(\frac{\nu}{\nu_c}\right)^{\tau} \mathrm{d}\nu \;\; \propto \nu_c \int_0^1 X^{\tau} \mathrm{d}X \;\; \propto \nu_c, \tag{6.18}$$

where $X = \nu/\nu_c$, τ is the power-law index, and ν_c is the upper frequency cut-off of the PSD. On the other hand, from the Wiener–Khinchin theorem, $\mathcal{P}_T = F_{var}^2 \propto (\sigma^2 - \sigma_N^2)$, where F_{var} gives a measure of the time signal variance above the noise and σ_N^2 is the variance in the noise measurable

from observations. This gives the relation between the measured quantity and ν_c as, $F_{var} \propto \nu_c^{0.5}$, where the cutoff ν_c provides a measure of the spin and mass of the black hole if the disk cuts off at the ISCO or MBSO radius; this implies $\nu_c^{0.5} \propto M_\bullet^{0.5}$. Using a more complicated PSD distribution expected from the ROM and using F_{var}, we can give better estimates for ν_c and hence extract $\{M_\bullet, a\}$, using F_{var}, and study statistical trends from a sample of sources with known $\{M_\bullet, a\}$.

Chapter 7

"Life is like riding a bicycle. To keep your balance you must keep moving"
In a letter to his son, Eduard, 1930

Summary, caveats, and conclusions

This thesis is devoted to the study of compact and analytic trajectory solutions and its fundamental frequencies for the most general and non-equatorial bound orbits around a Kerr black hole. These trajectory solutions are reduced to simpler formulae for the special cases, for example, equatorial eccentric, spherical, and non-equatorial separatrix trajectories. The bound orbit regions and curves along with corresponding mathematical expressions for binding conditions for these orbits are explored in the energy, angular momentum space (E, L) and eccentricity, inverse-latus rectum space (e, μ). We find that the $\{e, \mu, a, Q\}$ parameter space is more useful to write the trajectory solutions, which helps to remove the singularities at the turning points of the bound orbit. We also presented a general relativistic precession model (GRPM) for X-ray QPO frequencies observed in BHXRB using our analytic formulae for the fundamental frequencies which involve the integrals of motion. We applied the GRPM to a few cases of BHXRB and AGN having X-ray QPOs and presented a relativistic orbit model for the characteristic power spectral density (PSD) shape observed in AGN. We showed that the QPOs are

originated from a torus region containing non-equatorial and eccentric trajectories. We motivated a jet model to study the γ ray QPO frequencies observed in Blazars. In this chapter, we summarize the Thesis, discuss the novel aspects, and their impact. We will then discuss the implications for future theoretical models.

7.1 Highlights

We summarize the highlights of each chapter in the sequence below:

- *Chapter 1*: We discuss the basic physics and properties of the Kerr spacetime. We present the motivation for the study of integrals of motion, various kinds of orbits, and important radii. We also provide a summary of different types of black holes in astrophysics from BHXRB to AGN and their observational properties. We finally discuss various goals of this Thesis and provide a resource summary.

- *Chapter 2*: We derive the equations of motion for time-like trajectories in the Kerr spacetime using the Hamilton-Jacobi equation. We obtain the conserved quantities, E and L, as a consequence of symmetries of the Kerr geometry. We also derive the Carter's constant by separating θ and r part of the Hamilton-Jacobi equation. Finally, we discuss the method of the action-angle variable to obtain the fundamental frequencies for bound trajectories. We provide a resource summary.

- *Chapter 3*: We derive the translation relations between (E, L) and (e, μ) parameter space of the Kerr geometry, Eq. (3.17). We explore different types of bound orbits based on the properties of four roots of the radial effective potential, Eq. (3.24). We divide these orbits as regions and bounding curves in the dynamical (E, L) and conic (e, μ) parameter spaces, see Figs. 3.1-3.7.

The conditions for the equatorial orbits are obtained using the Cardano's method to derive three roots of the effective potential, Eqs. (3.45) and (3.46a-3.46c); Figs. 3.8-3.12. We write the mathematical expressions of these regions and curves in both parameter spaces, see Table 3.1. We finally present a prescription to choose the astrophysically relevant bound orbits in the dynamical and conic parameter spaces, Eqs. (3.59a-3.60d) and (3.61a-3.62d).

- *Chapter 4*: We present a novel, analytic, and compact form for the equations of motion of the most general, eccentric and non-equatorial, orbits in the Kerr geometry using the conic parameter space (e, μ, a, Q), Eqs. (4.3-4.5) and Table 4.1. These solutions are presented in terms of the standard Elliptic integrals. Our analytic expressions provide faster computation to obtain the trajectory solution for the bound orbits. We derive the bound orbit condition in the conic parameter space by implementing the condition of the reality of the Elliptic integrals, Eq. (4.8). We also derive the analytic form of the fundamental frequencies for these bound orbits, Eq. (4.11) and Table 4.2. We reduce our formulae to the special cases of equatorial eccentric and spherical trajectories and obtain simpler analytic forms, Eqs. (4.13-4.14), (4.15, 4.21, 4.23-4.25c) and Tables 4.3, 4.4. We write novel expressions for special radii, like MBSO, ISSO, and the light radius in terms of $\{r_s,\ a,\ Q\}$, Eqs. (4.28-4.30), see Fig. 4.2. We also study an important class of orbits, called non-equatorial separatrix; see Fig. 4.1. We derive the analytic expressions for e and μ as functions of (r_s, a, Q), where r_s is the radius of the unstable spherical orbit sharing E and L with the separatrix orbit. These formulae for (e, μ) provides the locus of the separatrix trajectories in the conic parameter space, Eqs. (4.26, 4.35). We also reduce our trajectory solutions for the non-equatorial separatrix case and obtain a solution in terms of the logarithmic and trigonometric functions, Eq. (4.40) and Table 4.5. We show the consistency of our results with the previously known formulae in §4.7 and discuss various astrophysical applications of our novel results. We

finally sketch different kinds of trajectories using our analytic solution and discuss their distribution in the (e, μ) space, see Figs. 4.3-4.11. A formulary of the novel results presented in this work is shown in Table 7.1.

- *Chapter 5*: In this chapter, we develop a general relativistic precession model (GRPM), see Figs. 5.1-5.3, to understand the origin of the frequencies of the quasi-periodic oscillations (QPOs) observed in BHXRB. The QPO frequencies are modeled as the azimuthal and precession frequencies $\{\nu_\phi, (\nu_\phi - \nu_r), (\nu_\phi - \nu_\theta)\}$, that were previously studied for the equatorial circular orbits, which is now generalized in the framework of GRPM by including the frequencies of non-equatorial eccentric, equatorial eccentric, and spherical trajectories, Figs. 5.7-5.12. We implement the GRPM using our analytic frequency formulae (presented in chapter 4) to study observed QPOs of 5 BHXRB, see Table 5.3, having either three or two simultaneous QPOs, and estimate the orbital parameters $\{e, r_p, a, Q\}$. We found non-equatorial eccentric orbit solution for QPO frequencies at $\{e = 0.230^{+0.067}_{-0.049}, r_p = 4.834^{+0.181}_{-0.268}, a = 0.299, Q = 2.362^{+1.519}_{-1.439}\}$ and spherical orbit solution at $\{r_s = 6.044^{+0.071}_{-0.072}, a = 0.321 \pm 0.013, Q = 6.113^{+2.124}_{-1.645}\}$ for BHXRB M82 X-1, implying degenerate solutions for this case; see Tables (5.4, 5.5, 5.7) and Figs. 5.16 and 5.24. We naturally found a near equatorial and low-eccentric solution for QPO frequencies of GRO J1655-40 at $\{e = 0.071^{+0.031}_{-0.035}, r_p = 5.25^{+0.171}_{-0.142}, a = 0.283, Q = 0^{+0.623}\}$; see Tables (5.4, 5.5) and Fig. 5.17. We find that these orbital trajectory solutions span a torus region near the inner edge of the accretion disk, close to ISSO (ISCO); see Fig. 5.22. This torus region contains precessing orbits giving quasi-periodic peaks in the Fourier power spectrum; see Figs. 5.18 and 5.29. For the cases of BHXRB 4U 1630-47 and GRS 1915+105, we found equatorial and highly eccentric solutions at $\{e = 0.734^{+0.066}_{-0.048}, r_p = 2.249^{+0.249}_{-0.353}\}$ and $\{e = 0.918 \pm 0.002, r_p = 1.744^{+0.025}_{-0.011}\}$ respectively; see Table 5.6 and Figs. 5.20 and 5.21, where spins were fixed to estimates of the previous analysis; see Table 5.3. This indicates high eccentric trajectory solutions for QPOs of black holes having high spin values,

TABLE 7.1: A list of novel formulae and advancement in the theoretical results made in this Thesis.

	Results presented in the previous studies	**Our new results presented in this thesis**
1.	*Bardeen et al. (1972)*: Analytic expressions of E and L for equatorial circular orbits, Eqs. (2.12) & (2.13).	Analytic expressions for E and L and equations for important radii, ISSO, MBSO, and light radius for general spherical orbits with $Q \neq 0$, Eqs. (4.15), (4.28-4.30) and Table 4.4.
2.	*Schmidt (2002)*: Expressions for fundamental frequencies, (ν_ϕ, ν_r, ν_θ), of general trajectories given in terms of quadratures using action-angle variables, Eqs. (59)-(61).	The t, ϕ, $r-\theta$ integrals are solved analytically and explicit expressions for fundamental frequencies are presented for $Q \neq 0$ using long-time average method, Eq. (4.11), Table 4.2.
3.	*Fujita and Hikida (2009)*: Analytic trajectory solutions are presented as a function of the variable Mino time, λ, Eq. (22-45); for $Q \neq 0$, where input variables are E, L, Q and a.	Analytic trajectory solutions are presented as a function of comparatively simple variable χ, which is directly related to the distance from the black hole, r, and using (e, μ, a, Q) space, Eqs. (4.3-4.5), Table 4.1. Specialized trajectory solutions and fundamental formulae for equatorial eccentric and spherical orbits are also obtained, Eqs. (4.13-4.14), (4.21, 4.23-4.25c), and Tables (4.3, 4.4)
4.	*Levin and Perez-Giz (2009)*: Expressions for the eccentricity, e_s, and inverse latus-rectum, μ_s, of equatorial separatrix orbits and the trajectory solutions ($Q = 0$) are presented, Eqs. (20), (21), & (26).	Expressions for e_s and μ_s and trajectory solutions are presented for general separatrix orbits with $Q \neq 0$, Eqs. (4.26, 4.35, (4.40)), Table 4.5. Bound orbit conditions in (e, μ, a, Q) space are derived, Eq. (4.8).
5.	*Hackmann et al. (2010)*: Different regions of bound orbits are identified in the (E, L) plane using roots of the effective potential, Fig. 5.	Expressions of conditions of these regions are identified in (E, L, a, Q) as well as in (e, μ, a, Q) space, Table 3.1, and turning points of the general trajectory are obtained for $Q \neq 0$, Eq. (3.24), and for $Q = 0$, Eqs. (3.46a-3.46c).
6.	*Bini2017*: Translation formulae from (e, μ, a) to (E, L, a) space for eccentric equatorial orbits are presented, Eqs. (15) & (18)-(20).	Translation formulae from (e, μ, a, Q) to (E, L, a, Q) space for general eccentric orbits with $Q \neq 0$ are presented, Eq. (3.17).

which is intrinsic to the framework of GRPM [see Figs. 5.7-5.12]. However, such a highly eccentric solution is unlikely in the accretion disk around a black hole, which implies that these BHXRB might not contain very high spin black holes and better estimates of their spins are required. In the case of BHXRB XTE J1550-564, we found degenerate solutions, equatorial eccentric solution at $\{e = 0.262^{+0.090}_{-0.062},\ r_p = 4.365^{+0.169}_{-0.279}\}$ (Table 5.6 and Fig. 5.19) and spherical orbit solution at $\{r_s = 5.538 \pm 0.054,\ Q = 2.697^{+1.738}_{-1.627}\}$ (Table 5.7 and Fig. 5.25). We show that the equatorial eccentric solution follows the PBK correlation observed in the case of BHXRB GRO J1655-40, see Figs. 5.26 and 5.27, We also find non-equatorial eccentric orbit solutions for the broad frequency components detected in RXTE observations of GRO J1655-40, see Table 5.8. We, finally, present the connection between our precessing particle orbit model with the GR fluid model. We find that the inner edge region and the geodesic region of the GR fluid model overlaps with the torus region found in our model; see Fig. 5.28 and Table 5.9. This indicates that the instabilities in the inner region of the accretion disk launch the plasma in the geodesic region where it follows geodesics spanning the torus region presented in our model; see Fig. 5.29. A summary of all results with tables and figures is given in Table 7.2.

- *Chapter 6*: In this chapter, we apply the GRPM to the cases of AGN with detected X-ray QPOs, see Table 6.1. We show that the QPOs are originated in the inner regions of the accretion disk, Fig. 6.2. We also present an equatorial and circular orbit solution at $\{r = 8.214^{+0.116}_{-0.359},\ a = 0.0662^{+0.2695}_{-0.0662}\}$ (see Fig. 6.3 and Table 6.2), and degenerate non-equatorial orbital solutions between $Q = 1 - 12$ (see Fig. 6.4 and Table 6.3) for the QPOs observed in the case of 1H 0707-495. For the spherical orbit solution, we found the most probable spin at $a = 0.139$ for 1H 0707-495, see Fig. 6.5. We motivate a detailed relativistic kinematic jet model by comparing the fundamental frequency with the observed QPO frequencies in optical and γ ray bands, see Table 6.4, where their ratio is found in the expected range of $1 - 20$. The

plasma is expected to relativistically follow the magnetic field lines in a rigid motion up to the light cylinder radius. The angular momentum conservation then sets a ratio between the observed and fundamental timescales which is expected in the range $\sim 1 - 20$. This motivates a detailed relativistic model for the motion of plasma along the jets. We, then, present a relativistic orbit model (ROM) for the observed PSD following a bending power-law, Eq. (6.4), in AGN. We associate the ISCO frequency with the observed break frequency, ν_b, in our model. We assume a power-law profile for the energy distribution of matter accreting near the black hole. We show that the distribution of fundamental frequencies of the spherical orbits in the inner spherical corona region provides the steep slope for the higher frequency region of the PSD (above ν_b). The lower frequency region of the PSD is explained by the distribution of equatorial circular orbit frequencies in the inner region of the accretion disk. We show that the bending power-law profile fits the PSD theoretically generated in our model with $\alpha_l \sim 1$ and $\alpha_h \sim 2$ that compares well with observations; see Figs. 6.9, 6.10 and Table 6.5. A unified picture of our orbit model for the QPOs and PSD shape observed in AGN is shown in Fig. 6.1. A summary of all results with tables and figures is given in Table 7.2.

7.2 Novel aspects and their impact

1. The identification of important radii like ISSO, MBSO, the light radius helps to classify the various regions in the $(r,\, a)$ plane corresponding to different types of bound orbits. We present, here in Table 7.3, a summary of all types of bound orbits and their corresponding regions, that we have identified, in the $(r,\, a)$ plane. This identification helps to study the geometric origin of various observed signals from black hole systems, for example, QPOs.

TABLE 7.2: A summary of the results, tables, and figures related to the GRPM parameter extraction for BHXRB and AGN, GR gas-flow model, PBK analysis, ROM model for PSD, and MHD jet model.

Physical context	**Figures and Tables**
GRPM, BHXRB M82 X-1	Tables (5.4, 5.5, 5.7) and Figs. (5.16, 5.24)
GRPM, BHXRB GRO J1655-40	Tables (5.4, 5.5) and Fig. 5.17
GRPM, BHXRB 4U 1630-47	Table 5.6 and Fig. 5.20
GRPM, BHXRB GRS 1915+105	Table 5.6 and Fig. 5.21
GRPM, BHXRB XTE J1550-564	Tables (5.6, 5.7) and Figs. (5.19, 5.25)
GRPM, AGN 1H 0707-495	Tables (6.2, 6.3) and Figs. (6.3, 6.4, 6.5)
GRPM, RE J1034+396, MS 2254.9-3712, Mrk 766, and MCG-06-30-15	Fig. 6.2
PBK correlation	Table 5.8 and Figs. (5.26, 5.27)
GR gas-flow model	Table 5.9 and Fig. 5.28
ROM for PSD	Table 6.5 and Figs. (6.9, 6.10, 6.1)
MHD jet model	Table 6.4 and Fig. 6.1

2. We constructed mathematical conditions for various bound orbits representing regions and curves in the (E, L) and (e, μ) space. We presented a prescription to choose the parameter combinations (E, L, a, Q) and (e, μ, a, Q) for astrophysically relevant bound trajectories. This helps us to identify the limitation of choosing the parameter combinations, which are inputs to the integrals of motion, and consequently to the fundamental frequency formulae used for various astrophysical applications.

3. We presented the most compact analytic forms (to date) of the most general, eccentric and non-equatorial, trajectories, and fundamental frequencies. These formulae are derived using the conic parameter space and provide much faster convergence to obtain the trajectory solutions than the previously available analytic forms (derived using the Mino time and in terms of r), for example, ~ 20 times faster in the equatorial case. The construction

TABLE 7.3: A list of various types of trajectories around a Kerr black hole with their description, and the region in the (r, a) plane where they are found, as shown in Fig. 5.4.
[a]The regions for $e0$ and 00 orbits are shown in Fig. 5.4(a), whereas eQ or $Q0$ orbits are shown in Fig. 5.4(b).
[†](Rana and Mangalam 2019a,b); [‡](Levin and Perez-Giz 2009; Perez-Giz and Levin 2009); [^](Glampedakis and Kennefick 2002).

Type of orbit or radius	**Description**	**Region or curve**[a]
Eccentric[†], eQ or $e0$	• They are the stable eccentric bound orbits.	1 and 2
Separatrix[†,‡], eQ or $e0$	• They are the intermediate case between bound and plunge orbits, while their periastron points correspond to an unstable spherical (or circular) orbit, where a particle reaches asymptotically. • The eccentricity of a separatrix orbit increases as its periastron moves closer to the black hole for a given a. • The r_p of a separatrix orbit with a given eccentricity defines the innermost radial limit for the eccentric bound orbits having the same eccentricity.	2
Zoom-whirl[†,^], eQ or $e0$	• They represent an extreme form of the periastron precession in the strong field regime. • A particle spends enough time near the periastron to make finite spherical (or circular) revolutions before zooming out to the apastron point. • They are found near and outside the separatrices.	1 and 2
Stable spherical (circular)[†], $Q0$ (00)	• They have a constant radius with the precession of orbital plane partially spanning the surface of a sphere around the black hole. • They are found outside ISSO (ISCO).	1
Unstable spherical (circular)[†], $Q0$ (00)	• They have a constant radius like stable spherical (circular) orbits. • They are found outside MBSO (MBCO).	2 and 3
ISSO (ISCO)[†], $Q0$ (00)	• Innermost stable spherical (circular) orbit. • Defined by Eq. (4.28).	Black curve
MBSO (MBCO)[†], $Q0$ (00)	• Marginally bound spherical (circular) orbit. • Defined by Eq. (4.29).	Blue curve
Light radius[†], $Q0$ or 00	• Only a photon orbit can exist at this radius. • Defined by Eq. (4.30). • It is the innermost boundary for the unstable spherical (circular) particle orbits.	Green curve

of the trajectory solutions, the bound orbit conditions, and fundamental frequencies is done using the translation relations between (E, L) and (e, μ) parameters, which are important to express the formulae completely in the conic parameter space. These analytic solutions have direct applications to various astrophysical scenarios, for example, the gravitational waves from extreme-mass ratio inspirals (EMRIs), relativistic precession, and QPOs (which we studied in our work), phase space study of orbits, gyroscope precession, etc.

4. We also obtained specialized formulae for the spherical and equatorial eccentric orbits, for example, their trajectory solutions, fundamental frequencies, and (E, L) as functions of (r_s, a, Q) for the spherical case. These formulae are tailor-made to many typical astrophysical applications like accretion disks and the corona, EMRIs, and Pulsars, etc while providing much faster computation.

5. We derived the locus of the non-equatorial separatrix trajectories in the (e, μ) space by obtaining a compact analytic form as functions of (r_s, a, Q) and also obtained the analytic form for their trajectory solutions. This has direct application to the study of EMRIs where a compact object passes through a separatrix while transiting from bound to plunge orbits. The study of the waveforms from EMRIs while such transition, in the non-equatorial scenario, involves the identification of locus of separatrix in the parameter space.

6. We developed a GRPM for QPO frequencies and applied it to 5 cases of BHXRB to estimate the parameters of eccentric and non-equatorial trajectories. We identified that these trajectories span a torus region near ISSO (ISCO) where these QPOs are originated. Our model also explains the PBK correlation observed in QPOs in the case of GRO J1655-40. We also make a connection between our particle model with the GR fluid model where we identify that our torus region overlaps with the geodesic region near the ISCO radius where such orbits are expected. This framework of the

particle-GR fluid model is the motivation for future GRMHD model including non-equatorial orbital dynamics.

7. We applied the GRPM to X-ray QPOs observed in a few cases of AGN, where further predictions can be made if there are more cases of AGN with two or three simultaneous QPOs. We also motivated a relativistic MHD model for jet (Mohan and Mangalam 2015) based on QPOs observed in γ ray and optical bands, which will also help to study the QPO timescales and cylindrical relativistic polarization signatures (Mangalam 2018). We developed a ROM for the PSD shape observed in AGN, which is demonstrated to fit the observed bending power-law, and it can be further generalized by involving non-equatorial and eccentric orbit frequencies. The fitting of the ROM with the AGN data will provide the estimates for mass and spin of the black holes.

7.3 Caveats

We list some of the caveats below:

1. In the GRPM for QPOs, we assumed a self-emitting blob of matter or plasma following the geodesics as the origin of the X-ray flux close to the Kerr black hole. A more detailed emission criterion of the X-ray flux is required for future modeling while including various GR effects like Doppler boosting, light bending, as implemented in Mohan and Mangalam (2015). A transfer function including these GR effects will provide the relation between the emitted and observed flux.

2. In the ROM for PSD, we assumed a power-law profile for the intrinsic dynamical energy distribution of particles in the accretion disk and the corona

region. We also assumed circular orbit in the accretion disk and spherical orbits in the spherical corona region, whereas the break frequency is assumed at the ISCO radius. However, it provides a good bending power-law profile. A future generalized model will include the eccentric and non-equatorial orbits also.

7.4 Future directions

A flowchart representing various applications and the future direction of our work is shown in Fig. 7.1 and elaborated below:

1. We plan to study the resonance conditions for the general and non-equatorial periodic orbits in the Kerr spacetime, for example

$$T_r = T_\phi \left(q_\phi + 1\right) = T_\theta \left(q_\theta + 1\right), \tag{7.1}$$

where T_r, T_ϕ, and T_θ are the radial, azimuthal, and vertical oscillation time periods of the periodic orbits. q_θ and q_ϕ are the rational numbers relating these time periods. We also plan to study the diagrammatic arrangement of the energy levels of these orbits.

2. We plan to derive the most compact and faster method to obtain the locus of the separatrix orbits by obtaining a single polynomial equation in terms of the parameters (e, μ, a, Q). This analytic form will also help us to find the upper limit for $Q \equiv Q_{max}$ for bound orbits in the Kerr geometry as a function of (e, μ, a).

3. We plan to develop a model for the light echoes in the Kerr geometry. This will involve a more general transfer function by including GR effects like

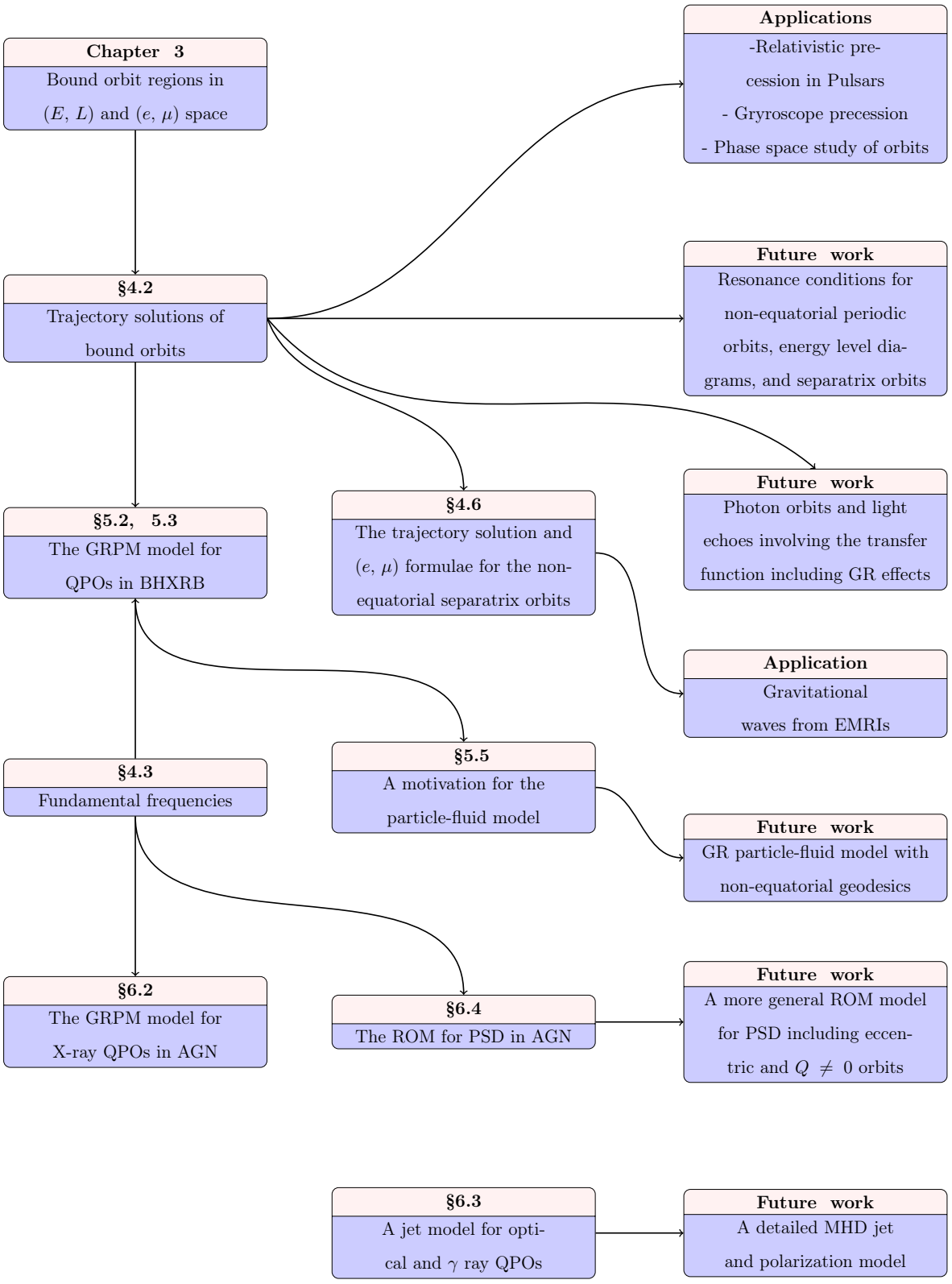

FIGURE 7.1: A flowchart of the theoretical development of work, the impact, and its future directions.

light bending, Doppler boosting, and gravitational redshift as developed by Mohan and Mangalam (2015). This transfer function will then relate the emitted and observed X-ray flux in the black hole systems and will have applications to various observations of AGN and BHXRB.

4. We plan to study a more general particle-fluid model involving GRMHD simulations of the non-equatorial trajectories around a Kerr black hole. This will provide a further test of our GRPM relating QPO frequencies with the non-equatorial geodesics in the edge and geodesic region. We also plan to further compare the GRPM and particle-fluid model predictions with the observational results from the currently operative Indian X-ray satellite, AstroSat, and from future missions, such as eXTP, which is proposed to have much higher sensitive instruments for X-ray timing.

5. We plan to generalize our ROM for PSD in AGN by including non-equatorial eccentric orbit frequencies in the inner corona region and the equatorial eccentric orbit frequencies in the outer corona and accretion disk regions.

THE END!

Appendix A

A.1 Solution of integrals I_1-I_8

In this appendix, we show the solutions of the integrals given in §4.2.1. First, we derive the radial integrals $I_1 - I_8$, given by the Eqs. (4.3a-4.3h). We make the substitution $1/r^{'} = \mu\,(1 + e\cos\chi)$, which reduces the integrals to

$$I_1 = \quad -2\mu\left(1-e^2\right)\int_{\pi}^{\chi}\frac{L-2\,(L-aE)\,\mu y}{\left[1-2\mu y+a^2\mu^2y^2\right]\sqrt{A\cos^2\chi+B\cos\chi+C}}\mathrm{d}\chi, \tag{A.1a}$$

$$I_2 = \quad \frac{2\,(1-e^2)}{\mu}\int_{\pi}^{\chi}\frac{E+a^2E\mu^2y^2-2a\,(L-aE)\,\mu^3y^3}{y^2\left[1-2\mu y+a^2\mu^2y^2\right]\sqrt{A\cos^2\chi+B\cos\chi+C}}\mathrm{d}\chi, \tag{A.1b}$$

where $y = (1 + e\cos\chi)$. Further, we implement the partial fraction method to reduce the integrals to

$$I_1 = \quad -\frac{2\,(1-e^2)}{\mu a^2}\int_{\pi}^{\chi}\left[\frac{A_1}{y-y_+}+\frac{B_1}{y-y_-}\right]\frac{1}{\sqrt{A\cos^2\chi+B\cos\chi+C}}\mathrm{d}\chi, \tag{A.2a}$$

$$I_2 = \frac{2\left(1-e^2\right)}{\mu^3 a^2}\int_\pi^\chi \left[\frac{A_2}{y^2}+\frac{B_2}{y}+\frac{C_2}{y-y_+}+\frac{D_2}{y-y_-}\right]\frac{1}{\sqrt{A\cos^2\chi+B\cos\chi+C}}\mathrm{d}\chi, \tag{A.2b}$$

where

$$y_\pm = \frac{r_\pm}{a^2\mu}, \tag{A.3a}$$

$$A_1 = \frac{La^2\mu-2\left(L-aE\right)\mu r_+}{2\sqrt{1-a^2}}, \quad B_1 = \frac{-La^2\mu+2\left(L-aE\right)\mu r_-}{2\sqrt{1-a^2}}, \tag{A.3b}$$

$$A_2 = Ea^2\mu^2, \quad B_2 = 2Ea^2\mu^3, \quad C_2 = \frac{a^2\mu^3}{r_-\sqrt{1-a^2}}\left(-La+2Er_-\right), \tag{A.3c}$$

$$D_2 = \frac{a\mu^3}{r_-\sqrt{1-a^2}}\left(-2Lr_-\sqrt{1-a^2}-2Ear_-+La^2\right). \tag{A.3d}$$

Next, we make the substitution, $\cos\chi = 2\cos^2\frac{\chi}{2}-1$ and $\psi = \frac{\chi}{2}-\frac{\pi}{2}$, which reduces the integrals to

$$I_1 = -\left[C_3\int_0^\psi \frac{\mathrm{d}\psi}{\left(1+p_2^2\sin^2\psi\right)\sqrt{1-m^2\sin^2\psi}\sqrt{1-n^2\sin^2\psi}}+\right.$$

$$\left.C_4\int_0^\psi \frac{\mathrm{d}\psi}{\left(1+p_3^2\sin^2\psi\right)\sqrt{1-m^2\sin^2\psi}\sqrt{1-n^2\sin^2\psi}}\right],$$

$$= -\left[C_3I_3+C_4I_4\right], \tag{A.4a}$$

$$I_2 = \left[C_5\int_0^\psi \frac{\mathrm{d}\psi}{\left(1+p_1^2\sin^2\psi\right)^2\sqrt{1-m^2\sin^2\psi}\sqrt{1-n^2\sin^2\psi}}+\right.$$

$$C_6\int_0^\psi \frac{\mathrm{d}\psi}{\left(1+p_1^2\sin^2\psi\right)\sqrt{1-m^2\sin^2\psi}\sqrt{1-n^2\sin^2\psi}}+$$

$$\left.C_7\int_0^\psi \frac{\mathrm{d}\psi}{\left(1+p_2^2\sin^2\psi\right)\sqrt{1-m^2\sin^2\psi}\sqrt{1-n^2\sin^2\psi}}+\right.$$

$$
\begin{aligned}
& C_8 \int_0^{\psi} \frac{\mathrm{d}\psi}{\left(1+p_3^2\sin^2\psi\right)\sqrt{1-m^2\sin^2\psi}\sqrt{1-n^2\sin^2\psi}}\Bigg], \\
= \quad & C_5 I_5 + C_6 I_6 + C_7 I_3 + C_8 I_4. \qquad \text{(A.4b)}
\end{aligned}
$$

where the constants, C_3-C_8, n^2, m^2, ${p_1}^2$, ${p_2}^2$, and ${p_3}^2$ are defined by Eq. (4.4) in §4.2.1. First, we solve the integrals I_6, I_3 or I_4 which are of the form given by

$$
I_a \equiv \int_0^{\psi} \frac{\mathrm{d}\psi}{\left(1+p^2\sin^2\psi\right)\sqrt{1-m^2\sin^2\psi}\sqrt{1-n^2\sin^2\psi}},
$$

$$
I_a = \int_0^{\psi} \frac{\mathrm{d}\psi}{\sqrt{1-m^2\sin^2\psi}\sqrt{1-n^2\sin^2\psi}} - p^2 \int_0^{\psi} \frac{\sin^2\psi\cdot\mathrm{d}\psi}{\left(1+p^2\sin^2\psi\right)\sqrt{1-m^2\sin^2\psi}\sqrt{1-n^2\sin^2\psi}},
$$

$$
I_a = \int_0^{\psi} \frac{\mathrm{d}\psi}{\sqrt{1-m^2\sin^2\psi}\sqrt{1-n^2\sin^2\psi}} + \frac{p^2}{m^2} \int_0^{\psi} \frac{\left(1-m^2\sin^2\psi-1\right)\cdot\mathrm{d}\psi}{\left(1+p^2\sin^2\psi\right)\sqrt{1-m^2\sin^2\psi}\sqrt{1-n^2\sin^2\psi}},
$$

$$
I_a = \frac{1}{(p^2+m^2)}\left[\int_0^{\psi} \frac{m^2\cdot\mathrm{d}\psi}{\sqrt{1-m^2\sin^2\psi}\sqrt{1-n^2\sin^2\psi}} + \int_0^{\psi} \frac{p^2\sqrt{1-m^2\sin^2\psi}\cdot\mathrm{d}\psi}{\left(1+p^2\sin^2\psi\right)\sqrt{1-n^2\sin^2\psi}}\right]. \qquad \text{(A.5)}
$$

Now, the substitution given by

$$
\sin\alpha = \frac{\sqrt{1-m^2}\sin\psi}{\sqrt{1-m^2\sin^2\psi}}, \qquad \text{(A.6)}
$$

reduces the integrals in Eq. (A.5) to

$$
I_a = \frac{1}{\sqrt{1-m^2}\,(p^2+m^2)}\left[m^2 F\left(\alpha, \frac{n^2-m^2}{1-m^2}\right) + p^2\Pi\left(\frac{-p^2-m^2}{1-m^2}, \alpha, \frac{n^2-m^2}{1-m^2}\right)\right]. \qquad \text{(A.7)}
$$

Hence, integrals given by Eqs. (4.3c, 4.3d, 4.3f) reduce to the forms given above. Next, we solve for I_5, which is of the form

$$
\begin{aligned}
I_b \equiv \quad & \int_0^{\psi} \frac{\mathrm{d}\psi}{\left(1+p^2\sin^2\psi\right)^2\sqrt{1-m^2\sin^2\psi}\sqrt{1-n^2\sin^2\psi}}, \\
= \quad & \int_0^{\psi} \frac{1+p^2\sin^2\psi-p^2\sin^2\psi}{\left(1+p^2\sin^2\psi\right)^2\sqrt{1-m^2\sin^2\psi}\sqrt{1-n^2\sin^2\psi}}\mathrm{d}\psi, \\
= \quad & I_a + \frac{p^2}{m^2}\int_0^{\psi} \frac{\sqrt{1-m^2\sin^2\psi}}{\left(1+p^2\sin^2\psi\right)^2\sqrt{1-n^2\sin^2\psi}}\mathrm{d}\psi - \frac{p^2}{m^2} I_b,
\end{aligned}
$$

$$I_b = \frac{1}{(m^2+p^2)}\left\{m^2 I_a + p^2\left[\int_0^{\psi}\frac{\sqrt{1-m^2\sin^2\psi}}{\left(1+p^2\sin^2\psi\right)\sqrt{1-n^2\sin^2\psi}}\mathrm{d}\psi - p^2\int_0^{\psi}\frac{\sin^2\psi\sqrt{1-m^2\sin^2\psi}}{\left(1+p^2\sin^2\psi\right)^2\sqrt{1-n^2\sin^2\psi}}\mathrm{d}\psi\right]\right\}, \tag{A.8}$$

where the substitution given by Eq. (A.6) reduces the second integral in the above equation to

$$I_b = \frac{1}{(m^2+p^2)}\left[m^2 I_a + \frac{p^2}{\sqrt{1-m^2}}\Pi\left(\frac{-p^2-m^2}{1-m^2}, \alpha, \frac{n^2-m^2}{1-m^2}\right) - p^4 I_c\right], \tag{A.9}$$

where

$$I_c \equiv \int_0^{\psi}\frac{\sin^2\psi\sqrt{1-m^2\sin^2\psi}}{\left(1+p^2\sin^2\psi\right)^2\sqrt{1-n^2\sin^2\psi}}\mathrm{d}\psi = -\frac{1}{n^2}\int_0^{\psi}\frac{\left(1-n^2\sin^2\psi-1\right)\sqrt{1-m^2\sin^2\psi}}{\left(1+p^2\sin^2\psi\right)^2\sqrt{1-n^2\sin^2\psi}}\mathrm{d}\psi,$$

$$I_c\left(1+\frac{p^2}{n^2}\right) = \frac{1}{n^2}\left[-\int_0^{\psi}\frac{\sqrt{1-n^2\sin^2\psi}\sqrt{1-m^2\sin^2\psi}}{\left(1+p^2\sin^2\psi\right)^2}\mathrm{d}\psi + \int_0^{\psi}\frac{\sqrt{1-m^2\sin^2\psi}}{\left(1+p^2\sin^2\psi\right)\sqrt{1-n^2\sin^2\psi}}\mathrm{d}\psi\right]; \tag{A.10}$$

the substitution given by Eq. (A.6) reduces the above expression to

$$I_c = \frac{1}{(n^2+p^2)\sqrt{1-m^2}}\left[-\int_0^{\alpha}\frac{\sqrt{1-k^2\sin^2\alpha}}{\left[1+\frac{p^2+m^2}{1-m^2}\sin^2\alpha\right]^2}\mathrm{d}\alpha + \Pi\left(\frac{-\left(p^2+m^2\right)}{1-m^2}, \alpha, k^2\right)\right], \tag{A.11}$$

and multiplying and dividing the first integral in above equation by $\sqrt{1-k^2\sin^2\alpha}$ gives

$$I_c = \frac{1}{(n^2+p^2)\sqrt{1-m^2}}\left[-\int_0^{\alpha}\frac{1}{\left[1+\frac{p^2+m^2}{1-m^2}\sin^2\alpha\right]^2\sqrt{1-k^2\sin^2\alpha}}\mathrm{d}\alpha + \Pi\left(\frac{-\left(p^2+m^2\right)}{1-m^2}, \alpha, k^2\right)\right.$$

$$+k^2\int_0^{\alpha}\frac{\sin^2\alpha}{\left[1+\frac{p^2+m^2}{1-m^2}\sin^2\alpha\right]^2\sqrt{1-k^2\sin^2\alpha}}\mathrm{d}\alpha\Bigg], \tag{A.12}$$

which can be further reduced to

$$I_c = \frac{1}{\sqrt{1-m^2}\,(m^2+p^2)}\left\{\Pi\left(\frac{-(p^2+m^2)}{1-m^2},\alpha,\frac{n^2-m^2}{1-m^2}\right)-I_d\right\}, \tag{A.13}$$

where

$$I_d=\int_0^{\alpha}\frac{1}{\left[1+\frac{p^2+m^2}{1-m^2}\sin^2\alpha\right]^2\sqrt{1-k^2\sin^2\alpha}}\mathrm{d}\alpha. \tag{A.14}$$

By defining integrals having a general form given by

$$T_n=\int\frac{\mathrm{d}y}{\left(h+g\sin^2 y\right)^n\sqrt{1-w^2\sin^2 y}}, \tag{A.15}$$

we use the following identity (Gradshteyn and Ryzhik 2007):

$$T_{n-3}=-\frac{g^2\sin y\cos y\sqrt{1-w^2\sin^2 y}}{\left(h+g\sin^2 y\right)^{n-1}(2n-5)\,w^2}-\frac{(2n-3)\left[g^2+2hg\left(1+w^2\right)+3h^2w^2\right]T_{n-1}}{(2n-5)\,w^2}$$

$$+\frac{2(n-2)\left[g\left(1+w^2\right)+3hw^2\right]T_{n-2}}{(2n-5)\,w^2}+\frac{2(n-1)\,h\,(g+h)\left(g+hw^2\right)T_n}{(2n-5)\,w^2}. \tag{A.16}$$

The integral I_d has a form similar to T_2 with $\left(h=1,g=\frac{p^2+m^2}{1-m^2},w=k\right)$, which yields

$$I_d=T_2=\frac{1}{2(1+g)\left(g+k^2\right)}\left\{\frac{g^2\sin\alpha\cos\alpha\sqrt{1-k^2\sin^2\alpha}}{\left(1+g\sin^2\alpha\right)}+\left[g^2+2g\left(1+k^2\right)+3k^2\right]T_1\right.$$
$$\left.-k^2T_{-1}\right\}, \tag{A.17}$$

where

$$T_{-1}=\int_0^{\alpha}\frac{\left(1+g\sin^2\alpha\right)\mathrm{d}\alpha}{\sqrt{1-k^2\sin^2\alpha}}=\int_0^{\alpha}\frac{\mathrm{d}\alpha}{\sqrt{1-k^2\sin^2\alpha}}-\frac{g}{k^2}\int_0^{\alpha}\frac{\left(1-k^2\sin^2\alpha-1\right)\,\mathrm{d}\alpha}{\sqrt{1-k^2\sin^2\alpha}}$$
$$=\left(1+\frac{g}{k^2}\right)F\left(\alpha,k^2\right)-\frac{g}{k^2}K\left(\alpha,k^2\right), \tag{A.18}$$

and

$$T_1 = \Pi\left(-g, \alpha, k^2\right), \tag{A.19}$$

were substituted. See Table 4.1 for the summary of the final expressions of $I_1 - I_7$ derived using the method given in this section.

A.2 Reduction to the equatorial plane ($Q = 0$)

In this appendix, we reduce the integrals of motion to the case of equatorial plane. We start with the final expressions of I_3, I_4, I_5, and I_6 (in §4.2.1) and take the limit $Q \to 0$. As shown in §4.4, that for $Q \to 0$, we have $n^2 \to 0$ which gives $k^2 = \dfrac{-m^2}{1-m^2}$. Now, we first reduce the expressions of I_3 and I_4, Eqs. (4.3c, 4.3d) under the limit $Q \to 0$. We use the following identity (cf. Byrd and Friedman (1971), Eq. 160.02) to write

$$\Pi\left(\alpha_1^2, \varphi, -k_1^2\right) = \frac{k_2^{'}\left[k_2^2 F\left(\beta_1, k_2^2\right) + {k_2^{'}}^2 \alpha_1^2 \Pi\left(\alpha_2^2, \beta_1, k_2^2\right)\right]}{\left(\alpha_1^2 {k_2^{'}}^2 + k_2^2\right)}, \tag{A.20a}$$

where

$$\sin\beta_1 = \frac{\sqrt{1+k_1^2}\sin\varphi}{\sqrt{1+k_1^2\sin^2\varphi}}, \tag{A.20b}$$

$\alpha_2^2 = \alpha_1^2 {k_2^{'}}^2 + k_2^2$, $k_2 = \frac{k_1}{\sqrt{1+k_1^2}}$ and $k_2^{'} = \frac{k_2}{k_1}$, which reduces I_3 and I_4 to the forms

$$I_3 = \frac{1}{\sqrt{1-m^2}\left(m^2+p_2^2\right)}\left[m^2 F\left(\alpha, k^2\right) + p_2^2 \Pi\left(\frac{-\left(p_2^2+m^2\right)}{1-m^2}, \alpha, k^2\right)\right] = \Pi\left(-p_2^2, \psi, m^2\right), \tag{A.21a}$$

$$I_4 = \frac{1}{\sqrt{1-m^2}\left(m^2+p_3^2\right)}\left[m^2 F\left(\alpha, k^2\right) + p_3^2 \Pi\left(\frac{-\left(p_3^2+m^2\right)}{1-m^2}, \alpha, k^2\right)\right] = \Pi\left(-p_3^2, \psi, m^2\right). \tag{A.21b}$$

The above expressions can be directly obtained if $n^2 = 0$ is substituted in the definition of I_3 and I_4 at the intermediate step, Eq. (A.4a). However, we aim

to directly validate the final forms of $(I_3 - I_7)$. Hence, we apply the reduced expressions of I_3 and I_4 to $(\phi - \phi_0)$ for the equatorial plane to obtain Eq. (4.13a).

Next, we reduce the coordinate time integral. The expression for I_6 also reduces in similar way to I_3 and I_4 by applying the identity, Eq. (A.20a), to

$$I_6 = \frac{1}{\sqrt{1-m^2}\,(m^2+p_1^2)}\left[m^2 F\left(\alpha, k^2\right) + p_1^2 \Pi\left(\frac{-\left(p_1^2+m^2\right)}{1-m^2}, \alpha, k^2\right)\right] = \Pi\left(-p_1^2, \psi, m^2\right), \tag{A.22}$$

which again can be directly obtained by substituting $n^2 = 0$ in the definition of I_6 in Eq. (A.4b). Next, we reduce the expression of I_5, Eq. (4.3e). We substitute for $\sin\alpha = \dfrac{\sqrt{1-m^2}\sin\psi}{\sqrt{1-m^2\sin^2\psi}}$, $\cos\alpha = \dfrac{\cos\psi}{\sqrt{1-m^2\sin^2\psi}}$, $k^2 = \dfrac{-m^2}{1-m^2}$ and $s^2 = -\dfrac{p_1^2+m^2}{1-m^2}$ into the expression of I_7, Eq. (4.3g), and use the following identities (cf. Byrd and Friedman (1971), Eq. 160.02)

$$F\left(\varphi, -k_1^2\right) = \quad k_2' F\left(\beta_1, k_2^2\right), \tag{A.23a}$$

$$K\left(\varphi, -k_1^2\right) = \quad \frac{1}{k_2'}\left[K\left(\beta_1, k_2^2\right) - \frac{k_2^2 \sin\beta_1\cos\beta_1}{\sqrt{1-k_2^2\sin^2\beta_1}}\right], \tag{A.23b}$$

and Eq. (A.20a) to transform $F\left(\alpha, k^2\right)$, $K\left(\alpha, k^2\right)$, and $\Pi\left(s^2, \alpha, k^2\right)$ to

$$F\left(\alpha, k^2\right) = \quad \sqrt{1-m^2} F\left(\psi, m^2\right), \tag{A.24a}$$

$$K\left(\alpha, k^2\right) = \quad \frac{1}{\sqrt{1-m^2}}\left[K\left(\psi, m^2\right) - \frac{m^2\sin\psi\cos\psi}{\sqrt{1-m^2\sin^2\psi}}\right], \tag{A.24b}$$

$$\Pi\left(s^2, \alpha, k^2\right) = \quad \frac{\sqrt{1-m^2}}{p_1^2}\left[\left(p_1^2+m^2\right)\Pi\left(-p_1^2, \psi, m^2\right) - m^2 F\left(\psi, m^2\right)\right] \tag{A.24c}$$

The substitution of the above equations reduces I_7 to

$$I_7 = \quad \left\{\frac{\left(p_1^2+m^2\right)^2\sqrt{1-m^2}\sin\psi\cos\psi}{2p_1^2\left(1+p_1^2\right)\sqrt{1-m^2\sin^2\psi}\left(1+p_1^2\sin^2\psi\right)} - \frac{\left(1-m^2\right)^{3/2} F\left(\psi, m^2\right)}{2\left(1+p_1^2\right)}\right.$$

$$+\frac{\left(p_1^4-2p_1^2m^2+2p_1^2-m^2\right)\sqrt{1-m^2}}{2p_1^4\left(1+p_1^2\right)}\left[\left(p_1^2+m^2\right)\Pi\left(-p_1^2,\psi,m^2\right)-m^2F\left(\psi,m^2\right)\right]$$
$$+\frac{\left(p_1^2+m^2\right)\sqrt{1-m^2}}{2p_1^2\left(1+p_1^2\right)}\left[K\left(\psi,m^2\right)-\frac{m^2\sin\psi\cos\psi}{\sqrt{1-m^2\sin^2\psi}}\right]\Bigg\}. \tag{A.25}$$

Now, the substitution of I_7 from the above equation and $\sin\alpha$, $\cos\alpha$, k^2, s^2 into Eq. (4.3e) reduces I_5 to

$$I_5 = \frac{p_1^4\sin\psi\cos\psi\sqrt{1-m^2\sin^2\psi}}{2\left(1+p_1^2\right)\left(m^2+p_1^2\right)\left(1+p_1^2\sin^2\psi\right)}+\frac{\left[p_1^4+2p_1^2\left(1+m^2\right)+3m^2\right]}{2\left(1+p_1^2\right)\left(m^2+p_1^2\right)}\Pi\left(-p_1^2,\psi,m^2\right)$$
$$-\frac{1}{2\left(1+p_1^2\right)}F\left(\psi,m^2\right)+\frac{p_1^2}{2\left(1+p_1^2\right)\left(m^2+p_1^2\right)}K\left(\psi,m^2\right). \tag{A.26}$$

The above expression of I_5 can also be directly obtained by substituting $n^2=0$ in its definition given in Eq. (A.4b) and applying the identity given by Eq. (A.16). Hence, the substitution of I_3, I_4, I_5 and I_6 from Eqs. (A.21a), (A.21b), (A.26) and (A.22) in Eq. (4.6b) gives the expression for coordinate time, t, which simplifies to Eq. (4.13b).

Now, we derive the small oscillation frequency in the θ direction about the equatorial plane for the equatorial and eccentric orbits. Using Eqs. (4.11a) and (4.11b), we can write

$$\frac{\nu_\theta}{\nu_r}=\frac{a\sqrt{1-E^2}z_+I_8\left(e,\mu,a,Q\right)}{2F\left(\frac{\pi}{2},\frac{z_-^2}{z_+^2}\right)}, \tag{A.27a}$$

where the substitution of $I_8\left(e,\mu,a,Q\right)$ from Eq. (4.3h) into the above equation yields

$$\frac{\nu_\theta}{\nu_r}=\frac{\mu\left(1-e^2\right)a\sqrt{1-E^2}z_+F\left(\frac{\pi}{2},k^2\right)}{\sqrt{C-A+\sqrt{B^2-4AC}}F\left(\frac{\pi}{2},\frac{z_-^2}{z_+^2}\right)}. \tag{A.27b}$$

By the substitution of A, B, and C using Eqs. (6.8e) and (4.4h), and using $Q=0$ for the equatorial orbits, we find

$$\sqrt{C-A+\sqrt{B^2-4AC}}=\mu^{1/2}\left(1-e^2\right)\left[1-\mu^2x^2\left(3-e^2-2e\right)\right]^{1/2}. \tag{A.28a}$$

Also, from Eq. (4.5d), we see that

$$z_- = 0, \qquad z_+ = \frac{\sqrt{L_z^2 + a^2\left(1 - E^2\right)}}{a\sqrt{\left(1 - E^2\right)}} = \frac{\sqrt{x^2 + a^2 + 2aEx}}{a\sqrt{\left(1 - E^2\right)}}, \tag{A.28b}$$

for $Q = 0$, which implies that

$$F\left(\frac{\pi}{2}, \frac{z_-^2}{z_+^2}\right) = \frac{\pi}{2}. \tag{A.28c}$$

Hence, Eqs. (A.27b)-(A.28c) together reduce ν_θ/ν_r for equatorial orbits to

$$\frac{\nu_\theta}{\nu_r} = \frac{2\mu^{1/2}\sqrt{x^2 + a^2 + 2aEx}\cdot F\left(\frac{\pi}{2}, k^2\right)}{\pi\left[1 - \mu^2 x^2\left(3 - e^2 - 2e\right)\right]^{1/2}}. \tag{A.29}$$

We see from Eqs. (4.4i) and (4.4k) that $k^2 = \left(n^2 - m^2\right)/\left(1 - m^2\right)$ can be written in terms of A, B, and C as

$$k^2 = \frac{2\sqrt{B^2 - 2AC}}{\left(-A + C + \sqrt{B^2 - 2AC}\right)}, \tag{A.30a}$$

where the substitution of A, B, and C using Eqs. (6.8e) and (4.4h) for $Q = 0$ gives

$$k^2 = m^2 = \frac{4ex^2\mu^2}{\left[1 - \mu^2 x^2\left(3 - e^2 - 2e\right)\right]}. \tag{A.30b}$$

Hence, we can write ν_θ for the equatorial orbits as

$$\nu_\theta\left(e, \mu, a\right) = \frac{2\nu_r\left(e, \mu, a\right)\mu^{1/2}\sqrt{\left(x^2 + a^2 + 2aEx\right)}\cdot F\left(\frac{\pi}{2}, m^2\right)}{\pi\left[1 - \mu^2 x^2\left(3 - e^2 - 2e\right)\right]^{1/2}}, \tag{A.31}$$

where $\nu_r\left(e, \mu, a\right)$ is given by Eq. (4.14b) and m^2 is given by Eq. (A.30b).

See Table 4.3 for the final expressions of (ϕ, t) and $(\nu_\phi,\ \nu_r,\ \nu_\theta)$ for the equatorial and eccentric trajectories derived using the method given in this section.

A.3 Innermost stable and marginally bound spherical radii

We discussed in §4.6.1 that ISSO and MBSO radii represent the end points of the separatrix curve defined by Eq. (4.26). Hence, we use this to write equations for ISSO and MBSO.

1. For the case of ISSO, we substitute $e = 0$ and $\mu = 1/r_s$ into Eq. (4.26), which gives

$$r_s^3 - 3r_s\left(Q + x^2\right) + 4a^2Q = 0, \tag{A.32}$$

which further expands, by the substitution of x^2 for spherical orbits, to

$$\begin{aligned} &r_s^6 - 9r_s^5 - 3a^2r_s^4 + 18r_s^4 + 4a^2Qr_s^3 - 7a^2r_s^3 - 18a^2Qr_s^2 + 24a^2Qr_s - 10a^4Q \\ &+6a\left(a^2 - 2r_s + r_s^2\right)\sqrt{a^2Q^2 - Q\left(r_s - 3\right)r_s^3 + r_s^5} = 0. \end{aligned} \tag{A.33}$$

The above equation has a complicated explicit expression of order twelve in r_s, which factorizes to

$$\begin{aligned} &\left(r_s^9 - 12r_s^8 - 6a^2r_s^7 + 36r_s^7 + 8a^2Qr_s^6 - 28a^2r_s^6 - 24a^2Qr_s^5 + 9a^4r_s^5 - 24a^4Qr_s^4\right. \\ &\left.+ 48a^2Qr_s^4 + 16a^4Qr_s^3 - 8a^4Qr_s^3 - 48a^4Q^2r_s^2 + 48a^4Q^2r_s - 16a^6Q^2\right) \\ &\cdot\left(r_s^3 - 6r_s^2 + 9r_s - 4a^2\right) = 0, \end{aligned} \tag{A.34}$$

where the second factor corresponds to the light radius (Bardeen *et al.* 1972) and the equation for ISSO is given by

$$\begin{aligned} &r_s^9 - 12r_s^8 - 6a^2r_s^7 + 36r_s^7 + 8a^2Qr_s^6 - 28a^2r_s^6 - 24a^2Qr_s^5 + 9a^4r_s^5 - 24a^4Qr_s^4 + \\ &48a^2Qr_s^4 + 16a^4Q^2r_s^3 - 8a^4Qr_s^3 - 48a^4Q^2r_s^2 + 48a^4Q^2r_s - 16a^6Q^2 = 0. \end{aligned} \tag{A.35}$$

For the equatorial plane, $Q = 0$ gives the following equation for the ISCO radius (Z)

$$Z^6 - 9Z^5 - 3a^2Z^4 + 18Z^4 - 7a^2Z^3 + 6a\left(a^2 - 2Z + Z^2\right)Z^{5/2} = 0; \quad \text{(A.36)}$$

this equation can be factorized as

$$Z^{5/2}\left(Z^{3/2} - 3Z^{1/2} - 2a\right)\left(Z^2 - 6Z + 8aZ^{1/2} - 3a^2\right) = 0, \quad \text{(A.37)}$$

where the first bracket gives the solution for light radius and the second bracket,

$$Z^2 - 6Z + 8aZ^{1/2} - 3a^2 = 0, \quad \text{(A.38)}$$

gives the solution for ISCO (Bardeen *et al.* 1972) given by

$$Z = \left\{3 + Z_2 \mp \left[(3 - Z_1)(3 + Z_1 + 2Z_2)\right]^{1/2}\right\}, \quad \text{(A.39a)}$$

$$Z_1 = 1 + \left(1 - a^2\right)^{1/3}\left[(1 + a)^{1/3} + (1 - a)^{1/3}\right], \quad \text{(A.39b)}$$

$$Z_2 = \left(3a^2 + Z_1^2\right)^{1/2}, \quad \text{(A.39c)}$$

where the upper sign represents the prograde and the lower sign represents the retrograde case.

2. The condition for MBSO is derived by substituting $e = 1$ and $\mu = 1/(2Y)$ in Eq. (4.26), which yields

$$Y^3 - Y\left(Q + x^2\right) + a^2Q = 0, \quad \text{(A.40)}$$

where r_a of the orbit reaches infinity and r_s in the above equation corresponds to the unstable radius. By substituting x^2 for spherical orbits, the above

equation reduces to

$$Y^6 - 7Y^5 + 12Y^4 - a^2Y^4 + a^2QY^3 - 5a^2Y^3 - 4a^2QY^2 + 5a^2QY - 2a^4Q$$
$$+2a\left(a^2 - 2Y + Y^2\right)\sqrt{a^2Q^2 - Q\left(Y-3\right)Y^3 + Y^5} = 0. \quad \text{(A.41)}$$

The above expression expands to an equation of eleventh order in r_s, which factorizes to

$$\left(\begin{array}{r} Y^8 - 8Y^7 - 2a^2Y^6 + 16Y^6 + 2a^2QY^5 - 8a^2Y^5 - 6a^2QY^4 + a^4Y^4 - 2a^4QY^3 \\ + 8a^2QY^3 + a^4Q^2Y^2 - 2a^4QY^2 - 2a^4Q^2Y + a^4Q^2 \end{array}\right)$$
$$\cdot\left(X^3 - 6X^2 + 9X - 4a^2\right) = 0, \quad \text{(A.42)}$$

where the second factor corresponds to the light radius (X) (Bardeen *et al.* 1972) and the equation for MBSO is given by

$$Y^8 - 8Y^7 - 2a^2Y^6 + 16Y^6 + 2a^2QY^5 - 8a^2Y^5 - 6a^2QY^4 + a^4Y^4 - 2a^4QY^3 +$$
$$8a^2QY^3 + a^4Q^2Y^2 - 2a^4QY^2 - 2a^4Q^2Y + a^4Q^2 = 0. \quad \text{(A.43)}$$

In the equatorial plane, $Q = 0$, this reduces to

$$Y^6 - 7Y^5 + 12Y^4 - a^2Y^4 - 5a^2Y^3 + 2a\left(a^2 - 2Y + Y^2\right)Y^{5/2} = 0, \quad \text{(A.44)}$$

which gets further factorized to

$$Y^{5/2}\left(Y + 2Y^{1/2} - a\right)\left(Y - 2Y^{1/2} + a\right)\left(X^{3/2} - 3X^{1/2} - 2a\right) = 0, \quad \text{(A.45)}$$

where the last bracket in above equation gives the solution for light radius and the first two brackets give retrograde and prograde solutions for

marginally bound orbit in the equatorial plane (Bardeen *et al.* 1972). According to the sign convention used in this paper ($-1 < a < 1$), both retrograde and prograde cases are covered by the formula given by

$$Y = 2 - a + 2\sqrt{1-a}. \tag{A.46}$$

A.4 Solution of (e_s, μ_s) in the equatorial separatrix case

The expressions for eccentricity and inverse-latus rectum for the non-equatorial separatrix orbits, given by Eqs. (4.35a) and (4.35b) can be written in the form

$$e_s = \frac{2u_s}{\left[-\frac{a'}{2} - \frac{1}{2}\sqrt{\left(a'+2u_s\right)^2 - \frac{4d'}{u_s^2}}\right]} - 1, \tag{A.47a}$$

$$\mu_s = \frac{1}{4}\left[-a' - \sqrt{\left(a'+2u_s\right)^2 - \frac{4d'}{u_s^2}}\right]. \tag{A.47b}$$

where the expressions for a' and d' are given by Eq. (4.31b). We solve for the factor in the denominator of e_s by substituting a' and d' and taking the limit $Q \to 0$, we find

$$\left[-\frac{a'}{2} - \frac{1}{2}\sqrt{\left(a'+2u_s\right)^2 - \frac{4d'}{u_s^2}}\right] = \left[\frac{x^2}{a^2Q} + \frac{1}{a^2} - \frac{x^2}{a^2Q}\left(1 + \frac{Q}{x^2} - \frac{u_s a^2 Q}{x^2} - \frac{a^2Q}{2u_s^2x^4} + \frac{E^2a^2Q}{2u_s^2x^4} + O[Q^2]\right)\right], \tag{A.48a}$$

$$= u_s + \frac{1}{2x^2u_s^2} - \frac{E^2}{2x^2u_s^2}. \tag{A.48b}$$

Substitution of Eq. (A.48b) in (A.47a, A.47b) gives

$$e_s = \frac{2u_s^3x^2 - 1 + E^2}{2u_s^3x^2 + 1 - E^2}, \quad \mu_s = \frac{1}{4}\left[2u_s + \frac{1-E^2}{x^2u_s^2}\right]. \tag{A.49}$$

Now, by substituting $x^2 = (L - aE)^2$ and E^2 from Eq. (4.16) into the above equations, we find

$$\begin{aligned} e_s = & -\frac{r_s^{7/2} - 9r_s^{5/2} + 6ar_s^2 - 3a^2r_s^{3/2} + 18r_s^{3/2} - 12ar_s - 7a^2r_s^{1/2} + 6a^3}{r_s^{7/2} - 5r_s^{5/2} - 2ar_s^2 + a^2r_s^{3/2} + 6r_s^{3/2} + 4ar_s - 3a^2r_s^{1/2} - 2a^3}, \\ = & -\frac{\left(r_s^{3/2} - 3r_s^{1/2} - 2a\right)\left(r_s^2 - 6r_s + 8ar_s^{1/2} - 3a^2\right)}{\left(r_s^{3/2} - 3r_s^{1/2} - 2a\right)(r_s^2 + a^2 - 2r_s)}, \\ = & -\frac{r_s^2 - 6r_s + 8ar_s^{1/2} - 3a^2}{r_s^2 + a^2 - 2r_s}, \end{aligned} \tag{A.50}$$

and

$$\begin{aligned} \mu_s = & \frac{r_s^4 - 5r_s^3 - 2ar_s^{5/2} + a^2r_s^2 + 6r_s^2 + 4ar_s^{3/2} - 3a^2r_s - 2a^3r_s^{1/2}}{4r_s\left(r_s^3 - 3r_s^2 + a^2r_s^2 + a^2r_s - 2ar_s^{5/2} + 4ar_s^{3/2} - 2a^3r_s^{1/2}\right)}, \\ = & \frac{(r_s^2 + a^2 - 2r_s)\left(r_s^2 - 3r_s - 2ar_s^{1/2}\right)}{4r_s\left(r_s + a^2 - 2ar_s{}^{1/2}\right)\left(r_s^2 - 3r_s - 2ar_s^{1/2}\right)}, \\ = & \frac{r_s^2 + a^2 - 2r_s}{4r_s\left(r_s^{1/2} - a\right)^2}, \end{aligned} \tag{A.51}$$

which are the expressions in Eq. (4.36) given in §4.6.1.

A.5 Reducing the radial integrals for the case of non-equatorial separatrix trajectories

Here, we reduce the radial integrals in our general trajectory solutions presented in §4.2.1, for the case of separatrix orbits with $Q \neq 0$. As shown in §4.6.2 that $k^2 = 1$ for the separatrix orbits, we use the identities given by Eq. (4.39) (Gradshteyn and Ryzhik 2007) to reduce the corresponding Elliptic integrals.

The substitution of these reduced form of the Elliptic integrals further reduces the integrals of the form S_3 and S_4, Eqs. (4.3c, 4.3d), to the general form

$$S \equiv \frac{1}{(1+p^2)}\left[\frac{p^2}{\sqrt{-(p^2+m^2)}}\ln\sqrt{\frac{\sqrt{1-m^2}+\sqrt{-(p^2+m^2)}\sin\alpha}{\sqrt{1-m^2}-\sqrt{-(p^2+m^2)}\sin\alpha}}+\frac{\ln(\tan\alpha+\sec\alpha)}{\sqrt{1-m^2}}\right], \tag{A.52}$$

where p^2 equals ${p_2}^2$ and ${p_3}^2$ for S_3 and S_4 respectively. Hence, from Eq. (4.3a) the expression of I_1 reduces in terms of S_3 and S_4 for the separatrix trajectories to

$$I_1 = -\frac{\sqrt{\mu(1+e)(3-e)}}{\sqrt{e\left[1+2a^2(-1+e^2)Q\mu^3\right](1-a^2)}}\left[\frac{\left[La^2-2xr_+\right]S_3}{(a^2\mu-a^2\mu e-r_+)}+\frac{\left[-La^2+2xr_-\right]S_4}{(a^2\mu-a^2\mu e-r_-)}\right]. \tag{A.53}$$

Further, Eqs. (4.39) reduce the integrals $S_5 - S_8$, Eqs. (4.3e-4.3h), to

$$\begin{aligned}
S_5 = \quad & \frac{1}{\sqrt{1-m^2}\,(m^2+p_1^2)^2}\left[\frac{m^2(m^2-p_1^2m^2+2p_1^2)}{(1+p_1^2)}\ln(\tan\alpha+\sec\alpha)+p_1^4S_7\right. \\
& \left.+\frac{2p_1^2m^2(1-m^2)}{(1+p_1^2)}\mid s\mid\tan^{-1}[\mid s\mid\sin\alpha]\right], && \text{(A.54a)}\\
S_6 = \quad & \frac{\ln(\tan\alpha+\sec\alpha)}{\sqrt{1-m^2}\,(1+p_1^2)}+\frac{p_1^2\sqrt{1-m^2}}{(m^2+p_1^2)(1+p_1^2)}\mid s\mid\tan^{-1}[\mid s\mid\sin\alpha], && \text{(A.54b)}\\
S_7 = \quad & \frac{1}{2(1-s^2)^2}\left[\frac{s^4\sin\alpha\cos^2\alpha}{\left(1-s^2\sin^2\alpha\right)}+2\ln(\tan\alpha+\sec\alpha)-s^2\sin\alpha\right. \\
& \left.+\left(3-s^2\right)\mid s\mid\tan^{-1}(\mid s\mid\sin\alpha)\right], && \text{(A.54c)}\\
S_8 = \quad & \frac{2\mu(1-e^2)}{\sqrt{C-A+\sqrt{B^2-4AC}}}\ln(\tan\alpha+\sec\alpha). && \text{(A.54d)}
\end{aligned}$$

Finally, the expression of I_2, Eq. (4.3b), reduces for the separatrix orbits in terms of $S_3 - S_6$ to

$$\begin{aligned}
I_2 = \frac{2\sqrt{(1+e)(3-e)}}{\sqrt{e\mu\left[1+2a^2(-1+e^2)Q\mu^3\right]}}\Bigg\{ & \frac{E}{\mu(1-e)^2}S_5+\frac{a^2\mu(-La+2Er_-)}{r_-\sqrt{(1-a^2)}\,(a^2\mu-a^2\mu e-r_+)}S_3 \\
& +\frac{2E}{(1-e)}S_6+\frac{a\mu\left(-2Lr_-\sqrt{1-a^2}-2Ear_-+La^2\right)}{r_-\sqrt{(1-a^2)}\,(a^2\mu-a^2\mu e-r_-)}S_4\Bigg\}.
\end{aligned} \tag{A.55}$$

See Table 4.5 for the summary of radial integrals for the separatrix trajectories.

A.6 Derivations for the consistency check with the previous results

1. *Equatorial separatrix orbits*: Here, we show the reduction of the separatrix trajectory formulae to the equatorial case. We substitute $Q = 0$ in the expression of the azimuthal angle given by Eq. (4.40a), which yields

$$\phi - \phi_0 = \frac{1}{2}\sqrt{\frac{\mu\,(1+e)\,(3-e)}{e\,(1-a^2)}}\left[\frac{[La^2 - 2xr_+]}{(a^2\mu - a^2\mu e - r_+)}I_3 + \frac{[-La^2 + 2xr_-]}{(a^2\mu - a^2\mu e - r_-)}I_4\right]. \tag{A.56}$$

We saw that $n^2 = 0$ for the equatorial orbits and m^2 reduces to 1 for separatrix orbits, which gives $\alpha = 0$ by definition, given by Eq. (A.6). Hence, we solve the integrals in the form of ψ variable. First, we solve integrals I_3 and I_4 for separatrix orbits using

$$I_3 = \int_0^{\psi} \frac{\mathrm{d}\psi}{\left(1 + p_2^2 \sin^2\psi\right)\cos\psi}, \quad I_4 = \int_0^{\psi} \frac{\mathrm{d}\psi}{\left(1 + p_3^2 \sin^2\psi\right)\cos\psi} \tag{A.57}$$

Using the substitution $p_2 \sin\psi = z$ for I_3 and $p_3 \sin\psi = z$ for I_4, and applying the method of partial fractions, we find

$$I_3 = \frac{1}{(1+p_2^2)}\left[p_2 \arctan\left(p_2 \sin\psi\right) + \operatorname{arctanh}\left(\sin\psi\right)\right], \tag{A.58a}$$

$$I_4 = \frac{1}{(1+p_3^2)}\left[p_3 \arctan\left(p_3 \sin\psi\right) + \operatorname{arctanh}\left(\sin\psi\right)\right]. \tag{A.58b}$$

Hence, when the above equations for I_3 and I_4 are substituted into the expressions for azimuthal angle, Eq. (A.56), yields

$$\phi - \phi_0 = \sqrt{\frac{\mu\,(1+e)\,(3-e)}{e\,(1-a^2)}}\left\{\frac{(La^2 - 2xr_+)\,p_2 \cdot \arctan\left(p_2 \sin\psi\right)}{2\,(a^2\mu + a^2\mu e - r_+)} +\right.$$

$$\left.\frac{\left(-La^2+2xr_-\right)p_3\cdot\arctan\left(p_3\sin\psi\right)}{2\left(a^2\mu+a^2\mu e-r_-\right)}+\frac{\sqrt{1-a^2}\left[L-2x\mu\left(1+e\right)\right]\operatorname{arctanh}\left(\sin\psi\right)}{\left[\mu^2a^2\left(1+e\right)^2-2\mu\left(1+e\right)+1\right]}\right\}. \tag{A.59}$$

Now, plugging in $Q=0$, reduces the expression for coordinate time of the separatrix orbits, Eq. (4.40b), to

$$t-t_0=\sqrt{\frac{\left(1+e\right)\left(3-e\right)}{e\mu}}\left\{\frac{E}{\mu\left(1-e\right)^2}I_5+\frac{a^2\mu\left(-La+2Er_-\right)}{r_-\sqrt{\left(1-a^2\right)}\left(a^2\mu-a^2\mu e-r_+\right)}I_3+\frac{2E}{\left(1-e\right)}I_6\right.$$

$$\left.+\frac{a\mu\left(-2Lr_-\sqrt{1-a^2}-2Ear_-+La^2\right)}{r_-\sqrt{\left(1-a^2\right)}\left(a^2\mu-a^2\mu e-r_-\right)}I_4\right\}. \tag{A.60}$$

And similarly, the integrals I_5 and I_6 reduce to

$$\begin{aligned}I_5 &= \int_0^{\psi}\frac{\mathrm{d}\psi}{\left(1+p_1^2\sin^2\psi\right)^2\cos\psi}\\ &= \frac{1}{\left(1+p_1^2\right)^2}\left[\frac{p_1}{2}\left(3+p_1^2\right)\arctan\left(p_1\sin\psi\right)+\operatorname{arctanh}\left(\sin\psi\right)+\frac{p_1^2\sin\psi\left(1+p_1^2\right)}{2\left(1+p_1^2\sin^2\psi\right)}\right],\end{aligned} \tag{A.61a}$$

$$I_6 = \int_0^{\psi}\frac{\mathrm{d}\psi}{\left(1+p_1^2\sin^2\psi\right)\cos\psi}=\frac{1}{\left(1+p_1^2\right)}\left[p_1\arctan\left(p_1\sin\psi\right)+\operatorname{arctanh}\left(\sin\psi\right)\right]. \tag{A.61b}$$

Hence, the substitution of I_3, I_4, I_5, I_6 into Eq. (A.60) yields the expression for coordinate time for equatorial separatrix orbits to be

$$t-t_0=\sqrt{\frac{\left(1+e\right)\left(3-e\right)}{e\mu}}\left\{\left[\frac{E\left[1+2\mu\left(1+e\right)\right]}{\mu\left(1+e\right)^2}+\frac{2\mu\left[-La\mu\left(1+e\right)+2E\right]}{\left[1+\mu^2a^2\left(1+e\right)^2-2\mu\left(1+e\right)\right]}\right]\cdot\right.$$

$$\operatorname{arctanh}\left(\sin\psi\right)+\frac{a\mu}{r_-\sqrt{1-a^2}}\left[\frac{\left(-La^2+2Ear_-\right)p_2\cdot\arctan\left(p_2\sin\psi\right)}{\left(a^2\mu+a^2\mu e-r_+\right)}+\right.$$

$$\left.\frac{\left(-2Lr_-\sqrt{1-a^2}-2Ear_-+La^2\right)p_3\cdot\arctan\left(p_3\sin\psi\right)}{\left(a^2\mu+a^2\mu e-r_-\right)}\right]+\frac{Ee\sin\psi}{\mu\left(1-e^2\right)\left(1-e+2e\sin^2\psi\right)}$$

$$\left.+\frac{E\left[3-e+4\mu\left(1-e^2\right)\right]p_1\cdot\arctan\left(p_1\sin\psi\right)}{2\mu\left(1-e^2\right)\left(1+e\right)}\right\}. \tag{A.62}$$

We have numerically matched these expressions of the azimuthal angle and coordinate time for equatorial separatrix orbits, Eqs. (A.59) and (A.62), with those derived in Levin and Perez-Giz (2009).

2. *Spherical orbits*: Now, we verify our frequency formulae with the spherical orbit case. From Eqs. (4.11c) and (4.11b), we have

$$\frac{\nu_\phi}{\nu_\theta} = \frac{2\left\{\left[-\frac{I_1\left(\frac{\pi}{2},e,\mu,1,Q\right)}{2I_8\left(\frac{\pi}{2},e,\mu,1,Q\right)} - L\right]F\left(\frac{\pi}{2},\frac{z_-^2}{z_+^2}\right) + L\cdot\Pi\left(z_-^2,\frac{\pi}{2},\frac{z_-^2}{z_+^2}\right)\right\}}{\pi\sqrt{1-E^2}z_+}. \tag{A.63}$$

In Wilkins (1972), the azimuthal to polar motion frequency ratio, ν_ϕ/ν_θ, for maximally rotating black hole, $a = 1$, was found to be

$$\frac{\nu_\phi}{\nu_\theta} = \frac{2\left\{L\cdot\Pi\left(z_-^2,\frac{\pi}{2},\frac{z_-^2}{z_+^2}\right) + \left(P\Delta^{-1} - E\right)F\left(\frac{\pi}{2},\frac{z_-^2}{z_+^2}\right)\right\}}{\pi\sqrt{1-E^2}z_+}, \tag{A.64}$$

where $P = \left[E\left(r^2+1\right) - L\right](r-1)^2 - E$ for $a = 1$.

For the case of spherical orbits, the limit $e \to 0$ reduces the ratio (I_1/I_8) to the ratio of their integrands, which yields

$$\left[\frac{-I_1}{2I_8} - L\right] = -E + \frac{\left[E\left(r^2+1\right) - L\right]}{(r-1)^2} = \left(P\Delta^{-1} - E\right); \tag{A.65}$$

this reduces ν_ϕ/ν_θ from, Eq. (A.63) to Eq. (A.64), and establishes the consistency of our frequency formulae with the spherical orbits case.

3. *Equatorial circular orbits*: We show this reduction from both the equatorial eccentric and the spherical orbits below:

   (a) *Reduction from equatorial eccentric orbits*: We see that for circular orbits ($e = 0$), the expressions of m^2, ${p_1}^2$, ${p_2}^2$, and ${p_3}^2$, Eqs. (4.12c) and (4.4k), reduce to

$$m^2 = {p_1}^2 = {p_2}^2 = {p_3}^2 = 0. \tag{A.66}$$

We first make the subtitution $m^2 = 0$ in Eqs. (4.14a, 4.14b, 4.14c) which gives

$$\nu_\phi = \frac{a_1\Pi\left(-p_2^2, \frac{\pi}{2}, 0\right) + b_1\Pi\left(-p_3^2, \frac{\pi}{2}, 0\right)}{2\pi\left\{\Pi\left(-p_1^2, \frac{\pi}{2}, 0\right)\left[a_2\frac{\left(p_1^2+2\right)}{2\left(1+p_1^2\right)} + b_2\right] + c_2\Pi\left(-p_2^2, \frac{\pi}{2}, 0\right) + d_2\Pi\left(-p_3^2, \frac{\pi}{2}, 0\right)\right\}}, \tag{A.67a}$$

$$\nu_r = \frac{1}{2\left\{\Pi\left(-p_1^2, \frac{\pi}{2}, 0\right)\left[a_2\frac{\left(p_1^2+2\right)}{2\left(1+p_1^2\right)} + b_2\right] + c_2\Pi\left(-p_2^2, \frac{\pi}{2}, 0\right) + d_2\Pi\left(-p_3^2, \frac{\pi}{2}, 0\right)\right\}}, \tag{A.67b}$$

$$\nu_\theta = \frac{\nu_r\mu^{1/2}\sqrt{(x^2 + a^2 + 2aEx)}}{\sqrt{1 - 3\mu^2x^2}}. \tag{A.67c}$$

Next, the substitution of ${p_1}^2 = {p_2}^2 = {p_3}^2 = 0$ in Eq. (A.67) yields

$$\nu_\phi = \frac{a_1 + b_1}{2\pi\left(a_2 + b_2 + c_2 + d_2\right)}, \tag{A.68a}$$

$$\nu_r = \frac{1}{\pi\left(a_2 + b_2 + c_2 + d_2\right)}, \tag{A.68b}$$

$$\nu_\theta = \frac{\nu_r\mu^{1/2}\sqrt{(x^2 + a^2 + 2aEx)}}{\sqrt{1 - 3\mu^2x^2}}. \tag{A.68c}$$

By substituting $e = 0$ in Eq. (4.13), we find that

$$a_1 + b_1 = \frac{2\mu^{1/2}\left(L - 2x\mu\right)}{\sqrt{1 - 3\mu^2x^2}\left(1 - 2\mu + a^2\mu^2\right)}, \tag{A.69a}$$

$$a_2 + b_2 + c_2 + d_2 = \frac{2\left(E + Ea^2\mu^2 - 2ax\mu^3\right)}{\mu^{3/2}\sqrt{1 - 3\mu^2x^2}\left(1 - 2\mu + a^2\mu^2\right)}. \tag{A.69b}$$

Now, by substituting Eq. (A.69) in Eq. (A.68), we get

$$\nu_\phi = \frac{\mu^2\left(L - 2x\mu\right)}{2\pi\left(E + Ea^2\mu^2 - 2ax\mu^3\right)}, \tag{A.70a}$$

$$\nu_r = \frac{\mu^{3/2}\sqrt{1 - 3\mu^2x^2}\left(1 - 2\mu + a^2\mu^2\right)}{2\pi\left(E + Ea^2\mu^2 - 2ax\mu^3\right)}, \tag{A.70b}$$

$$\nu_\theta = \frac{\mu^2\left(1 - 2\mu + a^2\mu^2\right)\sqrt{(x^2 + a^2 + 2aEx)}}{2\pi\left(E + Ea^2\mu^2 - 2ax\mu^3\right)}. \tag{A.70c}$$

The expressions of E, L, and x for equatorial circular orbits are given by (Bardeen *et al.* 1972)

$$E = \frac{\left(r_c^2 - 2r_c + a\sqrt{r_c}\right)}{r_c\left(r_c^2 - 3r_c + 2a\sqrt{r_c}\right)^{1/2}}, \tag{A.71a}$$

$$L = \frac{\sqrt{r_c}\left(r_c^2 + a^2 - 2a\sqrt{r_c}\right)}{r_c\left(r_c^2 - 3r_c + 2a\sqrt{r_c}\right)^{1/2}}, \tag{A.71b}$$

$$x = \frac{r_c\left(r_c^{1/2} - a\right)}{\left(r_c^2 - 3r_c + 2a\sqrt{r_c}\right)^{1/2}}, \tag{A.71c}$$

where r_c is the radius of the circular orbit. These expressions can be also be obtained by substituting $\{e = 0,\, Q = 0,\, \mu = 1/r_c\}$ in the more general expressions given by Eq. (3.14) (Rana and Mangalam 2019a,b). Finally, by substituting E, L, x, and $\mu = 1/r_c$ from Eq. (A.71) into Eq. (A.70), we recover the frequency formulae for equatorial circular orbits

$$\nu_\phi = \frac{1}{2\pi\left(r_c^{3/2} + a\right)}, \tag{A.72a}$$

$$\nu_r = \nu_\phi\left(1 - \frac{6}{r_c} - \frac{3a^2}{r_c^2} + \frac{8a}{r_c^{3/2}}\right)^{1/2}, \tag{A.72b}$$

$$\nu_\theta = \nu_\phi\left(1 + \frac{3a^2}{r_c^2} - \frac{4a}{r_c^{3/2}}\right)^{1/2}, \tag{A.72c}$$

as given by Eq. (5.1).

(b) *Reduction from spherical orbits*: We find that for circular orbits ($Q = 0$), the expressions of $z_\pm$, Eq. (4.5d), reduce to

$$z_- = 0, \qquad z_+ = \frac{\sqrt{L^2 + a^2\left(1 - E^2\right)}}{a\sqrt{1 - E^2}}. \tag{A.73}$$

The substitution of Eq. (A.73) in the frequency formulae of spherical orbits, Eqs. (4.23, 4.24b, 4.25c), yields

$$\nu_\phi = \frac{(-2Lr_c + Lr_c^2 + 2r_c aE)}{2\pi\left[E\left(a^2r_c^2 + r_c^4 + 2a^2r_c\right) - 2Lar_c\right]}, \tag{A.74a}$$

$$\nu_r = \frac{\sqrt{r_c^4\left(1-E^2\right) - 2x^2r_c}\Delta}{2\pi r_c\left[E\left(a^2r_c^2 + r_c^4 + 2a^2r_c\right) - 2Lar_c\right]}, \tag{A.74b}$$

$$\nu_\theta = \frac{\sqrt{L^2 + a^2\left(1-E^2\right)}\Delta}{2\pi\left[E\left(a^2r_c^2 + r_c^4 + 2a^2r_c\right) - 2Lar_c\right]}. \tag{A.74c}$$

Using the expressions of E, L, and x from Eq. (A.71), we find that

$$\left[E\left(a^2r_c^2 + r_c^4 + 2a^2r_c\right) - 2Lar_c\right] = \frac{r_c^{3/2}\Delta\left(r_c^{3/2} + a\right)}{\left(r_c^2 - 3r_c + 2ar_c^{1/2}\right)^{1/2}}, \tag{A.75a}$$

$$\left(-2Lr_c + Lr_c^2 + 2r_c aE\right) = \frac{r_c^{3/2}\Delta}{\left(r_c^2 - 3r_c + 2ar_c^{1/2}\right)^{1/2}}, \tag{A.75b}$$

$$\sqrt{r_c^4\left(1-E^2\right) - 2x^2r_c} = \frac{r_c^{3/2}\left(r_c^2 - 6r_c - 3a^2 + 8ar_c^{1/2}\right)^{1/2}}{\left(r_c^2 - 3r_c + 2ar_c^{1/2}\right)^{1/2}}, \tag{A.75c}$$

$$\sqrt{L^2 + a^2\left(1-E^2\right)} = \frac{\sqrt{r_c^3 + 3a^2r_c - 4ar_c^{3/2}}}{\left(r_c^2 - 3r_c + 2ar_c^{1/2}\right)^{1/2}}. \tag{A.75d}$$

Finally, substituting these factors, given by Eq. (A.75), in Eq. (A.74), we recover the expressions for equatorial circular orbits, that are given by

$$\nu_\phi = \frac{1}{2\pi\left(r_c^{3/2} + a\right)}, \tag{A.76a}$$

$$\nu_r = \nu_\phi\left(1 - \frac{6}{r_c} - \frac{3a^2}{r_c^2} + \frac{8a}{r_c^{3/2}}\right)^{1/2}, \tag{A.76b}$$

$$\nu_\theta = \nu_\phi\left(1 + \frac{3a^2}{r_c^2} - \frac{4a}{r_c^{3/2}}\right)^{1/2}. \tag{A.76c}$$

Appendix B

B.1 Source history

We summarize the history of each BHXRB below:

1. M82 X-1: It is the brightest X-ray source in the M82 galaxy. This source is thought to harbor an intermediate-mass black hole because of its very high X-ray luminosity, average 2-10 keV luminosity $\sim 5 \times 10^{40}$ erg s^{-1}, and variability characteristics (Patruno *et al.* 2006; Casella *et al.* 2008; Pasham and Strohmayer 2013a) although other models claim that it might contain a black hole of mass $\sim 20 M_{\odot}$ (Okajima *et al.* 2006). However, the discovery of twin-peak and stable QPOs at 3.32±0.06 Hz and 5.07±0.06 Hz in M82 X-1, which are nearly in 3:2 ratio, gave a shred of affirmative evidence that these QPOs are analogs of HFQPOs in stellar BHXRB (Pasham *et al.* 2014). Following and extrapolating the inverse-mass scaling that holds for HFQPOs in stellar mass BHXRB (McClintock and Remillard 2006), it was found that the mass of the black hole in M82 X-1 could be $428 \pm 105 M_{\odot}$ (Pasham *et al.* 2014), making it an intermediate-mass black hole system.

2. GROJ 1655-40: It is one among the few BHXRB in the Milky Way galaxy whose BH mass is known with good precession through the dynamical studies of the infrared and optical observations during the quiescent state (Beer and Podsiadlowski 2002). GROJ 1655-40 is also one of the BHXRB known to produce relativistic radio jets having a double-lobed radio structure (Mirabel and Rodríguez 1994). The first detection of two simultaneous HFQPOs near $\sim$ 450 and 300 Hz in GROJ 1655-40 was reported by (Strohmayer 2001a). The detection of 300Hz QPO was reported in BHXRB GROJ 1655-40 (Remillard *et al.* 1999a), and later the detection of simultaneous 450Hz QPO along with 300Hz in the same observations was confirmed (Strohmayer 2001a). A systematic study of the LF- and HFQPOs in 571 RXTE observations taken between the year 1996 to 2005 was carried out (Motta *et al.* 2014a), and they detected three simultaneous QPOs (two HF and one LFQPO) at 441$\pm$2 Hz, 298$\pm$4 Hz, and 17.3$\pm$0.1 Hz in one of these observations. Using these QPO frequencies, the mass, the spin of the black hole, and the radius of the equatorial circular orbit where these QPOs originated were estimated using Eqs. (5.1a-5.1c) assuming the RPM (Motta *et al.* 2014a).

3. XTEJ 1550-564: This BHXRB was first detected by ASM/RXTE on September 7, 1998. Since then, it has undergone four X-ray outbursts between the years 1998 to 2002 as observed by RXTE, among which the Sept 1998- May 1999 outburst was the most luminous one. XTEJ 1550-564 is also among the few BHXRB, which has shown HFQPOs; for example, QPOs with frequencies in the range 185-237 Hz were detected during the 1998-1999 outburst (Remillard *et al.* 1999b; Homan *et al.* 2001). After a quiescent period of a few months, XTEJ 1550-564 again underwent a short X-ray outburst in the period April-May 2000 following a fast rise and an exponential decay of the X-ray luminosity. The simultaneous occurrence of two HFQPOs at 268$\pm$3 Hz and 188$\pm$3 Hz frequencies during the 2000 outburst was reported (Miller *et al.* 2001), indicating a resonance phenomenon. However, no LFQPOs were detected simultaneously with these two HFQPOs. A systematic study of all

archival RXTE observations of XTEJ 1550-564 was carried out by Motta *et al.* (2014b), where they reported the detection of an HFQPO at ∼183 Hz along with a simultaneous type-C LFQPO at ∼13 Hz and type-B LFQPO at ∼5 Hz, but no second peak of HFQPO was detected during this observation.

4. 4U 1630-47: This soft X-ray transient was discovered by *Uhuru* satellite (Jones *et al.* 1976), which is known to have an inclination of ∼ 60-75° (Kuulkers *et al.* 1998). This source is one among the few BHXRB to show HFQPOs during its 1998 outburst in the frequency range ∼100-300 Hz, and also twin simultaneous HFQPOs with frequency ratio 1:4 (Klein-Wolt *et al.* 2004). It shows a regular X-ray outburst cycle after every ∼ 600-690 days (Jones *et al.* 1976; Priedhorsky 1986). The QPO frequencies in this system during the 1998 X-ray outburst were observed to increase during the rising phase, followed by a phase where the frequencies were found stable near ∼180 Hz, and then a decrease in QPO frequencies was observed during the decay of the outburst.

5. GRS 1915+105: This BHXRB is known to be a very bright system during the whole *RXTE* period, showing its peculiar behavior, and have also shown superluminal radio outflows (Mirabel and Rodríguez 1994). This is also the first BHXRB to show an HFQPO at a characteristic constant frequency of ∼67 Hz (Morgan *et al.* 1997) in the *RXTE* observations taken during April-May 1996. Later, simultaneous ∼67 Hz and ∼40 Hz QPOs were discovered in the *RXTE* observations taken during July and November 1997 (Strohmayer 2001b). A systematic study of all *RXTE* observations of GRS 1915+105 discovered 51 observations which showed detection of HFQPOs, out of which 48 observations showed the centroid frequency of QPOs in the range 63-71 Hz (Belloni and Altamirano 2013a). Another pair of simultaneous HFQPOs were also discovered at ∼34 Hz and ∼68 Hz (Belloni and Altamirano 2013b).

Bibliography

Abbott, R. and Abbott, T. D. et. al., 2020a, "Properties and Astrophysical Implications of the 150 M Binary Black Hole Merger GW190521", *Astrophys. J. Lett.*, **900**(1), L13. [DOI], [ADS], [arXiv:2009.01190 [astro-ph.HE]]

Abbott, R. and Abbott, T. D. et. al., 2020b, "GW190521: A Binary Black Hole Merger with a Total Mass of 150 M", *Physical Review L*, **125**(10), 101102. [DOI], [ADS], [arXiv:2009.01075 [gr-qc]]

Abbott et al., B. P., 2016, "Observation of Gravitational Waves from a Binary Black Hole Merger", *Physical Review L*, **116**, 061102. [DOI], [ADS]

Abramowicz, Marek A., Karas, Vladimir, Kluzniak, Włodzimierz, Lee, William H. and Rebusco, Paola, 2003, "Non-Linear Resonance in Nearly Geodesic Motion in Low-Mass X-Ray Binaries", *Publications of the Astronomical Society of Japan*, **55**, 467–466. [DOI], [ADS], [arXiv:astro-ph/0302183 [astro-ph]]

Ackermann, M., Ajello, M. and Albert, A. et al, 2015a, "Multiwavelength Evidence for Quasi-periodic Modulation in the Gamma-Ray Blazar PG 1553+113", *Astrophys. J. Lett.*, **813**(2), L41. [DOI], [ADS], [arXiv:1509.02063 [astro-ph.HE]]

Ackermann, M., Ajello, M. and Atwood, W. B. et al, 2015b, "The Third Catalog of Active Galactic Nuclei Detected by the Fermi Large Area Telescope", *Astrophys. J.*, **810**(1), 14. [DOI], [ADS], [arXiv:1501.06054 [astro-ph.HE]]

Alston, W. N., Parker, M. L., Markevičiūtė, J., Fabian, A. C., Middleton, M., Lohfink, A., Kara, E. and Pinto, C., 2015, "Discovery of an ∼2-h high-frequency

X-ray QPO and iron Kα reverberation in the active galaxy MS 2254.9-3712", *Mon. Not. Roy. Astron. Soc.*, **449**(1), 467–476. [DOI], [ADS], [arXiv:1411.0684 [astro-ph.HE]]

An, Tao, Mohan, Prashanth, Zhang, Yingkang, Frey, Sándor, Yang, Jun, Gabányi, Krisztina É., Gurvits, Leonid I., Paragi, Zsolt, Perger, Krisztina and Zheng, Zhenya, 2020, "Evolving parsec-scale radio structure in the most distant blazar known", *Nature Communications*, **11**, 143. [DOI], [ADS], [arXiv:2001.02809 [astro-ph.GA]]

Antonucci, Robert, 1993, "Unified models for active galactic nuclei and quasars.", *Ann. Rev. Astron. Astrophys.*, **31**, 473–521. [DOI], [ADS]

Bambi, Cosimo, 2019, "Astrophysical Black Holes: A Review", *arXiv e-prints*, arXiv:1906.03871. [ADS], [arXiv:1906.03871 [astro-ph.HE]]

Bardeen, J. M., Press, W. H. and Teukolsky, S. A., 1972, "Rotating Black Holes: Locally Nonrotating Frames, Energy Extraction, and Scalar Synchrotron Radiation", *Astrophys. J.*, **178**, 347–370. [DOI], [ADS]

Beer, M. E. and Podsiadlowski, P., 2002, "The quiescent light curve and the evolutionary state of GRO J1655-40", *MNRAS*, **331**, 351–360. [DOI], [ADS], [astro-ph/0109136]

Belloni, T., Soleri, P., Casella, P., Méndez, M. and Migliari, S., 2006, "High-frequency quasi-periodic oscillations from GRS 1915+105 in its C state", *MNRAS*, **369**, 305–310. [DOI], [ADS], [astro-ph/0603210]

Belloni, T. M. and Altamirano, D., 2013a, "High-frequency quasi-periodic oscillations from GRS 1915+105", *MNRAS*, **432**, 10–18. [DOI], [ADS], [arXiv:1303.4551 [astro-ph.HE]]

Belloni, T. M. and Altamirano, D., 2013b, "Discovery of a 34 Hz quasi-periodic oscillation in the X-ray emission of GRS 1915+105", *MNRAS*, **432**, 19–22. [DOI], [ADS], [arXiv:1303.4934 [astro-ph.HE]]

Belloni, T. M. and Stella, L., 2014, "Fast Variability from Black-Hole Binaries", *Space Science Reviews*, **183**, 43–60. [DOI], [ADS], [arXiv:1407.7373 [astro-ph.HE]]

Belloni, T. M., Sanna, A. and Méndez, M., 2012, "High-frequency quasi-periodic oscillations in black hole binaries", *MNRAS*, **426**, 1701–1709. [DOI], [ADS], [arXiv:1207.2311 [astro-ph.HE]]

Belloni, Tomaso, Psaltis, Dimitrios and van der Klis, Michiel, 2002, "A Unified Description of the Timing Features of Accreting X-Ray Binaries", *Astrophys. J.*, **572**(1), 392–406. [DOI], [ADS], [arXiv:astro-ph/0202213 [astro-ph]]

Bhatta, Gopal, 2019, "Blazar Mrk 501 shows rhythmic oscillations in its γ-ray emission", *Mon. Not. Roy. Astron. Soc.*, **487**(3), 3990–3997. [DOI], [ADS], [arXiv:1808.06067 [astro-ph.HE]]

Bhattacharyya, Dipanweeta and Mangalam, A., 2020, "Cosmic Spin and Mass Evolution of Black Holes and Its Impact", *Astrophys. J.*, **895**(2), 130. [DOI], [ADS], [arXiv:2004.05000 [astro-ph.HE]]

Bini, D., Geralico, A. and Jantzen, R. T., 2016a, "Gyroscope precession along bound equatorial plane orbits around a Kerr black hole", *Physical Review D*, **94**(6), 064066. [DOI], [ADS], [arXiv:1607.08427 [gr-qc]]

Bini, D., Geralico, A. and Jantzen, R. T., 2016b, "Gyroscope precession along unbound equatorial plane orbits around a Kerr black hole", *Physical Review D*, **94**(12), 124002. [DOI], [ADS], [arXiv:1610.06513 [gr-qc]]

Blandford, R. D. and Rees, M. J., 1992, "The standard model and some new directions", in *American Institute of Physics Conference Series*, (Eds.) Holt, Stephen S., Neff, Susan G., Urry, C. M., American Institute of Physics Conference Series, 254, [DOI], [ADS]

Boller, Th., Keil, R., Trümper, J., O'Brien, P. T., Reeves, J. and Page, M., 2001, "Detection of an X-ray periodicity in the Narrow-line Seyfert 1 Galaxy Mrk

766 with XMM-Newton", *Astron. Astrophys.*, **365**, L146–L151. [DOI], [ADS], [arXiv:astro-ph/0010646 [astro-ph]]

Bolton, C. T., 1972, "Identification of Cygnus X-1 with HDE 226868", *Nature*, **235**(5336), 271–273. [DOI], [ADS]

Brenneman, L. W., Reynolds, C. S., Nowak, M. A., Reis, R. C., Trippe, M., Fabian, A. C., Iwasawa, K., Lee, J. C., Miller, J. M., Mushotzky, R. F., Nandra, K. and Volonteri, M., 2011, "The Spin of the Supermassive Black Hole in NGC 3783", *Astrophys. J.*, **736**(2), 103. [DOI], [ADS], [arXiv:1104.1172 [astro-ph.HE]]

Brink, J., Geyer, M. and Hinderer, T., 2015, "Astrophysics of resonant orbits in the Kerr metric", *Physical Review D*, **91**(8), 083001. [DOI], [ADS], [arXiv:1501.07728 [gr-qc]]

Burgay, M., D'Amico, N., Possenti, A., Manchester, R. N., Lyne, A. G., Joshi, B. C., McLaughlin, M. A., Kramer, M., Sarkissian, J. M., Camilo, F., Kalogera, V., Kim, C. and Lorimer, D. R., 2003, "An increased estimate of the merger rate of double neutron stars from observations of a highly relativistic system", *Nature*, **426**, 531–533. [DOI], [ADS], [astro-ph/0312071]

Byrd, P. F. and Friedman, M. D., 1971, *Handbook of Elliptic Integrals for Engineers and Scientists*

Camenzind, M. and Krockenberger, M., 1992, "The lighthouse effect of relativistic jets in blazars. A geometric originof intraday variability.", *Astron. Astrophys.*, **255**, 59–62. [ADS]

Cardano, Girolamo 1501-1576, 1968, *The great art; or, The rules of algebra. Translated and edited by T. Richard Witmer. With a foreword by Oystein Ore*, M.I.T. Press Cambridge, Mass

Carter, B., 1968, "Global Structure of the Kerr Family of Gravitational Fields", *Physical Review*, **174**, 1559–1571. [DOI], [ADS]

Casella, P., Ponti, G., Patruno, A., Belloni, T., Miniutti, G. and Zampieri, L., 2008, "Weighing the black holes in ultraluminous X-ray sources through timing", *Mon. Not. Roy. Astron. Soc.*, **387**(4), 1707–1711. [DOI], [ADS], [arXiv:0804.3378 [astro-ph]]

Chandrasekhar, S., 1983, *The mathematical theory of black holes*. [ADS]

Chen, Liang, 2018, "On the Jet Properties of γ-Ray-loud Active Galactic Nuclei", *Astrophys. J. Suppl.*, **235**(2), 39. [DOI], [ADS], [arXiv:1803.05715 [astro-ph.HE]]

Cui, Wei, Zhang, S. N., Focke, W. and Swank, J. H., 1997, "Temporal Properties of Cygnus X-1 during the Spectral Transitions", *Astrophys. J.*, **484**(1), 383–393. [DOI], [ADS], [arXiv:astro-ph/9702073 [astro-ph]]

Drasco, S., 2006, "Strategies for observing extreme mass ratio inspirals", *Classical and Quantum Gravity*, **23**, S769–S784. [DOI], [ADS], [gr-qc/0604115]

Drasco, S. and Hughes, S. A., 2004, "Rotating black hole orbit functionals in the frequency domain", *Physical Review D*, **69**(4), 044015. [DOI], [ADS], [astro-ph/0308479]

Drasco, S. and Hughes, S. A., 2006, "Gravitational wave snapshots of generic extreme mass ratio inspirals", *Physical Review D*, **73**(2), 024027. [DOI], [ADS], [gr-qc/0509101]

Drasco, S., Flanagan, É. É. and Hughes, S. A., 2005, "Computing inspirals in Kerr in the adiabatic regime: I. The scalar case", *Classical and Quantum Gravity*, **22**, S801–S846. [DOI], [ADS], [gr-qc/0505075]

Dubus, G., Hameury, J. M. and Lasota, J. P., 2001, "The disc instability model for X-ray transients: Evidence for truncation and irradiation", *Astron. Astrophys.*, **373**, 251–271. [DOI], [ADS], [arXiv:astro-ph/0102237 [astro-ph]]

Event Horizon Telescope Collaboration, Akiyama, Kazunori, Alberdi, Antxon and Alef, Walter et al, 2019a, "First M87 Event Horizon Telescope Results. I. The

Shadow of the Supermassive Black Hole", *Astrophys. J. Lett.*, **875**(1), L1. [DOI], [ADS], [arXiv:1906.11238 [astro-ph.GA]]

Event Horizon Telescope Collaboration, Akiyama, Kazunori, Alberdi, Antxon and Alef, Walter et al, 2019b, "First M87 Event Horizon Telescope Results. II. Array and Instrumentation", *Astrophys. J. Lett.*, **875**(1), L2. [DOI], [ADS], [arXiv:1906.11239 [astro-ph.IM]]

Event Horizon Telescope Collaboration, Akiyama, Kazunori, Alberdi, Antxon and Alef, Walter et al, 2019c, "First M87 Event Horizon Telescope Results. III. Data Processing and Calibration", *Astrophys. J. Lett.*, **875**(1), L3. [DOI], [ADS], [arXiv:1906.11240 [astro-ph.GA]]

Event Horizon Telescope Collaboration, Akiyama, Kazunori, Alberdi, Antxon and Alef, Walter et al, 2019d, "First M87 Event Horizon Telescope Results. IV. Imaging the Central Supermassive Black Hole", *Astrophys. J. Lett.*, **875**(1), L4. [DOI], [ADS], [arXiv:1906.11241 [astro-ph.GA]]

Event Horizon Telescope Collaboration, Akiyama, Kazunori, Alberdi, Antxon and Alef, Walter et al, 2019e, "First M87 Event Horizon Telescope Results. V. Physical Origin of the Asymmetric Ring", *Astrophys. J. Lett.*, **875**(1), L5. [DOI], [ADS], [arXiv:1906.11242 [astro-ph.GA]]

Event Horizon Telescope Collaboration, Akiyama, Kazunori, Alberdi, Antxon and Alef, Walter et al, 2019f, "First M87 Event Horizon Telescope Results. VI. The Shadow and Mass of the Central Black Hole", *Astrophys. J. Lett.*, **875**(1), L6. [DOI], [ADS], [arXiv:1906.11243 [astro-ph.GA]]

Everitt, C. W. F., Muhlfelder, B. and DeBra, D. B. et al, 2015, "The Gravity Probe B test of general relativity", *Classical and Quantum Gravity*, **32**(22), 224001. [DOI], [ADS]

Fabian, A. C., Rees, M. J., Stella, L. and White, N. E., 1989, "X-ray fluorescence from the inner disc in Cygnus X-1.", *Mon. Not. Roy. Astron. Soc.*, **238**, 729–736. [DOI], [ADS]

Fabian, A. C., Nandra, K., Reynolds, C. S., Brand t, W. N., Otani, C., Tanaka, Y., Inoue, H. and Iwasawa, K., 1995, "On broad iron Kalpha lines in Seyfert 1 galaxies", *Mon. Not. Roy. Astron. Soc.*, **277**(1), L11–L15. [DOI], [ADS], [arXiv:astro-ph/9507061 [astro-ph]]

Falomo, Renato, Pian, Elena and Treves, Aldo, 2014, "An optical view of BL Lacertae objects", *Astron. Astrophys. Rev.*, **22**, 73. [DOI], [ADS], [arXiv:1407.7615 [astro-ph.HE]]

Fan, J. H., Kurtanidze, O., Liu, Y., Richter, G. M., Chanishvili, R. and Yuan, Y. H., 2014, "Optical Monitoring of Two Brightest Nearby Quasars, PHL 1811 and 3C 273", *Astrophys. J. Suppl.*, **213**(2), 26. [DOI], [ADS]

Farrell, S. A., Servillat, M., Pforr, J., Maccarone, T. J., Knigge, C., Godet, O., Maraston, C., Webb, N. A., Barret, D., Gosling, A. J., Belmont, R. and Wiersema, K., 2012, "A Young Massive Stellar Population around the Intermediate-mass Black Hole ESO 243-49 HLX-1", *Astrophys. J. Lett.*, **747**(1), L13. [DOI], [ADS], [arXiv:1110.6510 [astro-ph.CO]]

Farrell, Sean A., Webb, Natalie A., Barret, Didier, Godet, Olivier and Rodrigues, Joana M., 2009, "An intermediate-mass black hole of over 500 solar masses in the galaxy ESO243-49", *Nature*, **460**(7251), 73–75. [DOI], [ADS], [arXiv:1001.0567 [astro-ph.HE]]

Fender, R. and Belloni, T., 2012, "Stellar-Mass Black Holes and Ultraluminous X-ray Sources", *Science*, **337**, 540. [DOI], [ADS], [arXiv:1208.1138 [astro-ph.HE]]

Fender, R. P., Belloni, T. M. and Gallo, E., 2004, "Towards a unified model for black hole X-ray binary jets", *Mon. Not. Roy. Astron. Soc.*, **355**(4), 1105–1118. [DOI], [ADS], [arXiv:astro-ph/0409360 [astro-ph]]

Fender, Rob and Belloni, Tomaso, 2004, "GRS 1915+105 and the Disc-Jet Coupling in Accreting Black Hole Systems", *Ann. Rev. Astron. Astrophys.*, **42**(1), 317–364. [DOI], [ADS], [arXiv:astro-ph/0406483 [astro-ph]]

Fujita, R. and Hikida, W., 2009, "Analytical solutions of bound timelike geodesic orbits in Kerr spacetime", *Classical and Quantum Gravity*, **26**(13), 135002. [DOI], [ADS], [arXiv:0906.1420 [gr-qc]]

Germanà, C., Kostić, U., Čadež, A. and Calvani, M., 2009, "Tidal Disruption of Small Satellites Orbiting Black Holes", in *American Institute of Physics Conference Series*, (Eds.) Rodriguez, Jérôme, Ferrando, Phillippe, American Institute of Physics Conference Series, 1126, [DOI], [ADS], [arXiv:0902.2134 [astro-ph.HE]]

Ghez, A. M., White, Russel J. and Simon, M., 1997, "High Spatial Resolution Imaging of Pre-Main-Sequence Binary Stars: Resolving the Relationship between Disks and Close Companions", *Astrophys. J.*, **490**(1), 353–367. [DOI], [ADS]

Ghez, A. M., Morris, M., Becklin, E. E., Tanner, A. and Kremenek, T., 2000, "The accelerations of stars orbiting the Milky Way's central black hole", *Nature*, **407**(6802), 349–351. [DOI], [ADS], [arXiv:astro-ph/0009339 [astro-ph]]

Ghez, A. M., Salim, S., Weinberg, N. N., Lu, J. R., Do, T., Dunn, J. K., Matthews, K., Morris, M. R., Yelda, S., Becklin, E. E., Kremenek, T., Milosavljevic, M. and Naiman, J., 2008, "Measuring Distance and Properties of the Milky Way's Central Supermassive Black Hole with Stellar Orbits", *Astrophys. J.*, **689**(2), 1044–1062. [DOI], [ADS], [arXiv:0808.2870 [astro-ph]]

Gierliński, Marek, Middleton, Matthew, Ward, Martin and Done, Chris, 2008, "A periodicity of ~1hour in X-ray emission from the active galaxy RE J1034+396", *Nature*, **455**(7211), 369–371. [DOI], [ADS]

Glampedakis, K. and Kennefick, D., 2002, "Zoom and whirl: Eccentric equatorial orbits around spinning black holes and their evolution under gravitational radiation reaction", *Physical Review D*, **66**(4), 044002. [DOI], [ADS], [gr-qc/0203086]

Glampedakis, K., Hughes, S. A. and Kennefick, D., 2002, "Approximating the inspiral of test bodies into Kerr black holes", *Physical Review D*, **66**(6), 064005. [DOI], [ADS], [gr-qc/0205033]

Glampedakis, Kostas, 2005, "Extreme mass ratio inspirals: LISA's unique probe of black hole gravity", *Classical and Quantum Gravity*, **22**, S605–S659. [DOI], [ADS], [arXiv:gr-qc/0509024 [gr-qc]]

González-Martín, O. and Vaughan, S., 2012, "X-ray variability of 104 active galactic nuclei. XMM-Newton power-spectrum density profiles", *Astron. Astrophys.*, **544**, A80. [DOI], [ADS], [arXiv:1205.4255 [astro-ph.HE]]

Goodrich, Robert W., 1989, "Spectropolarimetry of "Narrow-Line" Seyfert 1 Galaxies", *Astrophys. J.*, **342**, 224. [DOI], [ADS]

Gradshteyn, I. S. and Ryzhik, I. M., 2007, *Table of integrals, series, and products*, Elsevier/Academic Press, Amsterdam, seventh edn. Translated from the Russian, Translation edited and with a preface by Alan Jeffrey and Daniel Zwillinger, With one CD-ROM (Windows, Macintosh and UNIX)

Graham, Matthew J., Djorgovski, S. G., Stern, Daniel, Glikman, Eilat, Drake, Andrew J., Mahabal, Ashish A., Donalek, Ciro, Larson, Steve and Christensen, Eric, 2015, "A possible close supermassive black-hole binary in a quasar with optical periodicity", *Nature*, **518**(7537), 74–76. [DOI], [ADS], [arXiv:1501.01375 [astro-ph.GA]]

Grossman, R., Levin, J. and Perez-Giz, G., 2012, "Harmonic structure of generic Kerr orbits", *Physical Review D*, **85**(2), 023012. [DOI], [ADS], [arXiv:1105.5811 [gr-qc]]

Grupe, Dirk, Wills, Beverley J., Leighly, Karen M. and Meusinger, Helmut, 2004, "A Complete Sample of Soft X-Ray-Selected AGNs. I. The Data", *Astron. J.*, **127**(1), 156–179. [DOI], [ADS], [arXiv:astro-ph/0310027 [astro-ph]]

Gupta, Alok C., Srivastava, A. K. and Wiita, Paul J., 2009, "Periodic Oscillations in the Intra-Day Optical Light Curves of the Blazar S5 0716+714", *Astrophys. J.*, **690**(1), 216–223. [DOI], [ADS], [arXiv:0808.3630 [astro-ph]]

Gupta, Alok C., Tripathi, Ashutosh, Wiita, Paul J., Gu, Minfeng, Bambi, Cosimo and Ho, Luis C., 2018, "Possible 1 hour quasi-periodic oscillation in narrow-line Seyfert 1 galaxy MCG-06-30-15", *Astron. Astrophys.*, **616**, L6. [DOI], [ADS], [arXiv:1808.05112 [astro-ph.HE]]

Gupta, Alok C., Tripathi, Ashutosh, Wiita, Paul J., Kushwaha, Pankaj, Zhang, Zhongli and Bambi, Cosimo, 2019, "Detection of a quasi-periodic oscillation in γ-ray light curve of the high-redshift blazar B2 1520+31", *Mon. Not. Roy. Astron. Soc.*, **484**(4), 5785–5790. [DOI], [ADS], [arXiv:1810.12607 [astro-ph.HE]]

Hackmann, E., Lämmerzahl, C., Kagramanova, V. and Kunz, J., 2010, "Analytical solution of the geodesic equation in Kerr-(anti-) de Sitter space-times", *Physical Review D*, **81**(4), 044020. [DOI], [ADS], [arXiv:1009.6117 [gr-qc]]

Hartle, James B., 2003, *Gravity : an introduction to Einstein's general relativity*. [ADS]

Healy, J., Levin, J. and Shoemaker, D., 2009, "Zoom-Whirl Orbits in Black Hole Binaries", *Physical Review Letters*, **103**(13), 131101. [DOI], [ADS], [arXiv:0907.0671 [gr-qc]]

Hille, E, 1979, *Analysis vol 2*, Malabar, FA: Krieger

Ho, Luis C., Kim, Minjin and Terashima, Yuichi, 2012, "The Low-mass, Highly Accreting Black Hole Associated with the Active Galactic Nucleus 2XMM J123103.2+110648", *Astrophys. J. Lett.*, **759**(1), L16. [DOI], [ADS], [arXiv:1210.0440 [astro-ph.CO]]

Homan, J., Wijnands, R., van der Klis, M., Belloni, T., van Paradijs, J., Klein-Wolt, M., Fender, R. and Méndez, M., 2001, "Correlated X-Ray Spectral and Timing Behavior of the Black Hole Candidate XTE J1550-564: A New Interpretation of Black Hole States", *ApJS*, **132**, 377–402. [DOI], [ADS], [astro-ph/0001163]

Homan, J., Klein-Wolt, M., Rossi, S., Miller, J. M., Wijnands, R., Belloni, T., van der Klis, M. and Lewin, W. H. G., 2003, "High-Frequency Quasi-periodic Oscillations in the Black Hole X-Ray Transient XTE J1650-500", *Astrophys. J.*, **586**, 1262–1267. [DOI], [ADS], [astro-ph/0210564]

Homan, J., Miller, J. M., Wijnands, R., van der Klis, M., Belloni, T., Steeghs, D. and Lewin, W. H. G., 2005, "High- and Low-Frequency Quasi-periodic Oscillations in the X-Ray Light Curves of the Black Hole Transient H1743-322", *Astrophys. J.*, **623**, 383–391. [DOI], [ADS], [astro-ph/0406334]

Hu, Chen, Wang, Jian-Min, Ho, Luis C., Bai, Jin-Ming, Li, Yan-Rong, Du, Pu and Lu, Kai-Xing, 2016, "IMPROVING THE FLUX CALIBRATION IN REVERBERATION MAPPING BY SPECTRAL FITTING:APPLICATION TO THE SEYFERT GALAXY MCG–6-30-15", *The Astrophysical Journal*, **832**(2), 197. [DOI]URL: `https://doi.org/10.3847%2F0004-637x%2F832%2F2%2F197`

Ingram, Adam and Done, Chris, 2011, "A physical model for the continuum variability and quasi-periodic oscillation in accreting black holes", *Mon. Not. Roy. Astron. Soc.*, **415**, 2323–2335. [DOI], [ADS], [arXiv:1101.2336 [astro-ph.SR]]

Ingram, Adam and Done, Chris, 2012, "Modelling variability in black hole binaries: linking simulations to observations", *Mon. Not. Roy. Astron. Soc.*, **419**, 2369–2378. [DOI], [ADS], [arXiv:1108.0789 [astro-ph.HE]]

Ingram, Adam, Done, Chris and Fragile, P. Chris, 2009, "Low-frequency quasi-periodic oscillations spectra and Lense-Thirring precession", *Mon. Not. Roy. Astron. Soc.*, **397**, L101–L105. [DOI], [ADS], [arXiv:0901.1238 [astro-ph.SR]]

Jones, C., Forman, W., Tananbaum, H. and Turner, M. J. L., 1976, "Uhuru and Ariel V observations of 3U 1630-47: a recurrent transient X-ray source.", *Astrophys. J. Lett.*, **210**, L9–L11. [DOI], [ADS]

Kato, S., 2004, "Resonant Excitation of Disk Oscillations by Warps: A Model of kHz QPOs", *Pub. Astron. Soc. Japan*, **56**, 905–922. [DOI], [ADS], [astro-ph/0409051]

Kato, Shoji, 2008, "Resonant Excitation of Disk Oscillations in Deformed Disks II: A Model of High-Frequency QPOs", *Publications of the Astronomical Society of Japan*, **60**(1), 111–123. [DOI]URL: `http://dx.doi.org/10.1093/pasj/60.1.111`

Kerr, R. P., 1963, "Gravitational Field of a Spinning Mass as an Example of Algebraically Special Metrics", *Physical Review Letters*, **11**, 237–238. [DOI], [ADS]

King, A. L., Walton, D. J., Miller, J. M., Barret, D., Boggs, S. E., Christensen, F. E., Craig, W. W., Fabian, A. C., Fürst, F., Hailey, C. J., Harrison, F. A., Krivonos, R., Mori, K., Natalucci, L., Stern, D., Tomsick, J. A. and Zhang, W. W., 2014, "The Disk Wind in the Rapidly Spinning Stellar-mass Black Hole 4U 1630-472 Observed with NuSTAR", *Astrophys. J.*, **784**, L2. [DOI], [ADS], [arXiv:1401.3646 [astro-ph.HE]]

King, O. G., Hovatta, T., Max-Moerbeck, W., Meier, D. L., Pearson, T. J., Readhead, A. C. S., Reeves, R., Richards, J. L. and Shepherd, M. C., 2013, "A quasi-periodic oscillation in the blazar J1359+4011.", *Mon. Not. Roy. Astron. Soc.*, **436**, L114–L117. [DOI], [ADS], [arXiv:1309.1158 [astro-ph.HE]]

Klein-Wolt, M., Homan, J. and van der Klis, M., 2004, "High frequency features in the 1998 outburst of 4U 1630-47", *Nuclear Physics B Proceedings Supplements*, **132**, 381–386. [DOI], [ADS], [astro-ph/0309436]

Komossa, S., 2008, "Narrow-line Seyfert 1 Galaxies", in *Revista Mexicana de Astronomia y Astrofisica Conference Series*, Revista Mexicana de Astronomia y Astrofisica Conference Series, 32, [ADS], [arXiv:0710.3326 [astro-ph]]

Kormendy, John and Ho, Luis C., 2013, "Coevolution (Or Not) of Supermassive Black Holes and Host Galaxies", *Ann. Rev. Astron. Astrophys.*, **51**(1), 511–653. [DOI], [ADS], [arXiv:1304.7762 [astro-ph.CO]]

Kramer, M., Stairs, I. H., Manchester, R. N., McLaughlin, M. A., Lyne, A. G., Ferdman, R. D., Burgay, M., Lorimer, D. R., Possenti, A., D'Amico, N., Sarkissian, J. M., Hobbs, G. B., Reynolds, J. E., Freire, P. C. C. and Camilo, F., 2006, "Tests of General Relativity from Timing the Double Pulsar", *Science*, **314**, 97–102. [DOI], [ADS], [astro-ph/0609417]

Kraniotis, G. V., 2004, "Precise relativistic orbits in Kerr and Kerr (anti) de Sitter spacetimes", *Classical and Quantum Gravity*, **21**, 4743–4769. [DOI], [ADS], [gr-qc/0405095]

Kraniotis, G. V., 2007, "Periapsis and gravitomagnetic precessions of stellar orbits in Kerr and Kerr de Sitter black hole spacetimes", *Classical and Quantum Gravity*, **24**, 1775–1808. [DOI], [ADS], [gr-qc/0602056]

Kuulkers, Erik, Wijnands, Rudy, Belloni, Tomaso, Méndez, Mariano, van der Klis, Michiel and van Paradijs, Jan, 1998, "Absorption Dips in the Light Curves of GRO J1655-40 and 4U 1630-47 during Outburst", *Astrophys. J.*, **494**(2), 753–758. [DOI], [ADS], [arXiv:astro-ph/9710024 [astro-ph]]

Levin, J. and Perez-Giz, G., 2008, "A periodic table for black hole orbits", *Physical Review D*, **77**(10), 103005. [DOI], [ADS], [arXiv:0802.0459 [gr-qc]]

Levin, J. and Perez-Giz, G., 2009, "Homoclinic orbits around spinning black holes. I. Exact solution for the Kerr separatrix", *Physical Review D*, **79**(12), 124013. [DOI], [ADS], [arXiv:0811.3814 [gr-qc]]

Lin, Dacheng, Irwin, Jimmy A., Godet, Olivier, Webb, Natalie A. and Barret, Didier, 2013, "A ~3.8 hr Periodicity from an Ultrasoft Active Galactic Nucleus Candidate", *Astrophys. J. Lett.*, **776**(1), L10. [DOI], [ADS], [arXiv:1309.4440 [astro-ph.HE]]

Luminet, J. P., 1979, "Image of a spherical black hole with thin accretion disk.", *Astron. Astrophys.*, **75**, 228–235. [ADS]

Lyne, A. G., Burgay, M., Kramer, M., Possenti, A., Manchester, R. N., Camilo, F., McLaughlin, M. A., Lorimer, D. R., D'Amico, N., Joshi, B. C., Reynolds, J. and Freire, P. C. C., 2004, "A Double-Pulsar System: A Rare Laboratory for Relativistic Gravity and Plasma Physics", *Science*, **303**, 1153–1157. [DOI], [ADS], [astro-ph/0401086]

Mangalam, A., 2018, "Polarization and QPOs from jets in black hole systems", *Journal of Astrophysics and Astronomy*, **39**(6), 68. [DOI], [ADS]

Mangalam, Arun V. and Wiita, Paul J., 1993, "Accretion Disk Models for Optical and Ultraviolet Microvariability in Active Galactic Nuclei", *Astrophys. J.*, **406**, 420. [DOI], [ADS]

Margalit, Ben and Metzger, Brian D., 2017, "Constraining the Maximum Mass of Neutron Stars from Multi-messenger Observations of GW170817", *The Astrophysical Journal*, **850**(2), L19. [DOI]URL: `https://doi.org/10.3847%2F2041-8213%2Faa991c`

McClintock, Jeffrey E. and Remillard, Ronald A., 2006, "Black hole binaries", in *In: Compact stellar X-ray sources. Edited by Walter Lewin & Michiel van der Klis. Cambridge Astrophysics Series, No. 39. Cambridge, UK: Cambridge University Press, ISBN 978-0-521-82659-4, ISBN 0-521-82659-4, DOI: 10.2277/0521826594, 2006, p. 157 - 213*, 39, [ADS]

McHardy, I., 2010, "X-Ray Variability of AGN and Relationship to Galactic Black Hole Binary Systems", in *Lecture Notes in Physics, Berlin Springer Verlag*, (Ed.) Belloni, Tomaso, 794, [DOI], [ADS]

McHardy, I. M., Papadakis, I. E., Uttley, P., Page, M. J. and Mason, K. O., 2004, "Combined long and short time-scale X-ray variability of NGC 4051 with RXTE and XMM-Newton", *Mon. Not. Roy. Astron. Soc.*, **348**(3), 783–801. [DOI], [ADS], [arXiv:astro-ph/0311220 [astro-ph]]

McHardy, I. M., Koerding, E., Knigge, C., Uttley, P. and Fender, R. P., 2006, "Active galactic nuclei as scaled-up Galactic black holes", *Nature*, **444**(7120), 730–732. [DOI], [ADS], [arXiv:astro-ph/0612273 [astro-ph]]

Middleton, M., 2016, "Black Hole Spin: Theory and Observation", in *Astrophysics of Black Holes: From Fundamental Aspects to Latest Developments*, (Ed.) Bambi, Cosimo, Astrophysics and Space Science Library, 440, [DOI], [ADS]

Miller, J. M., Wijnands, R., Homan, J., Belloni, T., Pooley, D., Corbel, S., Kouveliotou, C., van der Klis, M. and Lewin, W. H. G., 2001, "High-Frequency Quasi-Periodic Oscillations in the 2000 Outburst of the Galactic Microquasar XTE J1550-564", *Astrophys. J.*, **563**, 928–933. [DOI], [ADS], [astro-ph/0105371]

Miller, J. M., Parker, M. L., Fuerst, F., Bachetti, M., Harrison, F. A., Barret, D., Boggs, S. E., Chakrabarty, D., Christensen, F. E., Craig, W. W., Fabian, A. C., Grefenstette, B. W., Hailey, C. J., King, A. L., Stern, D. K., Tomsick, J. A., Walton, D. J. and Zhang, W. W., 2013, "NuSTAR Spectroscopy of GRS 1915+105: Disk Reflection, Spin, and Connections to Jets", *Astrophys. J.*, **775**, L45. [DOI], [ADS], [arXiv:1308.4669 [astro-ph.HE]]

Miller, M. C. and Miller, J. M., 2015, "The masses and spins of neutron stars and stellar-mass black holes", *PhysRep*, **548**, 1–34. [DOI], [ADS], [arXiv:1408.4145 [astro-ph.HE]]

Miller, M. Coleman and Colbert, E. J. M., 2004, "Intermediate-Mass Black Holes", *International Journal of Modern Physics D*, **13**(1), 1–64. [DOI], [ADS], [arXiv:astro-ph/0308402 [astro-ph]]

Mino, Y., 2003, "Perturbative approach to an orbital evolution around a supermassive black hole", *Physical Review D*, **67**(8), 084027. [DOI], [ADS], [gr-qc/0302075]

Mirabel, I. F. and Rodríguez, L. F., 1994, "A superluminal source in the Galaxy", *Nature*, **371**(6492), 46–48. [DOI], [ADS]

Misner, Charles W., Thorne, Kip S. and Wheeler, John A., 1973, *Gravitation*. [ADS]

Miyoshi, Makoto, Moran, James, Herrnstein, James, Greenhill, Lincoln, Nakai, Naomasa, Diamond, Philip and Inoue, Makoto, 1995, "Evidence for a black hole from high rotation velocities in a sub-parsec region of NGC4258", *Nature*, **373**(6510), 127–129. [DOI], [ADS]

Mohan, P. and Mangalam, A., 2014, "X-Ray Variability and the Inner Region in Active Galactic Nuclei", *Astrophys. J.*, **791**(2), 74. [DOI], [ADS], [arXiv:1406.6469 [astro-ph.HE]]

Mohan, P. and Mangalam, A., 2015, "Kinematics of and Emission from Helically Orbiting Blobs in a Relativistic Magnetized Jet", *Astrophys. J.*, **805**(2), 91. [DOI], [ADS], [arXiv:1503.06551 [astro-ph.HE]]

Mohan, P., Gupta, Alok C., Bachev, Rumen and Strigachev, Anton, 2016, "Kepler light-curve analysis of the blazar W2R 1926+42", *Mon. Not. Roy. Astron. Soc.*, **456**(1), 654–664. [DOI], [ADS], [arXiv:1511.05232 [astro-ph.HE]]

Morgan, E. H., Remillard, R. A. and Greiner, J., 1997, "RXTE Observations of QPOs in the Black Hole Candidate GRS 1915+105", *Astrophys. J.*, **482**, 993–1010. [DOI], [ADS]

Motta, S. E., 2016, "Quasi periodic oscillations in black hole binaries", *Astronomische Nachrichten*, **337**, 398. [DOI], [ADS], [arXiv:1603.07885 [astro-ph.HE]]

Motta, S. E., Belloni, T. M., Stella, L., Muñoz-Darias, T. and Fender, R., 2014a, "Precise mass and spin measurements for a stellar-mass black hole through X-ray timing: the case of GRO J1655-40", *MNRAS*, **437**, 2554–2565. [DOI], [ADS], [arXiv:1309.3652 [astro-ph.HE]]

Motta, S. E., Muñoz-Darias, T., Sanna, A., Fender, R., Belloni, T. and Stella, L., 2014b, "Black hole spin measurements through the relativistic precession

model: XTE J1550-564", *MNRAS*, **439**, L65–L69. [DOI], [ADS], [arXiv:1312.3114 [astro-ph.HE]]

Motta, S. E., Franchini, A., Lodato, G. and Mastroserio, G., 2018, "On the different flavours of Lense-Thirring precession around accreting stellar mass black holes", *Mon. Not. Roy. Astron. Soc.*, **473**, 431–439. [DOI], [ADS], [arXiv:1709.02608 [astro-ph.HE]]

Mudambi, Sneha Prakash, Rao, A., Gudennavar, S. B., Misra, R. and Bubbly, S. G., 2020, "Estimation of the black hole spin in LMC X-1 using AstroSat", *Mon. Not. Roy. Astron. Soc.*, **498**(3), 4404–4410. [DOI], [ADS], [arXiv:2008.12588 [astro-ph.HE]]

Narayan, R., 2005, "Black holes in astrophysics", *New Journal of Physics*, **7**, 199. [DOI], [ADS], [gr-qc/0506078]

Novikov, I. D. and Thorne, K. S., 1973, "Astrophysics of black holes.", in *Black Holes (Les Astres Occlus)*, [ADS]

Okajima, Takashi, Ebisawa, Ken and Kawaguchi, Toshihiro, 2006, "A Stellar-Mass Black Hole in the Ultraluminous X-Ray Source M82 X-1?", *Astrophys. J. Lett.*, **652**(2), L105–L108. [DOI], [ADS], [arXiv:astro-ph/0610430 [astro-ph]]

Oppenheimer, J. R. and Volkoff, G. M., 1939, "On Massive Neutron Cores", *Phys. Rev.*, **55**, 374–381. [DOI]URL: `https://link.aps.org/doi/10.1103/PhysRev.55.374`

Orosz, J. A., Steiner, J. F., McClintock, J. E., Torres, M. A. P., Remillard, R. A., Bailyn, C. D. and Miller, J. M., 2011, "An Improved Dynamical Model for the Microquasar XTE J1550-564", *Astrophys. J.*, **730**, 75. [DOI], [ADS], [arXiv:1101.2499 [astro-ph.SR]]

O'Shaughnessy, R., 2003, "Transition from inspiral to plunge for eccentric equatorial Kerr orbits", *Physical Review D*, **67**(4), 044004. [DOI], [ADS], [gr-qc/0211023]

Osterbrock, D. E. and Pogge, R. W., 1985, "The spectra of narrow-line Seyfert 1 galaxies.", *Astrophys. J.*, **297**, 166–176. [DOI], [ADS]

Padovani, P., Alexander, D. M., Assef, R. J., De Marco, B., Giommi, P., Hickox, R. C., Richards, G. T., Smolčić, V., Hatziminaoglou, E., Mainieri, V. and Salvato, M., 2017, "Active galactic nuclei: what's in a name?", *Astron. Astrophys. Rev.*, **25**(1), 2. [DOI], [ADS], [arXiv:1707.07134 [astro-ph.GA]]

Pan, Hai-Wu, Yuan, Weimin, Yao, Su, Zhou, Xin-Lin, Liu, Bifang, Zhou, Hongyan and Zhang, Shuang-Nan, 2016, "Detection of a Possible X-Ray Quasi-periodic Oscillation in the Active Galactic Nucleus 1H 0707-495", *Astrophys. J. Lett.*, **819**(2), L19. [DOI], [ADS], [arXiv:1601.07639 [astro-ph.HE]]

Papadakis, I. E., Brinkmann, W., Gliozzi, M. and Raeth, C., 2010, "XMM-Newton long-look observation of the narrow-line Seyfert 1 galaxy PKS 0558-504. II. Timing analysis", *Astron. Astrophys.*, **518**, A28. [DOI], [ADS]

Pasham, D. R., Strohmayer, T. E. and Mushotzky, R. F., 2014, "A 400-solar-mass black hole in the galaxy M82", *Nature*, **513**, 74–76. [DOI], [ADS], [arXiv:1501.03180 [astro-ph.HE]]

Pasham, Dheeraj R. and Strohmayer, Tod E., 2013a, "Can the 62 Day X-Ray Period of ULX M82 X-1 Be Due to a Precessing Accretion Disk?", *Astrophys. J. Lett.*, **774**(2), L16. [DOI], [ADS], [arXiv:1308.1682 [astro-ph.HE]]

Pasham, Dheeraj R. and Strohmayer, Tod E., 2013b, "On the Nature of the mHz X-Ray Quasi-periodic Oscillations from Ultraluminous X-Ray Source M82 X-1: Search for Timing-Spectral Correlations", *Astrophys. J.*, **771**(2), 101. [DOI], [ADS], [arXiv:1308.1677 [astro-ph.HE]]

Patruno, A., Portegies Zwart, S., Dewi, J. and Hopman, C., 2006, "The ultra-luminous X-ray source in M82: an intermediate-mass black hole with a giant companion", *Mon. Not. Roy. Astron. Soc.*, **370**(1), L6–L9. [DOI], [ADS], [arXiv:astro-ph/0602230 [astro-ph]]

Peng, ZHANG, Jing-zhi, YAN and Qing-zhong, LIU, 2020, "Two Quasi-periodic Oscillations in ESOÂă113-G010", *Chinese Astronomy and Astrophysics*, **44**(1), 32 – 40. [DOI]URL: http://www.sciencedirect.com/science/article/pii/S0275106220300023

Penna, Robert F., Sądowski, Aleksander and McKinney, Jonathan C., 2012, "Thin-disc theory with a non-zero-torque boundary condition and comparisons with simulations", *Mon. Not. Roy. Astron. Soc.*, **420**(1), 684–698. [DOI], [ADS], [arXiv:1110.6556 [astro-ph.HE]]

Penrose, R., 1969, "Gravitational collapse: The role of general relativity", *Riv. Nuovo Cim.*, **1**, 252–276. [DOI]

Perez-Giz, G. and Levin, J., 2009, "Homoclinic orbits around spinning black holes. II. The phase space portrait", *Physical Review D*, **79**(12), 124014. [DOI], [ADS], [arXiv:0811.3815 [gr-qc]]

Peterson, Bradley M., 1993, "Reverberation Mapping of Active Galactic Nuclei", *Pub. Astron. Soc. Pac.*, **105**, 247. [DOI], [ADS]

Priedhorsky, W., 1986, "Recurrent Population II X-ray transients — similarities to SU UMa cataclysmic variables", *Astrophys. Space Sci.*, **126**(1), 89–98. [DOI], [ADS]

Psaltis, Dimitrios, Belloni, Tomaso and van der Klis, Michiel, 1999, "Correlations in Quasi-periodic Oscillation and Noise Frequencies among Neutron Star and Black Hole X-Ray Binaries", *Astrophys. J.*, **520**, 262–270. [DOI], [ADS], [arXiv:astro-ph/9902130 [astro-ph]]

Rana, Prerna and Mangalam, A., 2019a, "Astrophysically relevant bound trajectories around a Kerr black hole", *Classical and Quantum Gravity (RM19a)*, **36**, 045009. [DOI], [ADS], [arXiv:1901.02730 [gr-qc]]

Rana, Prerna and Mangalam, A., 2019b, "Astrophysically relevant bound trajectories around a Kerr black hole", *arXiv e-prints, arXiv:1901.02730 (RM19b)*

Rana, Prerna and Mangalam, A., 2020a, "A Relativistic Orbit Model for Temporal Properties of AGN", *Galaxies*, **8**(3), 67. [DOI], [ADS], [arXiv:2009.03061 [astro-ph.HE]]

Rana, Prerna and Mangalam, A., 2020b, "A Geometric Origin for Quasi-periodic Oscillations in Black Hole X-Ray Binaries", *Astrophys. J.*, **903**(2), 121. [DOI], [ADS], [arXiv:2009.01832 [astro-ph.HE]]

Rana, Prerna and Mangalam, A., 2020c, "Bound orbit domains in the phase space of the Kerr geometry", *submitted as conference proceeding to The Fifteenth Marcel Grossmann Meeting.*

Rana, Prerna and Mangalam, A., 2020d, "Eccentric equatorial trajectories around a Kerr black hole as a QPO model for M82X-1", *submitted as conference proceeding to The Fifteenth Marcel Grossmann Meeting.*

Rees, Martin J., 1984, "Black Hole Models for Active Galactic Nuclei", *Ann. Rev. Astron. Astrophys.*, **22**, 471–506. [DOI], [ADS]

Remillard, R. A., Morgan, E. H., McClintock, J. E., Bailyn, C. D. and Orosz, J. A., 1999a, "RXTE Observations of 0.1-300 HZ Quasi-periodic Oscillationsin the Microquasar GRO J1655-40", *Astrophys. J.*, **522**, 397–412. [DOI], [ADS]

Remillard, R. A., Sobczak, G. J., Muno, M. P. and McClintock, J. E., 2002, "Characterizing the Quasi-periodic Oscillation Behavior of the X-Ray Nova XTE J1550-564", *Astrophys. J.*, **564**, 962–973. [DOI], [ADS], [astro-ph/0105508]

Remillard, R. A., McClintock, J. E., Orosz, J. A. and Levine, A. M., 2006, "The X-Ray Outburst of H1743-322 in 2003: High-Frequency QPOs with a 3:2 Frequency Ratio", *Astrophys. J.*, **637**, 1002–1009. [DOI], [ADS], [astro-ph/0407025]

Remillard, Ronald A., McClintock, Jeffrey E., Sobczak, Gregory J., Bailyn, Charles D., Orosz, Jerome A., Morgan, Edward H. and Levine, Alan M., 1999b,

"X-Ray Nova XTE J1550-564: Discovery of a Quasi-periodic Oscillation near 185 HZ", *Astrophys. J. Lett.*, **517**(2), L127–L130. [DOI], [ADS]

Sandrinelli, A., Covino, S. and Treves, A., 2014, "Quasi-periodicities of the BL Lacertae Object PKS 2155-304", *Astrophys. J. Lett.*, **793**(1), L1. [DOI], [ADS], [arXiv:1408.0015 [astro-ph.HE]]

Sandrinelli, A., Covino, S., Dotti, M. and Treves, A., 2016a, "Quasi-periodicities at Year-like Timescales in Blazars", *Astron. J.*, **151**(3), 54. [DOI], [ADS], [arXiv:1512.04561 [astro-ph.GA]]

Sandrinelli, A., Covino, S. and Treves, A., 2016b, "Gamma-Ray and Optical Oscillations in PKS 0537-441", *Astrophys. J.*, **820**(1), 20. [DOI], [ADS], [arXiv:1512.08801 [astro-ph.GA]]

Sandrinelli, A., Covino, S., Treves, A., Lindfors, E., Raiteri, C. M., Nilsson, K., Takalo, L. O., Reinthal, R., Berdyugin, A., Fallah Ramazani, V., Kadenius, V., Tuominen, T., Kehusmaa, P., Bachev, R. and Strigachev, A., 2017, "Gamma-ray and optical oscillations of 0716+714, MRK 421, and BL Lacertae", *Astron. Astrophys.*, **600**, A132. [DOI], [ADS], [arXiv:1701.04454 [astro-ph.HE]]

Sandrinelli, A., Covino, S., Treves, A., Holgado, A. M., Sesana, A., Lindfors, E. and Ramazani, V. F., 2018, "Quasi-periodicities of BL Lacertae objects", *Astron. Astrophys.*, **615**, A118. [DOI], [ADS], [arXiv:1801.06435 [astro-ph.HE]]

Schmidt, W., 2002, "Celestial mechanics in Kerr spacetime", *Classical and Quantum Gravity*, **19**, 2743–2764. [DOI], [ADS], [gr-qc/0202090]

Schödel, R., Ott, T., Genzel, R., Hofmann, R., Lehnert, M., Eckart, A., Mouawad, N., Alexander, T., Reid, M. J., Lenzen, R., Hartung, M., Lacombe, F., Rouan, D., Gendron, E., Rousset, G., Lagrange, A. M., Brandner, W., Ageorges, N., Lidman, C., Moorwood, A. F. M., Spyromilio, J., Hubin, N. and Menten, K. M., 2002, "A star in a 15.2-year orbit around the supermassive black hole at the centre of the Milky Way", *Nature*, **419**(6908), 694–696. [DOI], [ADS], [arXiv:astro-ph/0210426 [astro-ph]]

Schwarzschild, K., 1916, "On the Gravitational Field of a Mass Point According to Einstein's Theory", *Abh. Konigl. Preuss. Akad. Wissenschaften Jahre 1906,92, Berlin,1907*, **1916**, 189–196. [ADS]

Seifina, E., Titarchuk, L. and Shaposhnikov, N., 2014, "Black Hole Mass Determination in the X-Ray Binary 4U 1630-47: Scaling of Spectral and Variability Characteristics", *Astrophys. J.*, **789**, 57. [DOI], [ADS], [arXiv:1405.4711 [astro-ph.SR]]

Shakura, N. I. and Sunyaev, R. A., 1973, "Reprint of 1973A&A....24..337S. Black holes in binary systems. Observational appearance.", *Astron. Astrophys.*, **500**, 33–51. [ADS]

Sopuerta, C. F. and Yunes, N., 2011, "New Kludge scheme for the construction of approximate waveforms for extreme-mass-ratio inspirals", *Physical Review D*, **84**(12), 124060. [DOI], [ADS], [arXiv:1109.0572 [gr-qc]]

Steeghs, D., McClintock, J. E., Parsons, S. G., Reid, M. J., Littlefair, S. and Dhillon, V. S., 2013, "The Not-so-massive Black Hole in the Microquasar GRS1915+105", *Astrophys. J.*, **768**, 185. [DOI], [ADS], [arXiv:1304.1808 [astro-ph.HE]]

Stella, L. and Vietri, M., 1999, "kHz Quasiperiodic Oscillations in Low-Mass X-Ray Binaries as Probes of General Relativity in the Strong-Field Regime", *Physical Review Letters*, **82**, 17–20. [DOI], [ADS], [astro-ph/9812124]

Stella, L., Vietri, M. and Morsink, S. M., 1999, "Correlations in the Quasi-periodic Oscillation Frequencies of Low-Mass X-Ray Binaries and the Relativistic Precession Model", *Astrophys. J.*, **524**, L63–L66. [DOI], [ADS], [astro-ph/9907346]

Strohmayer, T. E., 2001a, "Discovery of a 450 HZ Quasi-periodic Oscillation from the Microquasar GRO J1655-40 with the Rossi X-Ray Timing Explorer", *Astrophys. J.*, **552**, L49–L53. [DOI], [ADS]

Strohmayer, T. E., 2001b, "Discovery of a Second High-Frequency Quasi-periodic Oscillation from the Microquasar GRS 1915+105", *Astrophys. J.*, **554**, L169–L172. [DOI], [ADS], [astro-ph/0105338]

Tagger, Michel and Varnière, Peggy, 2006, "Accretion-Ejection Instability, MHD Rossby Wave Instability, Diskoseismology, and the High-Frequency QPOs of Microquasars", *Astrophys. J.*, **652**, 1457–1465. [DOI], [ADS], [arXiv:astro-ph/0608123 [astro-ph]]

Tavani, M., Cavaliere, A., Munar-Adrover, Pere and Argan, A., 2018, "The Blazar PG 1553+113 as a Binary System of Supermassive Black Holes", *Astrophys. J.*, **854**(1), 11. [DOI], [ADS], [arXiv:1801.03335 [astro-ph.HE]]

Teukolsky, S. A., 1973, "Perturbations of a Rotating Black Hole. I. Fundamental Equations for Gravitational, Electromagnetic, and Neutrino-Field Perturbations", *Astrophys. J.*, **185**, 635–648. [DOI], [ADS]

Török, G., Abramowicz, M. A., Kluźniak, W. and Stuchlík, Z., 2005, "The orbital resonance model for twin peak kHz quasi periodic oscillations in microquasars", *Astron. Astrophys.*, **436**, 1–8. [DOI], [ADS]

Török, G., Kotrlová, A., Šrámková, E. and Stuchlík, Z., 2011, "Confronting the models of 3:2 quasiperiodic oscillations with the rapid spin of the microquasar GRS 1915+105", *A&A*, **531**, A59. [DOI], [ADS], [arXiv:1103.2438 [astro-ph.HE]]

Urry, C. Megan and Padovani, Paolo, 1995, "Unified Schemes for Radio-Loud Active Galactic Nuclei", *Pub. Astron. Soc. Pac.*, **107**, 803. [DOI], [ADS], [arXiv:astro-ph/9506063 [astro-ph]]

Varniere, P., Casse, F. and Vincent, F. H., 2019, "Rossby wave instability and high-frequency quasi-periodic oscillations in accretion discs orbiting around black holes", *Astron. Astrophys.*, **625**, A116. [DOI], [ADS], [arXiv:1905.03984 [astro-ph.HE]]

Vokrouhlicky, D. and Karas, V., 1993, "A Star Orbiting around a Supermassive Rotating Black-Hole - Free Motion and Corrections due to Star-Disc Collisions", *MNRAS*, **265**, 365. [DOI], [ADS]

Walton, D. J., Reis, R. C., Cackett, E. M., Fabian, A. C. and Miller, J. M., 2012, "The similarity of broad iron lines in X-ray binaries and active galactic nuclei", *Mon. Not. Roy. Astron. Soc.*, **422**(3), 2510–2531. [DOI], [ADS], [arXiv:1202.5193 [astro-ph.HE]]

Wang, T. and Lu, Y., 2001, "Black hole mass and velocity dispersion of narrow line region in active galactic nuclei and narrow line Seyfert 1 galaxies", *Astron. Astrophys.*, **377**, 52–59. [DOI], [ADS], [arXiv:astro-ph/0107528 [astro-ph]]

Warburton, Niels, Barack, Leor and Sago, Norichika, 2013, "Isofrequency pairing of geodesic orbits in Kerr geometry", *Physical Review D*, **87**(8), 084012. [DOI], [ADS], [arXiv:1301.3918 [gr-qc]]

Wilkins, D. C., 1972, "Bound Geodesics in the Kerr Metric", *Physical Review D*, **5**, 814–822. [DOI], [ADS]

Zhang, Bing-Kai, Zhao, Xiao-Yun, Wang, Chun-Xiao and Dai, Ben-Zhong, 2014, "Optical quasi-periodic oscillation and color behavior of blazar PKS 2155-304", *Research in Astronomy and Astrophysics*, **14**(8), 933-941. [DOI], [ADS], [arXiv:1405.6858 [astro-ph.HE]]

Zhang, Peng, Zhang, Peng-fei, Yan, Jing-zhi, Fan, Yi-zhong and Liu, Qing-zhong, 2017, "An X-Ray Periodicity of ÌČ1.8 hr in Narrow-line Seyfert 1 Galaxy Mrk 766", *Astrophys. J.*, **849**(1), 9. [DOI], [ADS], [arXiv:1707.03586 [astro-ph.HE]]

Zhang, Peng-fei, Zhang, Peng, Liao, Neng-hui, Yan, Jing-zhi, Fan, Yi-zhong and Liu, Qing-zhong, 2018, "Two Transient X-Ray Quasi-periodic Oscillations Separated by an Intermediate State in 1H 0707-495", *Astrophys. J.*, **853**(2), 193. [DOI], [ADS], [arXiv:1703.07186 [astro-ph.HE]]

Zhang, S. N., Cui, Wei and Chen, Wan, 1997, "Black Hole Spin in X-Ray Binaries: Observational Consequences", *Astrophys. J. Lett.*, **482**(2), L155–L158. [DOI], [ADS], [arXiv:astro-ph/9704072 [astro-ph]]

Zhao, Xue-Shan and Dong, Yan-Ting et. al., 2020, "Confirming the spin parameter of the black hole in Cygnus X-1 using the Insight-HXMT", *Journal of High Energy Astrophysics*, **27**, 53–63. [DOI], [ADS]

Zhou, Xin-Lin, Zhang, Shuang-Nan, Wang, Ding-Xiong and Zhu, Ling, 2010, "Calibrating the Correlation Between Black Hole Mass and X-ray Variability Amplitude: X-ray Only Black Hole Mass Estimates for Active Galactic Nuclei and Ultra-luminous X-ray Sources", *Astrophys. J.*, **710**(1), 16–23. [DOI], [ADS], [arXiv:0912.2636 [astro-ph.HE]]